Novel optoelectronic systems for use in absolute position sensing applications

Griffiths, Roger Phillip

Award date:
1998

Awarding institution:
University of Bath

Novel Optoelectronic Systems for Use in Absolute Position Sensing Applications

submitted by Roger Phillip Griffiths
for the degree of PhD of the University of Bath
1998

ProQuest LLC
789 East Eisenhower Parkway
P.O. Box 1346
Ann Arbor, MI 48106-1346

To Mum and Dad

SUMMARY

This thesis describes the development of two novel optoelectronic systems which have been designed for use in absolute position sensing applications. Chapter 1 provides an introduction to the work and reviews the wide variety of optical techniques which are presently available for position measurement.

The second chapter provides a synopsis of a new type of optical position sensor designed for medium range sensing applications. This novel system uses optical feedback to a semiconductor laser to measure position. Unlike other proposed feedback sensing systems, this arrangement monitors the frequencies of RF beat modes generated within the laser diode to produce a position measurement capable of micron scale accuracy. The system operates using low optical powers and may be configured to operate as a non-contact, contact or fibre-addressed sensor.

Chapter 4 examines the stability of the sensor. In particular, it assesses how the sensor is affected by variations in key operating parameters, such as bias current and feedback strength. Meanwhile, chapter 5 describes a number of signal processing systems which may be used to interface with the RF signal generated by the optical system to provide a real-time output of a suitable form.

In addition to examining the experimental operation of the sensor, a thorough theoretical analysis of the operation of the system is presented in chapters 3 and 6. Both steady-state and dynamic approaches are used to analyse the behaviour of the optical system. These allow accurate predictions of the sensor performance to be generated, both for general operation and for stability analysis.

Finally chapter 7 describes a separate novel optical position sensor, which provides absolute position measurement with accuracies of 0.004% of measurement range. This sensor utilises reflection from a novel dual track grating, which consists of a pseudo-random binary sequence written in parallel with a periodic asymmetric pattern.

Acknowledgements

Firstly I would like to thank my supervisor, Professor I.H.White for his constant guidance and encouragement throughout my studies. I am also grateful to Mr.P.J.Smith and Mr.R.D.Garbett of RDP Electronics Ltd, Wolverhampton, for their help, kindness and personal support through the EPSRC CASE award scheme. I would also like to acknowledge support for the work carried out as part of the 'Salome' project in DTI/EPSRC LINK Photonics Scheme, in conjunction with RDP Electronics.

There are a large number of people, too numerous to mention, who have helped me during the course of my studies. However I would like to thank Dr. Peter Ford of the University of Bath, Mr. Bob Bowden of the University of Bristol and Mr. Terry Hopkins at RDP Electronics and their staff for all their help and for the preparation of mounts and equipment to enable me carry out my work. Appreciation also goes to Dr Richard Penty, Dr. Frances Laughton, Dr. Mehdi Asghari, Prof. G.Saunders, Dr.W.Clarke, Ian Williams, Eva Ashford and the late Neil Forbes.

Special thanks must go to Kevin Williams and Adrian Wonfor for amongst many other things, introducing me to the joys of rate equation modelling of semiconductor laser diodes using 'C'. I am also very grateful to Ross Wilkinson for his help in the design and troubleshooting of problematic RF electronic circuits. The following colleagues also deserve a mention for their help and assistance during the course of my work and for making the research group an enjoyable place to work: Mark Owen, Benyuan Zhu, Huw Summers, Les, Casper, Lutz Raddatz, Julian Fells, Mike Cowin, Paul Snow, Christine Mignosi, and to Stewart Hughes and Stephen Smith of RDP Electronics Ltd. Further grateful thanks also go to all those who were brave enough to help proof read my thesis.

I would like to thank my parents for all the love and help they have always given me over the years, without which I would not have been able to achieve what I have. I know that my mother would have been very proud to see me complete my studies. Finally, to Nia, a special thank-you for all your love, patience, motivation, and for making me happy all of the time.

List Of Publications

[1] R.P.Griffiths and I.H.White, GB Patent Application No. GB9602772.7, 1994

[2] R.P.Griffiths and I.H.White, UK patent application No. 9608370.4, 23/4/96

[3] R.P.Griffiths and I.H.White, UK patent application No. 9704937.3, 10/3/97

[4] R.P.Griffiths and I.H.White, International PCT patent application No. CT/GB97/01123, 23/4/97

[5] R.P.Griffiths and I.H.White, "A high resolution optical position sensor using optical feedback to a semiconductor laser", *Proc. Sensors & their applications VIII*, Glasgow, UK, 7-10, pp.291-296, September 1997.

[6] R.P.Griffiths, C.Mignosi and I.H.White, "The cavity resonant optical position sensor : A new type of optical position sensor", *Proc. CLEO'98,* San Francisco, USA, May 1998.

[7] R.P.Griffiths, I.H.White, P.J.Smith, "A novel high resolution optical absolute position sensor", *Proc. Sensors and Transducers Conference at MTEC'98*, N.E.C. Birmingham, Session 3, pp.1, 1998

[8] N.Lieven, I.H.White, C.Mignosi, R.P.Griffiths and R.V.Penty, "External cavity laser diode sensing for vibration measurement in aerospace applications", *Proc SPIE Conf. on Laser vibrometry*, Italy, 1998 - to be published.

Table of Contents

CHAPTER 1

INTRODUCTION

In order to place the research work contained within this thesis in context this chapter provides a review of previously developed optical position sensing technology. The relative merits and disadvantages of these existing techniques are discussed, with particular emphasis on medium range sensing, thus enabling the stimulus of the work to be presented. In addition, industrial application areas which are likely be particularly suited to optical position sensors are identified, while a short analysis of non-optical techniques is also presented.

1.1. Introduction

The global position sensor market is predicted to grow over the next 10 years. In fact Frost and Sullivan [1] forecast that the European market alone is expected to produce a revenue of $1.78 billion by 2002. It is also predicted that by this time, the market share of traditional position measurement techniques for industrial applications will have decreased. These traditional techniques include such apparatus as the Linear Variable Differential Transformer (LVDT) which is a common means of measuring position and displacement and is applied to a large number of sensing applications in all spheres of industry. The reduction in the market share of traditional techniques will be due in part to the emergence of new technology sensors with enhanced performance characteristics. These improved devices are required because manufacturing industry is beginning to realise that accurate, fast, high performance sensing methods are essential for increased and improved industrial automation. This is driven by the need to improve quality, cut operating costs and improve safety at work. Of these novel devices, optoelectronic sensors are expected to lead the growth in new technology sensors.

Position sensing forms just one area of application for optical, optoelectronic and fibre-optic sensors. It has been shown in the past that such systems can be used

to measure an extremely wide variety of physical parameters which include pressure, temperature, strain, acceleration, velocity and pH. They may also be used in chemical applications where a measurement of the concentration of particular chemical compounds or gases is required. The whole sensing area is well described in a number of excellent texts and review papers [2,3] which includes the comprehensive series on Optical Fiber Sensors edited by Culshaw and Dakin [4].

Optoelectronic position sensors can come in many different forms, based on a wide variety of measurement principles. They may also be applied to a wide variety of applications, from extreme long-range distance measurement, to ultra accurate measurement on nanometre scales. However, possibly one of the greatest challenges is to devise and construct an optical sensor which can be engineered into a product which is rugged, reliable and economically competitive.

This chapter will describe some of the main techniques which have been developed in this area and through this discussion will explain the requirement for the further development of novel optical measurement systems.

1.2. Methods of optical position sensing

There are a rich variety of different methods for performing the measurement of position or displacement using optical means which have been developed over recent years. Some of these are based upon traditional electronic techniques while others are completely novel in their concept. Due to the variety of sensing systems that exist it is difficult to classify them with respect to measurement range as certain measurement principles can be applied to both short and long range techniques. However, it is generally true to say that optical range finders based upon geometrical and time-of-flight principles provide the longest measurement range. Then in typical order of decreasing measurement range come optical encoders, continuous wave ranging and triangulation techniques. For the measurement of extremely small displacements, interferometry, fibre-optic reflection and microbend sensors provide optimum performance. In order to appreciate the principles of measurement involved

with each of these techniques, they will be briefly described with examples given in the following sections.

1.2.1. Range-finding

One of the most long standing applications of optical systems to position measurement is in the field of range-finding. This definition covers a collection of optical techniques which are generally used for the non-contact measurement of long distances, normally greater than 10 metres, not only for civilian applications such as surveying, but also for military purposes.

Possibly the most simple optical range finder is the *stadia* range-finder [5]. This requires the sighting of a target object, whose width is known, or may be estimated. The principle of operation is based upon the fact that the width of the target, W will subtend an angle θ at a particular distance R. Therefore, using the apparatus shown in figure 1.1, the angle θ can be measured, allowing the range, R to be calculated through the relationship,

$$R = W / \theta . \qquad (1.1)$$

The adjustment of a rotatable mirror allows the user to superimpose the two optical beams so that the end of target object in one beam is superimposed upon the other. The angular position of the mirror would be calibrated in distance, allowing the range of the object to be ascertained.

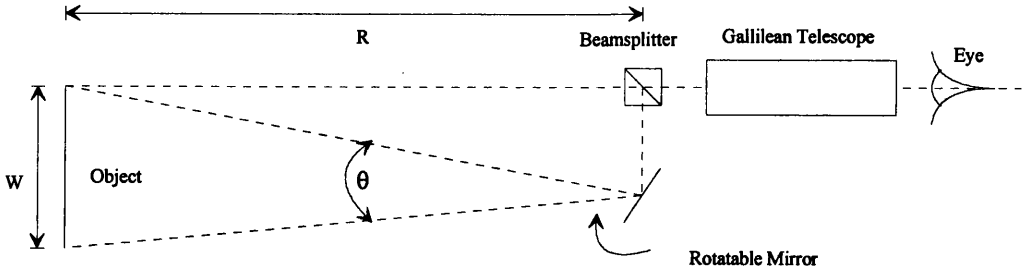

Figure 1.1. Schematic representation of a stadia range finder, (after [5]).

This method can be inaccurate due to the requirement of knowing the target width and orientation. Therefore, self-contained base range finders were introduced which measured the angle subtended by the base of the instrument, and not the target.

However, the field of range finding was dramatically reformed after the advent of the laser [6]. Within months of this discovery, the first time-of-flight laser rangefinder, had been developed [7]. This system measured the time delay for an optical pulse to travel to a remote target and return after reflection. Measurement of this time delay T_{DELAY}, along with the speed of light c, allowed the distance to the target, R to be measured since,

$$R = \frac{cT_{DELAY}}{2}. \qquad (1.2)$$

The arrangement shown in figure 1.2 is a typical representation of a time-of-flight measurement system. In practice the beamsplitter shown may not be required, since diffuse reflection from the target may be incident upon a detector adjacent to the laser. It should be appreciated that in many cases an output pulse of high peak power may be required along with a high sensitivity detector circuit, as it is possible that unless a retroreflecting target is attached to the body under test, only a very small fraction of the outgoing pulse will return to the detector. This is particularly true for extremely long range, rangefinding applications.

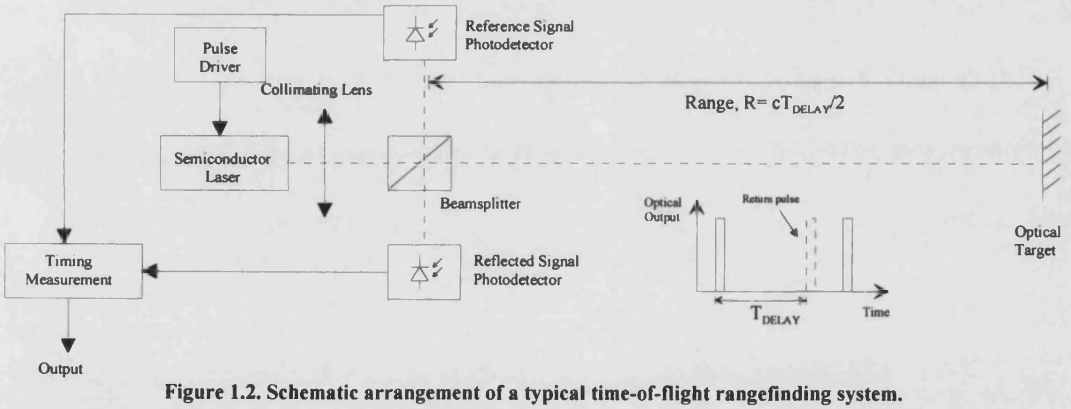

Figure 1.2. Schematic arrangement of a typical time-of-flight rangefinding system.

The resolution of such a system is determined by the temporal resolution of the timing circuitry incorporated within the sensor along with pulsewidth and timing jitter of the optical pulses emitted by the laser. Typical commercial systems can measure ranges to several kilometres, while resolutions are in practice typically limited to about 3cm. This fundamental timing resolution generally restricts the use of time-of-flight rangefinding to long range measurement applications. A distance resolution of 3cm corresponds to a timing resolution of 200ps. It is possible to

reduce this figure by employing extremely advanced timing systems or by the use of phase comparison techniques. This would involve the comparison of the modulating signal phase of the reflected and reference beam of a modulated optical source. Resolution enhancements of typically an order of magnitude can be obtained using this means, when used alongside the simple timing technique to avoid ambiguity.

In recent years there has been a proliferation in the usage of these systems as component costs reduce. Nonetheless, while simple time-of flight systems have become inexpensive, and more generally available, further research is being carried out into improved techniques and systems. For example, Kaisto et al, [8] have produced a range finding system based upon the time of flight method which is capable of measuring a range of 1.5-10m to a resolution of ±1mm, which uses a fast signal processing system. An alternative range finding system has been developed by DeWitt and Lyon [9] which uses near-field diffraction patterns to assess the target distance. The advantage of this system is that it can operate with very little target stand-off (reduced minimum operating distances).

Finally an example is given of one of the many extremely high performance systems used for topographical modelling and distance ranging by satellite [10]. This uses a complex dual streak camera based system which allows an intrinsic system resolution of 3mm to be achieved, although in typical operating conditions this is reduced to not greater than 1cm - this is over a measurement distance of 30km. This configuration has been used to monitor the relative shifts of geological plates. A full review of early systems designed for these extremely long range measurements is given by Bender [11].

1.2.2. Interferometry

A great deal of research into the use of interferometry for position measurement has been carried out in recent years. Interferometric sensors are especially suited to applications where very small displacements are required to be measured, although some systems can provide displacement measurement over

ranges of several cm. Detailed descriptions of the operation of particular types of interferometer can be found in many texts such as Born and Wolf [12].

The application of interferometers to displacement measurement can be immediately identified by considering a very simple example. The transfer function of the commonly used Michelson interferometer when illuminated with monochromatic light may be given by

$$I(k) = 1/2 + 1/2\cos(\frac{4\pi}{\lambda} l + \theta), \qquad (1.3)$$

where l is the optical path imbalance of the interferometer and λ is the wavelength of the light and θ is the dc relative phase difference between the two arms of the interferometer. Examination of equation 1.3 shows that the interferogram produced by this configuration will be raised cosinusoidal in nature with a fringe separation equal to half the wavelength of the monochromatic illumination. This is illustrated in figure 1.3. Therefore measurement of the interferogram allows the change in optical path difference to be determined. In order to ascertain the direction of motion, it is common to introduce a $\pi/2$ phase change to the system as shown in figure 1.3. Counting the number fringes which occur removes the ambiguity from the system and allows a large displacement to be monitored. The better the monochromaticity of the source (i.e. the longer the coherence length) the longer the distance which may be moved from the zero path difference of the interferometer before the visibility of the fringes drops to zero and continued measurement is impossible. Typically digital resolution of the interferogram may be used to provide $\lambda/4$ resolution, although this may be further enhanced through the use of analogue interpolation techniques. However, to achieve the required accuracy provided by analogue interpolation, extremely careful stabilisation of the lasing wavelength and reference path length is generally required. Variations on the simple interferometric system described by figure 1.3 may be found regularly in light industrial applications where particularly small displacement ranges and high accuracies are required [13]. It is important to note that measurements carried out in this manner are purely incremental and only referenced to the optical path length present at the switch-on of the system.

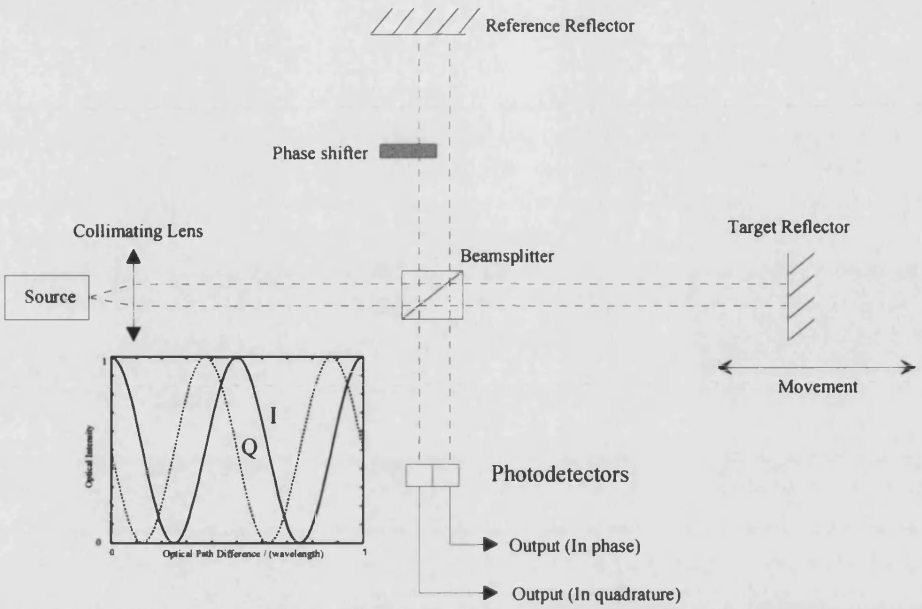

Figure 1.3. Schematic representation of a Michelson interferometer configured for displacement measurement.

In addition to the simple arrangement shown in figure 1.3, there is a rich variety of different interferometric sensors which have been developed in recent years. These include systems based upon other interferometric configurations such as the Fabry-Perot, Mach-Zehnder, and Sagnac interferometers. Details of the use of such configurations can be found in Culshaw and Dakin [4].

A commonly used variation on the system shown in figure 1.3 is to use two wavelength interferometry which allows a reduction in sensitivity and an increase in the unambiguous range to be obtained. This has been applied to both displacement [14-16] and vibrometry [17] measurements. By the principle of superposition, when two wavelengths are used to illuminate a Michelson interferometer, an interferogram is produced which consists of fine structure fringes along with a more slowly varying envelope corresponding to the 'synthetic wavelength', Λ. The intensity of the interference fringes may be given by [15]

$$I(k) = 2I_o + 2I_o \cos\left(\frac{2\pi l}{\xi} + \theta_2 + \theta_1\right)\cos\left(\frac{2\pi l}{\Lambda} + \theta_2 - \theta_1\right), \qquad (1.4)$$

$$\text{where } \Lambda = \left|\frac{\lambda_2\lambda_1}{\lambda_2 - \lambda_1}\right| \text{ and } \xi = \left|\frac{\lambda_2\lambda_1}{\lambda_2 + \lambda_1}\right|. \qquad (1.5)$$

This produces a much longer 'fringe length' according to the synthetic wavelength, hence the reduction in sensitivity and increase in unambiguous measurement range.

The use of tuneable lasers can allow synthetic wavelengths of over 10mm to be produced. However, to achieve meaningful results, care must be taken to ensure that the wavelengths of the two source must be interrelated so that the phase term(θ_2-θ_1) in equation 1.4 remains constant over time. One method of avoiding this potential stability problem is to use heterodyne detection.

In this technique the information is encoded in either the phase or frequency of the output signal rather than its amplitude. For example if both the optical frequencies in a synthesised source system are modulated at frequencies f_1 and f_2 respectively, then a photodetector signal of the following form will be obtained [14],

$$I = A\cos\left(2\pi(f_2 - f_1)t + \frac{4\pi l}{\Lambda}\right). \qquad (1.6)$$

It can be seen that the position measurement information is now encoded into the frequency of the photodetector signal instead of the amplitude. Therefore the resultant system is far more resilient to amplitude noise. In addition, since the output signal has been shifted from DC to a carrier frequency, the system is effectively immune from 1/f noise as well. This leads to a system which possess a higher stability with resolutions of 0.12nm possible over a range of 10mm [18]. Typically the frequency shifts required for heterodyne operation may be produced by using acousto-optic modulators [14,18] or by using Zeeman lasers [19,20].

Possibly the area of interferometry which has received the most interest in recent years has been low coherence interferometry (or as it is sometimes known 'white-light' interferometry) [21]. This is particularly suited to fibre based measurement systems due to its insensitivity to power fluctuations which occur within the fibre. A typical fiberised implementation of a low coherence interferometer sensor is shown in figure 1.4. As the name of the technique suggests, light from a low coherence source is coupled into optical fibre where it travels towards a coupler (or in a bulk optical version a beamsplitter). Light coupled into one arm of the coupler passes onto the sensing interferometer which is used to assess the measurand. The output from this fibre interferometer then passes back to the coupler where one part of it is coupled into a second interferometer known as the

receiving interferometer. This receiving interferometer is situated in a controlled environment away from any disturbance from the measurand in question. The output of this interferometer is finally incident upon a photodetector.

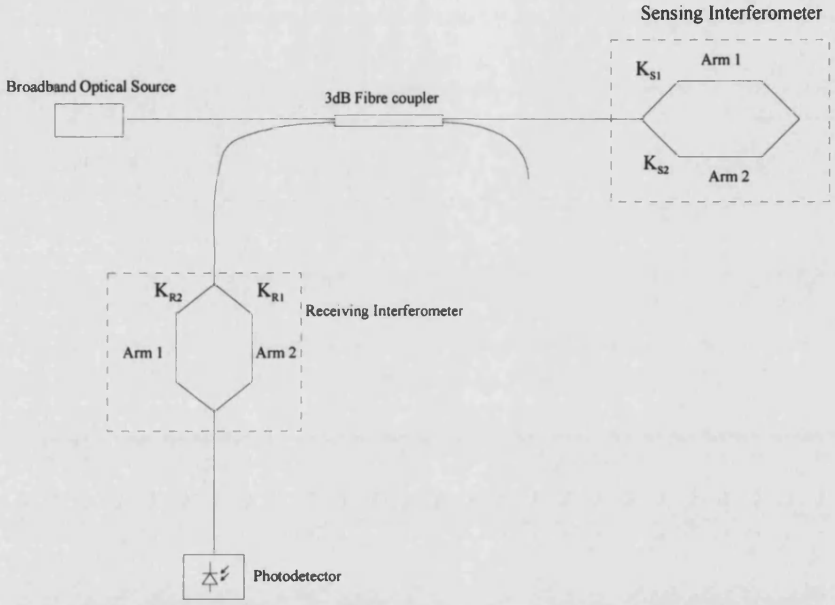

Figure 1.4. A typical implementation of a fibre-optic low coherence interferometry sensor (after [21]).

The optical path differences of both the interferometers are arranged so that they are several times larger than the coherence length of the optical source used. Therefore no fringes would be observed from either of the interferometers if individually illuminated. However, if the optical path difference (OPD) between the two interferometers is within the coherence length of the source then fringes will result from the combination of the two interferometers. The visibility and phase of the fringes which are produced will be a function of the difference of the OPDs of the two interferometers. For the case where the power split ratios of the interferometers are equal, the transfer function of this tandem arrangement may be given as [21],

$$I(X_R) = I_o\left(1+\frac{1}{2}\exp\left[-\left(2(X_R - X_S)/L_C\right)^2\right]\cos\left(k\left[X_R - X_S\right]\right)\right) \quad (1.7)$$

where X_R and X_S are the OPDs of the receiving and sensing interferometers respectively, while L_c is the coherence length and k the mean wavenumber of the source. Equation 1.7 describes the case when the power split ratios of the fibre couplers used are equal, which provides the optimum fringe visibility.

It can be seen that any change in the optical path difference of the sensing interferometer will lead to a change in both the fringe visibility and the phase of the output signal. The interferogram described by equation 1.7 can be tracked by scanning the receiving interferometer (i.e. by varying X_R). If the OPD of the sensing interferometer does change then a shift will occur in the position of the central maximum of the fringes. By measuring the equivalent shift in the OPD of the receiving interferometer the change in the OPD of the sensing interferometer can then be determined. A variety of interferometers may be used as both the sensing and receiving interferometers. However, in practice systems using a reflection type Fabry-Perot sensing interferometer and a Michelson receiving interferometer have proved popular [21-23]. Using such a system allows resolutions of 0.02μm over mm ranges to be obtained [24].

Alternative embodiments of these techniques have been demonstrated which include systems which use a two-wavelength synthesised source to aid accurate identification of the central fringe of the interferogram [25] or have included methods of temperature compensation [26], while systems designed for operation over long distances of optical fibre have been developed [27].

As an alternative to mechanically scanning one arm of the receiving interferometer, Taplin et al [28] have developed a novel system which uses a diffraction grating and CCD camera, while Sinha et al [29] have produced a time-delay scanner by variable coupling between two spatial modes in optical fibre by acousto-optical techniques. In contrast Wang et al [30] have eliminated the requirement for the receiving interferometer by using a tuneable laser as part of a two wavelength optical source.

While interferometric sensors can provide extremely high resolution over small displacements ranges, they are generally difficult to configure and subject to instabilities when compared to other techniques. This is mainly due to the number of optical components required and the alignment tolerances demanded by the application, both in the cases where bulk optical and fiberised configurations are employed. Therefore in recent years there has been much interest in the development of integrated optic sensors [20,31-32] where the majority of the passive and even

some active components [33-34,67] are integrated onto a single chip. This can potentially remove mutual alignment problems for these optical components providing a sensor which exhibits a greater stability. However, alignment difficulties may be still persist as light would have to be coupled into and out of the integrated optic structures with good stability and low loss. Furthermore, high volume production may be required to produce a cost-effective system.

1.2.3. Optical feedback techniques

Increasingly in recent years there has been much interest in the special area of interferometric sensors comprised by optical feedback systems. With the advent of high quality, low cost semiconductor laser diodes, optical feedback is becoming a very interesting area of position sensor development. Furthermore, complete optical sensing configurations can be constructed with very few optical components, allowing a practical sensing system to be developed, which is far more cost effective than many other, more complicated optical alternatives. This is not just due to the reduction in component cost, but also the manufacturing cost required to achieve the precise alignment required by many systems. A typical experimental arrangement which is often used for various optical feedback sensing system is shown in figure 1.5.

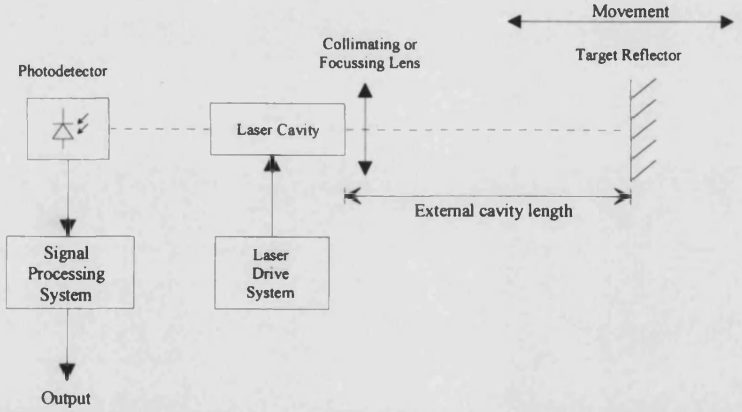

Figure 1.5. Schematic representation of a typical optical feedback position sensor.

Many feedback sensors operate by analysing the undulations that occur in the output power of the laser when the external reflector used to provide feedback to the device is moved through distances equal to half the lasing wavelength [35,36].

While it can immediately be seen that such systems can provide sub-micron resolution, the operating range is limited, although certain systems have been designed for operation in conjunction with pressure membrane applications [37,38]. In order to increase measurement range, more sophisticated versions of this system have been employed, such as simultaneous frequency modulation of the laser diode with phase detection [39] to produce 20cm range with sub-micron resolution. Similar techniques have provided a longer measurement range of ~1m [40,41] however, all these systems are quite sensitive to variations in operating temperature. Mode hop counting has also been a popular feedback measurement technique [42,43] producing accuracies of 0.2% for ranges approaching 1m [44].

Finally feedback techniques have been applied to vibrometry where simple diffuse scattering reflection to a single-mode laser has been used to dynamically modulate the lasing wavelength [45], for vibration and velocity measurements.

1.2.4. Frequency Modulated Continuous Wave Ranging (FMCW)

Another popular sensing technique is frequency modulated continuous wave ranging (FMCW). This technique is based upon a measurement principle used in RADAR [46], which has recently been applied to optical sensing. This technique provides means of remote or non-contact sensing which is independent upon the optical power loss of the system [47].

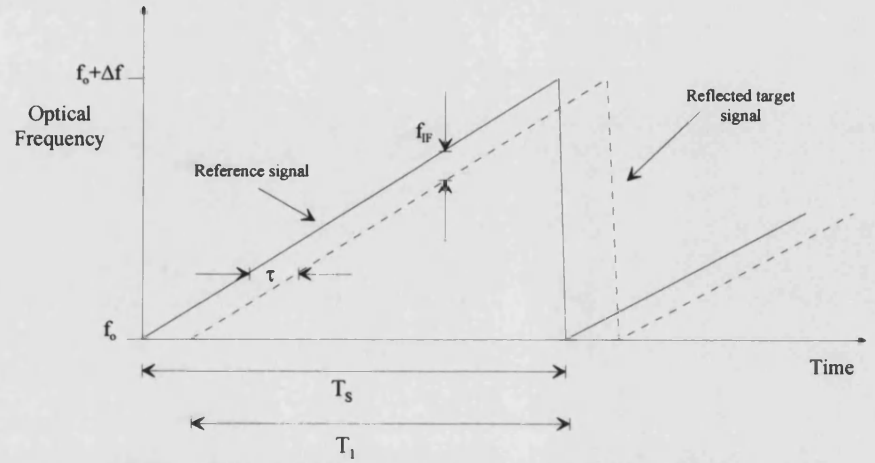

Figure 1.6. Schematic illustration of the concept of FMCW (after [52]).

The simplest form of FMCW uses a source whose optical frequency is sawtooth modulated as shown in figure 1.6. During the sweep time, T_s the laser is modulated linearly over a frequency range Δf. If a path imbalance exists in the interferometric system, such as that shown in figure 1.7, there will be a time delay between the return signals of τ. Therefore light of two optical frequencies will arrive at the photodetector and beat together, producing a beat signal within the photodetector with a frequency, f_{IF} corresponding to the frequency difference between the two optical signals. This may be given by,

$$f_{IF} = \frac{\Delta f \, \tau}{T_s}. \qquad (1.8)$$

The sinusoidal output signal will exist in the time interval T_1, as shown in figure 1.6. Since the delay time is directly related to the path imbalance, L of the interferometer ($\tau=2nL/c$ where n is the refractive index of the medium and c is the speed of light in vacuo), measurement of this beat frequency can determine the absolute position of the optical target. This can be measured by spectral analysis techniques, such as a swept source spectrum analyser, or by timing the period of the output sinusoid.

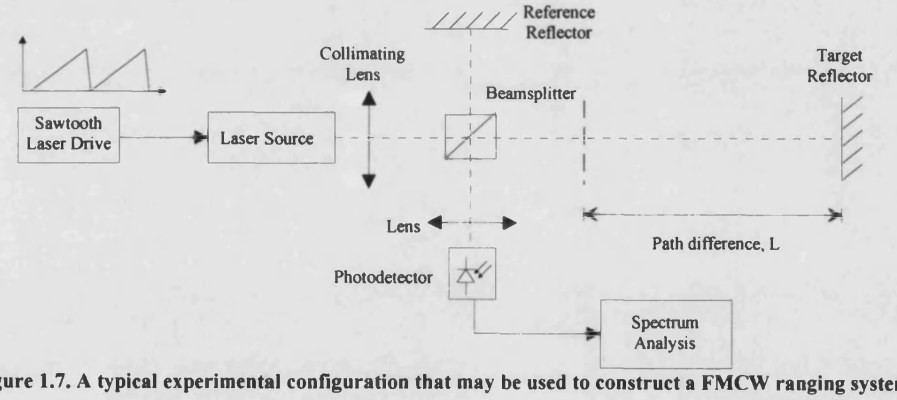

Figure 1.7. A typical experimental configuration that may be used to construct a FMCW ranging system.

One of the most important practical factors in the FMCW system, is the method of continuously tuning the frequency of the optical signal. Semiconductor lasers are particularly suited to this application as their operating frequency is found to vary as a function of bias current [48]. This allows the frequency of the laser diode to be tuned by simply ramping the bias current to the device. However, in order to achieve accurate, stable and repeatable modulation of the lasing frequency, care must

be taken as the inherent non-linear effects of the laser can provide a non-linear frequency sweep [49,53], leading to a beat signal which is not of a constant frequency. Therefore there has been much interest in developing a suitable source for this application. Strzelecki et al [49], used a coupled cleaved cavity laser (C^3 - see [50]) operated within an external cavity for increased stability to produce a system capable of measuring a range of up to 150m with a fractional measurement resolution of 0.1%. Alternatively, Burrows and Liou [51] used a two-section DFB laser which allowed a system to be produced which was capable of 1cm accuracy, while Dieckmann [52] used a tuneable twin-guide (TTG) laser to produce a system accuracy of 0.4%.

Taking a slightly different approach, Beheim and Fritsch [53] actively modulated the position of the reference mirror in order to adjust the phase of the output signal for greater stability. This allowed displacements to be resolved over a 2cm range with a standard deviation of 2μm.

An alternative approach, however, to the direct frequency modulation of the optical signal used in the above examples is to use a system of optical radar where the optical signal is modulated by a swept RF oscillator signal [54]. The frequency of this modulation is varied in the same manner as shown schematically in figure 1.6. Such a system has been found to produce a measurement resolution of 1mm with a maximum range of 5m.

1.2.5. Triangulation

Optical triangulation is a well established method of determining the distance to an object in non-contact applications. Today many commercial products have been developed using optical triangulation for use in a wide range of measurement applications. The basic measurement principle of optical triangulation is shown in figure 1.8. Light from a collimated laser or LED is incident upon a diffusely reflective surface, which is the object to be measured. A lens collects some of the light scattered from the target and images a illumination spot upon a position sensitive detector (PSD) which is capable of distinguishing the centre of

illumination. Suitable components may be either position sensitive photodiodes or CCD arrays. As the position of the target moves with respect to the optical source, the centroid of illumination on the detector varies according to the geometry of the configuration. It can be seen therefore that the output of the PSD is dependent upon the position of the target. For the arrangement shown in figure 1.8, when the target is at a distance x away from the source, the geometry of the configuration provides a shift in the illumination spot of Δx when compared to the central target position y. In this case x may be given by [55],

$$x = y - \frac{A\Delta x}{\Delta x \cos\theta + B\sin\theta}. \qquad (1.9)$$

In many cases, the optical source is pulsed in order to reduce the effects of ambient light and background emission from the surroundings. Typical applications include use in co-ordinate measuring machines [56] and industrial gauging applications [57] where the object being measured may be moving laterally to the axis of measurement e.g. a steel mill.

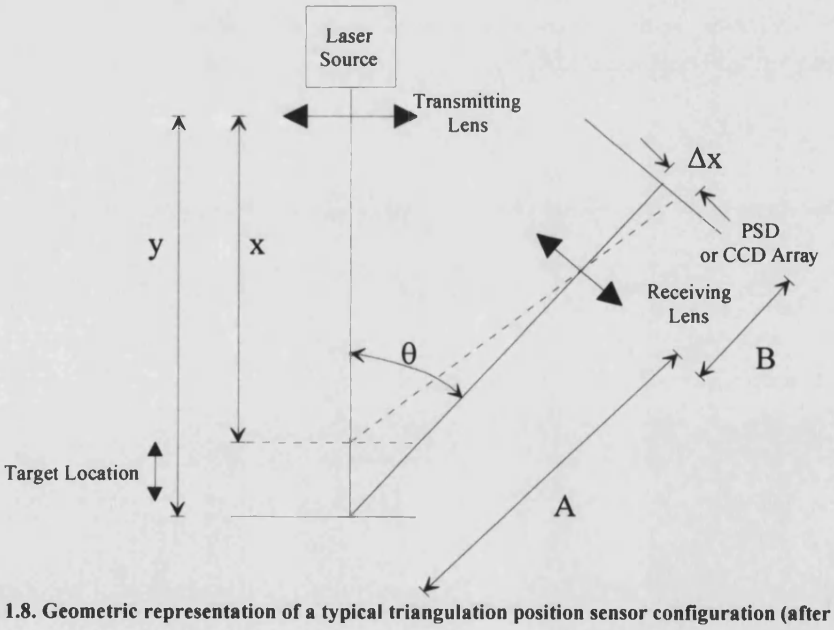

Figure 1.8. Geometric representation of a typical triangulation position sensor configuration (after [55]).

Triangulation sensors do suffer from the drawback that due to the geometrical nature of these systems, they require a stand-off distance from the front of the device. This can often be five times greater than the complete measurement range of the device. Therefore triangulation is not best suited to applications where

space is restricted. Sub-micron accuracies are obtainable using high cost systems (>£12,000 at the time of writing) [109], however range to resolution accuracies are typically limited by the resolution of the PSD used in the sensor. Presently in order to achieve accuracies of 0.1%, an expensive system is required [109].

Despite the maturity of this technique, research is continually being carried out to enhance the potential system performance of this technique. For instance the introduction of a dual axis system [58] can provide information on the tilt of the target sample as well as position measurement to 0.5% (limited by PSD resolution), while Butler and Gregoriou [59] have developed a version which uses a fibre optic bundle geometry to provide an increased measurement range. Furthermore, dual axis techniques can also be used to reduce the effect of 'shadow' points in co-ordinate measuring applications [60], while an actively deflected laser beam has been used to scan a target object [61] and in so doing provide a significant increase in measurement resolution (0.005%). Finally, a triangulation based system using a four-quadrant detector [62] has been successfully used to measure lateral movement (i.e. perpendicular to the optical axis) over ranges of 2.5m with 1% measurement accuracy.

1.2.6. Optical Encoders

Optical encoders are commonly used throughout industry in applications such as machine-tool and calibration measurements where high accuracy, contact measurements are required. Most encoders which are commercially available are generally derived from the Moiré fringe scanning technique [63] which is illustrated in figure 1.9. This technique operates by identifying and counting interference fringes generated by the superposition of two optical gratings and can be used to provide incremental displacement information. A smaller, scanning grating is maintained in a fixed position whilst another, longer grating is displaced with respect to it. The pitches of the two gratings differ so that over a distance d, one grating will have one extra period than the other. This will provide a fringe pattern the period of which is equal to the vernier distance d. Usually the optical signal is

detected by the means of four read heads positioned in quadrature [64] within the period of the fringe pattern as shown in figure 1.9. These allow the fringe period to be resolved into four states allowing both incremental position measurement and the direction of motion to be determined. Inherently, the resolution of the system is dependent upon the pitch of the grating, since this can be immediately resolved to one quarter pitch using the configuration shown in figure 1.9. However, increased resolution can be obtained by interpolation of the quadrature sinewave output of the system. Typically with stable analogue interpolation techniques micron resolution is achievable over ranges of >1m, albeit with the aid of expensive signal processing systems.

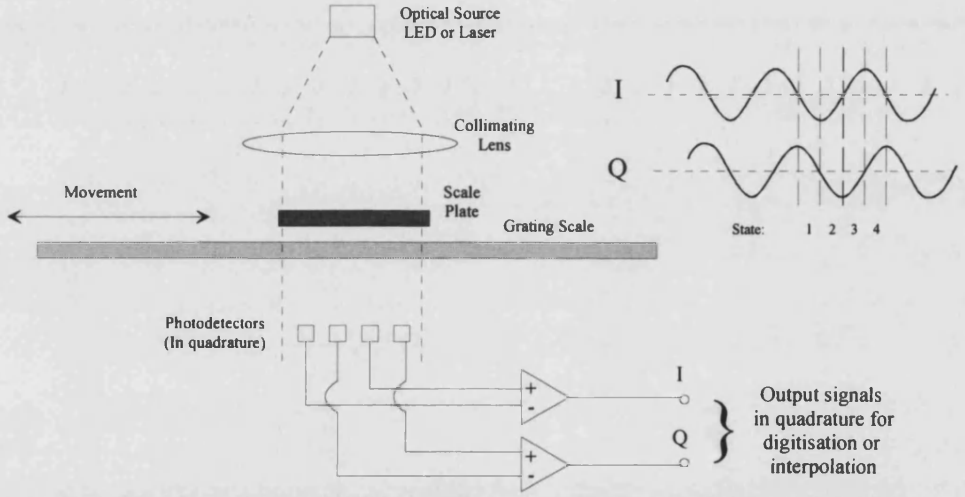

Figure 1.9. Schematic representation of a typical optical encoder position measurement system.

Increasingly, however, variant devices are being introduced which are capable of enhanced accuracy. Diffractive phase interference [65] has been used to provide to high accuracy encoding where the first order beams diffracted by the grating are interfered, one being subject to a prior $\pi/2$ phase shift. Such a system can provide resolutions of 0.1μm, although with this technique, alignment tolerances are critical. Further improvements in resolution can be obtained with the use of holographic gratings [66] which can provide resolutions of the order of 0.01μm with accuracies of 0.5μm over a 0.2m range. Component reduction has also been obtained using monolithic integrated optical systems [67] which allow sub-micron accuracy when used in conjunction with conventional grating scales.

In addition, much interest lies in the development of encoder systems which have absolute position sensing abilities rather than simply relying on fringe counting with a single reference point. These include the use of variable pitch gratings [68] to identify reference positions and systems which use pseudo-random binary sequences (PRBS). Due to the unique properties of the PRBS [69] their use allows absolute sensing systems to be developed which are either digital in nature [70], or which incorporate supplementary analogue methods for resolution enhancement [71]. This has allowed the development of systems capable of 0.1μm accuracy. Another method of absolute measurement is to use temporal addressing of multiple reflective digital code-plate channels [72]. This was achieved using a short pulsed optical source with an increasing optical delay to each successive channel.

Rotary encoders may also be used to measure linear position or displacement, particularly in machine tool applications. This can be accomplished by converting the linear movement into a rotational one by means of a threaded shaft. The pitch of the thread setting the rotation/translation index. Measurement of the rotational position may be carried out digitally using multiple read-head systems [73] or by novel encoding mechanisms [74] or using PRBS [75] or Gray [73] codes. However, it should be noted that the accuracy of any such system for measuring linear displacement is usually limited by the mechanical backlash of the shaft system.

1.2.7. Multiple Wavelength Position Sensing

In addition to using time domain multiplexing to monitor parallel channels in an encoder system using only a single transmission fibre [72], wavelength domain multiplexing is becoming increasingly popular. This is true for both linear and rotational encoders, with dispersive techniques used to separate a broad optical spectral bandwidth at both the sensor head and the reflected signal processor. Typically dispersion of the wavelength spectrum across the channels of the encoder is achieved by the use of diffraction gratings which possess a linear [76,77,107] or variable pitch [78].

Another method of wavelength encoding position sensing has been developed by using Fresnel zone plates as lenses to couple light into an optical fibre [73] as shown in figure 1.10. When used as lenses the focal length of these zone plates is found to vary quite considerably as a function of wavelength. Therefore, these components may be used in either transmission or reflection configurations to provide a simple linear displacement sensor, with signal processing used to track the peak wavelength in the optical spectrum of the light coupled into the fibre. In one particular application [79], two laser sources of differing wavelengths were modulated at different frequencies. This provided a far simpler signal processing system as the reflected signals could be separated using synchronous detection to provide a stable output. Ratioing these two signals provides an unambiguous output signal as a function of position.

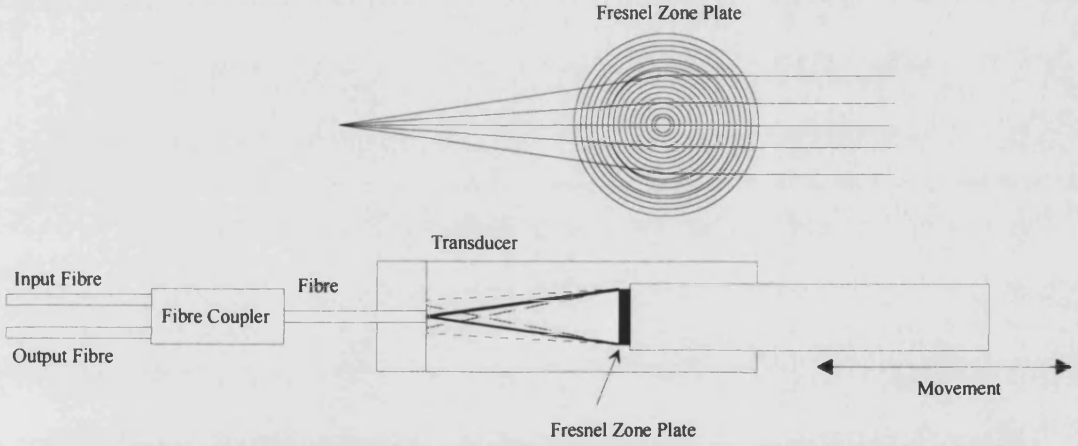

Figure 1.10. Example of the implementation of an optical position sensor using the wavelength dependent lens properties of a Fresnel zone plate, (after [73]).

Finally while in many cases conventional broad band optical sources have been used for WDM sensing applications (such as white light or LEDs) specialist devices are under development for use in sensing applications such as ultrabroad bandwidth LEDs called superluminescent diodes. Furthermore, advanced multiwavelength laser diode sources are undergoing considerable development not only for sensing but also for communications applications. One example of these is the Multichannel Grating Cavity (MGC) laser capable of generating several lasing wavelengths simultaneously [80].

1.2.8. Imaging/profilation techniques

One associated area of interest is the profilation and imaging of objects. Increasingly optical imaging techniques are replacing physical touch-probes for co-ordinate measurement machines, profilometry and other similar applications. A variety of optical techniques are used, some of which are applications of the conventional position sensing techniques discussed previously, while some are completely novel in their own right. New systems which are beginning to develop include the application of triangulation position sensors for profilation [81,82] while depth of focus range sensing has been used to produce a 512x480 image at a 30Hz refresh rate which has an accuracy of 0.3% full range [83]. Alternatively the technique of videogrammetry [84] uses a number of video cameras to produce complete three dimensional measurements in real time for objects up to 25m away. However, these techniques are generally applications of previously developed position sensing techniques.

In contrast, a new technique for profilation measurements has been developed which uses polarisation analysis of light reflected from a target object after interference with a reference beam [85]. No moving parts are required as a CCD camera is used to cover a wide area range. This provides an unambiguous measurement range of 20 microns. While this unambiguous measurement range is quite short, it is much larger than that obtained with a typical interferometry system. One direct result of this is that the sensor can resolve step changes in the target profile far easier than more conventional interferometry techniques [86].

1.2.9. Reflective fibre-optic techniques

One of the earliest means of measuring position using fibre optics that was developed was the reflective sensor [87,88]. This consists of a fibre optic system which delivers an optical signal to an external reflector. The optical signal is then reflected to a return fibre. The amount of light that is returned to the fibre is dependent upon the distance of the reflector from the output fibre.

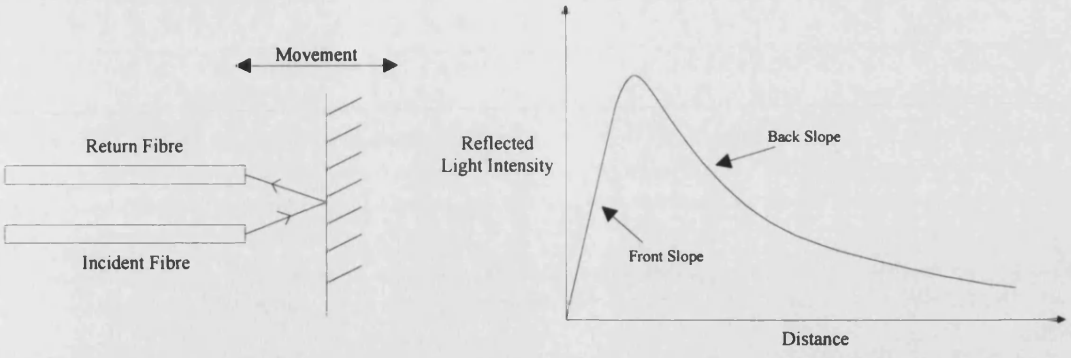

a). Two fibre reflection configuration b). Characteristic reflection response

Figure 1.11. Schematic representation of a dual fibre, reflection intensity position sensor. a). Implementation, b). Characteristic reflection response.

Figure 1.11.*b* shows the characteristic reflection response obtained from a typical dual-channel reflection sensor as shown in figure 1.11.*a*. It can be seen that there are two linear regions in the intensity response of the systems either side of the reflection intensity maxima. These are commonly known as the 'front slope' and the 'back slope'. Typically the front-slope covers a much shorter displacement range than the back slope, however, within this region, the sensitivity is higher than for the back slope. This allows two different operating configurations to be obtained from the same measurement system. A simple power detection system can be used to provide a suitable electronic output from this system, which can be positioned a long distance away from the target reflector. Therefore, this system can be applied to intrinsically safe applications (which will be discussed in section 1.3.1).

Typically these systems are best suited to short range applications for ranges of <5mm. However, they can provide sub-micron resolutions with typical accuracies of 0.5%. Many different fibre optic probe configurations are available [89] for this technique as shown in figure 1.12. In this figure, the white circles represent fibres transmitting the incident optical signal to the target reflector, while the dark circles denote receiving fibres. It is found that each of these configurations provides a different characteristic output response as shown in figure 1.13.

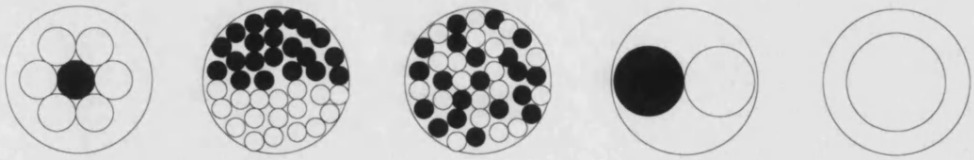

Figure 1.12. Examples of the variety of probe configurations which may be used (after [2]).

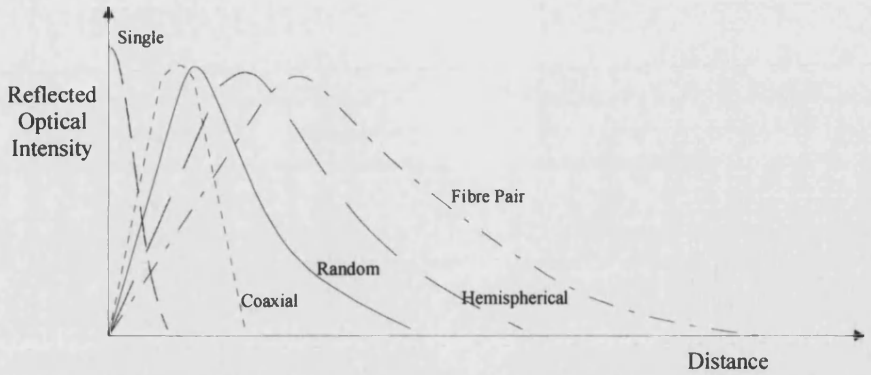

Figure 1.13. Reflected intensity characteristics corresponding to the probe configurations shown in figure 1.12 (after [2]).

Even though this particular technique is quite mature in its development, with commercial products produced by Philtec and Optec among others available on the market [90], there has still been a great deal of research interest in this topic over recent years. Much of this work has been connected with the theoretical [91-93] and experimental [94] assessment of optimum probe geometries for particular applications. Alternatively, the technique has been applied to different measurement situations, such as rotation measurement [95] and analysis of changes of both angular and linear position [96]. In addition a thorough theoretical analysis has been carried out to assess the affect of target tilt on the characteristic output response [97]. Furthermore, a modification of this technique by Shimamoto and Tanaka [98] used an ac-modulated tungsten light source to reduce thermal heating effects and improve stability so that subnanometre resolution could be obtained, although long term accuracy was limited to 400nm. Likewise while Ko et al [99] used a pulsed LED to achieve 0.01μm resolution with a long term accuracy of 0.5μm.

It must be remembered that as this technique is based upon intensity variation it will be affected by temporal variations in the attenuation encountered by the return beam signal. However, in general ratioing techniques are used so that any temporal change in the output power can be adjusted for. Care must be taken in the design of the detector system so that the effects of amplitude noise on the detector output signal can be minimised.

1.2.10. Fibre-optic transmission techniques

Another early development of fibre optic position sensing technology was the optical transmission sensor. These may work on transverse, longitudinal, angular or differential displacement of fibres [73,87], as shown in figure 1.14.

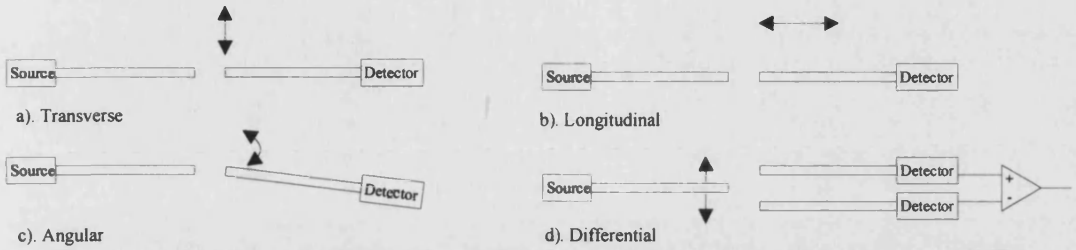

Figure 1.14. Schematic representation of a variety of fibre optic intensity displacement sensors (after [87]).

It can be seen that operation of these intrinsic devices is simple as the optical loss introduced into the system is dependent upon the displacement (be it linear or rotational) of the fibre. Other alternatives can be used where the fibres themselves remain stationary, such as when a shutter mechanically coupled to the body under test is used to modulate the system loss. Beam expansion may be required for this application to achieve a reasonable resolution. However, in general only moderate accuracy (0.1~1%) can be obtained with such devices, and consequently in general they are found in applications where a low-cost optical solution is required.

1.2.11. Microbend sensors

Microbend sensors are another example of an early fibre-optic displacement sensing technique. Once again, this technique is intrinsic in its nature. As a consequence, microbend systems are effectively simple in design and construction. In addition they possess typical intrinsic fibre-optic characteristics such immunity from electromagnetic interference.

An example of a microbend position sensor is shown in figure 1.15 [100]. This illustrates a multimode fibreoptic waveguide subjected to a mechanical perturbation or bending. The consequence of this bending is that the light travelling within the fibre in waveguiding modes is coupled into radiation modes. The more extreme the applied perturbation, the greater fraction of the transmitted signal is

coupled into radiative modes and is lost. Therefore the magnitude of the mechanical perturbation directly modulates the level of light transmitted by the fibre.

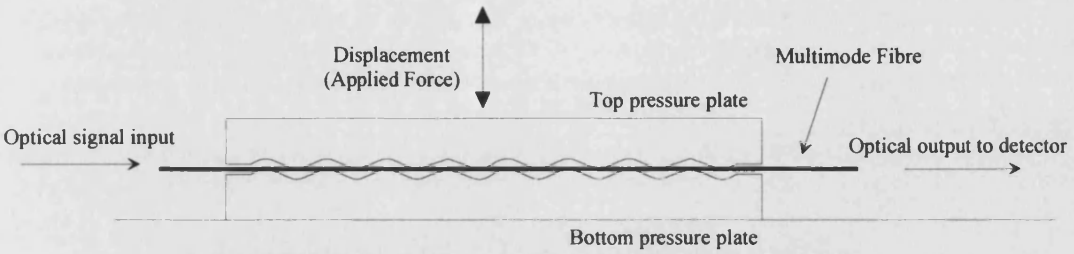

Figure 1.15. A typical configuration of a microbend sensor (after [100]).

It was demonstrated by Fields et al [101] that the effect of the microbending could be enhanced by squeezing the fibre by means of a series of periodic, corrugated blocks as shown in figure 1.15. It has been shown that if the wavenumber of the periodic deformation is equal to the difference in wavenumber of the propagating and radiating modes a particularly strong loss occurs [102].

The application of this technique to displacement sensing can be appreciated when the change in position of these blocks is considered. As the blocks are brought closer together, the sinusoidal amplitude of the fibre deformation is gradually increased leading to an increased loss in transmission. Considering the nature of the deformation that occurs, it can be seen that this technique is limited in use for the measurement of very small displacements (<100μm). Typical accuracies of 1% can be obtained when temperature compensation is applied, while device lifetimes can exceed 10^{10} cycles.

More recently Gauthier and Ross [103] have developed a variation on the microbending technique using single mode fibre. This has been found to be not only able to measure the strength of a single bend in the fibre path, but to also determine the position of the bend along the path of the fibre.

1.2.12. Discussion

Analysis of the systems described in the preceding sections show that many excellent optical techniques have been developed for position measurement. This is particularly the case for long range measurements where time-of-flight techniques have become commonplace and for very short range measurements where

interferometric and fibre optic techniques have proved to be successful. However, in the intermediate range covering distances of several centimetres to a few metres, it has been more difficult to develop accurate, compact, stable, cost effective techniques for industrial measurement applications. For example, most optical encoder systems provide purely incremental measurements with the possible provision for a reference mark somewhere along the scale. Also, triangulation techniques while excellently suited to certain non-contact applications, are hampered by a limited accuracy to range ratio and are generally subject to a large offset distance. Furthermore, other systems which perform well in the laboratory may be impractical in industrial applications due to the large number of optical and fibre-optic components required, leading to possible long-term stability problems and high system costs. It should also noted that systems which are dependent upon analogue amplitude variations (certain interferometers, fibre-optic and feedback sensors) may be susceptible to errors induced by amplitude noise. Therefore, it can be seen that there is still considerable scope for the development of optical position sensing apparatus for intermediate range position measurement applications.

It is therefore believed that this potential scope for development will, in the future, provide the stimulus for the further advancement of existing systems and importantly the formulation of novel techniques over this industrially important measurement range.

1.3. Potential application areas for optical position sensors

It is evident from the direction of the market [1] that optical sensors will begin to see an increased presence in most sectors of industry over the next decade. However, certain areas of industry will see particular growth in the installation of optical sensors in the near future. Some of the most interesting and important of these are outlined below.

1.3.1. Intrinsically safe sensing

Intrinsically safe sensors form a small, but rapidly increasing sector of the market. They are used in hazardous environments such as those found in the petrochemicals and mining industries, where the possibility of spark generation by electrical equipment has the most serious of consequences, due to the risk of explosions.

The origins of intrinsically safe sensing can be specifically traced back to the mining disaster which occurred at the Senghenydd Colliery, South Wales in 1913 [104]. At the subsequent Court of Inquiry there was great debate as to whether the disaster had been caused by the ignition of firedamp by sparks from signalling equipment. This stimulated much research which eventually lead to the issue of Certificates of Intrinsic Safety in 1936 governing equipment used in mines. A modern definition of an intrinsically safe electrical apparatus is provided by the following paragraph [104].

> "Apparatus which is so constructed that when installed and operated under the conditions specified by the Certifying Authority, any electrical sparking that may occur in normal working, either in the apparatus or in the circuit associated therewith, is incapable of causing an ignition of the prescribed flammable gas or vapour."

From this definition, it can seen that within the area of intrinsically safe sensing there is an immediate application for optical position sensors which contain no electrical signals whatsoever within the sensor head. Presently, many position measurement applications are carried out using LVDTs [73]. These are fitted with Zener barrier diodes to limit the amount of stored energy within the inherent inductance of the constituent coils [105]. However, if suitable optical sensors can be developed which provide, an equivalent or enhanced, cost effective performance, it is likely that they will begin to replace these traditional devices. These new optical systems would use optical fibre to address the sensor in a 'remote' hazardous area, with any required electronics and signal processing situated in a designated safe area. These may include intrinsic fibre-optic sensors where the optical signal is modulated

while still within the fibre, or extrinsic systems where the fibre is merely used as a means of addressing a passive sensor head.

1.3.2. Aerospace applications

In recent times, the term 'fly-by wire' has come to represent the replacement of traditional hydraulic controls of aircraft by remote electronic systems. However, the next generation of avionic control systems is likely to be considered as 'fly-by-light', with photonic control and communications systems being used throughout the aircraft. The potential benefits of using optical systems are numerous [106]. For example, optical systems can potentially provide improved performance in terms of bandwidth, cross-talk and sensitivity. However, other attributes which are likely to become of importance in the future are reduced mass, intrinsic safety and resistance to ionising radiation. Furthermore, they are potentially immune to electromagnetic interference and do not interfere with other equipment. This is useful for both stealth and security reasons. In return however, the hostile aerospace environment will provide some unique challenges to optical sensor designers, as the extremes met in operational parameters such as temperature (including cycling), pressure, acceleration, vibration and stress are much higher than may be encountered in normal industrial applications.

It has been identified [106,107] that displacement / position sensors will be required for both linear and rotary aerospace applications in absolute and incremental forms. Particular applications which have been identified include control of flight surfaces and monitoring of fuel valves.

1.3.3. Defence applications

As well as the use of optical sensors for ranging, LIDAR, and other general applications, it is likely that new techniques of measurement will be required for use in the next generation of weapons and counter-measures developed for defence applications into the next century. For example, much effort is being put into the development of electromagnetic (EM) pulse weapons which can disable the

computer, communication and control systems of a variety of military targets, by the use of extremely high power EM pulse signals. Therefore, any reliable position measurement which is required to be performed within the vicinity of one of these weapons facilities should be immune to interference from the intense EM pulse signals. The attributes of optical sensors described in the preceding two sections illustrate their suitability for this application. Furthermore, it is likely that there will be an even higher demand for such sensors for counter-measure techniques to these potentially crippling weapons [108]. Once again, in this application the potential EM immunity of optical sensors will again be of extreme importance.

1.4. Competing Techniques and Market Awareness

In addition to the wide variety of optical techniques that have been developed in recent years, there are a large number of other measurement principles available for position measurement. These include the LVDTs, magnetic linear encoders, tuned circuit gauges ('digital probes'), capacitive techniques, potentiometric transducers, variable reluctance transducers and magnetostrictive transducer systems, many of which are discussed in detail in general texts such as Bentley [73].

Even though a wide variety of commercial position measurement products exist, using a variety of different operating principles, if the performance of a sample of these products is compared as a function of selling price, a definite correlation exists. This is illustrated in figure 1.16. While the fact that the highest performance devices attract the highest price is not in itself surprising, it can be seen that there is rather a wide spread of data. The reason for this spread is the degree to which many of these measurement systems are application specific. Consequently, these systems should not be considered solely on the grounds of price and performance. Furthermore, the environment within which the sensors are to be placed must also be considered as this can impose certain restrictions upon the design and operation of the sensor. These restrictions, in turn, cause a decrease in sensor performance and/or increase in system cost.

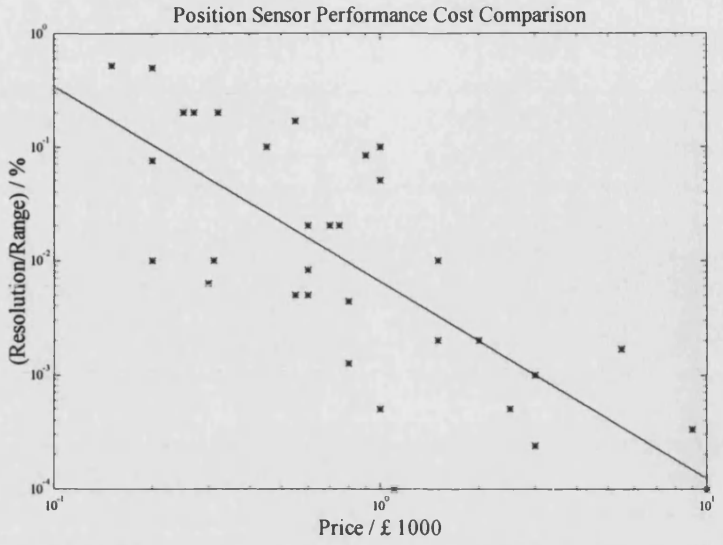

Figure 1.16. Comparison of resolution to range ratio and selling price of a large number of different optical position sensors capable of medium range measurement (after 109).

What the least squares fit shown in figure 1.16 does provide, however, is a rule of thumb which can be used as a guide when designing a new system. It can be used to identify performance and component cost goals at an early stage in the design process, and in general be used to assess whether a particular arrangement may be generally competitive.

This wide variety of possible measurement techniques leads to an increasingly wide variety of products. These vary considerably in complexity, performance, price and design application. However, by comparing the operating parameters of these diverse systems, the relative merits of the techniques may be assessed. Figure 1.17 provides a comparison of the performance and selling price of some of the techniques listed above, along with a number of commercially available optical techniques which are applicable to medium range position sensing. This intermediate range covers the range of distances between several centimetres and a few metres. It should be appreciated that each of these techniques differ widely in their performance criteria, and that figure 1.17 attempts to show mean values.

Traditional techniques such as potentiometric systems and LVDTs tend to provide only modest performance at the lower end of the cost scale. However, the use of these devices has been proven over many decades with product designs being optimised over this time. Further up the scale, magnetic techniques (often based

upon magnetic recording technology) provide an improved performance with a corresponding increase in unit cost. Ranking alongside these systems are magnetostrictive measurement techniques which are particularly suited to measurements in the range of 30cm to 8m.

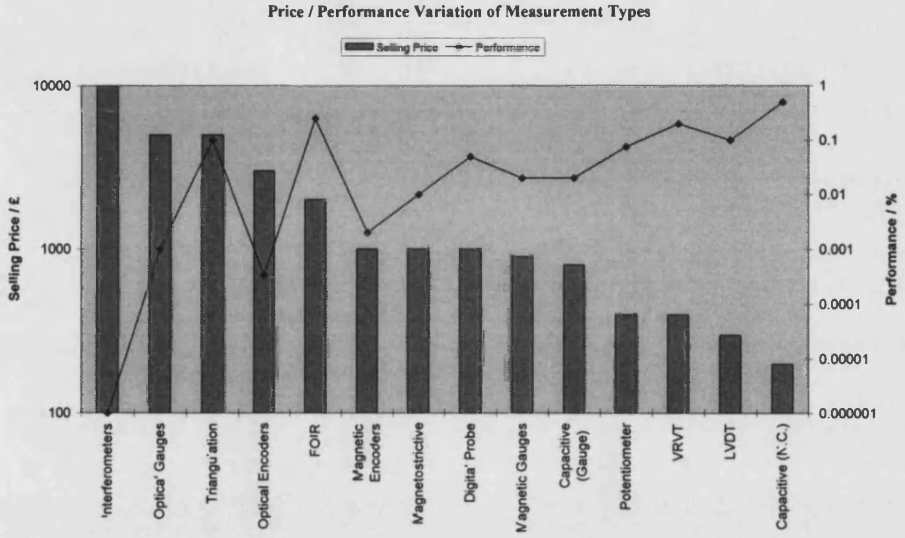

Figure 1.17. A comparison of a variety of techniques for position sensing, (after [109]). Performance is defined as the range to resolution ratio expressed as a percentage.

It can also be seen from this figure that the optical techniques while providing improved performance, are generally more expensive than more traditional systems such as the LVDT. It is imperative therefore that during the development of new optical sensing products, care should be taken to ensure that the unit cost (in relation to their performance and area of application) is acceptable to the market. This is underlined by the fact that traditionally cautious industrialists may be wary of the 'newness' of novel optical products and the fact that they have little track record when compared to traditional sensing means.

1.5. Context of work

It was stated at the beginning of this chapter that possibly one of the greatest challenges working in the field is to produce an optical sensor which can be engineered into a product which is rugged, reliable and economically competitive. Indeed while many excellent ideas for optical position sensing systems have been proposed, in practice many of the key operational parameters listed above have

restricted system development and limited industrial uptake to certain specialised areas. This is particularly true in the intermediate sensing range of a few centimetres to several metres, where it has been more difficult to develop simple, compact, robust, low-cost techniques for optical sensing, which provide *absolute* position measurements. Consequently this has provided the stimulus for the research which is described and discussed within this thesis.

The main aim of the work described in this thesis is to develop novel optical position sensing concepts which can provide excellent performance which when coupled with operational stability and cost effectiveness will allow the development of a successful product for industrial use. Chapter 2 will provide a synopsis of a novel sensor which uses optical feedback to a semiconductor laser to achieve absolute position sensing. The sensor operates with low optical powers and is capable of operation with a minimum of three optical components, namely the laser, a collimating lens and a suitable external reflector. The external reflector may be coupled to or be part of the body under test. This sensor may be configured as a free space sensor for non-contact sensing applications or as a fibre coupled unit for use in environments where intrinsically safe sensing is required. In chapter 3 a steady-state theoretical analysis of the operation of the sensor is developed which allows predictions of the operation of the sensor to be generated. Subsequently, chapter 4 provides details of the stability of the measurement system as a function of key operating parameters. Chapter 5 examines the design, construction and performance of several signal processing systems which may be used to interface with the optical sensor. Further theoretical insight to the operation of the sensor is provided in chapter 6 where a different approach is used to the simple, but descriptive, method followed in chapter 3. This allows the analysis of stability effects encountered during sensor operation to be considered. Finally in chapter 7 details are given of the design, construction and operation of another novel optical position sensor. This uses pseudo-random binary sequences encoded onto a grating along with a novel asymmetric periodic pattern to provide absolute position sensing to accuracies of

0.004%. Furthermore, this sensor uses solely optical addressing to the sensor head and as such is directly suited to intrinsically safe sensing applications.

1.6. References

[1] Frost and Sullivan, "European position sensing market", Analysts Report 1996.

[2] D.A.Krohn, "Fiber Optic Sensors: Fundamentals and applications", Instrument Society of America, 1988.

[3] T.G.Giallorenzi, J.A.Bucaro, A.Dandridge, G.H.Sigel Jr., J.H.Cole, S.C.Rashleigh and R.G.Priest, "Optical fiber sensor technology", *IEEE . Quantum Electron*, **QE-18**, No.4, 1982.

[4] Optical Fiber Sensors, volumes 1-4, J.P.Dakin and B.Culshaw eds., Artech House, London, 1988.

[5] F.B.Patrick "Military Optical Instruments", Chapter 7, Applied Optics and Optical Engineering, ed. R.Kingslake, Volume 5 - Optical Instruments Part II, Academic Press, New York and London.

[6] T.H.Maiman, *Nature* **187**, pp.493 (1960).

[7] M.L.Stich, E.J.Woodbury and J.H.Morse, *Electronics*, **34**, pp.51, 1961.

[8] I.Kaisto, J.Kostamovaaram M.Manninen and R.Myllyla, "Optical range-finder for 1.5-10m distances", *Appl. Opt.*, **22**, No.20, pp.3258-3264, 1983.

[9] T.D.DeWitt and D.A.Lyon, "Range-finding method using diffraction gratings", *Appl. Opt.*, **34**, No.14, pp.2510-2521, 1995.

[10] M.Takeichi, Y Warishina, A.Takeshima, I.Ogawa, K.Ichie and Y.Mizushima", "Streak-camera-based long-distance range finder with 10^{-7} resolution", *Appl. Opt.*, **33**, No.13, pp.2502-2509, 1994.

[11] P.L.Bender, "Laser measurements of Long Distances", *Proc. IEEE.*, **55**, No.6, pp.1039-1045, 1967.

[12] M.Born and E.Wolf, "Principles of Optics", 6th edition, Pergamon Press, New York, 1986.

[13] Zygo Corp., Middlefield, CT, USA, "ZMI-5000 Displacement measurement interferometer system", Product catalogue, 1994.

[14] R.Dändliker, R.Thalmann and D.Prongué, "Two-wavelength laser interferometry using superheterodyne detection", *Opt. Lett.*, **13**, No.5, pp.339-341, 1988.

[15] C.-L.Wang, Y.-H.Chuang and C-L.Pan, "Two-wavelength interferometer based on a two-colour laser diode array and the second-order correlation technique", *Opt. Lett.*, **20**, No.9, pp.1071-1073, 1995.

[16] P.-Y.Chien, "Two-frequency displacement measurement interferometer based on a double-heterodyne technique", *Rev. Sci. Instrum.*, **62**, No.1, pp.254-255, 1991.

[17] O.B.Wright, "Stabilised dual-wavelength fibreoptic interferometer for vibration measurement", *Opt. Lett.*, **16**, No.1, pp.56-58, 1991.

[18] P.G.Charette, I.W.Hunter and C.J.H.Brenan, "A complete high performance heterodyne interferometer displacement transducer for microactuator control", *Rev. Sci. Instrum.*, **63**, No.1, pp.241-248, 1992.

[19] Y.-J.Lin and C.-L.Pan, "Precision displacement measurement by active heterodyne interferometry", *Appl. Opt.*, **30**, No.13, pp.1648-1652, 1991.

[20] H.Toda, M.Haruna and H.Nishihara, "Integrated-optic heterodyne interferometer for displacement measurement", *J. Lightwave Technol.*, **9**, No.5, pp.683-687.

[21] Y-J.Rao, and D.A.Jackson, "Recent progress in fibre-optic low coherence interferometry", *Meas. Sci. Technol.*, **7**, pp.981-999, 1996.

[22] Y.N.Ning, K.T.V.Grattan and A.W.Palmer, "Fibre-optic interferometric systems using low-coherence light sources", *Sensors and Actuators A*, **30**, pp.181-192, 1992.

[23] A.D.Kersey, D.A.Jackson and M.Corke, "A simple fibre Fabry-Perot sensor", *Opt. Commun.*, **45**, pp.71-74, 1983.

[24] A.Koch and R.Ulrich, "Fibre optic displacement sensor with 0.02μm resolution by white light interferometry", *Sensors and Actuators A*, **25-27**, pp.201-207, 1991.

[25] Y.J.Rao and D.A.Jackson, "Long-distance fibre-optic white light displacement sensing system using a source-synthesising technique", *Electron. Lett.*, **31**, No.4, pp.310-312, 1995.

[26] S.Chen, B.T.Meggitt, A.W.Palmer, K.T.V.Grattan and R.A.Pinnock, "An intrinsic optical - fibre position sensor with schemes for temperature compensation and resolution enhancement", *J. Lightwave Technol.*, **15**, No.2, pp.261-266, 1997.

[27] A.B.L.Ribeiro and D.A.Jackson, "Low coherence fibre optic system for remote sensors illuminated by a 1.3μm multimode laser diode", *Rev. Sci. Instrum.*, **64**, No.10, pp.2974-2977, 1993.

[28] S.Taplin, A.Gh.Podoleanu, D.J.Webb and D.A.Jackson, "Displacement sensor using channelled spectrum dispersed on a linear CCD array", *Electron. Lett.*, **29**, No.10, pp.896-897, 1993.

[29] P.G.Sinha, E.Kollveit and K.Bløtekjaer, "Two-mode fibre-optic time-delay scanner for white-light interferometry", *Optics Lett.*, **20**, No.1, pp.94-96, 1995.

[30] D.N.Wang, Y.N.Ning, A.W.Palmer, K.T.V.Grattan and K.Weir, "Scanning in a white light interferometer using a tuneable laser", *Proc 10th Conference on Optical Fibre Sensors*, Glasgow, Scotland, pp.592-595, 1994.

[31] O.G.Hellesø, P.Benech and R.Rimet, "Interferometric displacement sensor made by integrated optics on glass", *Sensors and Actuators A*, **46-47**, pp.478-481, 1995.

[32] J.Lizet, P.Gidon and S.Valette, "Integrated optics displacement sensor achieved on silicon substrate", *Proc. 4th European Conference on Integrated Optics*, Glasgow, UK, pp.210-212, 1987.

[33] D.Hofstetter, H.P.Zappe and R.Dändliker, "Optical displacement measurement with GaAs/AlGaAs-based monolithically integrated Michelson interferometers", *J. Lightwave Technol.*, **15**, No.4, pp.663-669, 1997.

[34] D.Hofstetter, H.P.Zappe and R.Dändliker, "A monolithically integrated double Michelson interferometer for optical displacement measurement with direction determination", *IEEE Photon. Technol. Lett.*, **8**, No.10, pp.1370-1372, 1996.

[35] R.Yoshino, M.Nara, S.Mnatzakanian, B.S.Lee and T.C.Strand, "Laser diode feedback interferometer for stabilisation and displacement measurements", *Appl. Opt.*, **26**, pp.892-897, 1987.

[36] P.J.DeGroot, G.Gallatin and R.Dixon, "Laser feedback metrology of optical systems", *Appl. Opt.*, **28**, pp.2462-2464, 1989.

[37] A.Dandridge, R.O.Miles, A.B.Tventen, T.G.Giallorenzi, "External Cavity Diode Laser Sensor", *Proc SPIE*, **412**, pp.28-36, 1983.

[38] J.-Y.Kim, R.W.Chung, J.C.Mulder, "Measurement of photothermally induced distortion of thin films using an external cavity laser diode sensor", *Electron. Lett.*, **29**, pp.354-355, 1993.

[39] J.Kato, N.Kikuchi, I.Yamaguchi and S.Ozono, "Optical feedback displacement sensor using a laser diode and its performance improvement", *Meas. Sci. Technol.*, **6**, pp,45-52, 1995.

[40] T.Kawakami, M.Endo and T.Iwasaki, "Adaptive multifrequency modulation method for an advanced laser range finder", *IEEE Trans. Instrum. & Meas.*, **43**, No.6, pp.857-860, 1994.

[41] S.Donati, G.Giuliani and S.Merlo, "Laser diode feedback interferometer for measurement of displacements without ambiguity", *IEEE J. Quantum. Electron.*, **31**, No.1, pp.113-119, 1995.

[42] G.Beheim & K.Fritsch, "Range finding using frequency-modulated laser diode", *Appl. Opt.*, **25**, pp.1439-1442, 1986.

[43] S.Shinohara, H.Yoshida, H.Ikeda, K.-I.Nishide and M.Sumi, "Compact and high-precision range finder with wide dynamic range and its application", *IEEE Trans. Instrum. Meas.*, **41**, No.1, pp.40-44, 1992.

[44] S.Shinohara, M.Andou, M.Miyata, H.Yoshida, H.Ikeda, J.Yoshida, K.-I.Nishide, T.Kondo, M.Sumi, "High-resolution range finder with wide dynamic range of 0.2m to 1m using a

frequency-modulated laser diode", *Proc 15th Annual Conference of the IEEE Industrial Electronics Society*, **3**, pp646-651, 1989.

[45] P.A.Roos, M.Stephens and C.E.Wieman, "Laser vibrometer based on optical feedback-induced frequency modulation of a single-mode laser diode", *Appl. Opt.*, **35**, No.34, pp.6734-6761, 1996.

[46] A.J.Hymans and J.Lait "Analysis of a frequency-modulated continuous-wave ranging system", *Proc. IEEE*, **107-B**, pp.365-372, 1960.

[47] D. Uttam and B.Culshaw, "Precision time domain reflectometry in optical fibre systems using a frequency modulated continuous wave ranging technique", **LT-3**, No.5, pp.971-977, 1985.

[48] A. Dandridge and L.Goldberg, "Current-induced frequency modulation in diode lasers", *Electron. Lett.*, **18**, pp.302-304, 1982.

[49] E.M.Strzelecki, D.A.Cohen and L.A.Coldren, " Investigation o tuneable single frequency diode lasers for sensor applications", *J. Lightwave Technol.*, **6**, No.10, pp.1610-1618, 1988.

[50] J.Buus, "Single frequency semiconductor lasers", *SPIE Tutorial Texts in Optical Engineering*, vol. 5, 1991.

[51] E.C.Burrows and K.-Y.Liou, "High resolution laser LIDAR utilising two-section distributed feedback semiconductor laser as a coherent source", *Electron. Lett.*, **26**, No.9, pp.577-579, 1990.

[52] A.Dieckmann, "FMCW-LIDAR with tuneable twin-guide laser diode" *Electron. Lett.*, **30**, No.4, pp.308-309, 1994.

[53] G.Beheim and K.Fritsch, "Remote displacement measurement using a laser diode", *Electron. Lett.*, **21**, No.3, pp.93-94, 1985.

[54] M.Taylor and D.A.Jackson, "High precision non-contacting optical level gauge", *Optica acta*, **33**, No.12, pp.1571-1586, 1986.

[55] M.Buzinski, A.Levine and W.H.Stevenson, "Laser triangulation range sensors: a study of performance limitations", *J. Laser Applications*, **4**, No.1, pp.29-36, 1992.

[56] D.C.Williams, "Optical methods in engineering metrology", Chapman & Hall, London, pp.65, 1993.

[57] J.Saltzberger, "Application examples of precision non-contacting displacement sensors", *Proc. The Sensor and transducer conference,* MTEC'98, NEC, Birmingham, UK, 1998.

[58] H.Wang and D.Malacara, "Optical triangulation: A dual-channel configuration", *Rev. Sci. Instrum.*, **67**, No.7, pp.2606-2611, 1996.

[59] C.Butler and G.Gregoriou, "A novel non-contact sensor for surface topography measurement using a fibre optic principle", *Sensors and Actuators A*, **31**, pp.68-74, 1992.

[60] L.Zhang, H.Matsumoto and K.Kawachi, "Two-directional scanning method for reducing shadow effects in laser triangulation", *Meas. Sci. Technol.*, **8**, pp.262-266, 1997.

[61] V.Bodlaj and E.Klement, "Remote measurement of distance and thickness using a deflected laser beam", *Appl. Opt.*, **15**, No.6, pp.1432-1436, 1976.

[62] A.J.Makynen, J.T.Kostamovaara and R.A.Myllylä, "A high-resolution lateral displacement sensing method using active illumination of a co-operative target and a focused four-quadrant position sensitive-detector", *IEEE trans. Instrum. Meas.*, **44**, No.1, pp.46-52, 1995.

[63] A.T.Shepherd, "25 years of Moiré fringe measurement", *Precision Eng.*, **1**, pp.61-69, 1979.

[64] Dr. Johannes Heidenhain Gmbh, Traunreut, Germany, "NC linear encoders", Product catalogue, September 1993.

[65] J.-D.Lin and H.-B.Kuo, "Development of a new optical scale system by the diffractive phase interference method", *Meas. Sci. Technol.*, **6**, pp.293-296, 1995.

[66] Sony Magnascale Inc., Tokyo, Japan, "Sony Laserscale: 1/100 micron digital scale", Product catalogue No. 293., December 1991.

[67] T.Suhara, T.Taniguchi, M.Uemukai, H.Nishihara, T.Hirata, S.Iio and M.Suehiro, "Monolithic integrated-optic position/displacement sensor using waveguide gratings and QW-DFB laser", *IEEE Photon. Technol Lett.*, **7**, No.10, pp.1195-1197, 1995.

[68] J.Akedo, Y.Kato and H.Kobayashi, "High precision detection method for the reference position in an optical encoder", *Appl. Opt.*, **32**, No.13, pp.325-2319, 1993.

[69] F.J.MacWilliams and N.J.Sloane, "Pseudo-random sequences and arrays", *Proc. IEEE*, **64**, No.12, pp.1715-1729, 1976.

[70] J.T.M.Stevenson and J.R.Jordan, "Absolute position measurement using optical detection of coded patterns", *J. Phys. E: Sci. Instrum.*, **21**, pp.1140-1145, 1988.

[71] M.Durana, R.Gallay, Ph.Robert and F.-C.Pruvot, "Novel type submicrometre resolution pseudorandom position optical encoder", *Electron. Lett.*, **29**, No.20, pp.1792-1794, 1993.

[72] A.R.Nelson, D.G.Mcmahon and R.L.Gravel, "Passive multiplexing system for fibre optic sensors", *Appl. Opt.*, **19**, pp.2817-2920, 1980.

[73] J.P.Bentley, "Principles of measurement systems", 2nd edition, Longman, London, 1989.

[74] T.A.Kwa and R.F.Wolffenbuttel, "Optical angular displacement sensor with high resolution integrated in silicon", *Sensors and Actuators A*, **32**, pp.591-597, 1992.

[75] E.M.Petriu, "Absolute-type position transducers using a pseudorandom encoding", *IEEE Trans. Instrum. Meas.*, **IM-36**, No.4, pp.950-955, 1987.

[76] M.Maghoo, "A wavelength encoded rotary displacement fibre sensor", *Meas. Sci. Technol.*, **5**, pp.260-266, 1990.

[77] K.Fritsch and G.Beheim, "Wavelength-division multiplexed digital optical position transducer", *Optics Lett.*, **11**, No.1, pp.1-3, 1986.

[78] W.B.Spillman Jr., D.R.Patriquin and D.H.Crowne, "Fibre optic linear displacement sensor based on a variable period diffraction grating", *Appl. Opt.*, **28**, No.17, pp.3550-3553, 1989.

[79] X.P.Liu, R.C.Spooncer and B.E.Jones, "An optical fibre displacement sensor with extended range using two-wavelength referencing", *Sensors and Actuators A*, **25-27**,pp.197-200, 1991.

[80] I.H.White, "A multichannel grating cavity laser for wavelength division multiplexing applications", *J. Quantum Electron.*, **9**, No.5, pp.893-899.

[81] M.Gounelle, V.Loriette, A.C.Boccara and R.Nahoum, "A compensated optical profilometer for wavefront control of Virgo gravitational wave antenna optics", *Meas. Sci. Technol.*, **7**, pp.1032-1037, 1996.

[82] G.C.Bakos, N.F.Tsagas, J.Lygouras and J.Lucas, "Long distance non-contact high precision measurements", *Int. J. Electron.*, **75**, No.6, pp.1269-1279, 1993.

[83] S.K.Nayar, M.Watanabe and M.Noguchi, "Real-time focus range sensor", *Proc. 5th IEEE International Conference on Computing*, MIT, Cambridge MA, USA, June 1995.

[84] *Article*, "Data in video speed up accurate manufacture", *Optics and Laser Europe*, IoP Publishing, Bristol, Issue 50, pp.27-29, May 1998.

[85] J.P.Lesso, A.J.Duncan, W.Sibbett and M.J.Padgett, "Optical surface-profilometry based on polarisation analysis", *to be published.*

[86] L.Dick and P.de Groot, "High-speed non-contact profiler based on scanning white light interferometry", *Appl. Opt.*, **33**, pp.7334-7448, 1994.

[87] B.E.Jones, R.S.Medlock and R.C.Spooncer, " Intensity and wavelength-based sensors and optical actuators", *Chapter 12, Optical Fibre Sensors: Systems and applications, volume 2*, 1989.

[88] C.Menadier, C.Kissinger and H.Adkins, "The fotonic sensor", *Instr. Contr. Sys.*, **40**, p.114-120, 1967.

[89] D.A.Krohn, "Fibre optic sensors: Fundamentals and applications", Chapter 6, Instrument Society of America, 1988.

[90] S.D.Crossley, "Commercially available fibre optic sensors - 10 years of progress?", *Proc. 10th International Conference on Optical Fibre Sensors*, B.Culshaw and J.D.C.Jones eds, Proc. SPIE 2360, pp.249-252, 1994.

[91] M.Ali Shaik, "Design and analysis of fibre optic position sensor", *SPIE Vol. 1169*, Fibre Optic and Laser Sensors VII, pp.473-484, 1989.

[92] Z.Zhao, W.S.Lau, A.C.K.Choi and Y.Y.Shan, "Modulation function of a reflective fibre sensor with random fibre arrangement based on a pair model", *Optical Eng.*, **34**, No.10, pp.3055-3061, 1995.

[93] A. Shimamoto and K.Tanaka, "Geometrical analysis of an optical fibre bundle displacement sensor", *Appl. Opt.*, **35**, No.34, pp.6767-6774, 1996.

[94] R.O.Cook and C.W.Hamm, "Fibre optic lever displacement transducer", *Appl. Opt.* , **18**, No.19, pp.3230-3241, 1979.

[95] S.G.Hanson and B.H.Hansen, "Laser-based measurement scheme for rotational measurement of specularly reflective shafts", *SPIE Vol. 2292, Fibre optic and Laser Sensors XII*, pp.143-153, 1994.

[96] A.M.Scheggi, M.Brenci, G.Conforti, R.Falciai and A.G.Mignani, "Optical fibre displacement sensor", *SPIE Vol. 798, Fibre Optic Sensors II*, 73-75, 1987.

[97] H.Wang, "Reflective fibre optical displacement sensors for the inspection of tilted objects", *Optical & Quantum Electron.*, **28**, No.11, pp.1655-1668, 1996.

[98] A.Shimamoto and K.Tanaka, "Optical fibre bundle displacement sensor using an ac-modulated light source with subnanometer resolution and low thermal drift", *Appl. Opt.* ,**34**, No.25, pp.5854-5860, 1995.

[99] W.H.Ko, K.-M.Chang and G.-J.Hwang, "A fibre-optic reflective displacement micrometer", *Sensors and Actuators A*, **49**, pp.51-55, 1995.

[100] J.W.Berthold III, "Historical review of microbend fibre-optic sensors", *J. Lightwave Technol.*, **13**, No.17, pp.1193-1199, 1995.

[101] J.N.Fields, C.K.Asawa, O.G.Ramer and M.K.Barnoski, "Pressure sensor", *J. Acoust. Soc. Am.*, **67**, pp.816-818, 1980.

[102] N.Lagakos, T.Litovitz, P.Macedo, R.Mohr and R.Meister, "Multimode optical fibre displacement sensor", *Appl. Opt.* ,**20**, No.2, pp.16-168, 1981.

[103] R.C.Gauthier and C.Ross, "Theoretical and experimental considerations for a single-mode fibre-optic bend-type sensor", *Appl. Opt.*, **36**, No.25, pp.6264-6273, 1997.

[104] R.J.Redding, "Intrinsic safety - The use of electronics in hazardous locations", McGraw-Hill, London, 1971.

[105] RDP Electronics Ltd., "Displacement Transducers for hostile environments", product catalogue, update 1997.

[106] "Applications of Photonics in Avionics - A statement of anticipated requirements", Subcommittee on equipment and systems technology, The Society of British Aerospace Companies, Issue 1, February 1996.

[107] B.Culshaw, "Applications of fibre optic sensors in the aerospace and marine industries", Chapter 18, *Optical fibre sensors: systems and applications, volume 2,* eds. B.Culshaw and J.P.Dakin, Artech House, 1989.

[108] Private communication with D.A.Brown, BAe-Matra Defence Systems.

[109] R.P.Griffiths, "A market assessment of position sensing technology", Internal report, RDP Electronics Ltd., March 1998.

CHAPTER 2

THE RESONANT CAVITY OPTICAL POSITION SENSOR

A new form of optical position sensor is described within this chapter. Termed the Resonant Cavity Optical Position Sensor, the sensor uses a semiconductor laser diode that is subject to optical feedback, in order to measure absolute position. This sensor is designed for medium range position measurement and is potentially capable of high resolution. It uses low optical powers to achieve this and may be configured to operate as a non-contact, contact or fibre-addressed sensor. The rudimentary operation of this novel sensor is described and experimental results are discussed.

2.1. Introduction

In general, optical displacement sensors exhibit excellent operating characteristics when used for long range applications such as time-of-flight range-finding, or very short range applications where very accurate interferometric techniques may be used. These measurement principles have now become standard measurement techniques in industry [1-4]. However, the production of medium range, cost effective optical position sensors for use in harsh industrial environments has, to date, proved difficult.

The use of optical feedback to a semiconductor laser as a basis for intermediate range position measurement has been well established. It has been applied to short range systems for use in pressure membrane applications [5,6], with longer range position sensing achieved using modulation dynamics [7,8], optical bistability [9] and mode-hop counting [10,11]. However, application of these novel techniques has provided working ranges which have been limited to approximately 1 metre. Therefore, it would be advantageous to be able to produce a device capable of position measurement over a range of several centimetres to several metres, with enhanced performance when compared to more traditional industrial measurement techniques.

In order to meet the above requirements, a novel optical position sensor has been developed which is capable of absolute position measurement, by applying delayed optical feedback from a distant reflector to a semiconductor laser. This *resonant cavity optical position sensor* operates using an extremely simple optical configuration, which requires the use of only a single optoelectronic component. Furthermore, it can not only be engineered to be rugged and stable, but may also be potentially low-cost. It operates with low optical powers and may be implemented both as a free space or fibre coupled position sensor, with a measurement range over a range of between a few centimetres and several metres.

2.2. Sensor Overview

Figure 2.1 shows a schematic diagram of the most simple form of the sensor. The collimated optical output from a semiconductor laser driven with a constant bias current is incident upon an external reflector. This reflector is aligned so that a significant portion of the optical signal is fed back into the laser. An external cavity is therefore in operation.

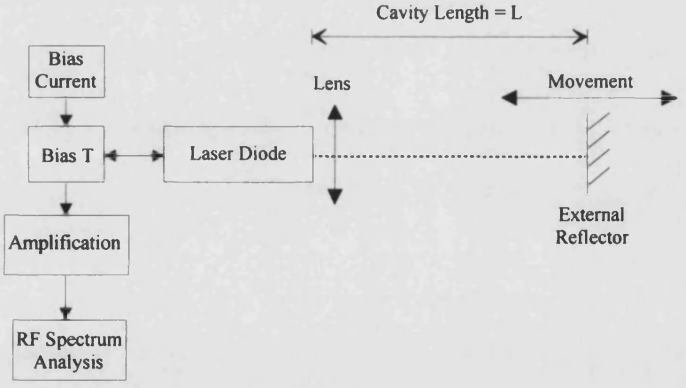

Figure 2.1. Schematic representation of a typical optical sensor arrangement using a simple external cavity configuration.

The external reflector may be considered as an optical target. For position sensing applications the optical target may be either attached to, mechanically coupled to or be part of the device under test. Accordingly, measurement of the position of this optical target allows determination of the absolute position (or displacement) of the body under test.

By biasing the laser appropriately, it is found that the presence of the external cavity causes the laser to oscillate in a number of longitudinal, external cavity modes. The frequency spacing between the modes is determined by the length of the external cavity [12,13]. The dynamic physical processes which govern the behaviour of these external cavity modes, are quite complex and will be theoretically analysed in some depth in chapters 3 and 6. However, it can be shown [12,13,] that these optical, external cavity modes will interact within an active medium such as a laser or photodiode and in so doing will generate a RF signal. The optical intensity incident upon such a photodetector may be expressed in terms of the total electric field present within the cavity,

$$I(t) = \left(\sum_{i}^{n} \varepsilon_i(t) \right)^2 , \tag{2.1}$$

where $\varepsilon_i(t)$, the time varying electric field of a particular mode is of the form,

$$\varepsilon_i(t) = E_i \cos(\omega_i t + \phi_i) . \tag{2.2}$$

It should be assumed that as the optical intensity is being considered, the amplitude coefficient of the electric field is normalised to unit area. It should also be noted that the phases ϕ_i of the optical modes are not necessarily locked in any way. Equation 2.1 may be expanded to provide a series of cross-product terms,

$$I(t) = \sum_{i}^{n} [E_i \cos(\omega_i t + \varphi_i)]^2 + \sum_{j=2}^{n} \sum_{k=1}^{j-1} E_j E_k \left[\cos((\omega_j - \omega_k)t + \phi_j - \phi_k) + \cos((\omega_j + \omega_k)t + \phi_j + \phi_k) \right] \tag{2.3}$$

The photodetector cannot respond to the 'sum' components of the optical intensity, the frequencies of which are several hundred THz. However, the 'difference' components are of much lower frequencies and these disturbances may give rise to signal generation within the detector. Depending upon the length of the external cavity, these signals can vary in frequency from several MHz to several tens of GHz. These self-heterodyned *difference* or *beat* frequencies can be measured by analysing the junction voltage of the laser diode or by using a photodiode suitably placed in the optical path. If the frequency spectrum of the output signal from the detector is

subsequently analysed, it can be observed that it consists of a series of *resonance peaks* as illustrated in figure 2.2. These peaks occur at positions in the frequency spectrum which approximately correspond to the round trip frequency of the external cavity and its harmonics [14-18],

$$f_m \approx \frac{mc}{2L_{ext}}, \tag{2.4}$$

where m is an integer number defining the order of the resonance peak. The speed of light in vacuo is denoted by c, while L_{ext} is the total effective external cavity length (taking into account any changes in refractive index along the path of the optical beam within the cavity).

It will be demonstrated in chapters 3 and 6 that while the relationship detailed in equation 2.4 is a very close approximation, it is not exact. Nevertheless, from examination of this it can be immediately understood that the optical system described by figure 2.1, may be employed in position measurement applications. Measurement of the frequencies at which the resonance peaks occur (or the frequency separation between them) can be used to determine an accurate value for the external cavity length. Accordingly, the absolute position of the optical target and hence the body under test is therefore determined.

The measurement principle used in this sensor therefore, has the advantage of producing an output which is an *absolute* measurement of the position of the optical target. This is in contrast to many optical measurement systems which are *incremental* and therefore dependent upon a particular reference point. This reference point may be lost on power down of the instrument or following an unexpected loss of power supply. If this datum or reference is lost then so is the absolute position information, thereby imposing limits upon switch off and multiplexing of the sensor. Such inherently incremental systems include interferometric fringe-counting apparatus [19] and many linear encoder systems [20,21].

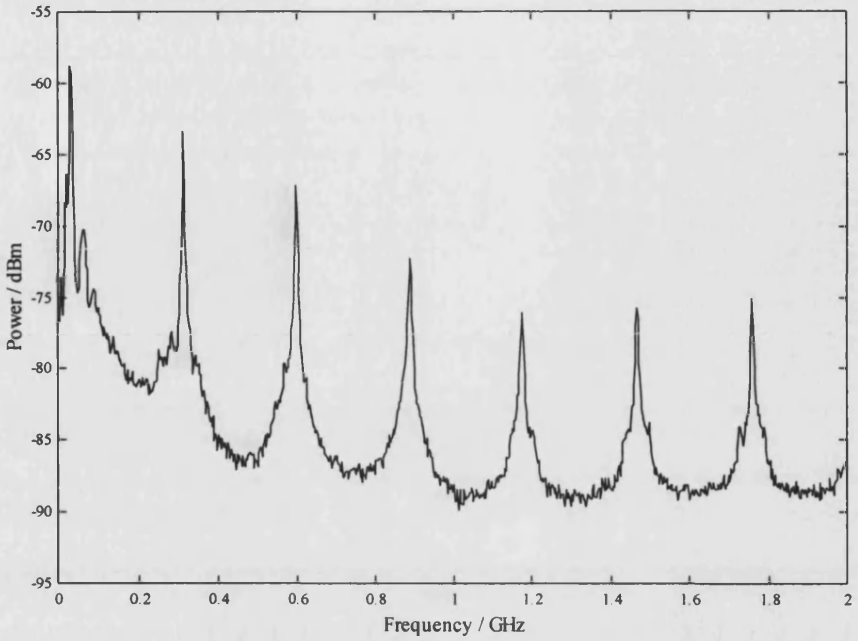

Figure 2.2. Typical RF spectrum derived from the junction voltage of semiconductor laser used in the external cavity measurement arrangement.

Figure 2.2 shows a typical frequency spectrum obtained from a measurement of the laser diode junction voltage. It can be seen that the spectrum consists of a series of clearly identifiable, sharp, resonance peaks, separated by regular frequency intervals. The value of maximum signal-to-noise ratio observed in this example (in excess of 20dB) is typical of that obtained with a variety of lasers and external optical cavity configurations when operated at their optimum conditions. The roll-off of signal-to-noise ratio that can be seen at higher frequencies is partly due to amplifier bandwidth limitations. However, the relative intensities of the particular peaks are also dependent upon such variables as bias current, level of optical feedback and laser device parameters.

Figure 2.2 demonstrates the application of using a semiconductor laser not only as a source, but also as a photodetector by monitoring the variation in the diode junction voltage. This is feasible when the laser is being driven continuous wave (cw). The use of the laser as a photodetector is a concept widely used in Doppler velocimetry [22,23]. However, in this case, using the laser as a detector in this way minimises the number of optical components which are required. The need for a

separate photodetector as well as other additional optical components that might be required such as lenses and beamsplitters is therefore eliminated. This means that the optical system can be engineered to allow rugged implementation for high stability in real industrial applications. This provides a very important practical advantage over other novel optical position sensing techniques which may require a high number of optical components [24]. Large numbers of components may present potential practical engineering difficulties, as well as increasing system costs. It should be noted, however, that while it may be advantageous in most cases to employ the laser diode as both source and detector, in certain applications, it may be more convenient to use a conventional photodiode to detect the beat frequency signals.

2.3. Demonstration of the Measurement Principle

The sensor may be successfully operated using a variety of components and configurations as will be explained in this chapter. However, in order to demonstrate the basic operation of the sensor the experimental arrangement shown in figure 2.3 was used.

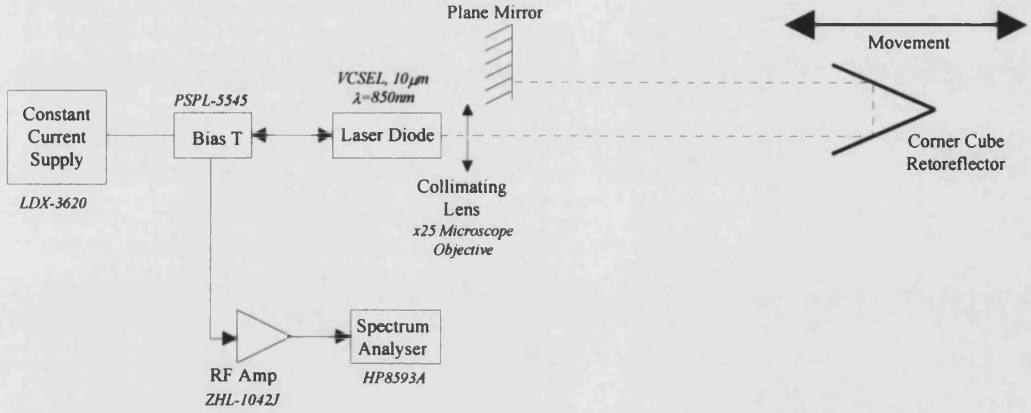

Figure 2.3. Experimental arrangement used to demonstrate principle of measurement.

2.3.1. Practical Experimental Arrangement and Procedure

In this particular example, a Vertical Cavity Surface Emitting Laser (VCSEL), was used as both as the optical source and the detector. These devices differ substantially from conventional Fabry-Perot semiconductor lasers whose mirrors are formed by cleaving the semiconductor material along the material plane.

A VCSEL consists of an active gain region sandwiched between two distributed Bragg reflectors [25] which produces a laser which unlike a Fabry-Perot laser, emits normal to the plane of the device [26,27]. By keeping the length of the active region within the laser cavity short, the device can be engineered so that only a single allowable longitudinal cavity mode lies within the gain region of the material. VCSELs of varying structure and design have now been developed [28-31] for a variety of applications. Although designed predominantly for use in short haul communications applications, these devices may be readily applied to other areas due to their convenient properties [32]. These devices have been found to be particularly convenient for use in this sensing application due to their low astigmatism circular beamshape, low operating current and good response to optical feedback [33].

The VCSEL used in this experiment lased at a wavelength of 850nm. For optimum operation the device it was biased cw at 9.0mA, just below its threshold current of 9.6mA using a constant current supply (ILX Lightwave *LDX-3620*). This current was fed via a high frequency 'Bias-T' (PSPL 5545C) so that the RF component of the junction voltage, generated as a result of the delayed optical feedback, could be analysed. As the RF signal induced within the laser was rather small [18], (of the order of -80dBm peak power), the signal required a degree of amplification to allow satisfactory frequency analysis to take place. This was applied by using a general purpose RF amplifier which provided a gain of 25dB over a bandwidth of 2.5 GHz (Mini-Circuits ZHL-1042J). The amplified output signal was subsequently monitored using a swept source RF spectrum analyser (HP8593A). This experimental arrangement allowed off-line the frequencies of the resonance peaks produced by the beating of the external cavity modes to be measured and their structure noted.

The optical beam was collimated using a standard microscope objective lens (x25), with a folded cavity arrangement being used to provide angular alignment stability. In order to construct this external cavity reflector arrangement, a hollow corner cube retroreflector was used to fold the optical beam around on itself so that it

ran parallel, but displaced a small distance from the original optical axis as shown in figure 2.3. A plane mirror was then used to close the external cavity. Correct alignment of this mirror caused the light incident upon it to be reflected in such a way that it was fed back into the laser, via the retroreflector. The retroreflector was mounted onto a precision positioning stage with a movement range of 30cm to allow variation of the external cavity length. A stepper motor was connected to the stage and controlled by a computer to allow precise positioning of the optical target.

The folded cavity configuration was used to improve the stability of the external cavity. Accurate alignment of the plane mirror was required to achieve the required degree of feedback to the laser. Such a configuration is less susceptible to optical alignment variations during movement than a cavity constructed in an axial configuration with a plane mirror as the target (as shown in figure 2.6.*a*). As the retroreflector is relatively alignment insensitive, it may be moved back and fore along the optical axis without loss of alignment. Such a system was found to be best suited to bench-top experimental investigations.

To analyse the variation of the sensor output as a function of the optical target position, the change in the cavity length was measured using a Linear Variable Differential Transformer (LVDT) displacement sensor (RDP Electronics Ltd. ACT6000), which has a range of 30cm and an accuracy of 50 microns. This provided an incremental measurement to which an absolute datum was added by carefully measuring the cavity length at a convenient point using an accurate steel rule. Care was taken to ensure that the movement of the optical target was along the optical axis in order to minimise the possibility of a parallax error occurring.

2.3.2. Analysis of Experimental Results

Figure 2.4 illustrates the noticeable change in the nature of the frequency spectrum which occurs when the external cavity length is varied. The fact that the frequencies of the resonance peaks within the spectrum are inversely proportional to the external cavity length can be clearly seen. It can also be seen that as the cavity

length increases, then the decrease in peak separation is accompanied by a corresponding decrease in the linewidth of the peaks.

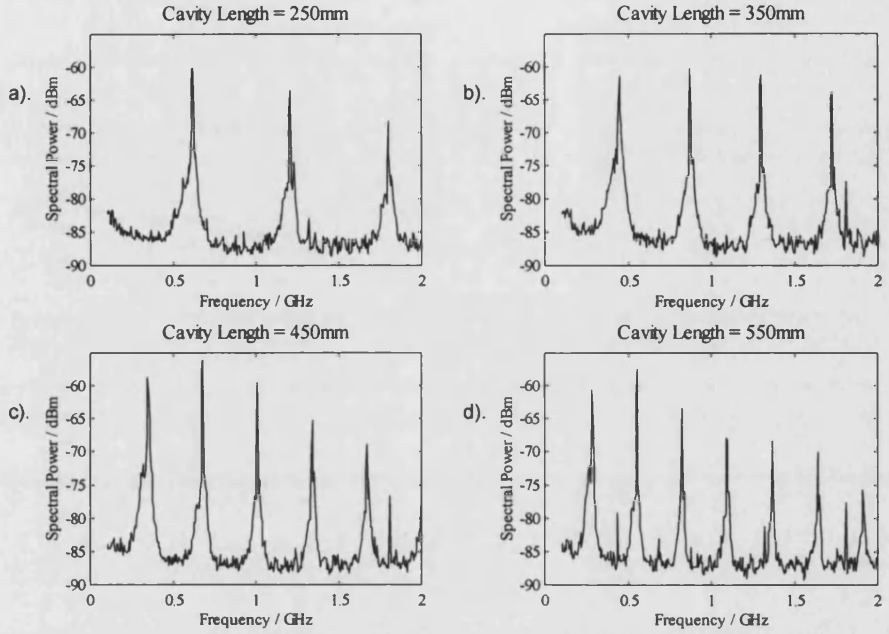

Figure 2.4. Variation in frequency spacing as a function of external cavity length. a). L_{ext}=250mm, b). L_{ext}=350mm, c). L_{ext}=450mm, d). L_{ext}=550mm.

The positions of the resonance peaks present in the RF spectrum were measured using the spectrum analyser as a function of cavity length and hence optical target position. In order to ascertain the peak position as accurately as possible, 100 scan video averaging was used in order to smooth out any temporal noise contributions in the vicinity of the resonance peak. Furthermore, the span of the frequency sweep of the analyser was reduced as much as possible to allow the most accurate possible measurement to be made. Considering these factors, an estimation of the typical measurement error produced was 0.2MHz.

Figure 2.5 shows the variation in frequency of the second resonance peak in the spectra as a function of the reciprocal of cavity length, as measured using the spectrum analyser. The quality of the linearity (0.3% average error) of the frequency variation when plotted against the reciprocal of cavity length can be clearly seen. These results demonstrate the ability of this arrangement to produce an accurate position measurement.

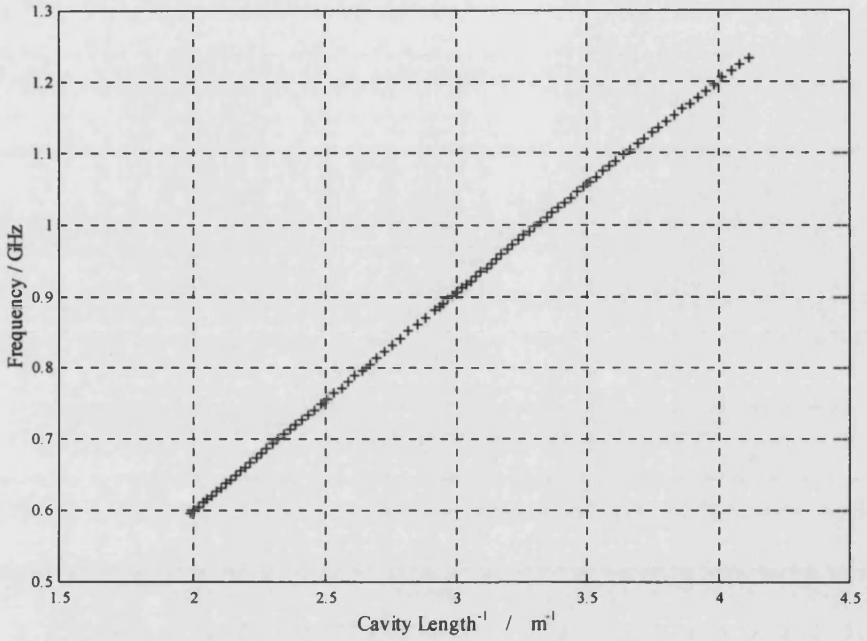

Figure 2.5. Variation in frequency of first harmonic peak as a function of the reciprocal of external cavity length.

2.3.3. Alternative Optical Configurations

Alternative external cavity configurations which may be used in the sensor are shown in figure 2.6. This figure shows the simple plane mirror arrangement (figure 2.6.*a*) and the folded cavity arrangement (figure 2.6.*b*) previously discussed. In addition, figure 2.6.*c*, illustrates the use of a lensed reflector as the optical target. The lensed reflector operates in an analogous way to a 'cat's-eye' reflector and as in the case of the folded cavity, provides an optical target which is subject to a far larger angular positioning tolerance than a plane mirror. This allows the target to be moved along the direction of the optical axis without alignment problems, which for example, may be due to small off-axis vibrations. In contrast, disturbances such as this could cause serious problems for a plane mirror target.

Use of the lensed reflector can provide an extremely compact practical optical system, with target and lens diameters as small as 5mm providing a good reduction in scale. In addition the lensed reflector possesses an improved angular alignment tolerance which is typically an order of magnitude better than that of a plane mirror. Another particular advantage of this configuration is that a minimum

number of optical components are required, unlike the folded cavity arrangement. However, as the retroreflector used in the folded cavity arrangement has such a high angular tolerance (~±20°), it is often found that for general laboratory work it is more convenient to use the folded cavity approach. Furthermore, this configuration allows longer cavities to be constructed in a limited working space.

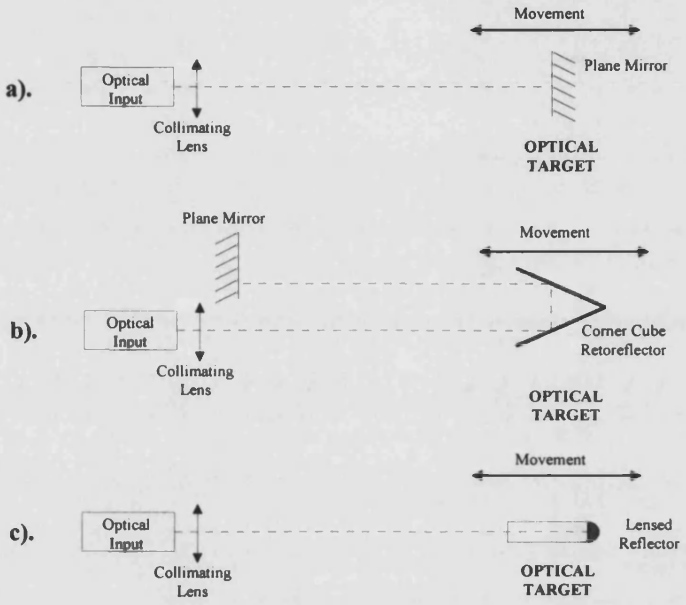

Figure 2.6. Examples of different optical configurations for the sensor: a). Simple plane mirror reflector, b). 'Folded' cavity, c). Lensed reflector target.

2.3.4. Discussion

While the data illustrated in figure 2.5 covers the cavity length range 0.2 to 0.5m the system has been successfully operated in the laboratory with cavity lengths of up to 4m. Due to the obvious physical constraints, it is difficult to test the bulk optical cavity configuration over longer cavity lengths than this. It should be noted, however, that as the sensor is dependent upon the application of optical feedback to the laser, losses due to the divergence of the beam within the external cavity and other loss mechanisms, should be minimised. However, this is offset by the fact that the *strength* of the feedback effect is increased with increasing cavity length [34], as will be explained in chapter 3.

At the other extreme of operation, very short cavity lengths correspondingly dictate the existence of large resonance peak frequency separations. This will eventually provide difficulties as the frequency separation of the peaks approaches

the bandwidth limit of the signal processing systems used to analyse the sensor output. However, in practice, cavity lengths of greater than eight centimetres have been accommodated.

The stability of this system can be observed, when one considers the 'off-line' manner in which these measurements were carried out. It should be noted, that acquisition of this data set in the manner described above took over an hour. Any large instability present would have led to a large degradation of linearity of the data during that measurement period. This cannot be perceived from examination of figure 2.5. The stability of the system can be further demonstrated when it is considered that the laser diode was not subject to any temperature control during the course of these measurements. The long term stability and performance of the sensor is discussed in detail in chapter 5.

Therefore, a simple optical system has been presented which has been demonstrated to be capable of measuring the absolute position of an optical target to a high resolution, limited by measurement method. The simple optical system leads to an easily aligned configuration with few components leading to a low-cost technique which can be engineered with improved robustness and stability than other, more complicated optical techniques. The development of this novel position sensing technique has led to a number of patent applications being filed, for both UK [35,36] and International [37] intellectual property rights coverage.

2.4. Performance of various types of semiconductor laser in sensor

Examination of the measurement principle outlined in section 2.2, where the semiconductor laser may be used both as the optical source and detector, asserts the belief that successful operation of the sensor is heavily dependent upon the performance of the device selected for use. Consideration of the changing nature of the commercial marketplace, the fast development of new products and the inevitable discontinuation and obseletion of other products, identifies the importance that the operation of the sensor is not solely dependent upon any one particular device. It is important therefore, to demonstrate that the sensor can be operated using

a variety of different semiconductor laser diodes. Indeed, it may be found that a particular type of laser diode may be best suited to a certain application of the measurement principle. Conversely, if one can take advantage of high volume products designed for other general applications then one can reap the benefits of cost reduction. This cost reduction may not be available if the technique was dependent upon a specialised device in the way that certain otherwise good alternative sensing techniques may be [38]. Therefore, considering the above argument several types of laser diodes were tested in addition to the VCSELs discussed so far (figure 2.2), in order to assess their suitability for operation in this system.

Figure 2.7 illustrates typical RF spectra obtained using several different types of laser diode. A similar experimental arrangement to that shown in figure 2.3 was used to test the devices. Figure 2.7.*a* illustrates the response obtained from a typical, low-cost, medium power, Fabry-Perot type laser. This SHARP LTO26MD lases at a wavelength of 780nm, and is of a type commonly found in compact disk players and laser-printers [39]. The threshold bias current of this device is approximately 40mA. Figure 2.7.*b* shows a spectrum obtained using another type of Fabry-Perot laser. This device, manufactured by BNR Europe, lases at 1300nm and has a threshold bias current of approximately 20mA. Finally, figure 2.7c) shows a typical RF spectrum obtained from an anti-reflection (AR) coated laser, again manufactured by BNR Europe.

Inspection of figure 2.7 shows that the different laser diodes produce quite similar responses, with several common features being present in all the spectra. It can be seen that each device when operating with the required amount of optical feedback produces a series of resonance peaks at frequencies corresponding to the round-trip frequencies of the external cavity. It is noticeable that each resonance peak consists of a sharp peak which is set upon a broader resonance noise floor structure, the sides of which have a noticeable 1/f like response as noted previously by Besnard et al [40,41]. Furthermore, the presence of minor subsidiary 'side-band' peaks can be seen around the vicinity of major resonance peaks. A good example of

this fine structure can be seen around the first peak in the spectrum of figure 2.7.*a* and 2.7.*b*, where a subsidiary peak of ~3dB height above the apparent noise floor can be seen to the lower frequency side of the main peak.

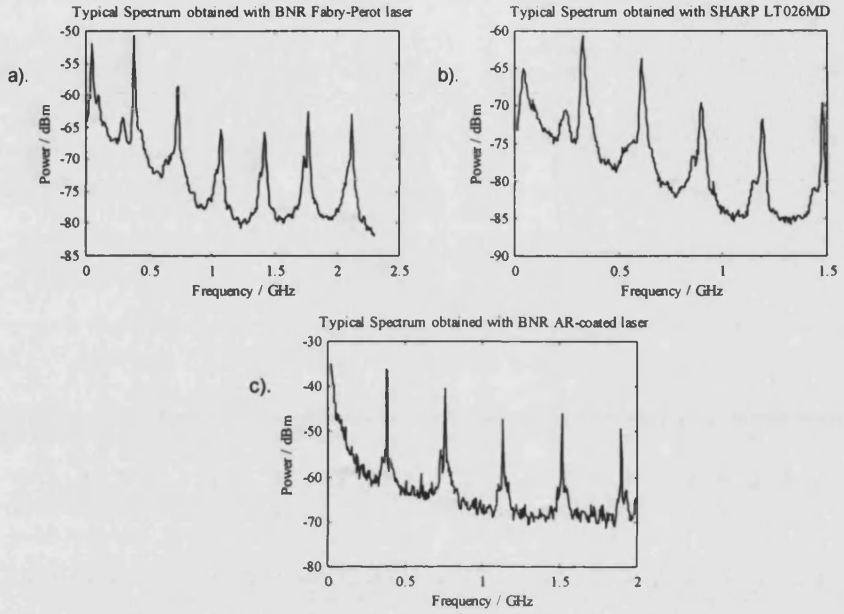

Figure 2.7 Typical output spectra from the sensor system at different external cavity lengths, obtained using the following lasers: a) A Fabry-Perot laser of lasing wavelength 1330nm (BNR GT217Ex34), b) A SHARP LT026MD Fabry-Perot laser of lasing wavelength 780nm, c) An anti-reflection coated Fabry-Perot laser (BNR).

Another common effect which is noticeable in each of the spectra is the presence of a low frequency peak, which does not correspond to an external cavity round trip resonance. The strength of this peak can be seen to be of the same order of magnitude as the first round-trip resonance peak. The existence of this feature is also evident in figure 2.2. The presence of this low frequency peak explains the quasi-periodic low frequency fluctuations (LFFs) evident in the optical output of a laser subjected to delayed optical feedback [42]. The theoretical analysis given in chapters 3 and 6, will confirm the existence of this low frequency fluctuation. Whilst this effect has been studied in some depth [41-46], the exact causes of the LFF are still debated. In chapters 3 and 4 however, an alternative explanation as to the origins of this peak will be given.

It is important to note that the spectra shown in figures 2.2 and 2.7 were processed using a RF spectrum analyser, with its resolution bandwidth set to 30kHz.

Furthermore, in the case of figures 2.7.*a* and 2.7.*b*, one hundred scan video averaging was performed on the raw input data, in order to average out any slight temporal variations which occur in the spectrum. When the raw frequency spectrum, was displayed by the spectrum analyser without any video averaging, the heights of the resonance peaks were found to vary slightly with respect to one another in an apparently random way from scan to scan of the analyser. It can be shown that due to the inherent noise present within the system [47], the phases of the optical modes are not locked together. Therefore the noise will appear as temporal variations in the amplitudes of the resonance peaks from scan to scan when viewed using a swept source spectrum analyser.

The results shown in figures 2.2 and 2.7 indicate that semiconductor lasers of several different types and structures are capable of providing satisfactory output signals when applied to the resonant cavity sensor. Consequently, the important conclusion that can be reached is that the measurement principle outlined in section 2.2, is not dependent upon a particular type of specialised laser diode, which might limit the application of the sensor due to device cost or availability.

2.5 Assessing optimum laser bias current

During the initial investigations carried out to assess the viability of the measurement principle, it was found that the signal-to-noise ratios and the relative intensities of the resonance peaks, were dependent upon the bias current applied to the laser. This effect was examined in detail using the experimental arrangement shown in figure 2.8. In this case a VCSEL (the performance of which has been previously described) was used as the active device in the system.

As shown in figure 2.8, the laser diode temperature was actively controlled so that any variation in appearance of the RF spectra obtained could be only directly attributed to the variation in laser bias current. A closed loop temperature controller (LDT-5910) was used to maintain the temperature of the device at a constant value of 22.7°C. The controller made use of a thermistor and a Peltier effect heat pump operated in a feedback loop with the controller's own *pid* (*p*roportional, *i*ntegral,

*d*ifferential, [48]), control system to stabilise the device temperature. Both the thermistor and heat pump were mounted in good thermal contact with the brass laser sub-mount. The thermistor was mounted as close as possible to the device whilst maintaining good thermal contact with the laser sub-mount. A small heat sink was employed to dissipate any excess thermal energy removed from the laser mount by the heat pump.

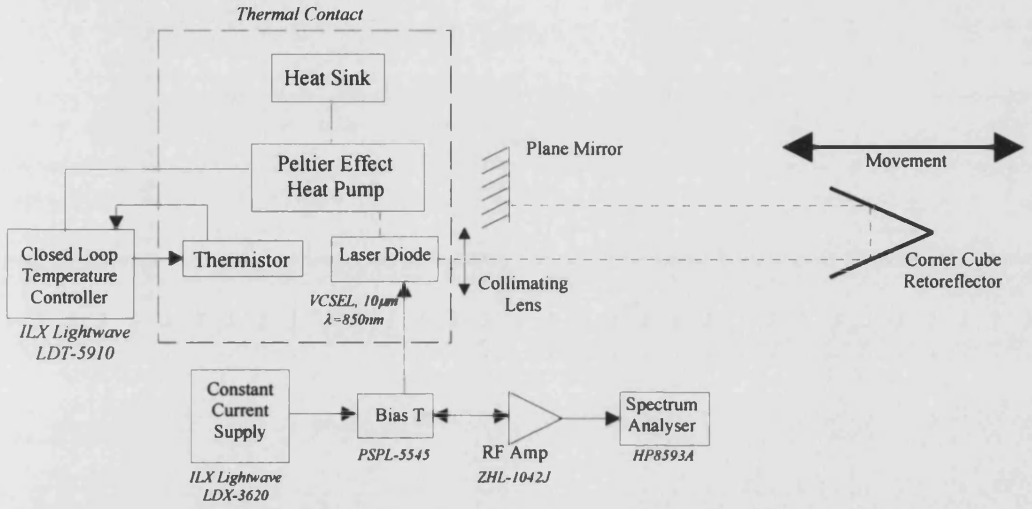

Figure 2.8. Experimental arrangement employed for assessment of optimum laser bias current.

In addition to controlling the device temperature, care was taken to ensure that all parameters other than the bias current, (including the external cavity length) were kept constant during the course of these measurements.

It was found that at very low bias currents, well below the threshold current of the solitary laser no resonance peaks were formed. As the bias current was increased, the resonance peaks began to form above the noise floor of the spectrum (figure 2.9.*a*) growing in magnitude until they become maximal (figure 2.9.*c*). This typically occurs at a bias level very close to the solitary laser threshold current. As the bias current was increased still further, the signal-to-noise ratio decreased with an increase in peak structure distortion occurring. Secondary peaks situated in-between the main peaks were found to increase in magnitude (figure 2.9.*e*) so that they were of comparable size (figure 2.9.*f*) to the original resonance peaks. Ultimately, as the bias current was increased still further (figure 2.9.*h*) the increased distortion removes almost all structure within the area of the resonance peaks,

leaving an enhanced average noise floor level when compared with the sub-threshold conditions.

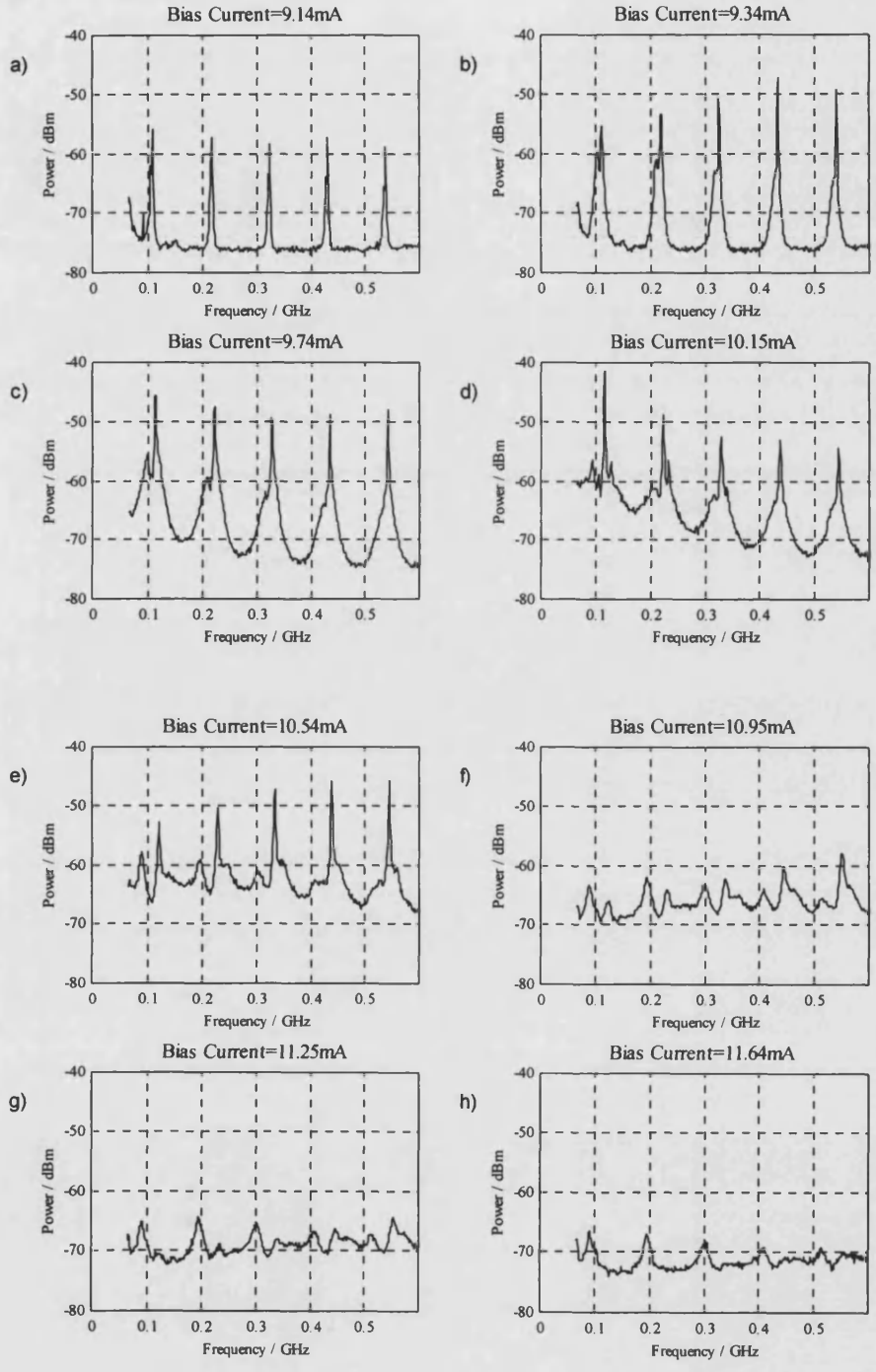

Figure 2.9. Variation of resonance peak structure as a function of laser bias current for the VCSEL.

When operation of the system as a sensor is considered, it may be appreciated that the ideal RF spectrum is achieved when the signal-to-noise ratios of the resonance peaks are maximised and the resonance peaks possess similar peak

power levels. It can therefore be argued that the optimum biasing point of the laser when used in this application occurs when these criteria are met. Experimental investigations showed that for this particular laser diode, (the VCSEL), this optimum bias point occurs at a bias current of approximately 9.5mA (±0.1mA). This is very close to the threshold current of the device which is approximately 9.6mA.

This fact also appears to hold true for other lasers. Figure 2.10 illustrates the variation in the RF spectrum as a function of bias current obtained when the VCSEL is replaced in the experimental arrangement of figure 2.8 by a SHARP LT026MD semiconductor laser diode (the same device used to produce the spectra shown in figure 2.7.*b*.

As the threshold current of this laser is approximately 39mA, it can be seen that the optimum bias current for this device is once again situated close to the threshold current of the laser. Further examination of figure 2.10 shows that the behaviour of the mode structure as a function of bias current is of a very similar form to that encountered when using the VCSEL even though the devices possess quite different physical structures.

The operating characteristics of these laser diodes shown in figures 2.9 and 2.10 have also been found to hold true for several other lasers which have been tested. Obviously, while the optimum operating bias current may be different for each laser, it is always found to occur close to the threshold current, which is a fact that is noted in the research literature [17,40]. Importantly however, the mechanism of operation appears to be of a similar nature for each device.

Finally, it is important to note that as the optimum bias current for this application lies very close to the normal solitary laser threshold, the average optical output power of the system is quite low. Accordingly, this means that the output power of the system is typically much less than 0.5mW, with the ensuing reduction in the likelihood of any eye-safety problems, when compared with laser operation at higher bias currents.

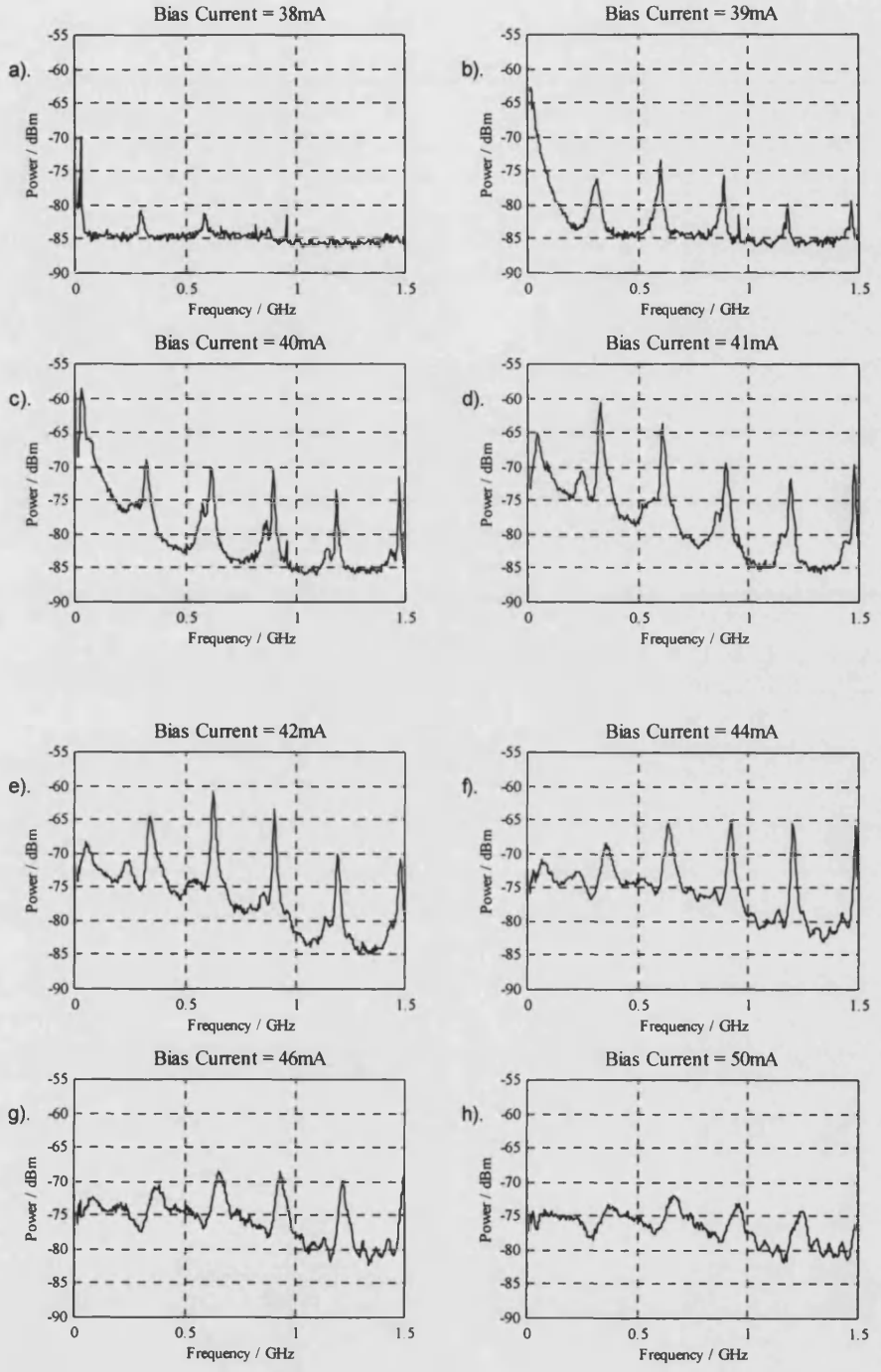

Figure 2.10. Variation in resonance peak structure as a function of bias current for SHARP LT026MD Fabry-Perot laser.

2.6. Quantifying feedback levels to the laser

In order to gain a reasonable understanding of the behaviour of the external cavity arrangement used in the sensor, it is useful to know the amount of feedback that is being applied to the laser. These data can be used to theoretically analyse the

response of the sensor system. The aim of this analysis is to verify the experimental results obtained, and to predict improvements which may be made to the system in order to optimise performance.

Unfortunately, it is difficult to measure exactly how much optical feedback is applied to the laser at any one time. However, a reasonably accurate estimate may be made by examining the change in threshold current which occurs when the device is operated with feedback. It is found that the threshold current is reduced on application of external optical feedback, in the manner shown schematically by figure 2.11 [40].

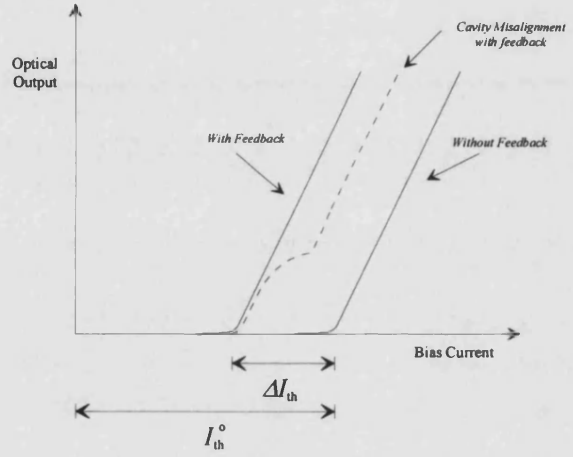

Figure 2.11. Schematic representation of change in threshold current of laser after application of external optical feedback (after [40]).

If a linear relationship is assumed between bias current and optical gain, it can be shown [49-51], that the reduction in threshold current on application of feedback ΔI_{th}, may be quantified by the following relationship:

$$\frac{\Delta I_{th}}{I_{th}^{o}} = \frac{1}{\left(\alpha_s L - \ln(r_1 r_2)\right)} . \ln\left[\frac{r_3 + r_2}{r_2\left(1 + r_2 r_3\right)}\right], \qquad (2.5)$$

In this relation I_{th}^{o}, is the threshold current of the solitary laser. The length of the laser is denoted by L, whilst α_s quantifies the amount of scattering losses present within the laser material. The field reflectivities of the external reflector and the laser facet nearest to it are given by r_3 and r_2 respectively. Rearrangement of this relationship provides a quantitative expression for the external reflectivity

$$r_3 = \frac{r_2\left(\exp\left[\frac{\Delta I_{th}}{I_{th}^o}\left(\alpha_S L - \ln(r_1 r_2)\right)\right] - 1\right)}{\left(1 - r_2 \exp\left[\frac{\Delta I_{th}}{I_{th}^o}\left(\alpha_S L - \ln(r_1 r_2)\right)\right]\right)}. \qquad (2.6)$$

Figure 2.12 shows the light-current characteristic of the VCSEL used to produce the RF spectrum shown in figure 2.2. The two curves shown in figure 2.12 detail the optical output of the device as a function of the bias current when operated both with and without optical feedback. The feedback was applied in the manner described by figure 2.13. As shown in this figure a non-polarising beamsplitter was inserted into the external cavity in order to allow the optical power output to be measured using a photodiode. The beamsplitter was aligned so that any back-reflections from its front face did not feed back into the laser. However, the losses incurred from using the beamsplitter must be taken into account when assessing the total external cavity power reflectivity which might exist if the beamsplitter were not used.

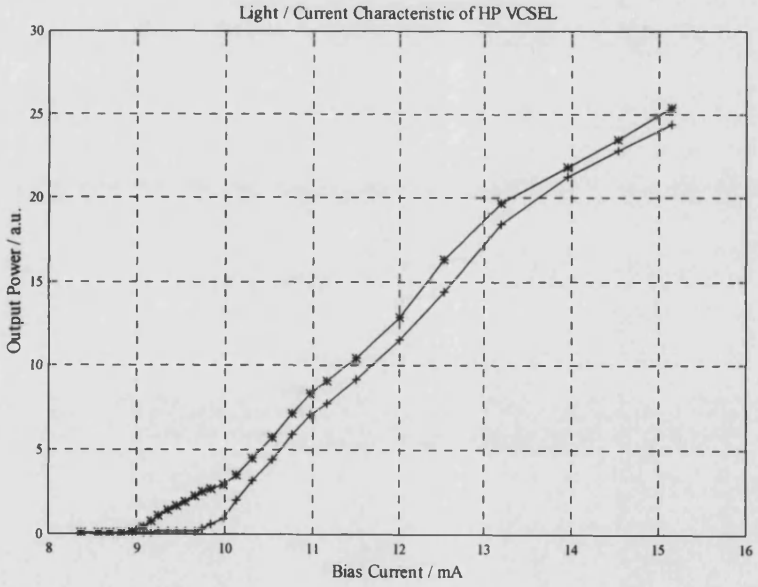

Figure 2.12. Light / Current characteristic of HP VCSEL with active diameter of 10 μm. Key: '+' Solitary laser response, '*' response after application of optical feedback in manner described by figure 2.13.

The solitary state of laser operation was achieved by blocking the external cavity with a suitable non-reflective material, between the beamsplitter and the corner cube. This allows the same fraction of the laser output to proceed directly to

the photodetector, thus allowing a directly comparable optical power measurement to be carried out.

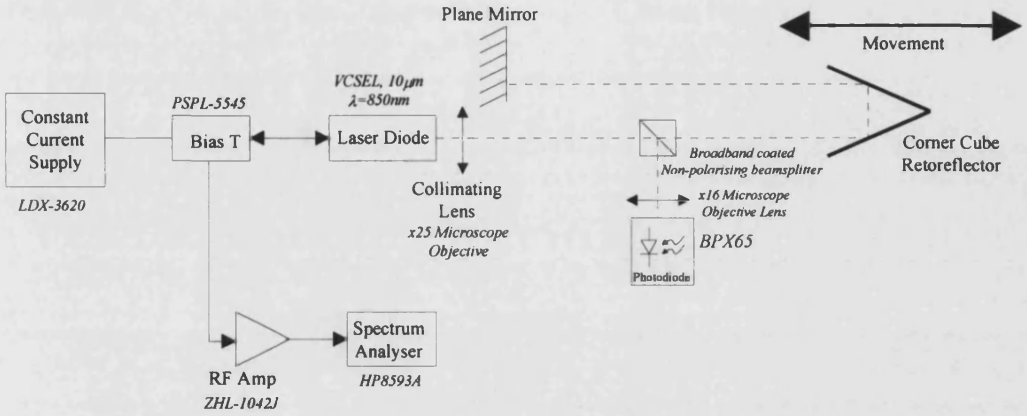

Figure 2.13. Experimental arrangement used for characterisation of VCSEL performance when applied to the external cavity system.

Figure 2.12 verifies experimentally the fact that application of external feedback to the laser diode leads to a reduction in the threshold current. In this case, it was found that a reduction in threshold current of 0.6mA occurred from a solitary laser threshold of 9.6mA. These data can be used along with the device parameters listed in table 2.1 to calculate the effective external field reflectivity r_3.

By applying the expression given in equation 2.6, the effective external cavity field reflectivity was found to be 0.12. This value signifies the total effective field reflectivity which takes into account losses occurring from diffraction effects, coupling losses, unwanted reflections as well as the true reflectivity of the external reflector, r_3', so that

$$r_3 = Ar_3' \qquad (2.7)$$

It must also be noted that the presence of the beamsplitter in figure 2.13 introduces an optical loss of at least 6dB into the system. Therefore the final value for r_3, if the beamsplitter was not used would be approximately 0.24, leading to an approximate 5% power reflectivity.

Parameter	HP VCSEL	SHARP LT026MD	AR Coated BNR laser
Wavelength, λ	850nm	780nm	1550nm
Rear facet reflectivity, r_1	0.999	0.57	0.57
Front facet reflectivity, r_2	0.99	0.57	0.1
Laser length, L	2 microns	250 microns	500 microns
Scattering losses, α_σ	$30cm^{-1}$	$30cm^{-1}$	$15cm^{-1}$
Solitary threshold current, I^o_{th}	9.6mA	39mA	35mA
Threshold reduction	0.6mA	1.5mA	9mA
External reflectivity, r_3	**0.24**	**0.22**	**0.21**

Table 2.1. Parameters for calculation of external reflectivity, r_3.

The feedback fraction in operation when other types of laser diodes are used may be assessed using similar means. Figure 2.14 shows the L/I characteristics of both the SHARP laser and the BNR AR coated laser whose performance within the external cavity system was previously illustrated in figure 2.7. The parameter values for these devices are again given in table 2.1.

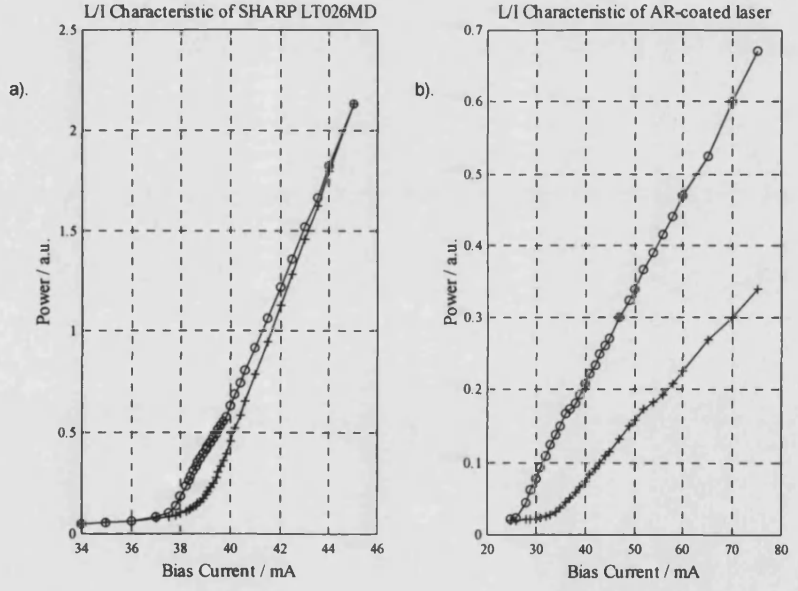

Figure 2.14. Light / current characteristics of a). SHARP LT026MD Fabry-Perot C.D. type laser diode & b). BNR AR-coated laser both with and without optical feedback. Key: '+' no optical feedback applied, 'o' with feedback.

An analysis of the L/I curves obtained using the SHARP laser produce a value for the external reflectivity of 0.11, which rises to approximately 0.22, once the loss due to the beamsplitter has been taken into account.

A slightly different experimental method was used to obtain the measurements taken with the AR coated laser (figure 2.14b). In this case a beamsplitter was not used to 'tap-off' a portion of the optical output as the output from the second facet of the laser could be accessed. Instead, the output from the rear facet of the device was monitored with a *pin* photodiode (New Focus v_{2011}). This produced an effective reflectivity value of 0.21.

Therefore, it can be seen that values for the effective reflectivity of ~5% are consistently obtained for each of the devices tested. This is as expected as essentially the same configuration has been applied at all times. Consequently, this value can be used with confidence for subsequent theoretical analysis of the experimental arrangement, in order to obtain predictions of system behaviour and a greater understanding of the optoelectronic system in operation. The theoretical analysis which has been carried out is described in chapters 3 and 6.

2.7. The Fiberised Sensor Configuration

In some applications, it may be advantageous to use a fiberised external cavity system. This may be so that the sensor head may be addressed using solely optical means, allowing use of the sensor in *inherently safe* sensing applications. Alternatively a length of fibre may be used to reduce the physical dimensions of a transducer by providing a minimum external cavity length, thereby limiting the maximum frequency difference between successive resonance peaks. This may also be done to allow convenient signal processing systems to be adopted.

2.7.1. Configuration of Fiberised Cavity

The fibre launched system may be constructed in the manner shown in figure 2.15. An arrangement is used to effectively couple light from the laser diode directly into single mode optical fibre. In many practical cases, a connectorised, commercial pigtailed device may be used, which possesses good coupling efficiency into the fibre. As the sensor is dependent upon feedback to the laser diode, it is important that the laser package does not contain an optical isolator. In laboratory experiments

a fibre lens may be the most convenient option in order to couple light from any suitable unpackaged laser diode into the single mode fibre. Another alternative is to use a butt-coupled fibre approach.

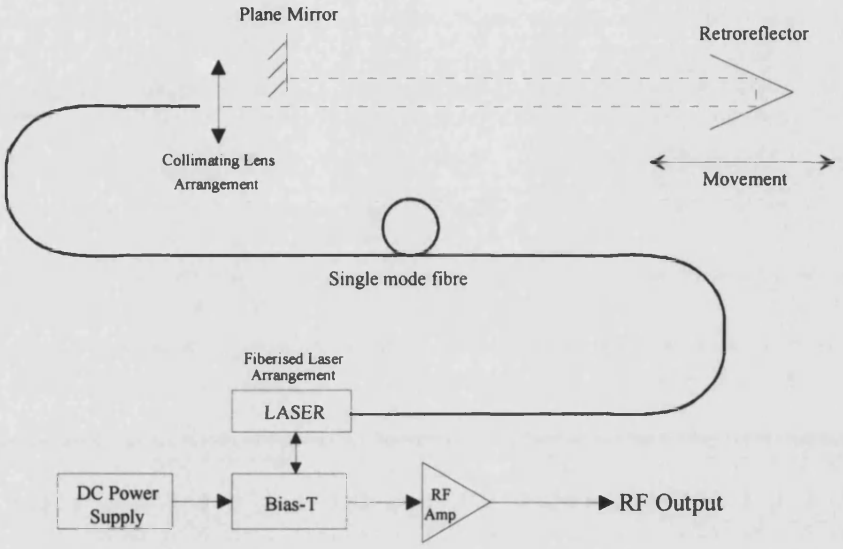

Figure 2.15. Schematic arrangement showing how a fibre coupled laser system may be used in conjunction with the bulk optical cavity configuration to provide a fibre launch arrangement.

It can be seen from figure 2.15 that the fibre coupled sensor possesses an optical configuration somewhat different to the free space version of the sensor described in section 2.2. However, it is found that the sensor operates in essentially the same manner as before, with one main difference. Rather than having the laser placed in situ, light from the active device is coupled into the optical fibre and guided into a bulk external cavity. This is arranged so that the reflected light re-enters the optical fibre and travels back towards the laser to provide the optical feedback. In the example shown in figure 2.15 a folded cavity arrangement is depicted with a suitable collimating lens being used to ensure a parallel, low divergence, optical beam travels down the external cavity. The bulk section of the external cavity remains essentially unchanged with the fibre launch replacing the laser diode. Although a folded cavity has been depicted, as was the case for direct bulk optical operation, any other suitable target arrangement might be employed to construct the sensor, as shown in figure 2.6.

2.7.2. Simple fiberised cavity configuration

In some applications the collimator unit may be anti-reflection (AR) coated for the wavelength of operation. This is in order to prevent any back reflections from occurring at the point where the fibre launches into the external cavity. This ensures that the simplicity of the external cavity remains without the presence of any back-reflections which may cause distortion or disrupt the pattern of the resonance peaks observed in the frequency spectrum of the laser junction voltage.

Such a system may be used in the cases where a minimum external cavity length may be stipulated due to the restrictions imposed by signal processing methods. Owing to the finite bandwidth of processing electronics, it may be necessary to restrict the maximum allowable frequency separation between the resonance peaks, hence the requirement for a minimum external cavity length, or stand-off distance. Unfortunately, this would lead to an increase in the physical size of the sensor in respect to its stroke length. A useful alternative may be to incorporate this stand-off distance into the transducer as a length of optical fibre. This piece of fibre may be used as a connection from the transducer to the controlling electronics. As a consequence, the physical dimensions of the transducer may be reduced. Another method of reducing the physical dimensions of the transducer would be to incorporate the stand-off distance in a short length of fibre which may be placed inside the transducer unit (possibly coiled for further improved size reduction).

2.7.3. Compound cavity operating configuration

In contrast to the applications of the fibre based configuration discussed above, a compound cavity operating configuration may be desirable, if a long optical fibre connection is required to link the optical transducer or sensor head to its electrical signal processing system. The compound cavity behaviour is caused by the presence of back-reflections at the fibre /air interface. The reason for using such an arrangement for this application may be best explained by considering the following example.

If for instance, a 20m length of fibre was used to address a bulk optical external '*sensing*' cavity of maximum length 1m, then the RF spectrum would consist of a series of resonance peaks with a spacing of the order of 5MHz. If the length of the sensing cavity was changed by, for example, 100 microns, this would lead to a change in the resonance peak spacing of only 15Hz. To measure a change in the peak positions to this degree of accuracy would require a very sophisticated signal processing system indeed. Even if the optical transducer is moved through its full stroke (a change in bulk external cavity of 1m) the change in peak separation is only ~160kHz. This equates to a maximum possible measurand variation of only 3%. Therefore on initial impression it may seem as though this measurement principle may not be best suited to the measurement application in which it has been placed.

However, if the cavity is constructed so that there is a significant back-reflection occurring at the fibre/air interface, it will be found that a compound cavity arrangement arises. The consequence of this compound cavity operation is that superimposed upon the fine structure of resonance peaks of 5MHz spacing will be an envelope function with a peak separation corresponding to the length of the bulk optical external cavity.

If a 100 micron change in cavity length occurs now, then the separation of the fine structure resonance peaks will change only slightly as described above. However, as the period of the envelope function is dependent upon the bulk optical sensing cavity length, the peak separation of the envelope function will be found to change by ~15kHz - an increase in sensitivity of three orders of magnitude. It can immediately be seen that the requirements placed upon the measuring system used to processes the signals generated by the sensor are now far less for this arrangement where use has been made of the back reflections now present. Figure 2.16, illustrates this point by showing the RF spectra generated by a fiberised system for various different bulk optical *sensing* cavity lengths.

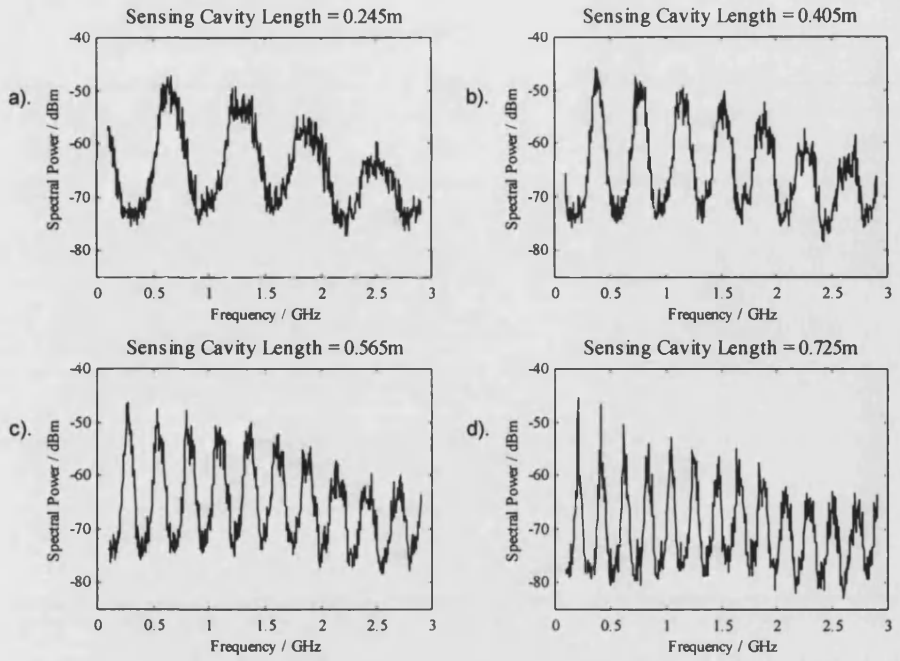

Figure 2.16. Variation in peak separation of envelope function for coupled cavity fiberised sensor configuration. Resolution bandwidth of 30kHz used for all spectra.

The spectra shown in figure 2.16 were obtained using an experimental arrangement of the form shown in figure 2.15. In this case output from the AR coated laser described earlier has been coupled into approximately 55m of single mode fibre. It can be seen that the fine structure of individual resonance peaks is lost in these figures due the limited number of sample points in each figure (800) which effectively pick out the envelope function. It can be clearly seen from these figures that instead of measuring the frequency separation of individual peaks, the sensing cavity length may be determined by measuring the separation of successive maxima or minima of the envelope function.

Figure 2.17 illustrates the quality of measurement that can be obtained by using this measurement technique, with good agreement shown between the experimentally measured data and the simple inverse law prediction of equation 2.4. To date, fibre lengths of up to 100m have been successfully used in off-line measurements demonstrating the suitability of the system for application to inherently safe applications. However, studies have not yet been carried out to find the fundamental limit on the external cavity length.

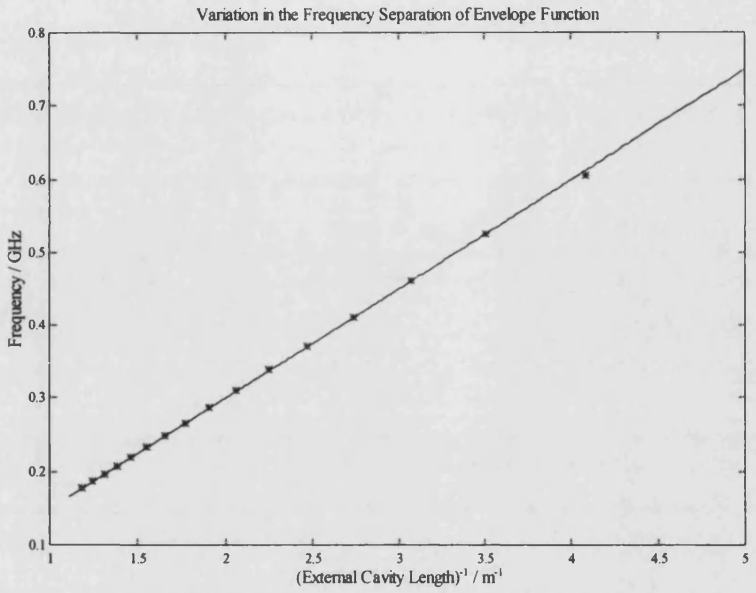

Figure 2.17. Determination of sensing cavity length by measurement of successive maxima of envelope function - Key: 'x' Experimental Measurement, '-' Prediction of simple inverse law.

2.8. Conclusions

A novel technique for optical position sensing has been demonstrated using a semiconductor laser which is subjected to delayed optical feedback. This measurement principle has been formulated in order to develop an intermediate range, cost-effective, stable sensor for use in real industrial environments.

It has been shown that the application of the optical feedback to the laser leads to the generation of a series of resonance peaks in the frequency spectra of the junction voltage of the laser. The frequency spacing of these resonance peaks is inversely proportional to the external cavity length. It has been demonstrated that measurement of the frequencies at which these resonance peaks occur provides an accurate measurement of the external cavity length. Since the external reflector is either coupled to, or part of the body under test, it can be seen that an absolute position measurement is achieved. Therefore, the measurement is not dependent upon a reference point which may be lost on power down of the sensor. The simplicity of the sensor is demonstrated by considering that a minimum of only three optical components are required to construct the optical system. Therefore, the sensor may be engineered to be rugged and stable for use in real industrial

environments. Operation of the sensor has been demonstrated with cavity lengths of up to 4m in the laboratory.

The sensor system has been demonstrated using a wide variety of laser diodes of quite different design and structure. Therefore demonstrating the fact that the measurement principle is not dependent upon a specialised device which may cause inconveniences due to cost and availability issues.

Furthermore, it has been shown that the sensor performance may be optimised by biasing the laser very close to its threshold current. It can therefore be seen that the sensor will operate with very low optical powers, reducing the possibility of any eye hazard occurring.

Finally, it has been demonstrated how the sensor may be fibre coupled for application in inherently safe sensing applications or to just reduce the physical size of the required transducer. It has been shown how an envelope function is present in the frequency spectrum due to the presence of a coupled cavity arrangement. Operation of the fibre coupled arrangement has been demonstrated with up to 100m of fibre inserted into the optical path.

2.9. References

[1] R.J.Wangler and R.A.Olsen, "Pulsed diode-laser rangefinders find many commercial uses", *Laser Focus World*, pp.105-109, July 1993

[2] D.Flint "Laser ranging meets the distance-measurement challenge", *Photonics Spectra*, pp.116-118, April 1994.

[3] Zygo Corp., Middlefield, CT, USA, "ZMI-5000 Displacement measurement interferometer system", Product catalogue, 1994.

[4] Hewlett-Packard Ltd., "Non-contact measurements with laser interferometers", Application Note 325-12, November 1991.

[5] A. Dandridge, R.O.Miles, A.B.Tveten and T.G.Giallorenzi, "External Cavity Diode Laser Sensor", *Proc SPIE*, **412**, pp.28-36, 1983.

[6] J_Y. Kim, R.W.Chung and J.C.Mulder, "Measurement of photothermally induced distortion of thin films using an external cavity laser diode sensor", *Electron. Lett.*, **29**, pp.354-355, 1993.

[7] J.Kato, N.Kikchi, I.Yamaguchi and, S.Ozono, "Optical feedback displacement sensor using a laser diode and its performance improvements", *Meas. Sci. Technol*, **6**, pp.45-52, 1995.

[8] G.Beheim and K.Fritsch, "Range finding using frequency-modulated laser diode", *Appl. Opt.*, **25**, pp.1439-1442, 1986.

[9] S.Donati, G.Guiliani and, S.Merlo, "Laser diode feedback interferometer for measurement of displacements with ambiguity", *IEEE J, Quantum Electron.*, **31**, pp.113-119, 1995.

[10] S.Shinohara, H.Yoshida, H.Ikeda, K._I.Niside and M.Sumi, "Compact and high-precision range finder with wide dynamic range and its application", *IEEE. Trans. Instrum. Meas.*, **41**, pp.40-44, 1992.

[11] S.Shinohara, M.Andou, M.Miyata, H.Yoshida, H.Ikeda, J.Yoshida, K.-I.Nishide, T.Kondo and, M.Sumi, "High-resolution range finder with wide dynamic range of 0.2m to 1m using a frequency-modulated laser diode", *Proc 15th Annual Conference of the IEEE Industrial Electronics Society*, **3**, pp.646-651, 1989.

[12] K.Petermann, "Laser diode modulation and noise", Kluwer Scientific Publishers, Chapter 9, pp 250-290, 1991.

[13] G.P.Agrawal and N.K.Dutta, "Semiconductor lasers", 2nd Edition, Van Nostrand Reinhold, New York, pp.306, 1993.

[14] R.F.Broom, E.Mohn, C.Risch and R.Salathé, "Microwave self-modulation of a diode laser coupled to an external cavity", *IEEE J. Quantum Electron.*, **QE-6**, No.6, pp.328-334, 1979.

[15] I.Ikushima and M.Maeda., "Self-coupled phenomena of semiconductor lasers caused by an optical fibre", *IEEE J.Quantum Electron.*, **QE-14**,No.5, pp.331-332, 1978.

[16] I.Ikushima and M.Maeda., "Lasing spectra of semiconductor lasers coupled to an optical fiber", *IEEE J.Quantum Electron.*, **QE-15**,No.9, pp844-845, 1979.

[17] N.Schunk and K.Petermann, "Minimum bit rate of DPSK transmission for semiconductor laser with a long external cavity and strong linewidth reduction", *J. Lightwave Technol.*, **LT-5**, No.9, pp.1309-1314, 1987.

[18] R.P.Griffiths and I.H.White, " A high resolution optical position sensor using optical feedback to a semiconductor laser", *Proc Sensors and their applications VIII,* Glasgow, pp 291-296, 1997.

[19] CSO de Measures, Grenoble, France, "HC250 micro-laser interferometer", Product catalogue, January 1995.

[20] Dr. Johannes Heidenhain Gmbh, Traunreut, Germany, "NC linear encoders", Product catalogue, September 1993.

[21] Sony Magnascale Inc., Tokyo, Japan, "Sony Laserscale: 1/100 micron digital scale", Product catalogue No. 293., December 1991.

[22] M.J.Rudd, "A laser Doppler velocimeter employing the laser as a mixer oscillator", *J.Scientif. Instrum.*, **1**, pp.723-726, 1968.

[23] Y.Mitsuhasi, T.Morikawa, J.Sakurai, A.Seko and J.Shimada, "Self-coupled optical pickup", *Opt. Commun.*, **17**, pp95-97, 1976.

[24] S.Kakuma, R.Ohba, M.Kondoh and N.Takahashi, "Time based length measurement method by optical heterodyne beat counting", *Proc Sensors and their Applications VIII*, Glasgow, pp 285-290, 1997.

[25] A.Yariv, "Quantum Electronics", John Wiley and Sons, New York, 1989.

[26] H.Soda, K.Iga, C.Kitahara and Y.Suematsu, "GaInAsP/InP surface emitting injection lasers", *Japanese Journ. Appl. Physics*, **18**, pp.2329-2330, 1979.

[27] P.L.Gourley, K.L.Lear and R.P.Schneider Jnr., "Surface-emitting lasers", *IEEE Spectrum*, **31**, No.4, pp.31-37, 1994.

[28] L.Raddatz, "Light sources for communication systems using multimode optical fibre", MPhil. Thesis, University of Bath, UK, 1995.

[29] P.Dowd, "Vertical Cavity Surface Emitting Lasers", PhD Thesis, University of Bristol, UK, chapter 1, 1997.

[30] M.Shimada, T.Asaka, Y.Yamasaki, H.Iwano, M.Ogura and S.Mukai, "Low-threshold surface-emitting laser with distributed Bragg reflectors and current blocking layers", *Appl. Phys. Lett.*, **57**, pp.1289-1291, 1990.

[31] L.M.Zinkiewicz, T.J.Roth, L.J.Mawst, D.Tran and D.Boetez, "High-power vertical-cavity surface emitting AlGaAs/GaAs diode lasers", *Appl. Phys. Lett.*, **54**, pp.1959-1961, 1989.

[32] J.E.Carroll, L.M.Zhang and M.E.Bray, "A Bragg about lasers", *Electron. & Comm. Engineering Journ.*, pp.325-337, 1993.

[33] P.Dowd, I.H.White, M.R.T.Tan, S.Y.Wang, "Narrow linewidth millimetre-wave generation by optical heterodyning of two vertical-cavity surface emitting lasers", paper CMC7, *Proc. CLEO Europe'96*, Hamburg, Germany, 8-13 September 1996.

[34] T.Sano, "Antimode dynamics and chaotic itinerancy in the coherence collapse of semiconductor lasers with optical feedback", *Phys. Rev. A*, **50**, No.3, pp.2719-2726, 1993.

[35] R.P.Griffiths & I.H.White, UK patent application No. 9608370.4, 23/4/96

[36] R.P.Griffiths & I.H.White, UK patent application No. 9704937.3, 10/3/97

[37] R.P.Griffiths & I.H.White, International PCT patent application No. CT/GB97/01123, 23/4/97

[38] A.Dieckmann, "FMCW-LIDAR with tunable twin-guide laser diode", 1994, *Electron Lett.*, **30**, No.4, pp.308-309, 1994.

[39] SHARP Laser diode data book.

CHAPTER 3

A STEADY-STATE THEORETICAL ANALYSIS OF AN EXTERNAL CAVITY SYSTEM USING THE CONCEPT OF EFFECTIVE REFLECTIVITY

In this chapter details are given of a theoretical approach for analysing the operation of a semiconductor laser operating within an external cavity. This approach, whilst simplistic in its concept facilitates a good physical understanding of the optical system employed within the external cavity sensor. The analytical method used is based upon a steady-state approach which assesses the effective reflectivity of the external cavity configuration. From this analysis approximate theoretical RF spectra can be generated which predict the performance of the external cavity sensor arrangement. Finally, the relative advantages and disadvantages of using this theoretical approach are assessed.

3.1. Introduction

The novel measurement technique described in the previous chapter uses a simple optical system to provide accurate position measurement. While the construction of the optical system appears to be uncomplicated, a study of the dynamics of a semiconductor laser which is subjected to delayed optical feedback is not as straightforward as it first appears. However, for the purposes of sensor development, formulation of such a theoretical model enables predictions to be made as to the performance of the optical system, as well as providing information which can be used for optimisation of the optical sensor configuration. Furthermore, theoretical analysis of the system can provide a greater understanding of the physical processes involved in the sensor system and an explanation of the concepts behind the experimentally observed phenomena.

3.2. Theoretical Analysis of External Cavity Response

The presence of an external reflector comprising an external optical cavity significantly modifies the operation of a semiconductor laser diode [1-9]. To analyse

such a system, the amplitude and phase conditions required for normal operation must be considered.

3.2.1. Concept of effective reflectivity and its control of cavity behaviour

In the case of a simple Fabry-Perot laser operating with delayed optical feedback, the amplitude and phase conditions may be assessed by examining the compound optical cavity system that has been constructed. The schematic arrangement of this cavity is shown in figure 3.1. Here we have a semiconductor laser of length L and emission wavelength λ_o, which possesses facet field reflectivities of r_1 and r_2. The facet in closest proximity to the external reflector is denoted by r_2. The reflector used to form the external cavity has a field reflectivity of r_3 and is situated a distance L_{EXT} away from the second laser facet. This parameter r_3 also takes into account any coupling and diffraction losses which may occur within the external cavity. For reasons of simplicity, only a single longitudinal mode of the laser will be considered, since any changes to the lasing structure should affect each mode in a similar manner.

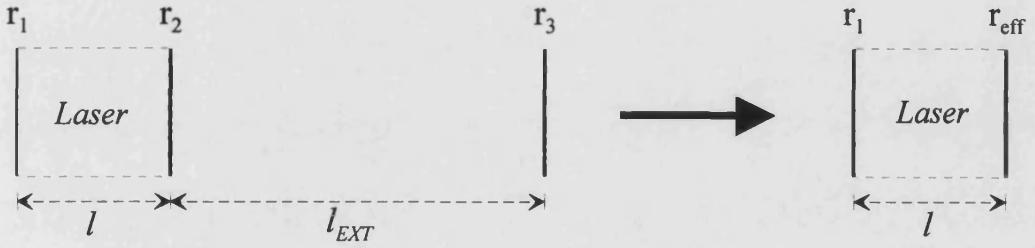

Figure 3.1. The reflection model defined by a Fabry-Perot laser operating within an external cavity may be simplified by considering the complex effective reflectivity (r_{eff}) produced at the laser facet by the external cavity.

By considering the multiple reflections that occur in such an optical system, the reflectors r_2 and r_3 may be replaced by an effective reflectivity r_{eff} situated at the position of the second laser facet. This effective reflectivity is given by [10,11]:

$$r_{eff} = r_2 + t_2 r_3 t_2' e^{-j\theta} + t_2 r_3^2 (-r_2) t_2' e^{-2j\theta} + \ldots + t_2 r_3 t_2' (-r_2 r_3)^n e^{-(n+1)j\theta} \quad (3.1)$$

where $\theta = 4\pi L_{ext}/\lambda_o$ is the round trip phase change of the external cavity. The field transmission through the laser facet 2 is given by t_2 for an outwards travelling wave and t_2' for a wave returning from the external cavity reflector. The above

geometrical progression may be simplified, remembering that the transmission factors through the second laser facet are related to the field reflectivity by, $t_2 t_2' = \left(1 - r_2^2\right)$ [12], providing the following equation for r_{eff},

$$r_{eff}(\nu) = r_2 + \frac{t_2 r_3 t_2' e^{-j\theta}}{1 - \left(-r_3 r_2\right) e^{-j\theta}}, \tag{3.2}$$

which reduces to,

$$r_{eff}(\nu) = \frac{r_2 + r_3 e^{-j\theta}}{1 + r_2 r_3 e^{-j\theta}}. \tag{3.3}$$

Unlike some treatments of external cavity theory [1,3,11-14], which do not account for multiple reflections, the above expression is a general case valid for all values of r_2 and r_3, not just when $|r_2 r_3| << 1$, (characterising either the strong or weak feedback effects).

As shown by equation 3.3, r_{eff} is a complex quantity and as such may be written as,

$$r_{eff}(\nu) = |r_{eff}| e^{-j\phi}, \tag{3.4}$$

where $$|r_{eff}| = \left(r_{eff}^{*}(\nu).r_{eff}(\nu)\right)^{1/2} = \left[\frac{r_2^2 + r_3^2 + 2r_2 r_3 \cos\theta}{1 + \left(r_2 r_3\right)^2 + 2r_2 r_3 \cos\theta}\right]^{1/2}, \tag{3.5}$$

and $$\phi = \tan^{-1}\left[\frac{-r_3 \sin\theta}{r_2 + r_3 \cos\theta}\right] - \tan^{-1}\left[\frac{-r_2 r_3 \sin\theta}{1 + r_2 r_3 \cos\theta}\right]. \tag{3.6}$$

These expressions can now be used to consider the separate amplitude and phase conditions which dictate the allowed lasing modes within the *effective* cavity arrangement which is described by figure 3.1.

The amplitude condition requires that the threshold gain of this *effective* cavity, g_c satisfies the following relation [11],

$$r_1^2 |r_{eff}|^2 \exp\left(\left[g_c - \alpha_s\right] 2l\right) = 1, \tag{3.7}$$

where α_s is the loss due to optical scattering by material defects within the laser.

The threshold gain g_c, as one might expect is the amount of gain required to reach the lasing threshold where the round-trip material gain is equal to the total

cavity round-trip losses. Equation 3.7 can be rearranged to yield an expression for the effective cavity threshold gain.

$$g_c = \alpha_s + \frac{1}{l}\log_e\left(\frac{1}{r_1|r_{eff}|}\right). \tag{3.8}$$

Meanwhile, the phase requirement of the laser cavity requires that the round trip phase within the effective cavity is an integer multiple of 2π, yielding the phase condition

$$\frac{4\pi\mu_e \nu L}{c} + \phi = 2\pi m, \tag{3.9}$$

where m is an integer, ν is the particular frequency being considered and μ_e is the effective refractive index of the active region of the laser. Equation 3.9 shows that due to the applied optical feedback the emission frequency of the laser may change as a function of the feedback phase. However, as the effective refractive index may also change dynamically, the round trip phase relationship may be rewritten by following the approach of Petermann [11] as,

$$\Delta\Phi_L = \frac{4\pi L}{c}\left[\nu_{th}\Delta\mu_e + \mu_e(\nu - \nu_{th})\right] + \phi, \tag{3.10}$$

where $\Delta\Phi_L$ corresponds to a round trip phase change of the effective cavity when compared with $2\pi m$, (this is not to be confused with the round-trip phase change within the external cavity, θ). In equation 3.10 ν_{th} is the lasing frequency of the particular solitary lasing mode being considered. The change in the effective index may be expressed as [11],

$$\Delta\mu_e = \frac{\partial\mu_e}{\partial n}(n - n_{th}) + \frac{\partial\mu_e}{\partial\nu}(\nu - \nu_{th}) \tag{3.11}$$

where n_{th} corresponds to the threshold carrier density with no feedback present. However, the variations in refractive index are also correlated to the variations in gain through the linewidth enhancement factor α_H [15,16], which interrelates the real and imaginary components of the refractive index. It can be shown that [11],

$$\frac{\partial\mu_e}{\partial n}(n - n_{th}) = -\frac{\alpha_H c}{4\pi\nu_{th}}(g_c - g_{th}), \tag{3.12}$$

with g_{th} denoting the threshold gain without feedback. However this may be replaced if one considers that g_{th} is defined as,

$$g_{th} = \alpha_s + \frac{1}{L}\ln\left(\frac{1}{r_1 r_2}\right). \tag{3.13}$$

Finally, by combining equations 3.9, 3.11, 3.12, and 3.13, the following expression for round trip phase may be obtained,

$$\Delta\Phi_L = -\alpha_H \ln\left(\frac{r_2}{|r_{eff}|}\right) + \frac{4\pi\mu_e L}{c}(\nu - \nu_{th}) + \phi. \tag{3.14}$$

Consequently, it can be seen that possible emission frequencies correspond to the solutions of equation 3.14, when the phase condition is satisfied, i.e. when $\Delta\Phi_L$=0.

3.2.2. Characterisation of Feedback Strength

It is common in the literature to characterise the feedback strength of the system using the parameter γ [17,18] which is given by,

$$\gamma = \frac{1}{\tau_l}\ln\left(\frac{r_2 + r_3}{r_2(1 + r_2 r_3)}\right), \tag{3.15}$$

although, when $|r_2 r_3| << 1$, this expression may be simplified to,

$$\gamma \approx \frac{\kappa_{ext}}{\tau_l} = \frac{r_3(1 - r_2^2)}{\tau_l r_2}, \tag{3.16}$$

where κ_{ext} is commonly referred to as the feedback strength parameter which is considered when either weak or strong feedback is in operation [1,11,13,19].

Equation 3.14 provides a general expression which is valid for all arbitrary values of r_2 and r_3. This is not to be confused with the result quoted in Petermann [11] and elsewhere [13], where the assumption that $|r_2 r_3| << 1$, leads to the following expression for the round trip phase change:

$$\Delta\Phi'_L = \frac{4\pi\mu_e L}{c}(\nu - \nu_{th}) + \kappa_{ext}\sqrt{1 + \alpha_H^2}\,\sin\left(2\pi\nu\tau_{ext} + \tan^{-1}\alpha_H\right), \tag{3.17}$$

with τ_{ext} being the external cavity round trip time. This equation is an accurate expression for describing only the weak or strong feedback regimes of operation.

Consequently, care must be taken if it is to be applied with any sort of generality. $\Delta\Phi'_L$ denotes that the weak or strong feedback assumption has been made.

In order to preserve generality throughout this work, equation 3.14 will be applied as opposed to equation 3.17, since in many practical sensor configurations, it will be found that the magnitude of r_2 and r_3 will be comparable.

3.2.3. Solution of the External Cavity Round Trip Phase Condition

Since an expression for the round trip phase change within the effective cavity has been derived, it is now possible to consider how the external cavity arrangement behaves as a function of various different physical parameters. Figure 3.2 illustrates how the round trip phase change varies as a function of frequency for a particular external cavity arrangement.

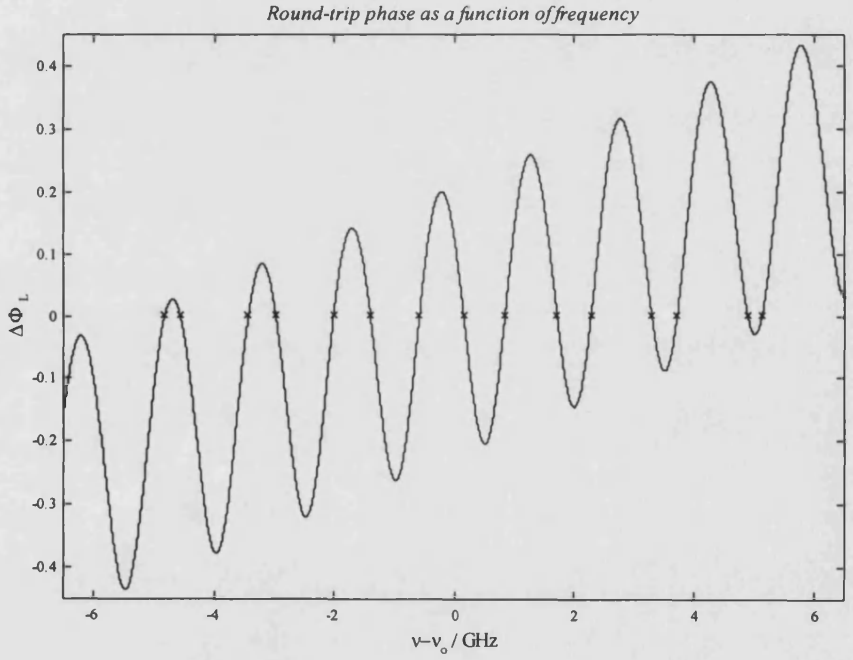

Figure 3.2. The round trip phase change for a typical Fabry-Perot laser diode of wavelength 1300nm. In this example it is operating within an external cavity of length 0.1m formed by an external reflector of field reflectivity 0.03. The laser facet reflectivities are both 0.57. 'x' indicates the frequencies of the allowed effective cavity modes.

For the purposes of comprehension and simplicity the external reflector considered in this example is of low field reflectivity ($r_3=R_3^{1/2}=0.03$), so that the system is subject to a fairly weak feedback effect. The round-trip phase change

appears to take the form of a sinusoid superimposed upon a ramp function. This shows that a weak feedback regime is in operation since this is exactly the form of equation 3.17.

The permitted lasing modes of this system can be ascertained from figure 3.2 by identifying the zero crossing points of the round trip phase change. These are denoted by the marker points '*x*'. The acronym XCM (e***X***ternal ***C***avity ***M***ode) is often assigned to these modes after Goldberg et al [6,20]. As one might expect, the feedback regime considered in the example shown in figure 3.2 leads only to a small number of permitted effective cavity modes. In contrast figure 3.3 illustrates two configurations where higher levels of optical feedback are present in operation.

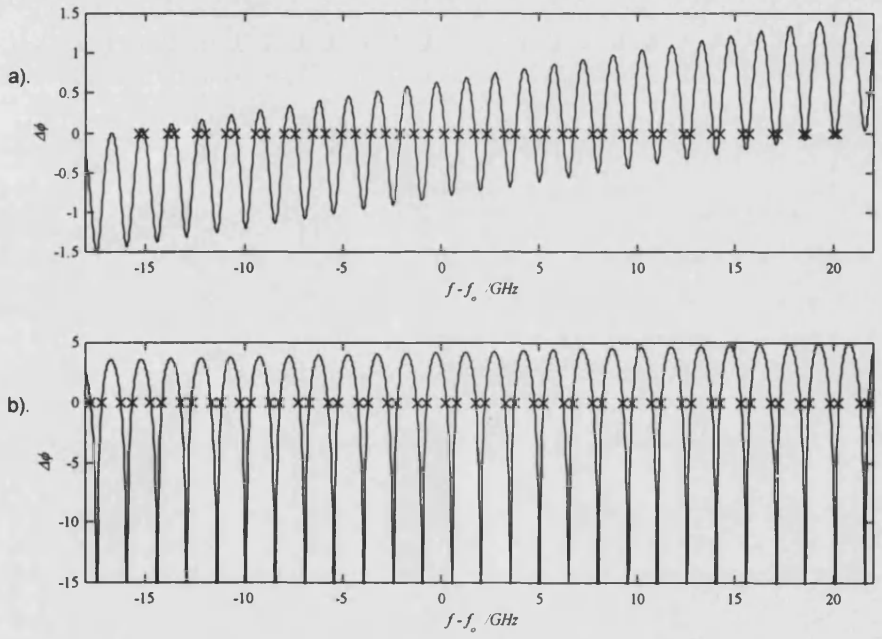

Figure 3.3. Round trip phase change for the same laser described by figure 3.2, when subject to different external cavity parameters. a). $R_1=R_2=0.57$, $R_3=0.1$, $L_{ext}=0.1$m. b). $R_1=0.57$, $R_2=R_3=0.1$, $L_{ext}=0.1$m.

Figure 3.3.*a* illustrates the case where the external field reflectivity has been increased to 0.1, but all the other physical parameters considered in the example of figure 3.2 have remained constant. The most notable change evident in the round-trip phase change is that the act of increasing the level of feedback has in turn increased the number of allowed effective cavity modes that may exist.

In contrast, figure 3.3.*b* illustrates the case where the laser used in the example of figure 3.3.*a* has been anti-reflection (AR) coated. It can be seen that the act of AR coating the device has lead to yet another increase in the number of allowed modes when compared to the example shown in figure 3.2. In fact, it can now be seen that the sinusoidal appearance of the round-trip phase variation has become quite distorted, and has become much larger in magnitude in relation to the linear ramp component of the function. Therefore in this example it can be seen that the assumptions made during the formulation of equation 3.17 do not hold. If this equation had been applied to this system then erroneous values for the allowed modes would have been obtained.

Note that by inspection of figure 3.3.*b* it can be seen that the scale of the frequency axis shown forms only a part of the region where legitimate effective cavity modes may exist. The complete range in this case covers several tens of gigahertz. If the complete range was illustrated in figure 3.3, then it would not be possible to make out the structure of the $\Delta\Phi_L$ variation. It should also be reiterated that only a single laser chip (solitary operation) mode has been considered in this approach. As the XCMs are formed according to a distribution centred on the arbitrary lasing mode, each distribution corresponding to multiple chip modes should be of very similar form and only minor changes should result in the theoretical predictions produced.

3.2.4. Modal Separation

An examination of figures 3.2 and 3.3 will show that the frequency spacing of the allowed modes is not constant but in fact varies quite markedly. Furthermore, examination of the frequency differences between the allowed modes produces what is at first glance a surprising result. On examination, it is found that it is not the adjacent solutions of equation 3.14 which provide a frequency spacing roughly comparable to the round-trip frequency of the external cavity. It is in fact the frequency spacing between *every other* allowed lasing mode which corresponds approximately to this value. This statement may be best explained and illustrated by

examining figure 3.4. This considers the frequency separation of allowed effective cavity modes of a typical sensor arrangement with, $r_1=r_2=0.57$, $r_3=0.1$ and $L_{ext}=0.5$. Figure 3.4.*a* depicts in histogram form (20 bins), the frequency difference between adjacent modes of the optical system whilst figure 3.4.*b* illustrates the frequency separation between every second allowed effective cavity lasing mode. It can be seen that the frequency difference between nearest neighbours has a wide frequency spread centred at approximately half the external cavity resonance frequency. However, in contrast, the frequency separation between every second mode can be seen to follow a distribution with a much smaller spread, centred around the external cavity resonance frequency.

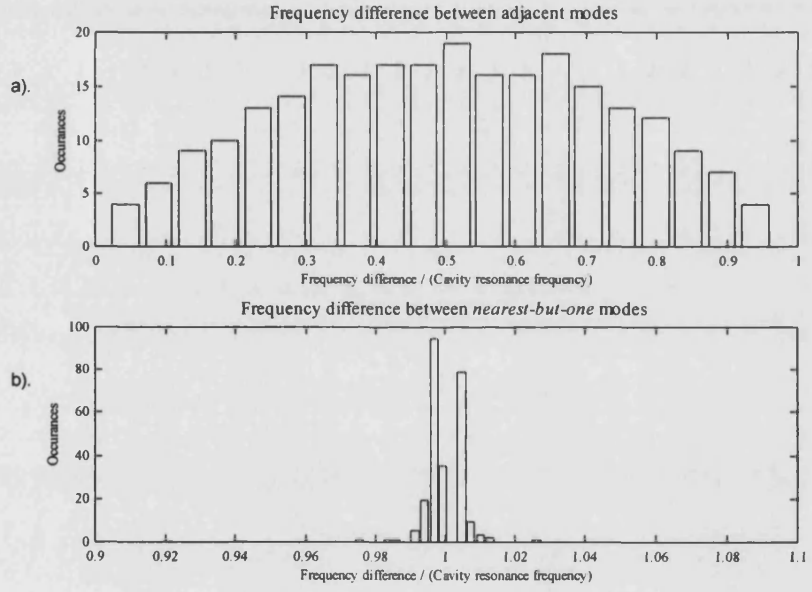

Figure 3.4. Histograms showing the frequency separation between: a). Adjacent allowed effective cavity modes, b). Every second allowed effective cavity mode, for a system with $r_1=r_2=0.57$, $r_3=0.1$ and $L_{ext}=0.5$ (20 data bins per histogram).

If this is the case, the question then arises as to why the RF spectra generated by the sensor configuration do not contain wide peaks situated at frequencies corresponding to half the external cavity resonance frequency. To answer this question, the threshold gains of the effective cavity modes, must also be considered.

It is interesting to note that while the histogram of figure 3.4.*a* follows approximately a normal distribution, the distribution of occurrences of figure 3.4.*b*

follows a much more irregular distribution, suggesting a multiple peak or peak splitting effect. This will be discussed later in the chapter.

3.2.5. Consideration of the threshold gain associated with the external cavity modes.

The threshold gain g_c, of the allowed XCM's varies as a function of frequency as can be seen by considering equation 3.8. It was shown by Henry and Kazarinov [21] that the threshold gains (or variation in equilibrium gain between the solitary and feedback situations which is often considered) of the allowed lasing modes actually lie on the perimeter of an ellipse, which is illustrated in figure 3.5. The variation in equilibrium gain achieved when the laser is operated with applied feedback compared with solitary operation is represented by ΔG which is directly proportional to g_{th}.

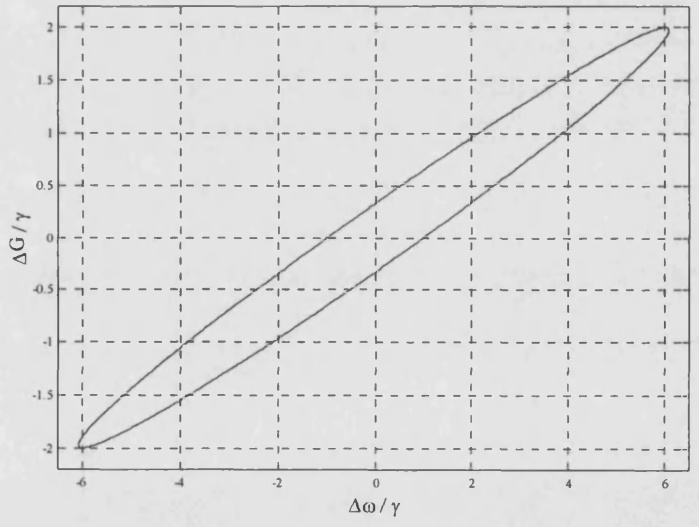

Figure 3.5. The ellipse locus on which the allowed external cavity modes lie. As the product $\gamma\tau_{ext}$ increases, then the density of allowed modes on the ellipse tends to a continuum (after [21]). α_H=6 in this example, while $\Delta\omega=2\pi(\nu-\nu_o)$.

The conditions for the XCM distribution are developed from the rate equations describing the weak or strong feedback regimes [1]. The equation of the ellipse being given by [21]

$$\left(\Delta\omega - \frac{\alpha\Delta G}{2}\right)^2 + \frac{\Delta G^2}{4} = \gamma^2, \qquad (3.18)$$

where ΔG is the variation in equilibrium gain and $\Delta\omega$ is the angular frequency variation from the solitary laser operation. However, for convenience in this chapter the distribution between the threshold gain distribution and $(\nu-\nu_o)$ the frequency variation from the solitary laser operation will be considered throughout.

The product $\gamma\tau_{ext}$ has been used by several authors in order to classify the regime of operation of the external cavity system [3,22]. It has been found that the density of the allowed modes on the ellipse increases as a function of both the feedback strength of the system, and the external cavity delay. As $\gamma\tau_{ext}$ is continually increased, the points representing the allowed states on the ellipse become almost a continuum as shown by figure 3.6.

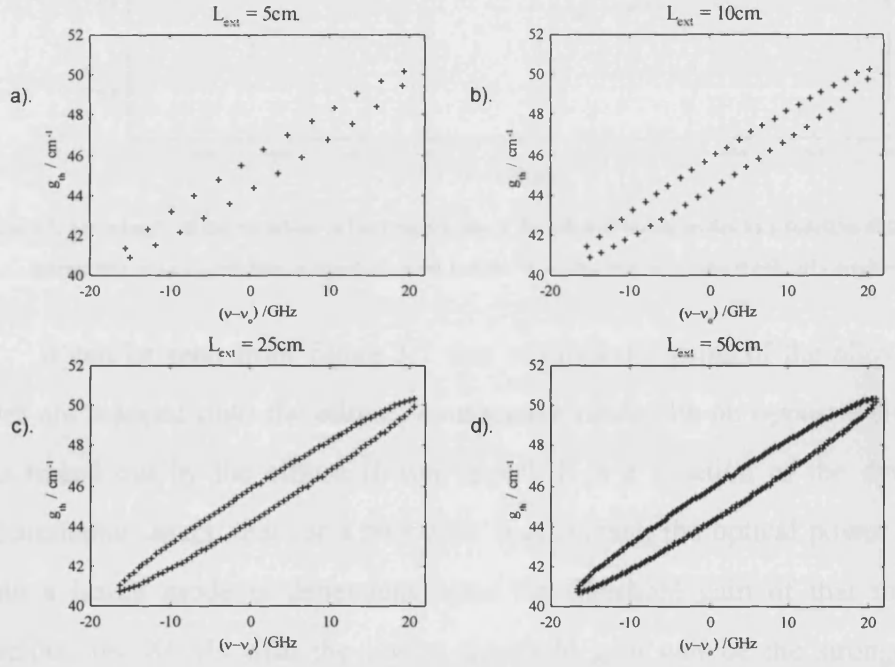

Figure 3.6. The variation in distribution of allowed effective cavity lasing modes as a function of external cavity length, for a typical Fabry-Perot type laser (λ=1300nm) - $r_1=r_2=0.57$, $r_3=0.1$. a).L_{EXT} = 5cm., b).L_{EXT} = 10cm., c).L_{EXT} = 25cm., d).L_{EXT} = 50cm.

The parameter $\omega\tau_{ext}$ detunes the value of the allowed modes around the ellipse perimeter. It is found that an increase in $\omega\tau_{ext}$ merely changes the location of an allowed mode in a clockwise direction around the ellipse. Therefore an increase in the lasing frequency due to changes in refractive index acts so as to vary the position of the allowed lasing modes on the locus as indicated in figure 3.7. As can

be seen from figures 3.5 and 3.7, the solution with the lowest possible gain occurs at a frequency $\alpha\gamma$ away from the solitary laser operating mode. However, the mode with the minimum linewidth occurs when $\omega\tau=2\pi n-\arctan(\alpha)$ [21].

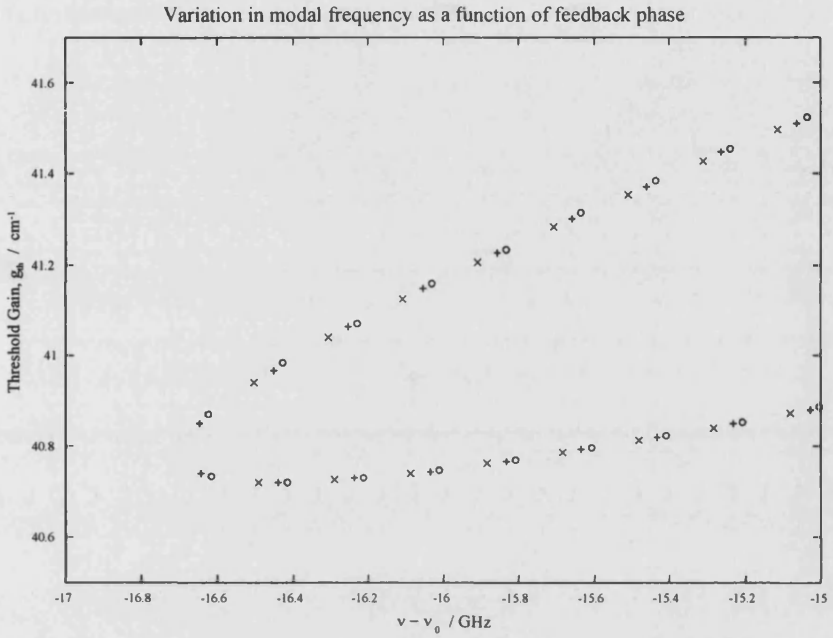

Figure 3.7. An example of the variation in the frequencies of the allowed lasing modes as a function of the detuning parameter $\omega\tau_{ext}$. L_{ext}=0.75m, $r_1=r_2$=0.57, r_3=0.1. Key: 'x' - $\omega\tau_{ext}=\pi$, '+' - $\omega\tau_{ext}=\pi/2$, 'o' - $\omega\tau_{ext}=\pi/4$.

It can be seen from figure 3.7 that as threshold gains of the allowed lasing modes are mapped onto the ellipse, consecutive modes lie on opposite sides of the locus traced out by the ellipse (lower/upper). It is a function of the dynamics of semiconductor lasers, that for a particular bias current, the optical power contained within a lasing mode is dependent upon the threshold gain of that mode [23]. Therefore, the XCMs with the lowest threshold gain will be the strongest in the frequency spectrum. It is found that the modes with the lowest threshold gain lie predominately on the lower side of the ellipse and therefore have a frequency separation which is approximately that of the external cavity resonance frequency. Examination of figures 3.4 and 3.5 illustrates this point. Consequently, when the lasing modes beat together within a detector, the frequency spectrum so produced, is dominated by beat modes derived from those lasing modes which have the lowest threshold gain, and hence possess the most optical power. Therefore by considering these points carefully, it can be reasoned that if the relative powers of each of the

effective cavity modes are known, a theoretical prediction of the RF spectrum of the optical signal may be constructed. However, before such a prediction can be obtained, means of assessing the exact steady-state output power of the effective cavity modes must be found.

3.2.6. Examination of Equilibrium Conditions of External Cavity System

As explained in the preceding section, in order to theoretically determine the RF response of the external cavity laser system, the equilibrium conditions of the optical configuration must be considered. By examining the equilibrium conditions, the relative powers of the XCMs may be ascertained, which will in turn allow the beat frequency products and hence an approximate prediction of the resultant RF frequency spectrum of the optical output to be calculated.

The transient behaviour of the laser may be analysed using the following multimode rate equations [24]:

$$\frac{dn(t)}{dt} = -\frac{c}{\mu_e}\frac{\partial g}{\partial n}(n-n_o)\frac{\sum_m P_m(t)}{1+\varepsilon\sum_m P_m(t)} - \frac{n(t)}{\tau_s} + \frac{j}{ed} \qquad (3.19)$$

$$\frac{dP_m(t)}{dt} = \frac{\Gamma c}{\mu_e}\frac{\partial g}{\partial n}(n-n_o)\frac{P_m(t)}{1+\varepsilon\sum_m P_m(t)} - \frac{P_m(t)}{\tau_p} + \Gamma\beta Bn^2(t) \qquad (3.20)$$

These equations describe the rate of change of $P_m(t)$, the photon density of the m^{th} XCM, and $n(t)$, the total carrier density within the laser respectively. For the purposes of this analysis, these equations have been adapted so that rather than describing the performance of a conventional multimoded semiconductor laser, they are used to analyse the multiple XCMs which exist in the vicinity of where a single longitudinal mode of the solitary laser may have previously existed. As only a small range is covered in this application, then no frequency dependency will be assigned to the gain of the various external cavity modes other than that derived from the threshold gain ellipse - i.e. no parabolic gain model will be implemented as only the region close to a single solitary lasing mode is being considered.

These rate equations provide a dynamic analysis of a laser of active layer thickness d and with a material related gain constant denoted by $\partial g/\partial n$. The spontaneous emission coefficient is denoted by β, while the radiative recombination rate is given by B. The laser is operated with an applied current density, j. Also included in these rate equations are the optical confinement factor Γ and the phenomenological non-linear gain compression parameter ε [25,26].

The carrier lifetime is denoted in equation 3.19 by τ_s which takes into account carrier loss from the physical mechanisms of spontaneous emission, non radiative recombination and Auger recombination [27]. The photon lifetime τ_p describes the optical losses which occur within the cavity which are a function of both scattering loss and facet loss.

$$1/\tau_p = \frac{cg_{th}}{\mu_e} = \frac{c}{\mu_e}\left(\alpha_s + \frac{1}{L}\ln\left(\frac{1}{r_1|r_{eff}|}\right)\right). \qquad (3.21)$$

It can be seen from equation 3.21 that the photon lifetime is inversely proportional to the threshold gain, g_{th}. Since the threshold gain defined by equation 3.8 is different for each XCM, it can be seen that the value of the photon lifetime will vary for each XCM.

When the steady-state conditions are considered, these rate equations may be solved to yield the relative optical power of the allowed XCMs. Several authors have used normalised rate equations to study steady-state effects [13,28]. In most cases the use of normalised rate equations leads to a set of expressions which are easily separable. However, in order to do this several important physical mechanisms may be neglected. Whilst this is a convenient and most illuminating way of showing the certain features of the theoretical systems, only an approximation is obtained.

When the full rate equations are considered however, the steady-state conditions provide a set of equations which are not easily separable, particularly when non-linear gain is included in the system. Indeed, a more straightforward, practical and satisfactory procedure is to actually solve the rate equations

dynamically and extract the final values of XCM optical power once the system has settled to equilibrium.

A multimode rate equation model was therefore developed in order to find the steady-state XCM optical powers for a particular laser under varying conditions.

3.2.7. Solutions to multimode rate equations for external cavity system

Equations 3.19 and 3.20 were solved numerically using a 4th order Runge-Kutta algorithm based multimode rate equation model. Device parameters for a typical Fabry-Perot laser of operating wavelength of 1300nm were used [29]. These are listed in table 3.1.

Parameter	**Description**	**Value used**
Γ	Optical confinement factor	0.35
$\partial g/\partial n$	Differential gain constant ($n \approx n_{th}$)	$3\text{x}10^{-16}$ cm^2
d	Depth of laser active region	0.2 μm
w	Width of laser active region	5 μm
l	Length of laser	250 μm
τ_s	Carrier lifetime $1/\tau_s = An + Bn^2 + Cn^3$, where *A is the non-radiative recombination coefficient,* *B is the radiative recombination coefficient,* *C is the Auger effect coefficient*	A=$1\text{x}10^8$ s^{-1} B=$1\text{x}10^{-10}$ cm^{3}s^{-1} C=$1\text{x}10^{-30}$ cm^{6}s^{-1}
n_o	Carrier density for zero material gain	$1\text{x}10^{18}$ cm^{-3}
ε	Non-linear gain coefficient	$2\text{x}10^{-17}$cm^3
μ_e	Effective refractive index	3.7
β	Spontaneous emission coefficient	$1\text{x}10^{-4}$
α_H	Linewidth enhancement factor	6.0
α_S	Scattering losses	30 cm^{-1}
R_1	Power reflectivity of facet 1	0.32
R_2	Power reflectivity of facet 2	0.32

Table 3.1. Laser device parameters

Initially the device parameters were used along with the external cavity parameters in order to calculate the frequencies and threshold gains of the allowed

external cavity modes (XCMs) as described in the previous sections. This calculated information was subsequently used to solve the rate equations with the optical output power of facet 1 (i.e. the facet furthest from external cavity) used to determine relative mode strength.

By way of example, figure 3.8 shows some sample results for the case where an external cavity of length 10cm and a power reflectivity of 0.1 has been analysed. In this case, only 20 external cavity modes have been considered. Figure 3.8a) shows how the modes change dynamically after a current step of 25mA has been applied to the laser (at t=0ns) whose solitary threshold current is approximately 19mA. It can be seen that the modes with the lowest threshold gain dominate the system, and after equilibrium has been reached these modes have the highest relative power. However, this physical case is used purely as an illustration of the theoretical method, and is not necessarily one which would be equivalent to any practical configuration used within the optical sensor.

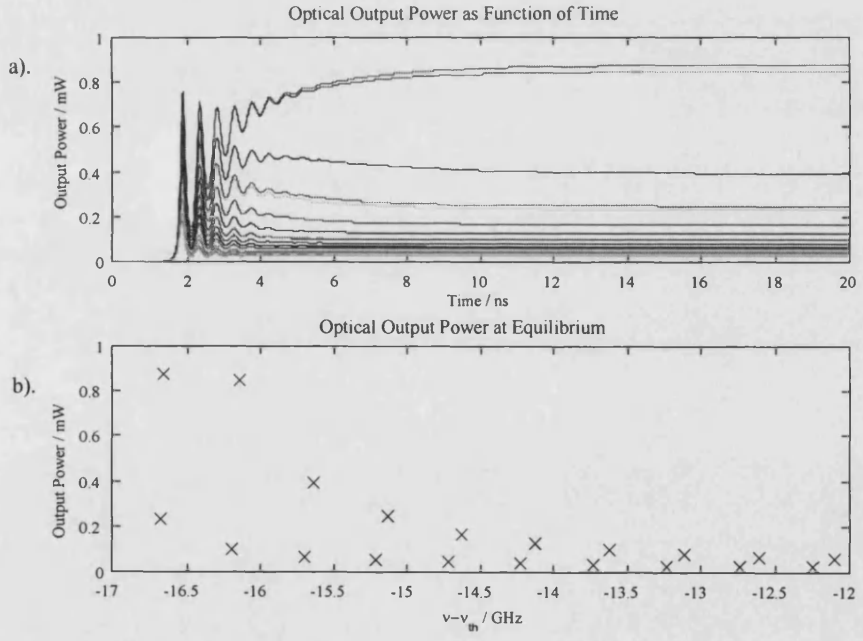

Figure 3.8. a). The temporal evolution of the optical power of the various XCM considered. b). A direct comparison of the equilibrium optical power values of the XCM system.

Figure 3.9 illustrates a more realistic case, in which all allowed external cavity modes of the laser have been considered. In this more realistic example, the external cavity consists of an external reflector of power reflectivity of 0.2 situated

25cm from the laser facet, with a bias current of 25mA again being applied to the laser.

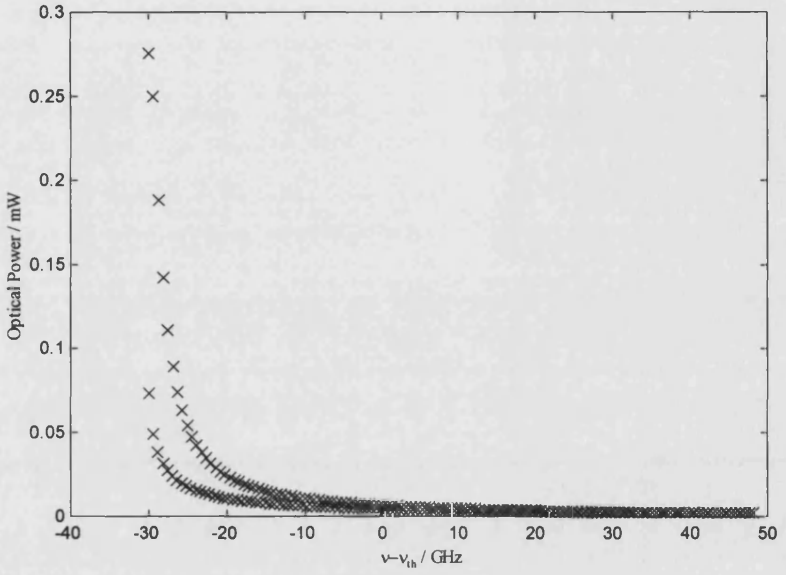

Figure 3.9. Power output of external cavity modes (XCMs) with conditions similar to that which may be in operation in the sensor system. R_1=R_2=0.32, R_{ext}=0.2, L_{ext}=0.25m.

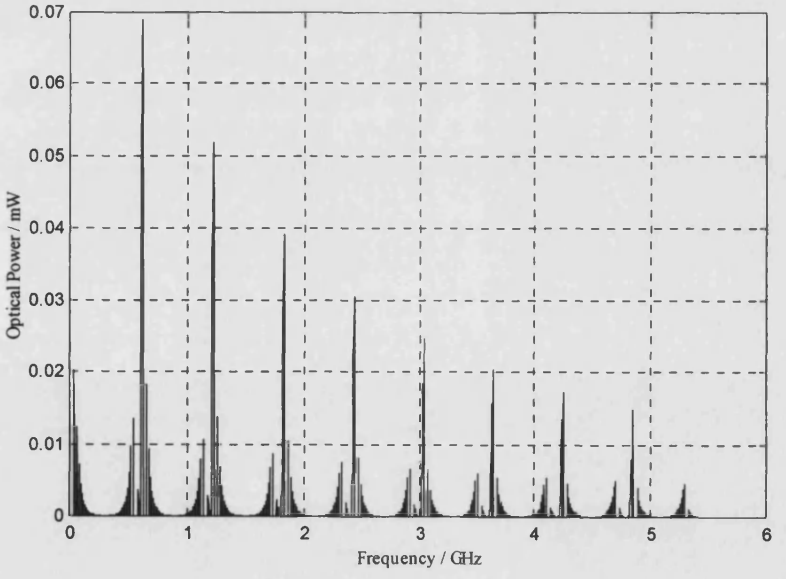

Figure 3.10. Approximate RF spectrum produced by beating together theoretically predicted external cavity modes. The conditions for operation are the same as for figure 3.9.

The information gained from the rate equations regarding the relative optical powers of the external cavity modes may now be used to simulate an approximate

RF spectrum. By beating each of the modes together, a picture can be formed of the possible lasing modes within the cavity. Figure 3.10 shows the beat modes that may be derived from the system characterised by figure 3.9, with each mode beating with every other mode providing a delta function contribution at the frequency corresponding to the frequency separation of the two modes concerned. This delta function will be scaled by the product of the optical powers of the two constituent modes.

It can be seen that there are a large number of beat modes present in the portion of the RF spectra shown in figure 3.10. These appear to be ordered so as to constitute the familiar series of peaks that are observed experimentally. Furthermore, it can be seen that each expected resonance peak has been split into a irregular peak arrangement. The irregular peak consists of a series of beat modes of lower intensity grouped within an area below the predicted external cavity resonance frequency, with higher intensity modes grouped at a slightly higher frequency. This irregular peak effect was suggested by the histogram shown in figure 3.4.*b*, detailing the frequency separation between every second mode in the XCM modal frequency distribution. If the area around the external cavity round-trip frequency is monitored, it can be seen that no allowed effective cavity modes exist at this frequency. This can be shown by examining figure 3.11. It can be seen that there is a group of allowed XCMs at a lower frequency than the external cavity round-trip frequency, f_c with a larger group of modes of higher power situated above f_c. However, in the immediate vicinity of and at f_c itself, there is a clear gap where no allowed beat modes exist. This occurrence is completely independent of the value of the detuning parameter $\omega\tau_{ext}$, as shown by figure 3.11. This figure shows the positions and powers of the beat modes produced by the system described by the threshold gain dependency shown in figure 3.7, with the frequency axis normalised to the value of the expected external cavity resonance frequency ($f_c=c/2L_{ext}$). This is shown as a function of the detuning parameter. In figure 3.11.*a* $\omega\tau_{ext}=\pi$, whilst in figure 3.11.*b* and figure 3.11.*c* the detuning parameter is $\pi/2$ and $\pi/4$ respectively. It can be seen that in all cases there are no modes present at the expected resonance frequency. Therefore, it

can be seen that this theoretical analysis predicts a shift in the frequency of the resonance peaks away from the predicted value.

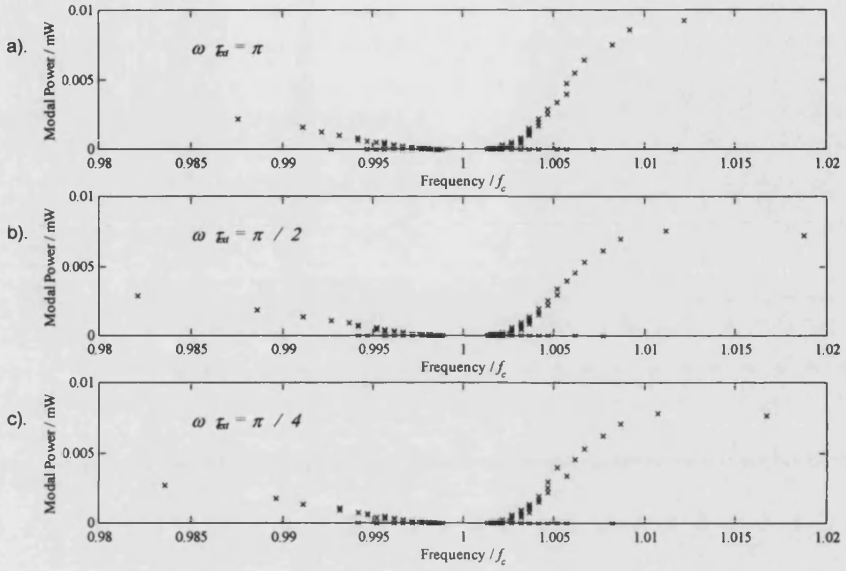

Figure 3.11. Comparison of the modal power distribution obtained when using the system described in figure 3.7. a). $\omega\tau_{ext}=\pi$, b). $\omega\tau_{ext}=\pi/2$, c). $\omega\tau_{ext}=\pi/4$. Note the absence of modes at the expected cavity resonance frequency, f_c.

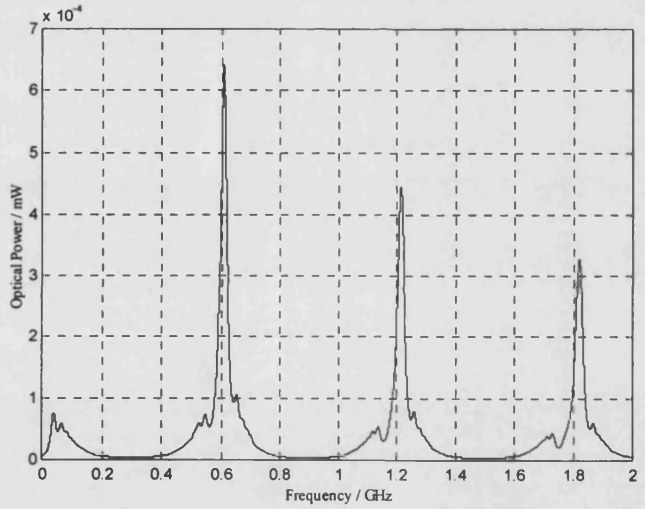

Figure 3.12. Resultant RF spectrum obtained after introduction of Lorentzian linewidth into beat mode system.

Figure 3.10 also demonstrates the existence of a low frequency fluctuation peak, which is an effect that has been observed experimentally and noted previously in chapter 2. The dynamic behaviour of the LFF is described in chapter 4 along with a full discussion of how it affects the frequencies of the other peaks in the RF spectrum.

Since the beat modes have only been considered as delta functions within the frequency spectra, to achieve a true theoretical approximation for the spectrum, each mode must be assigned a lineshape. In order to do this, the approximation is made that for this particular external cavity length, each beat mode possesses a Lorentzian lineshape of linewidth 17% of external cavity resonance peak separation. This value is chosen by examination of experimental results and other theoretical investigations [19]. This introduction of lineshape into the theoretical model produces the result shown in figures 3.12 and figure 3.13. Figure 3.12 shows the linearly scaled RF spectrum while in figure 3.13, the response is depicted using a logarithmic scale. It may now be seen that good qualitative agreement with experimental results is obtained, with the approximate beat spectra shown exhibiting many of the characteristics observed experimentally.

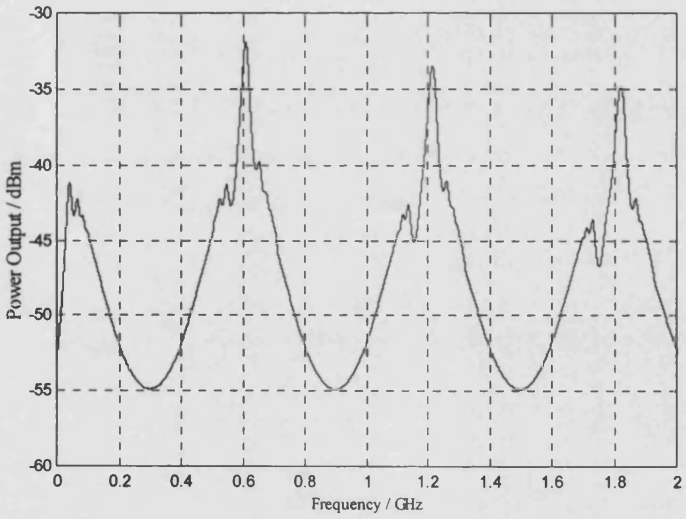

Figure 3.13. Logarithmic version of RF spectrum illustrated in figure 3.12.

3.2.8. Effect of a variation in external cavity length

The effect of a variation in external cavity length on the positions of the effective cavity modes is shown in figure 3.14. This figure describes the relative output powers at equilibrium of the effective cavity modes, as a function of frequency. In this example $r_1=r_2=0.57$ whilst $r_3=0.1$, which are typical values for the external cavity parameters for operation of the sensor. Inspection of this figure shows that as the cavity length is increased, the density of the allowed cavity modes

on the threshold gain ellipse locus also increases as previously discussed. Furthermore, it can be seen that the relative powers of the allowed effective cavity modes also change quite dramatically as a function of cavity length. Figure 3.14.*a* shows that one particular mode has a much higher output power relative to the remainder of the allowed modes. However, as the cavity length is increased, it can be seen that the modes possessing the highest power become progressively closer to the main body of modes, as can be seen by examination of figures 3.14.*b*- 3.14.*d*. It can be seen that the locus traced out by the mode positions changes from that of a *'right angle'* to more of a *'boomerang'* shape as L_{ext} changes from 0.25m to 1.00m.

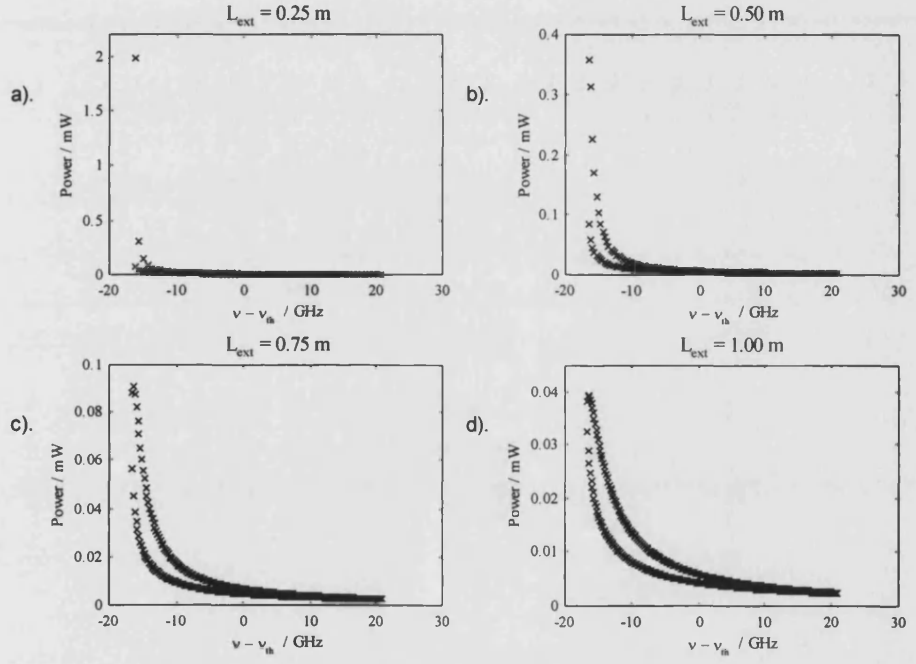

Figure 3.14. Effect of a variation in external cavity length on the frequencies and strengths of the allowed cavity modes. r_1=r_2=0.57, r_3=0.1. a). L_{ext}=0.25m, b). L_{ext}=0.50m, c). L_{ext}=0.75m, d). L_{ext}=1.00m.

As previously demonstrated the modal power distributions shown in figure 3.14 can be used to construct approximate predictions of the optical output frequency spectrum. These predictions, shown in figure 3.15, demonstrate, (as expected), that when the length of the external cavity is increased, the separation of the resonance peaks present in the spectra is reduced. It can be seen that the positions

of these peaks approximately follow the simple inverse relationship of external cavity length.

Furthermore, it can be seen that as the cavity length is increased, then not only does the modal frequency separation decrease, but the frequency of the low frequency fluctuation also decreases. It also appears to reduce in power relative to the other XCMs as the cavity length and therefore the feedback strength of the system is increased.

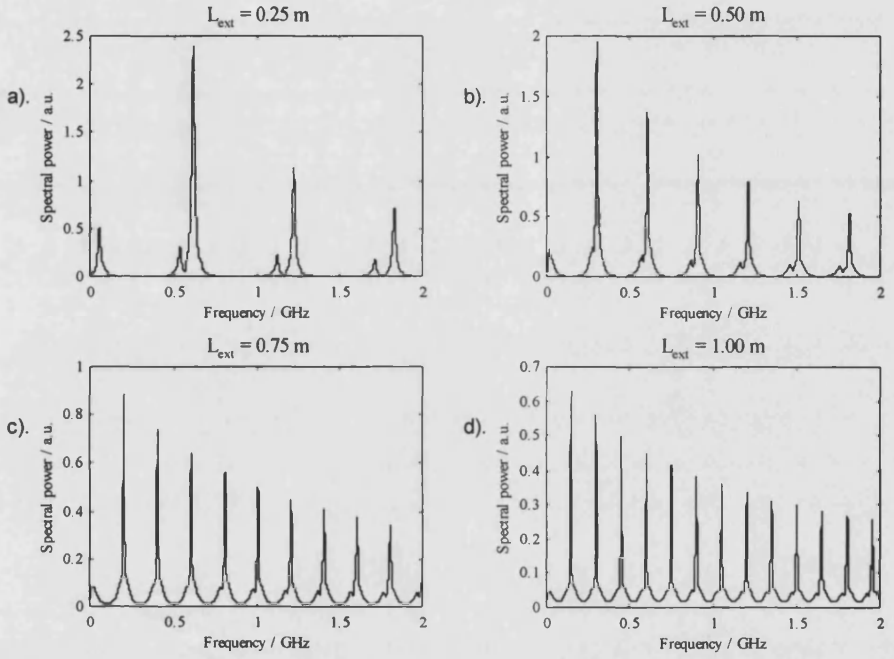

Figure 3.15. Theoretical prediction of RF spectra of optical signal when the external cavity is arranged according to the parameters given in figure 3.14.

3.3. Limitations of Theoretical Treatment

Whilst the results obtained by the theoretical approach so far have been found to provide qualitative results which show good agreement with experiment, some experimental features and observations are not explained by this system. Further enhancements to the theoretical model would be required in order to explain these effects.

For example a *'perfect'* mixing process has been employed whereby the external cavity modes have been mixed together theoretically, without any insertion of detector dynamics whatsoever. Furthermore, whilst XCM linewidth has been

taken into account to good effect in the theoretical analysis presented in this chapter, an approximation has been made as to what the XCM linewidth might in fact be, after analysis of previous experimental results. Also in some cases where the quantity $\gamma\tau_{ext}$ is large, an extremely large number of allowed external cavity modes are found to exist. However, in many cases it would not be practical to take into account the contributions from all these modes due to limitations on computing power. Furthermore, other effects regarding the stability of the system cannot be explained using the theoretical model detailed in this chapter. This includes the variation of the structure and shape of the output frequency spectrum as a function of bias current.

Whilst the operation of the laser system may have been considered in detail, no account has been taken of the detector dynamics of the laser system, leading to an idealised response which is detector insensitive. Most importantly however, no mechanism has been presented within this theoretical approach for the use of the laser diode itself as a detector. To fully understand the physical mechanisms involved, and fully predict the experimental results obtained these concepts need to be integrated into the model.

It must also be noted that no account has been made of the phase of the various external cavity modes. These are not phase locked in any way and will vary dynamically during operation due to carrier induced variations in refractive index and spontaneous noise effects.

Therefore, in chapter 6 an improved theoretical model is introduced which tackles the problem using a slightly different approach. In this case, the laser arrangement is considered as single moded system subject to delayed optical feedback from the external cavity, which causes dynamic changes in the operation of the laser. However, while the theoretical approach used in chapter 6 can be used to provide a more rigorous interpretation of the system dynamics, the approach considered in this chapter is fundamentally more instructive, providing a clear insight to the workings of this essentially simple but dynamically complex optical arrangement.

3.4. Conclusions

This chapter has taken the approach of using the concept of effective reflectivity to study the equilibrium behaviour of a semiconductor laser operated within an external optical cavity. It has been shown that by adopting this approach a qualitative representation of the response of the optical configuration can be obtained. It has been predicted that the frequency spectrum of the optical output of the system will consist of a series of resonance peaks, made up from the beating of many separate external cavity modes. The position of these modes roughly correspond to the round trip frequencies of the external cavity ($f_c=c/2L_{ext}$). However, the analysis does predict that at exactly this frequency, no beat mode contributions will exist. This suggests that each resonant peak will be offset to a small degree away from f_c, or the particular harmonic multiple of f_c in question. These are all characteristics of the system which have been observed experimentally.

A low frequency fluctuation (LFF) is also predicted by the theory, which again has been observed experimentally. The frequency of the LFF appears to scale along with the external cavity length so that when the cavity length increases, then the frequency at which the LFF occurs reduces.

While this method of analysing the external cavity configuration is quite instructive and provides a excellent understanding of the physical processes involved in the optical system, it is only an approximation, and is unable to account for certain physical phenomena which are observed. An appraisal has been given of the relative advantages and disadvantages of this theoretical approach, and it has been concluded that in order to analyse the behaviour of the laser junction voltage, an alternative technique is required. The application and results of this alternative analysis will be discussed in chapter 6.

3.5. References

[1] R.Lang and K.Kobayashi, "External optical feedback effects on semiconductor injection laser properties", *IEEE J.Quantum Electron.*, **QE-16**, No.3, pp.347-355, 1980.

[2] A.Olsson and C.L.Tang, "Coherent optical interference effects in external-cavity semiconductor lasers", *IEEE J.Lightwave Technol.*, **LT-4**, pp.1655-1661, 1986.

[3] R.W.Tkach, and A.R.Chaplyvy, "Regimes of feedback effects in 1.5μm distributed feedback lasers", *J.Lightwave Technol.*, **LT-4**, No.11, pp.1655-1661, 1986.

[4] F.Faver, D.Le Guen and J.C.Simon "Optical Feedback effects upon laser oscillation field spectrum", *IEEE J.Quantum Electron.*, **QE-18**, pp.1712-1717, 1980.

[5] J.H.Osmundsen and N.Gade, "Influence of optical feedback on laser frequency spectrum and threshold conditions", *IEEE J.Quantum Electron.*, **QE-19**, pp.465-469, 1983.

[6] L.Goldberg, H.F.Taylor, A.Dandridge, J.F.Weller and R.O.Miles, "Spectral characteristics of semiconductor lasers with optical feedback", *IEEE J. Quantum Electron.*, **QE-18**, No.4, pp.555-564, 1982.

[7] H.Temkin, N.A.Olsson, J.H.Abeles, R.A.Logan and M.B Panish, "Reflection noise in index-guided InGaAsP lasers", *IEEE J. Quantum Electron.*, **QE-22**, No.2, pp.286, 1986

[8] G.P.Agrawal and T.M.Shen, *J. Lightwave Technol.*, **LT-4.**, pp.58, 1986.

[9] S.Jiang, Z.Pan , M.Dagenais, R.A.Morgan, K.Kojima, "Influence of external optical feedback on threshold and spectral characteristics of vertical-cavity surface-emitting lasers", *IEEE Photon. Technol. Lett.*, **6**, No.1, pp.34-36, 1994.

[10] J.Buus, "Single frequency semiconductor lasers", Tutorial texts in optical engineering, vol. 5, SPIE, pp.16-18, 1991.

[11] K.Petermann, "Laser diode modulation and noise", 1991, Kluwer Academic Publishers, Chapter 9.

[12] M.Born and E. Wolf, "Principles of Optics", Pergamon, Oxford, 1970.

[13] T.Sano, "Antimode dynamics and chaotic itinerency in the coherence collapse of semiconductor lasers with optical feedback", *Phys. Rev. A.*,**50**, No.3, 1994, pp.2719-2726.

[14] M.-W.Pan, B.-P.Shi and G.R.Gray, "Semiconductor laser dynamics subject to strong optical feedback", *Opt. Lett.*, **22**, No.3, 1997, pp.166-168.

[15] C.H.Henry, "Theory of the linewidth of semiconductor lasers", *IEEE J.Quantum Electron.*, **QE-18**, pp.259-264, 1982.

[16] L.D.Landau and E.M.Lifshitz, "Electrodynamics if continuous media", Pergamon Press, pp.256, 1960.

[17] H.Rong-Qing and T.Shang-Ping, "Improved rate equations for external cavity semiconductor lasers", *IEEE J.Quantum Electron.*, **25**, No.6, pp.1580-1584, 1989.

[18] P.Besnard, B.Meziane, G.M. Stéphan, "Feedback phenomena in a semiconductor laser induced by distant reflectors", *IEEE J.Quantum Electron.*, **29**, No.5, pp.1271-1284, 1993.

[19] N.Schunk and K.Petermann, "Minimum bitrate of DPSK transmission for semiconductor lasers with a long external cavity and strong linewidth reduction", *J. Lightwave Technol*, **LT-5**, pp.1309-1314, 1987.

[20] L.Goldberg, H.F.Taylor, A.Dandridge, J.F.Weller and R.O.Miles, "Spectral characteristics of semiconductor lasers with optical feedback", *IEEE T. Microwave Theory and Techniques*, **MTT-30**, pp.401-409, 1982.

[21] C.H.Henry and R.F.Kazarinov, "Instability of semiconductor lasers due to optical feedback from distant reflectors", *IEEE J.Quantum Electron.*, **QE-22**, No.2, pp.294-301.

[22] N.Schunk and K.Petermann, "Numerical analysis of the feedback regimes for a single-mode semiconductor laser with external feedback", *IEEE J. Quantum Electron.*, **QE-24**, pp.1242-1247, 1988.

[23] G.P.Agrawal and N.K.Dutta, "Semiconductor lasers", 2nd Edition, Van Nostrand Reinhold, New York, pp.302., 1993.

[24] L.Raddatz, "Light sources for communication systems using multimode optical fibre", MPhil. Thesis, University of Bath, UK, 1995.

[25] J.E.Bowers, T.L.Koch, B.R.Hemenway, D.P.Wilt, T.J.Bridges and E.G.Burkhardt, "High frequency modulation of 1.52μm vapour-phase transported InGaAsP laser", *Electron. Lett.*, **21**, pp.297-299, 1985.

[26] G.P.Agrawal, "Modulation bandwidth of high power single-mode semiconductor lasers : Effect of intraband gain saturation", *Appl. Phys. Lett.*, **48**, pp.613-615, 1986.

[27] J.E.A.Whiteaway, A.P.Wright, B.Garrett, G.H.B.Thompson, J.E.Carroll, L.M.Zhang, C.F.Tsang, I.H.White and K.A.Williams, "Detailed large-signal dynamic modelling of DFB laser structures and comparison with experiment", Optical and Quantum Electron., **26**, S817-S842, 1994.

[28] B.Meziane, P.Besnard and G.M.Stephan, "Low Frequency resonances in asymmetric external cavity semiconductor lasers: theory and experiment", *IEEE J. Quantum Electron.*, **31**, No.4, pp.617-622, 1995.

[29] A.Wonfor, private communication.

CHAPTER 4

FURTHER OPERATIONAL AND STABILITY ANALYSIS OF THE RESONANT CAVITY SENSING TECHNIQUE

This chapter presents an examination of a number of stability issues connected with the optical position sensing technique described in chapter 2. It assesses how the output of the sensor is affected by variations in key operating parameters such as bias current and feedback strength. It also considers departures from the simple inverse law given in chapter 2 which predicts the frequencies of the resonance peaks. In addition, the existence and behaviour of the low frequency fluctuation (LFF) peak is discussed with particular consideration given to its affect upon the operation of the sensor.

4.1. Introduction

The experimental results outlined in chapter 2 demonstrate that the resonant cavity optical position sensor operates in a manner which allows it to be used in a wide variety of sensing applications. However, in order to design a sensor which can be successfully applied to real industrial environments, it is essential that the system operates in a reliable manner over a long time scale. Before the design of such a system can be finalised, it is important to be fully aware of the full operating characteristics of the system and how it is affected by changes in key operating parameters.

In chapter 2, the basic operating conditions of the sensor were discussed in some detail. While it was shown that the position dependency of the resonance peaks produced by the sensor are governed by an inverse law, the departures from it were not analysed. The detailed position dependence behaviour of the frequency spectra has therefore been studied and is described in the following section.

Furthermore, no analysis was carried out in chapter 2 of how the frequencies of the resonance peaks are dependent upon physical parameters other than the external cavity length. Several experimental investigations were carried out to assess

quantitatively how the output of the sensor is affected by changes in parameters such as bias current, feedback strength and temperature. These investigations are described in the following sections, along with a full discussion of the results obtained.

4.2. Deviations from the simple inverse law predicting peak positions

It was suggested in chapter 2 that the frequencies of the resonance peaks generated by the sensor are governed by an inverse relationship,

$$f_m \approx \frac{mc}{2l}. \tag{4.1}$$

However, it has been noted experimentally that while the frequencies of the resonance peaks do approximately follow this relationship, it does not predict the exact positions of the peaks. To quantitatively assess the deviations from this simple inverse law the experimental arrangement shown in figure 4.1 was used.

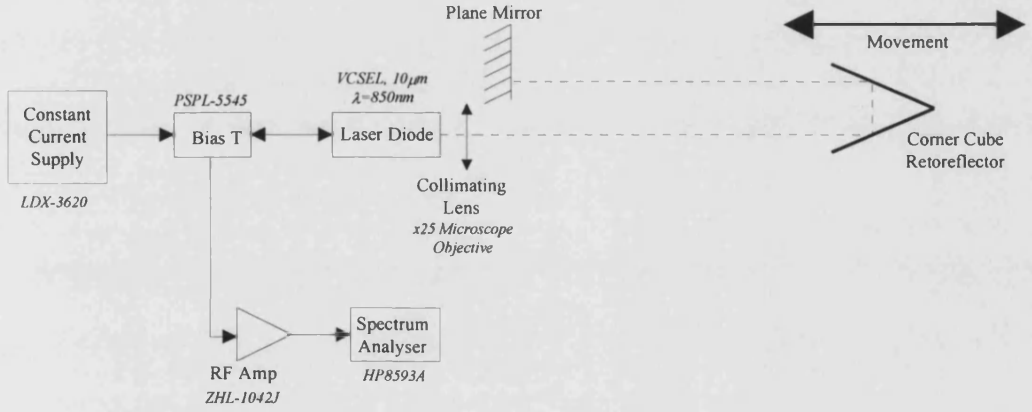

Figure 4.1. Experimental arrangement used to assess adherence to simple inverse law.

The laser used to carry out these investigations was a VCSEL of the same structure and form as the device described in chapter 2. However, this particular VCSEL possessed a different threshold bias current which was 8.9mA. During the experiment, the laser was driven with a constant bias current of 9.0 mA by a precision, low noise current source (ILX Lightwave LDX-3620). The position of the retroreflector was varied using a computer controlled translation stage, which allowed a maximum change in the external cavity length of 60cm. At a number of discrete positions the frequencies of the first four resonance peaks were accurately

measured using a RF spectrum analyser (HP8593A). This is a frequency synthesised, swept source spectrum analyser which has a measurement range of 100kHz to 29.9GHz. In order to provide as accurate a measurement as possible, video averaging (100 scans) was applied to the raw data on the analyser in order to smooth out any temporal noise contributions in the vicinity of the resonance peaks. In addition, the frequency span of the analyser was reduced to a minimum to allow the identification of the exact centre of the resonance peak to be made at a higher resolution.

The results obtained from this experiment are shown in figure 4.2. This figure shows the frequency variation apparent for each of the first four modes in the spectrum of the junction voltage of the laser, plotted as a function of position. This figure also shows the theoretical predictions for the frequencies of the resonance peaks as derived from equation 4.1. It can be clearly seen that there is a distinct mismatch between the simple relationship of equation 4.1 and the experimental results. This deviation is most noticeable for the lowest order resonance peak (figure 4.2.*a*).

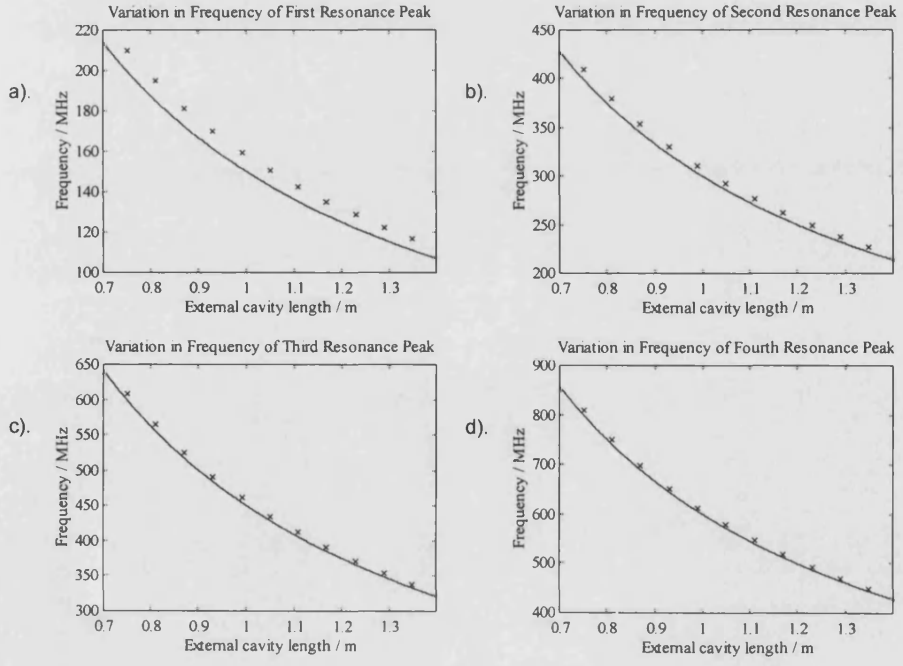

Figure 4.2. Variation of resonance peak frequencies as a function of position.

— Theoretical prediction 'x' Experimental data

Examination of the experimentally measured and theoretically predicted results for the other resonance peaks shows that this discrepancy is not due to a simple error in assigning the absolute datum to the external cavity length. If this was the case, the discrepancy between the measured and predicted values would in fact increase, in a harmonic fashion. However, as peaks of higher harmonic number are examined, it can be seen that the discrepancy decreases as a percentage of the peak frequency, as shown in figure 4.2. In real terms, however, the deviation remains approximately constant for each peak. This illustrates that there is some sort of frequency offset or frequency splitting present within the system causing this apparent departure from the 'ideal', simple inverse law behaviour.

Further examination shows that the offset is not a constant value, but that it varies as a function position, as shown by figure 4.3. This illustrates how the deviation between the measured frequency and the theoretical prediction for the fundamental peak varies as a function of cavity length.

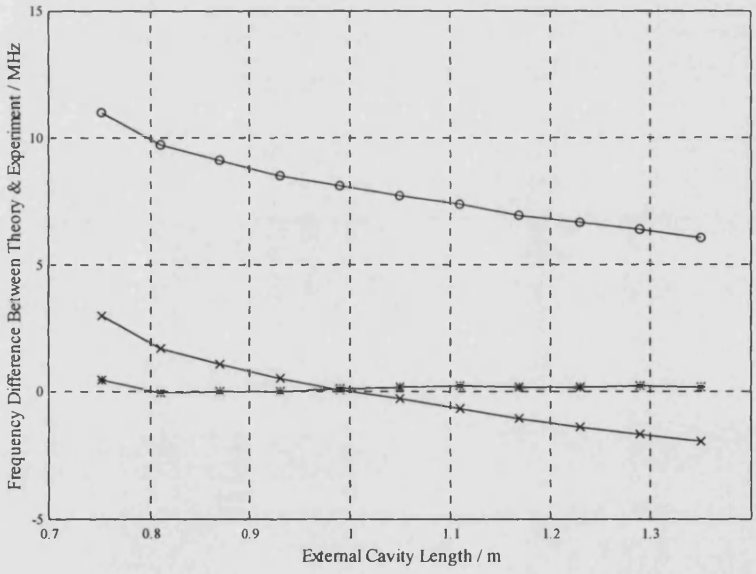

Figure 4.3. Graph showing the variation of the deviation in frequency from the theoretically predicted values for the first resonance peak. Key: 'o' Real frequency deviation, 'x' Frequency deviation minus 8 MHz, '*' Frequency deviation minus 5% of frequency value.

A deviation of between 6 and 11 MHz is evident for the first resonance peak over the cavity length shown. If this data set is adjusted by subtracting 8 MHz from each data point, it can be seen that while the total deviation is reduced, complete

correction is only obtained at one particular cavity length (at approximately 1m). At either side of this point the deviation remains non-zero. This suggests that if there is indeed an offset of some kind superimposed upon the frequencies of the resonance peaks, then it is cavity length dependent. This hypothesis is confirmed when each data point is adjusted by subtracting 5% from the original measured peak frequencies. Figure 4.3 illustrates that this adjustment produces a close match to the predicted value over the whole range of cavity lengths shown. In fact, this adjusted data set now lies almost exclusively within the experimental error inherent in the original measurement (0.2 MHz). This equates to 0.1% of the frequency of the fundamental peak at a cavity length of 0.75m. In this case, it appears as though the frequency offset accounts for a positive increase in the frequency of the peak which amounts to 5% of its final value.

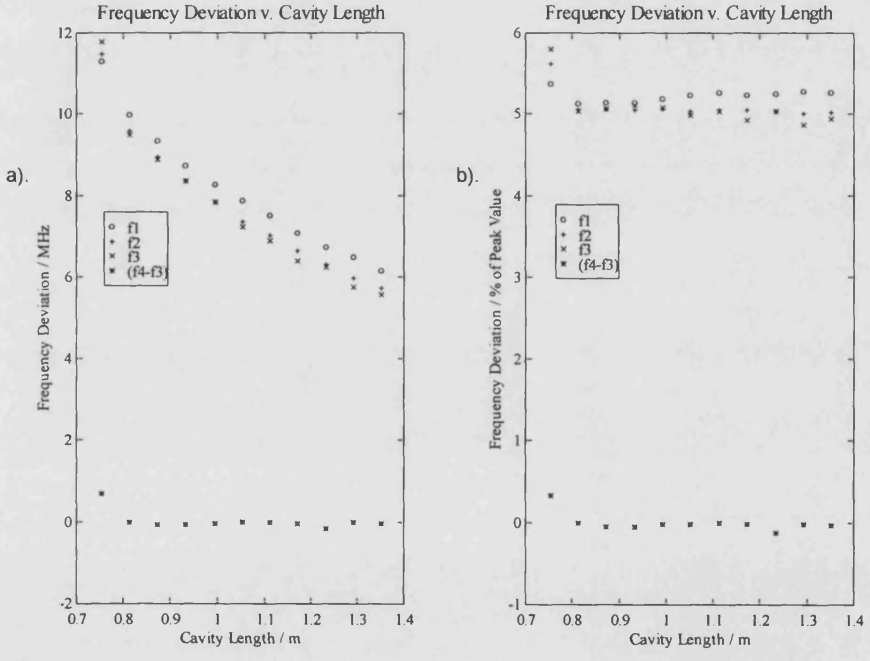

Figure 4.4. An illustration of the reduction in frequency discrepancy between the experimentally measured and theoretically predicted values of the frequency peaks. a). Deviation expressed in frequency, b). Deviation is expressed as a percentage of the peak frequency. Key: 'o' first peak, '+' second peak, 'x' third peak, '*' difference between fourth and third peaks.

Considering the fact that all the resonance peaks appear to be equally subject to this frequency offset, a measurement of the separation between the peaks should provide a result which is very accurately described by the simple inverse law of

equation 4.1. This is illustrated in figure 4.4, which shows the discrepancy between the experimentally measured and theoretically predicted frequencies of the first three resonance peaks, as a function of cavity length. It can be seen that a significant measurement discrepancy occurs for each of these peaks, the value of which varies between 5.5 and 11 MHz at the extremities of the external cavity range used in this experiment. However a fourth data series is presented on the graph which is obtained by measuring the frequency separation between the fourth and third resonance peaks and assessing the deviation between this and the predicted value. It can be seen that the deviation is far less than that obtained when considering the measurement of a single resonance peak. There also appears to be no correlation between the value of the deviation and the external cavity length, unlike the absolute peak position.

Therefore, the approach of measuring the frequency separation between the peaks has succeeded in greatly reducing any deviation between the experimentally measured and theoretically predicted peak frequencies generated from the simple inverse relationship of equation 4.1. It can be concluded that this simple inverse law exhibits a far closer agreement with experimental measurements when it is used to describe the frequency separation of the resonance peaks, rather than the absolute position of peaks within the frequency spectrum.

While this offset is found to occur, it is important to note that all the experimental results obtained are found to be very stable and repeatable. It should be noted that the suitability of this system for sensing applications is not diminished. While the presence of this offset is an important physical characteristic of the external cavity system which must be noted for completeness, if it does not vary temporally, then the sensor can be calibrated to provide an absolute position measurement.

Considering the values of the offset and the fact that it scales as a function of external cavity length, it appears that it may be connected in some way with the low frequency fluctuation (LFF) identified in the preceding two chapters. This will be discussed in more detail in section 4.4.

4.3. Stability Analysis As A Function Of Key Operating Parameters

In order to assess the stability of the system as a function of various key parameters, a series of experiments were carried out. These analysed the output of the sensor as a function of parameters such as current, feedback strength and temperature. The details of these experiments are given below.

4.3.1. Variation of Peak Positions as a Function of Bias Current

In chapter 2, the optimum biasing conditions of the semiconductor laser in the external cavity system were determined by analysis of the *quality* of the resultant RF spectra. It was generally the case that the optimum bias point was determined to be the current at which the signal to noise ratios of the resonance peaks within the spectrum were maximised, with approximately equal powers present in each of the main resonance peaks. While the qualitative appearance of the frequency spectra as a function of bias current was discussed in chapter 2, no analysis was made of how the frequencies of the resonance peaks may be quantitatively affected by any variation in bias current. As this factor is important to the stability of the sensor, experimental investigations were undertaken in order to accurately determine the behaviour of the resonance peaks as a function of current.

The experimental arrangement used to examine the effect of a change in bias current upon the operation of the sensor is shown in figure 4.5. Under normal operation, the laser would be driven with a constant bias, although in this case the bias current was varied in discrete steps by means of a precision laser diode driver (ILX Lightwave LDX-3620). A RF spectrum analyser (HP8593A) was used to measure the centre frequencies of the resonance peaks. To obtain accurate measurements of the exact positions of the peaks in the frequency spectrum, video averaging was again used to refine the spectrum analyser output display. During the course of these measurements, the external cavity was maintained at a constant length so that any variation in peak frequency could not be attributed to a variation of optical path length. In practice, a convenient external cavity length of approximately 744mm was used. The VCSEL referred to in section 4.2 was used as

the optical source. The bias current of this device was varied discretely over the full current range within which noticeable resonance peaks are present in the spectra.

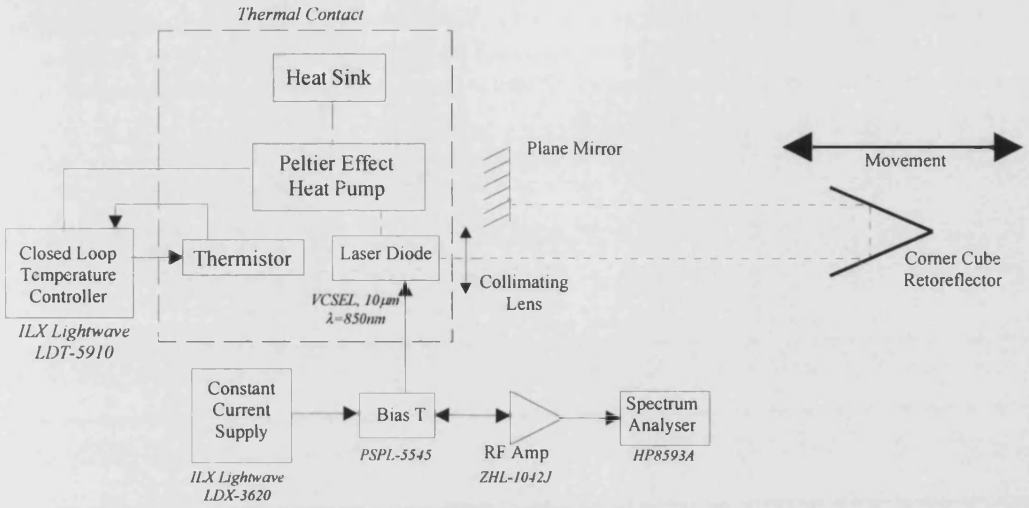

Figure 4.5. Experimental arrangement used to assess the effect of a variation of bias current upon the resonance peak frequencies.

The variation in frequency of the first three resonance peaks within the RF spectrum due to the variation in bias current is shown in figures 4.6.*a* to 4.6.*c*. These figures show that a clear, linear dependency exists for each peak. The slope of this shift is similar for each peak and ranges between 4.3 MHz/mA to 4.7 MHz/mA, the total shift equating to approximately 3% of the maximum frequency peak value.

In the context of position measurement, it can be clearly seen that if the position of only a single peak is monitored, a drift in the bias current of the device may lead to a significant measurement error. In contrast, figure 4.6.*d* illustrates the correlation between the frequency separation of two peaks and the applied bias current. This shows that the current-induced frequency variation so clearly observed in the absolute peak frequency measurements has been greatly reduced by considering the frequency separation between peaks. Three data series are plotted in this figure. These quantify the variation in frequency separation between the first and second, second and third and half the separation between the first and third resonance peaks as a function of bias current. Most importantly, it can be seen that at the lower end of the current range, where the qualitatively defined optimum bias

point exists, the frequency variation lies within the nominal experimental error of ±0.2MHz, which equates to approximately 0.1%.

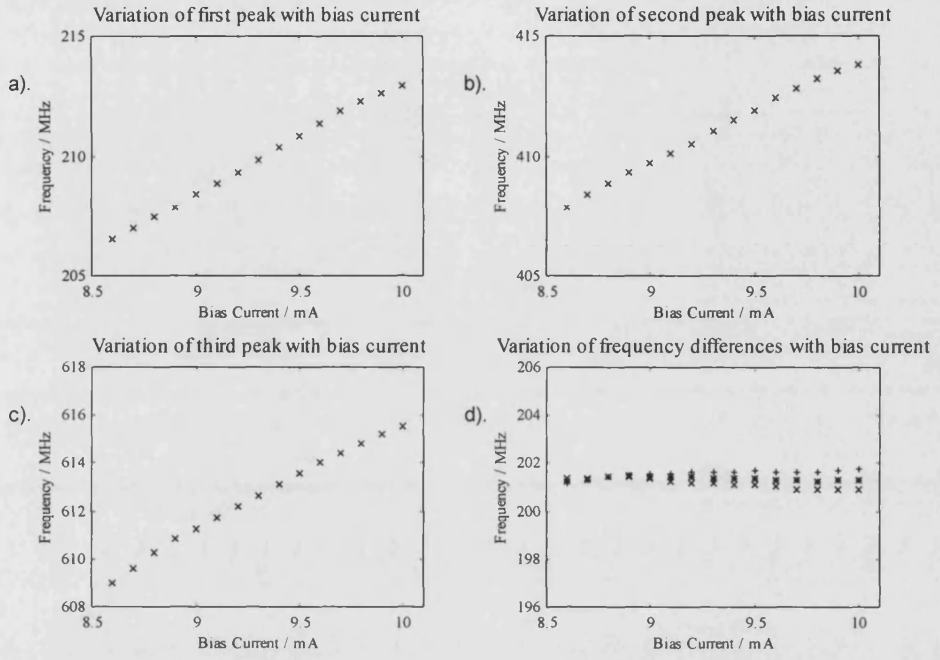

Figure 4.6. Variation in peak position as function of bias current. a). First peak, b). Second peak, c). Third peak, d). Frequency differences, Key: 'x' - (peak2-peak1), '+' - (peak3-peak2), '*' - (peak3-peak1)/2.

At higher currents the frequency separation of the peaks does diverge somewhat from one common line. However, any error which is produced is still greatly reduced when compared to that observed from measurement of the absolute position of the peaks themselves. One contributory factor to this divergence is the fact that the 'shape' and 'form' of the resonance peaks become increasingly distorted with measured bias current. This brings a degradation of the previously well defined, 'sharp' peak, with an increase in the linewidth and a reduction in the signal-to-noise level clearly apparent. This was previously illustrated in figure 2.9 of chapter 2 where the shape of the spectra was qualitatively assessed as a function of bias current. Inspection of this figure reveals that this increased deformation makes the exact identification of the frequency at which the maxima of the resonance peaks occur increasingly awkward.

It should be noted that any practical system developed around this principle would be operated close to the equivalent point (for a particular laser) denoted by

8.8mA in figure 4.6.*d*. Even using the most rudimentary of bias current drives, it should be ensured that the operation of the device does not extend further than the equivalent of 0.1mA in figure 4.6.*d*. A slightly more complex system should even be able to cope with degradation of the laser performance over extremely long time scales due to ageing. Therefore, the stability due to current variations should remain at an accuracy level of 0.1%.

These results show that the resonance peaks are subject to a positive shift in frequency as the bias current is increased. Due to the non-harmonic nature of this shift, the peaks are found to be subject to a varying offset rather than a variation in the fundamental position of each resonance peak. If this were the case, then the variation in the higher order resonance peaks would be expected to scale harmonically. Once again, this effect appears to be inexorably linked with the apparent existence of a frequency offset on each peak as discussed in section 4.2. It would appear as though the current induced frequency variation is in some way connected with the offset which appears to have its origins in the low frequency fluctuation which is present in the spectra.

In summary, it can be seen that a variation in bias current leads to an approximately linear shift of the resonance peak frequencies. However, this effect should not be problematic for long term system operation as long as the frequency separation between peaks is measured (as opposed to the absolute frequency measurement of a single peak).

4.3.2. Variation in Peak Frequency as a Function of Optical Loss

It was shown in the preceding section that the frequencies of the resonance peaks produced by the external cavity arrangement are to an extent affected by a variation of the bias current applied to the laser. Similarly, a shift in the peak frequencies was also found to occur when the optical signal within the cavity was subject to some attenuation. In order to accurately assess this variation, the experimental arrangement shown in figure 4.7 was used.

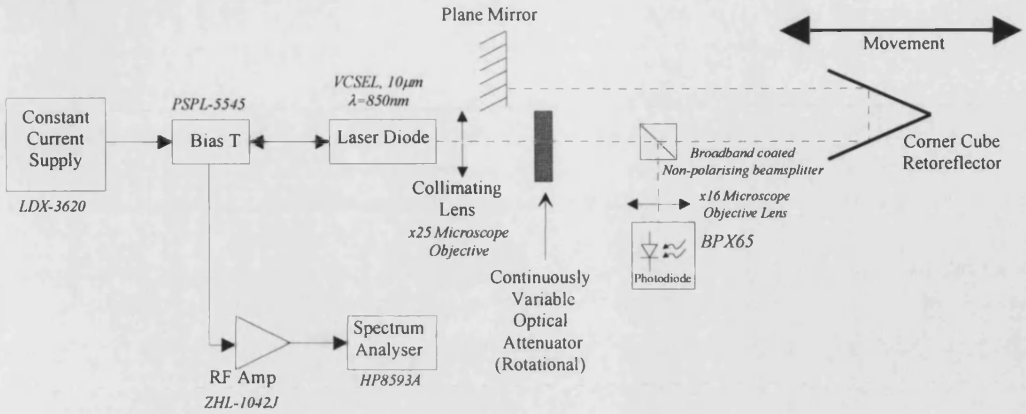

Figure 4.7. Experimental arrangement used to analyse the shift in peak frequencies, caused by optical attenuation.

It can be seen from figure 4.7 that this arrangement is quite similar to the configuration that was used in section 4.3.1 to study the variation in resonance peak frequencies as a function of bias current. However, in this investigation a variable optical attenuator was inserted into the external cavity along with a non-polarising beamsplitter. The beamsplitter was used to tap off a portion of the optical power in the external cavity so that the attenuation applied to the external cavity could be quantified using a photodiode. A silicon photodiode (BPX65) was used for this purpose, with a microscope objective lens used to focus the optical beam onto the detector. The output of the photodetector was subsequently measured using a digital multimeter.

The variable attenuator used was of the bulk optical rotary type, allowing continuous variation of the optical attenuation level by rotating the attenuator wheel about its axis. The total optical attenuation introduced into the cavity was quantified by comparing the photodiode output with the external cavity blocked at some point after the beamsplitter. An absolute reference was then applied to these values by measuring the photodiode output obtained when the attenuator was completely removed from the cavity at the end of the measurements, again with the external cavity blocked. To calculate the total amount of optical attenuation within the cavity, it should be remembered that during a round-trip of the external cavity, two passes are made through both the attenuator and the beamsplitter. Therefore, the total attenuation can be assumed to be twice the attenuation imposed by the variable attenuator, plus 6dB due to the presence of the beamsplitter in the cavity.

As the amount of attenuation in the cavity was varied, the frequencies of the resonance peaks were measured using the spectrum analyser in the same manner described in the preceding section. During the course of this experiment the bias current to the laser diode was maintained at a constant value, and in addition the external cavity length was kept constant.

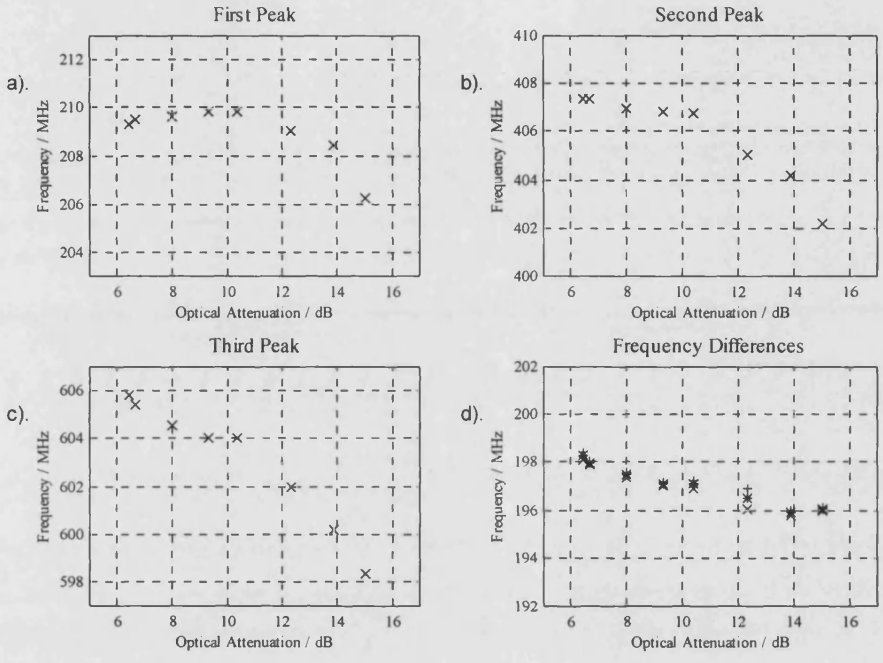

Figure 4.8. The variation in resonance peak position as a function of the amount of optical attenuation present within the external cavity. a). First Peak, b). Second Peak, c) Third Peak, d). Fourth Peak - Key: *'x' - Peak 2 - Peak 1*, '+' - *Peak 3 - Peak 2*, '*' - *1/2 (Peak 3 - Peak 1).*

On examination of the RF response of the optical system, it was found that as the optical attenuation present in the external cavity was increased, the frequency of the resonance peaks slightly decreased, with all peaks following this general trend. Inspection of figures 4.8.*a*-4.8.*c* illustrates this point. It can be seen that initially, for low values of optical attenuation, there is very little change in the resonance peak frequencies (<0.5%). However, after approximately 11dB of attenuation has been applied, these frequencies begin to decrease, the rate of decrease increasing with increased attenuation.

In contrast, figure 4.8.*d* shows the dependency of *peak* separation on optical attenuation. As in the case of bias current variation, it can be seen that the peak

separation exhibits a smaller variation than do the individual mode positions. In this case however, the improvement in optical loss insensitivity gained from measuring the frequency separation is not as great as in the case of the bias current variation. However, this variation still only amounts to a change of 2MHz over a 10dB range, whereas a 6MHz variation was typical for the absolute peak measurement.

Importantly, however, from the view of practical sensing, it can be seen that with only a moderate change in optical feedback strength (say less than 8 dB), the variation in the absolute frequency of the resonance peaks is small (<0.5%). This small reduction may be further reduced by measuring the separation between the peaks and not the absolute values themselves. Yet again, therefore, it may be seen that measurement of the frequency separation between peaks provides a more stable measurement than that of a single absolute peak.

It is interesting to note that while the relationship between resonance peak frequency and bias current is approximately linear, the relationship with optical loss is a highly non-linear one. Indeed it appears from further work that there are in practice, several regimes of operation which may be assessed by monitoring the system performance as a function of feedback strength [1]. A detailed discussion of these regimes is beyond the scope of this thesis. However, it is worth mentioning that the results of this additional work support the fact that a change in the feedback strength of <10dB will only have a minor affect on the sensor output.

It should also be noted that it may be possible for the shift in the frequency separation shown in figure 4.8.*d* to be due to variations of other parameters which include the alignment of the optical components. As the optical system used in this experiment is constructed using individually mounted components, these may drift slightly over the course of the measurements, leading to this shift. However, a properly designed prototype system should be far more insensitive to changes of this kind as all of the components will be securely mounted in a single housing.

4.3.3. Variation in peak frequency as a function of device temperature

As the stability of the sensor system has been tested for the influences of bias current and feedback strength variations, it is also useful to assess the effect of temperature on the resonance peak frequencies. An investigation was therefore carried out to determine the nature of any temperature induced frequency shift within the system. To accomplish this, the experimental arrangement used in section 4.3.1 (figure 4.5) to assess the current induced frequency shift was employed. Once again, the VCSEL was used as the optical source in this experiment, but in this investigation, the closed loop temperature controller which had been previously used to maintain a constant device temperature was used to vary the temperature over a range of values. During the investigation, care was taken to ensure that the system was allowed to reach an equilibrium before the measurements of peak frequency were taken. Once an equilibrium had been reached, the frequency of the fundamental resonance peak was measured using the spectrum analyser.

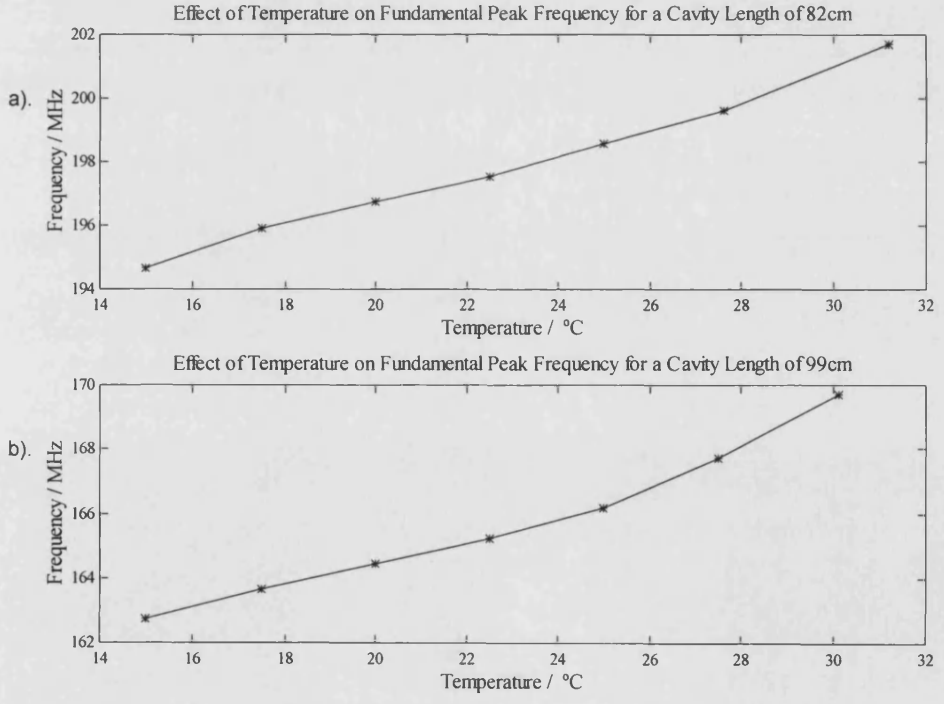

Figure 4.9. Example of temperature induced variation in fundamental resonance peak at two different external cavity lengths. Cavity lengths: a). L_{ext}=82cm, b). L_{ext}=99cm.

Figure 4.9 illustrates the results obtained, with the measurement being carried out at two different external cavity lengths. Examination of figure 4.9 shows that in both cases a frequency shift of approximately 7 MHz was resultant from a temperature variation of 15.2 °C. The similarity in the variation at the two separate cavity lengths, once again suggests a shift in the frequency offset of the resonance peaks.

It is interesting to note that after a temperature variation had been made using the ILX Temperature controller, it took approximately two minutes for the optical system to reach equilibrium, even though the individual changes were typically only 2 °C. Therefore, it is likely that the temperature induced frequency shift which is described in figure 4.9 is not solely due to temperature induced variations in the operation of the laser such as the effect on the threshold bias current. While this would have a direct affect on the frequencies of the resonance peaks, as described in section 4.3.1, the temperature induced variation may also be caused by a slight misalignment of the optical system due to thermal expansion. As the laser was mounted upon a brass mount with all the other components individually mounted upon the optical bench, it is likely that the change in temperature has caused small alignment variations to take place. Consequently it is likely that the temperature effect shown in figure 4.9 is heavily dependent upon the laser mount design that is employed.

Due to the thermal expansion which is present, it is difficult to ascertain what is the dominant cause of the temperature induced frequency variation, whether it be a dynamic laser effect or a misalignment due to the thermal expansion. It is therefore recommended that further studies are carried out to determine the exact behaviour of prototype systems as a function of temperature. Finally, it can be seen that over general operation the effect of any temperature variation should be easily compensated by using a closed loop temperature controller. This would require only a minimal increase in system complexity, with the addition of a Peltier heat pump and a simple electronic control circuit. Furthermore, monitoring the DC component

of the laser junction voltage with feedback loop control to the bias current, should further reduce any temperature induced biasing effects that may remain.

4.4. The Low Frequency Fluctuation (LFF)

The existence of a low frequency fluctuation (LFF) has been identified in the preceding chapters, with its presence observed in both experimental measurements and theoretical predictions made in chapters 2 and 3 respectively. Over the past decade there has been much interest in the study of the experimental effects of the LFF [2-5], although as yet no definitive theoretical hypothesis has emerged to describe the behaviour of this phenomenon. However, many suggestions have been made as to the origins of this effect. These include optical bistability [6], multiple external cavity reflections [7], a downshift in the laser relaxation oscillation [8], cavity asymmetries [9] and non-linear instabilities caused by spontaneous emission [10]. However, in chapter 3 a simple alternate conceptual approach was considered where the LFF is generated by the mixing together of multiple external cavity modes (XCMs). The frequency separation of these particular XCMs is much less than the first round-trip harmonic frequency. Due to the nature of the threshold gain ellipse [10] described in chapter 3 and the relative intensities of these modes, a distribution is formed which gives rise to the LFF. While the relative size of the LFF peak generated in this way is not as great as the main resonance peaks, it is believed that the beat frequency distribution which comprises the LFF is enhanced by spontaneous noise effects in the laser. The resultant enhancement can be observed in chapter 6, where a dynamic rate equation analysis of the system is carried out. The frequency spectra produced using this technique feature a LFF peak which agrees qualitatively with experimental arrangements in both frequency and amplitude. The amplitude of the peak is enhanced when compared to the predictions of chapter 3.

While to date no studies have analysed the variation in the resonance peaks obtained from the frequency spectrum of the laser junction voltage variations, Temkin et al [11] assessed the behaviour of the RF spectrum of the optical output. They found that the bias current induced variations in the LFF quantitatively

mirrored those observed in the fundamental resonance peak. These observations correspond to the experimental measurements discussed in section 4.3.1.

Furthermore, Morikawa et al [12] established that the LFF was a function of the external cavity length. It can therefore be seen that the experimental observations discussed in section 4.3.1 are in agreement with this conclusion. This can be confirmed by considering the distribution of allowed lasing modes around the characteristic threshold gain ellipse [10] as a function of external cavity length.

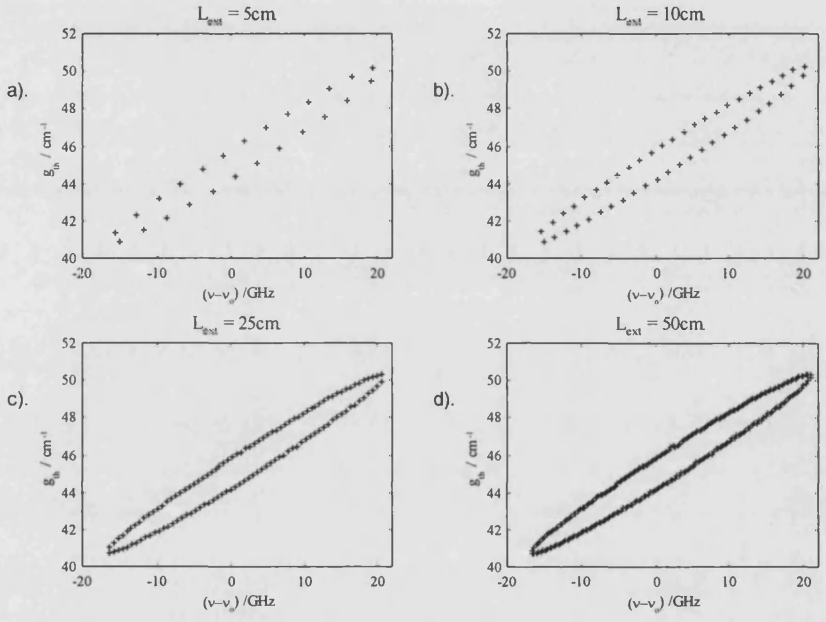

Figure 4.10. The variation in distribution of allowed effective cavity lasing modes as a function of external cavity length, for a typical Fabry-Perot type laser (λ=1300nm) - $r_1=r_2=0.57$, $r_3=0.1$. a).L_{EXT} = 5cm, b).L_{EXT} = 10cm, c).L_{EXT} = 25cm, d).L_{EXT} = 50cm.

Figure 4.10 shows how the allowed lasing modes are distributed on the locus of an ellipse which describes the threshold gain as a function of frequency. As the length of the external cavity is increased, it can be seen that the density of the allowed modes increases, requiring closer frequency spacing. As discussed in chapter 3, the modes with the lowest threshold gain dominate the optical spectrum. However, close analysis of figure 4.10 shows that those modes which possess the lowest threshold gain are very closely spaced. When these modes beat together, they produce a number of beat frequencies in a low frequency distribution which gives rise to the LFF. As figures 4.10.*a* to 4.10.*d* are considered in turn, it can be seen that

the frequency separation of these highest power optical modes decreases as the cavity length is decreased. As a consequence, the frequency of the LFF scales inversely as a function of position, in the same way as the main resonance peaks.

4.4.1. Correspondence of LFF to the observed frequency offset

In more general terms, the experimental evidence detailed previously in this chapter suggests that the LFF is inexorably interlinked with the positions of the main resonance peaks observed within the spectra. Figure 4.11 describes the frequencies of the resonance peaks generated by the BNR Fabry-Perot laser, the operation of which was described in detail in chapter 2. The frequencies at which the resonance peaks occur are plotted against the order of the resonance peak, with the LFF plotted as the zeroth order peak. It can be seen that the data points which represent the peaks follow a linear relationship, which confirms the fact that the frequency separation of the peaks is constant. This upholds the suggestion that equation 4.1 provides an accurate prediction of the frequency separation of the resonance peaks. However, most importantly, it can be seen that the intercept of the least squares fit of this data set does not pass through zero but coincides with the LFF (~50MHz). This categorically demonstrates that the positions of the resonance peaks within the spectrum are subject to an offset which is equal to the LFF.

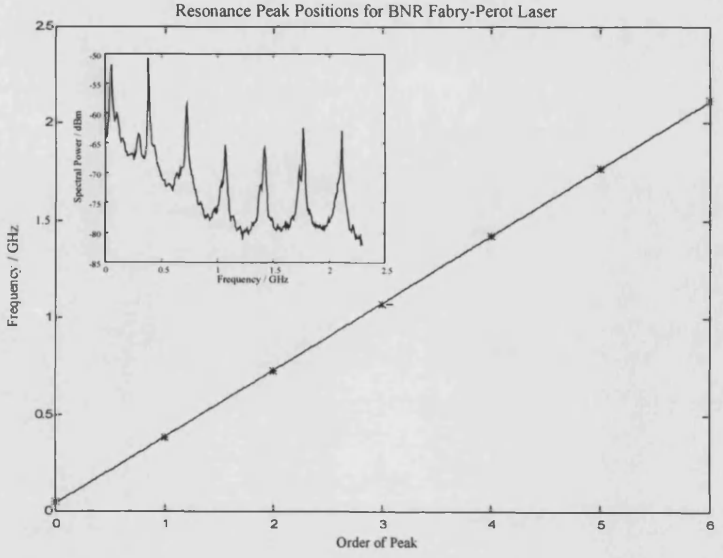

Figure 4.11. The frequencies at which the maxima of the resonance peaks occur for a BNR Fabry-Perot laser. *Inset:* The frequency spectrum from which the main graph has been derived. Note: The zeroth order peak denotes the low frequency fluctuation.

This provides an insight as to why there is a variation in the positions of the peaks as a function of other external parameters, since if the LFF is subject to a change then so are the frequencies of the resonance peaks. This is illustrated by figure 4.12, which shows the effect of a current induced offset variation. In this example, a change in the bias current applied to the BNR Fabry-Perot laser from 23mA to 30mA produces a shift in the frequency of the LFF of 35MHz. It can be seen that the shift in the LFF has caused the shift of the main resonance peaks. However, the slope of the response remains the same, indicating that the frequency separation remains unaltered.

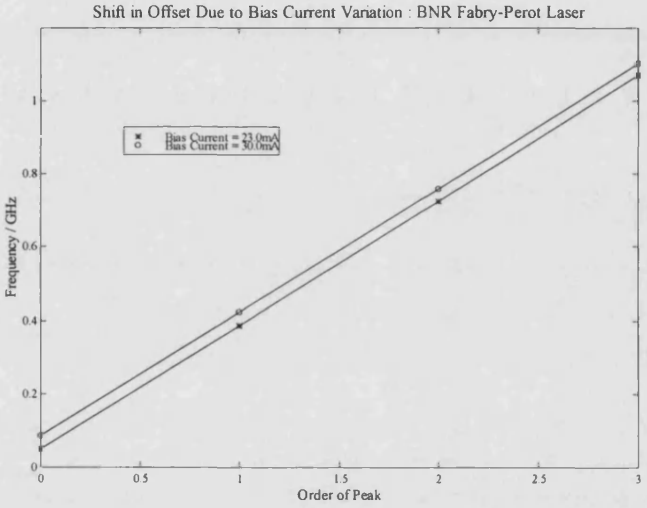

Figure 4.12. An illustration of the frequency shift produced by a variation in bias current to the BNR Fabry-Perot laser. Key: '*' Bias current = 23.0mA, 'o' Bias current =30.0mA.

Figure 4.13 provides further evidence for the support of this phenomenon. Here the existence of the LFF induced frequency shift from the simple inverse law is demonstrated with two other laser diodes. Figure 4.13.*a* shows the positions of the peaks generated by the VCSEL described earlier in this chapter. In this example, it was driven with a bias current of 8.8mA. A frequency offset of 30MHz can be seen to be present at the intercept of the 'order of peak' axis. Similarly, figure 4.13.*b* describes the frequencies of the resonance peaks generated by the SHARP LT026MD laser diode, the performance of which was described in chapter 2. In this case, a frequency offset of 46MHz was observed. As these three lasers of different

structure all exhibit the LFF peak which provides this offset, it can be seen that this phenomenon is not peculiar to a particular device. Moreover, the value of this offset is dependent upon the operating conditions of the device as discussed in the preceding sections of this chapter.

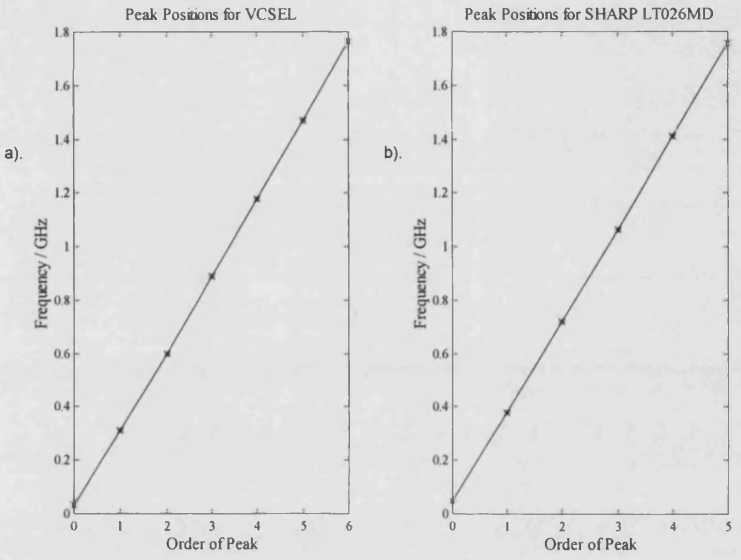

Figure 4.13. Evidence of LFF offset in the positions of the resonance peaks generated using a). HP VCSEL and b). SHARP LT026MD.

4.4.2. Anti-reflection (AR) coated devices

In contrast to the general operating conditions used to generate the results shown in figures 4.11 to 4.13, when a very high level of feedback is applied to the laser diode, the frequency of the LFF and the associated offset is greatly reduced. This is demonstrated in figure 4.14 which shows the positions of resonance peaks generated by an AR coated laser operated within the external cavity sensor arrangement. The low facet field reflectivity (r_2=0.1) produced by the AR coating allows a high level of feedback to be attained. It can be seen that this device produces a similar set of results to that of the uncoated Fabry-Perot laser shown in figure 4.11, save for one important difference. It can be seen that in this case, the least squares line fitting the positions of the peaks passes virtually through the origin. (Experimental measurement errors mean that in this case it actually passes through the origin at -0.6MHz). It can therefore be seen that while there is an increase in the characteristic 1/f noise distribution noticeable in figure 4.14, there is

effectively no LFF peak generated by this particular laser when operated within an external cavity arrangement. The inverse relationship of equation 4.1 therefore demonstrates a far better agreement when predicting the absolute peak frequencies for this example of high level feedback operation.

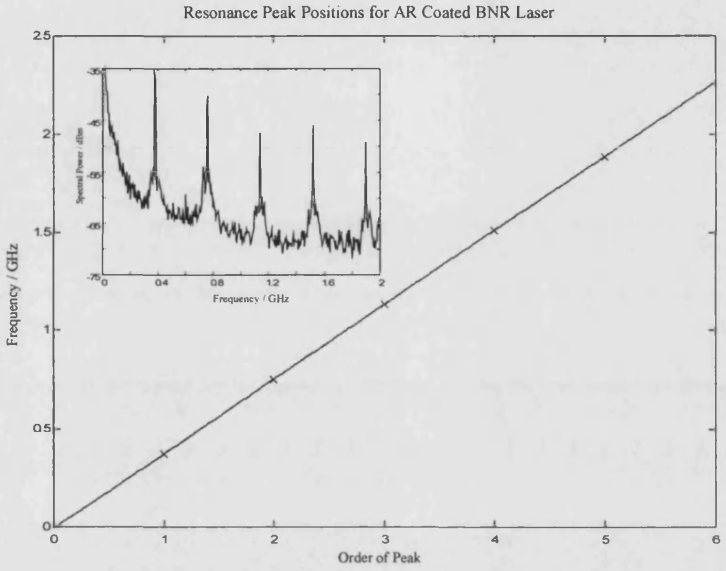

Figure 4.14. The frequencies at which the maxima of the resonance peaks occur for an AR coated laser. *Inset:* The frequency spectra from which the main graph was derived, (r_2=0.1).

This experimental observation may be consolidated theoretically by again considering the locus which describes the threshold gain of the external cavity modes as a function of frequency. Figure 4.15 illustrates the locus that is obtained when an AR coated Fabry-Perot laser is subject to delayed optical feedback. This simulated device is governed by the operating parameters given in table 3.1, save for its coated facet which has a power reflectivity of 0.5%. It can be seen from figure 4.15 that the previously elliptical locus before coating (inset) has become quite distorted.

In the uncoated case, there are a far greater number of XCMs on the upper portion of the locus which possess a reasonably high optical power in relation to the other XCMs in the distribution, than is the case for the AR coated laser. These 'upper' modes are interspersed in frequency with the modes on the lower sector of the locus. The 'lower' XCMs being spaced by a frequency close in value to the cavity round-trip frequency, f_c, as explained in chapter 3. Therefore, it can be seen

that for the uncoated case, there will be a higher occurrence of significant beat frequency components due to these high power upper XCMs mixing with 'lower' XCMs than would be the case for the AR coated laser. Consequently, in the uncoated case, a significant LFF results which is of comparable power to that of the 'conventional' resonance peaks, whereas in the AR coated case, the presence of the LFF is greatly reduced. Furthermore, in the distorted AR coated distribution, the separation of the 'lower' XCMs is on average far closer to f_c than is the case for the 'lower' XCMs in the corner of the ellipse of the uncoated distribution, therefore removing the effective offset on the frequencies of the resonance peaks in the beat signal.

Using the same methodology as used in chapter 3 to construct approximate theoretical predictions of the RF spectrum, the threshold gain information contained within figure 4.15 can be incorporated into a multimode rate equation model, to assess the equilibrium modal power distribution of the system. This distribution can then be used to assess the beat frequency products which constitute the characteristic RF output spectrum.

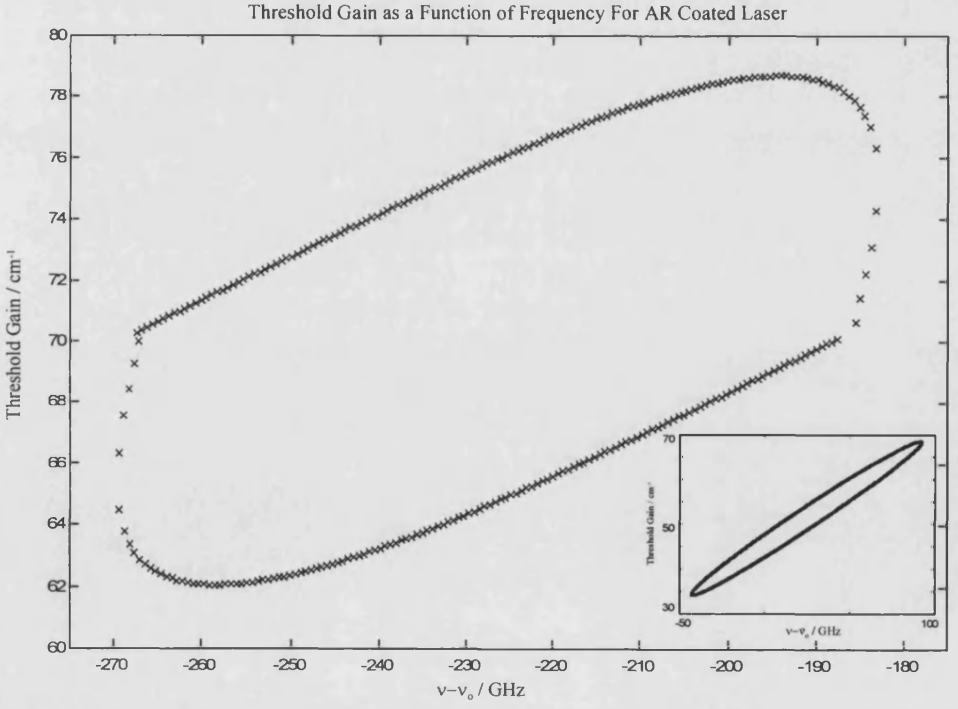

Figure 4.15. Locus defining the threshold gain of the theoretically allowed external cavity modes for an AR coated laser. R_2=0.005, R_3=0.1 and L_{ext} =0.25m. Inset: Ellipse locus obtained for same device without AR coating, (R_2=0.32).

A spectrum constructed in this way from the data of figure 4.15 is shown in figure 4.16. Here figures 4.16.*b* and 4.16.*d* denote theoretical predictions for spectra which may be obtained from the uncoated and AR coated devices respectively. Meanwhile, figures 4.16.*a* and 4.16.*c* illustrate the corresponding equilibrium modal power distributions. If the theoretically predicted spectra of figure 4.16 are compared, it can be seen that the presence of the low frequency fluctuation is indeed greatly reduced in the case of the AR coated laser. (Bearing in mind that the LFF shown in figure 4.16.*b* is likely to be enhanced by spontaneous effects). Therefore, agreement is reached with the experimental observations for the reduction of the LFF in lasers which have been AR coated.

Further credence may be given to the theoretical findings given in figures 4.15 and 4.16 if the extreme case of AR coating the device is considered. In this situation, the system reduces to a cavity of length (l+L_{ext}), with the front facet reflectivity, R_2 tending to zero. Therefore a cavity of length L_{TOT} exists which has only a short gain section operating within a mainly passive resonator. This cavity will have allowed modes given by,

$$f_m = \frac{mc}{2L_{TOT}}, \text{ where } L_{TOT} = l + L_{ext} \approx L_{ext}, \qquad (4.2)$$

which is simply the expression of equation 4.1.

It can be seen that lasers operating in the high feedback regime [13,14] are far less prone to the existence of a LFF as illustrated by figure 4.14. It is therefore possible that, in many cases, an AR coated laser can provide an enhanced operational stability when compared to alternative, otherwise excellent devices. As the LFF is greatly reduced in frequency and influence, it is likely that the output signals generated by an optical system based on such a device will be far more tolerant to variations in key operating parameters.

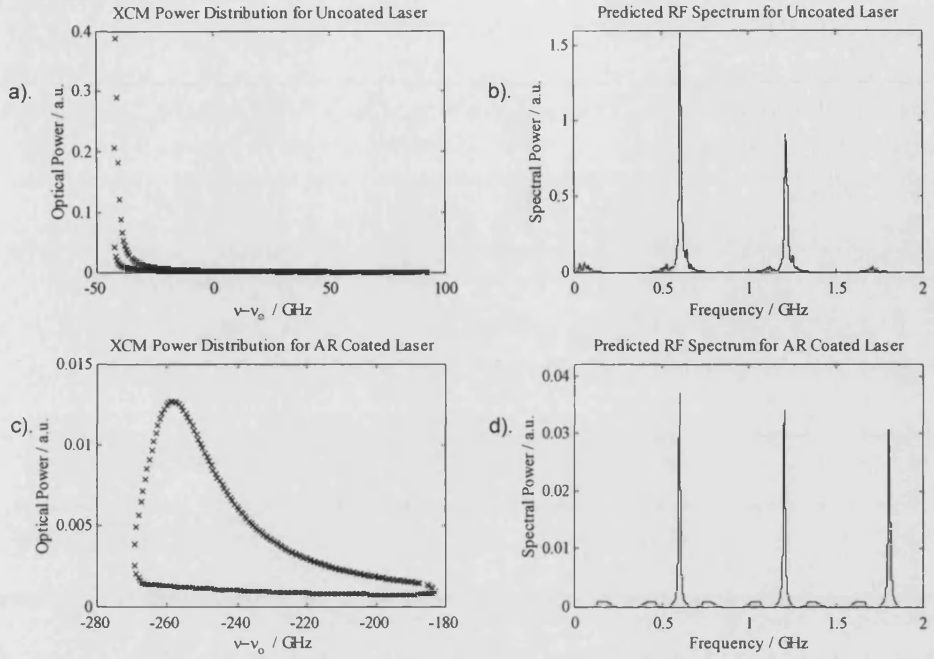

Figure 4.16. Reduction of LFF fluctuation by AR coating device. Operational parameters are as given in figure 4.15. a). XCM power distribution for uncoated laser, b). Predicted output spectrum for uncoated device c). XCM power distribution for AR coated laser, d). Predicted output spectrum for AR coated device.

Finally, in summary, it can be seen that the LFF provides a distinct shift in frequency of the complete set of resonance peaks. However, it is found that the separation if these peaks is generally unaffected by the frequency of the LFF. Therefore, dynamic changes in the value of the LFF caused by physical influences such as bias current and optical attenuation within the external cavity will provide dynamic changes in the absolute values of the peaks but not their separation. Considering this, it is recommended that for enhanced stability, the separation between the resonance peaks be measured rather than the absolute position of a single peak. Use of an AR coated laser may provide a more stable operation.

4.5. Conclusions

Within this chapter, a detailed analysis of the experimental performance of the resonant cavity optical position sensor has been carried out. This has included analysis of the stability of the optical system output as a function of several key parameters. These included the effects of operational variation of bias current,

optical feedback strength and device temperature. It was found that changes in these dynamic variables caused shifts in the frequencies of the resonance peaks. However, the effect of these shifts could be minimised by measuring the frequency separation of the peaks and not the absolute positions of the peaks within the spectra. Typically, even for extreme changes in bias current, this measurement technique allowed any variation in output to remain less than 0.1% of the reading value. A slightly larger figure of <0.5% was obtained for variations in feedback strength of up to 8dB, although this may be due in part to variations in alignment. Furthermore, while investigations carried out into the temperature dependency of the system showed a distinct frequency change as a function of temperature, it appears as though this was at least in part due to variations in alignment caused by expansion of the brass laser submount. Therefore further studies are recommended to assess the true affect of a device temperature variation on the frequencies of the resonance peaks. However, in practice it should be realised that for most general applications, any temperature variation effect can be avoided by actively controlling the device temperature, if required.

Furthermore, detailed experimental analysis of the frequency spectra produced by the sensor showed that for uncoated or as-cleaved semiconductor lasers, there was a discrepancy between the measured frequencies of the resonance peaks and the predictions given by the simple, inverse relationship of equation 4.1. It has been confirmed that this expression provides only an approximate prediction of these peaks as they are subject to an offset, this offset being a function of external cavity length. However, it was found that measurement of the frequency separation provides an output which is much closer to the simple inverse law.

All the effects listed above were found to be linked with the behaviour of the low frequency fluctuation (LFF) present in the frequency spectrum. It is this LFF which provides the frequency offset on the position of the modes. Correspondingly, dynamic changes in operational parameters cause a shift in the LFF and consequently in the frequencies of all the resonance peaks. As it is a simple shift in frequency which is occurring and not a harmonic change, it can be concluded that a

measurement of the frequency separation of the peaks provides an output which is not only closer to the inverse law of equation 4.1, but also more insensitive to laser conditions than a single peak measurement.

Finally, as the LFF appears to have such a dramatic effect upon the performance of the system, it would be advantageous to remove it. It has been shown by experimental and theoretical arguments that AR coated lasers are subject to an LFF which is greatly reduced in frequency, to the extent that a zero offset can be obtained. Therefore, for future work, it is likely that the optimum device for use in the sensor will be an AR coated laser, providing that it satisfies all the relevant operating criteria set out in chapter 2.

4.6. References

[1] C.Mignosi, "Report of research work carried out into free-space optical position sensors", *Internal report*, University of Bristol, July 1997.

[2] I.Fischer, G.H.M. van Tartwijk, A.M.Levine, W.Elsässer, E.Göbel and D.Lenstra, "Fast pulsing and chaotic itinerancy with a drift in the coherence collapse of semiconductor lasers", *Phys. Rev. Lett.*, **76**, No.2, pp.220-223, 1996.

[3] M.-W.Pan, B.-P.Shi and G.R.Gray, "Semiconductor laser dynamics subject to strong optical feedback", *Opt. Lett.*, **22**, No.3, pp.166-168, 1997.

[4] R.O.Miles, A.Dandridge, A.B.Tveten, T.G.Giallorenzi and H.F.Talyor, "Low-frequency noise characteristics of channel substrate planar GaAlAs laser diodes", *Appl. Phys. Lett.*, **38**, pp.848-850, 1981.

[5] J.W.Biesterbos, A.J.Den Boef, W.Linders and G.A.Acket, "Low frequency mode-hopping optical noise in AlGaAs channelled substrate lasers induced by optical feedback", *IEEE J. Quantum Electron.*, **QE-19**, No6, pp.986-990, 1983.

[6] J.Mørk, B.Tromborg and P.L.Christiansen, "Bistability and low frequency fluctuations in semiconductor lasers with optical feedback: A theoretical analysis", *IEEE J. Quantum Electron.*, **24**, No.2, pp.123-133, 1988.

[7] J.D.Park, D.S.Seo, and J.G.McInerney, "Self pulsations in strongly asymmetric external semiconductor lasers", *IEEE J. Quantum Electron.*, **26**, pp.1353-1361, 1990.

[8] M.Fujiwara, K.Kubota and R.Lang, "Low frequency intensity fluctuation in laser diodes with external optical feedback", *Appl. Phys. Lett.*, **38**, No.4, pp.217-220, 1981.

[9] B.Meziane, P.Besnard and, G.M.Stéphan, "Low-frequency resonances in asymmetric external cavity semiconductor lasers : Theory and experiment", *IEEE J. Quantum Electron.*, **31**, No.4, pp.617-622, 1995.

[10] C.H.Henry & R.F.Kazarinov, " Instability of semiconductor lasers due to optical feedback from distant reflectors", *IEEE J. Quantum. Electron.*, **QE-22**, No.2, pp.294-301, 1986.

[11] H.Temkin, N.A.Olsson, J.H.Abeles, R.A.Logan and M.B.Panish, "Reflection Noise in Index-Guided InGaAsP Lasers", *IEEE J. Quantum Electron*, **QE-22**, No.2, pp.286-293, 1986.

[12] T.Morikawa, Y.Mitsuhashi, J.Shimada and Y.Kojima, "Return-beam-induced oscillations in self-coupled semiconductor lasers", *Electron. Lett.*, **12**, No.17, pp.435-436, 1976.

[13] R.W.Tkach and A.R.Chaplyvy, "Regimes of feedback effects in 1.5 m distributed feedback lasers", *J. Lightwave Technol.*, **LT-4**, No.11, pp.1655-161, 1986

[14] N.Schunk and K.Petermann, "Minimum bit rate of DPSK transmission for semiconductor laser with a long external cavity and strong linewidth reduction", *J. Lightwave Technol.*, vol. **LT-5**, No.9, pp.13-09-1314, 1987.

CHAPTER 5

PRACTICAL INTERFACING SCHEMES FOR USE WITH THE RESONANT CAVITY OPTICAL POSITION SENSOR

This chapter describes the electronic systems used for interfacing with the resonant cavity optical position sensor. These arrangements decode the position information which is held within the complex RF beat frequency signals generated by the semiconductor laser diode. Schemes which have been used include RF swept source downconverter, slope detection systems and application specific frequency measurements. Details of the design and construction of these systems are given, along with evidence of their satisfactory operation. In addition, results are presented which detail the stability performance of one of these systems in long term testing.

5.1. Introduction

In general, most optical sensors require a degree of associated electrical signal processing. This is required in order to communicate with controlling systems as well as conditioning the raw optical signal in which the measurement data may be encoded. For example, simple intrinsic fibre-optic displacement sensors based upon changes in transmitted optical intensity modulation [1] and reflected intensity changes [2-4] require a low level of signal processing. However, more sophisticated methods of displacement / position measurement such as code-plate sensors [5], interferometry [6-8] and frequency modulated continuous wave ranging (FMCW) [9] require far more complex signal conditioning systems. Like these systems, the resonant cavity optical position sensor described in the preceding chapters also requires a degree of signal processing.

The resonant cavity sensor can be used to determine the absolute position of an optical target. This measurement may be carried out manually in an off-line arrangement, using a RF spectrum analyser to ascertain the exact frequencies of beat notes generated in the laser junction voltage. However, in order to develop a

practical system which can provide on-line, real-time measurements, some means must be found of translating the information held in the frequency spectrum of the output signal, into a suitable form to allow conventional signal processing to be carried out. The output of the sensor must also be stable, reliable and repeatable, otherwise, it is of no practical use. Furthermore, for the sensor to be successful, it is important that the unit price is attractive. Therefore any signal processing system used in conjunction with the optical sensor must be cost-effective as well as operationally sound.

With these factors in mind, several methods of interfacing with the optical sensor and conditioning its output signal were examined. Using these techniques, several prototype systems were constructed. The operation and performance of these systems are described in the following sections.

5.2. RF Downconversion system

Although off-line, experimental analysis of the output of the optical sensor system can be carried out using a RF spectrum analyser, practical, real-time, on-line interfacing can be achieved using a similar system, this on-line arrangement being based upon the operation of a swept oscillator downconversion unit. This system works in an analogous way to a swept source spectrum analyser in that it provides an output signal which is a temporal representation of the frequency spectrum of the input signal [10], as illustrated in figure 5.1.

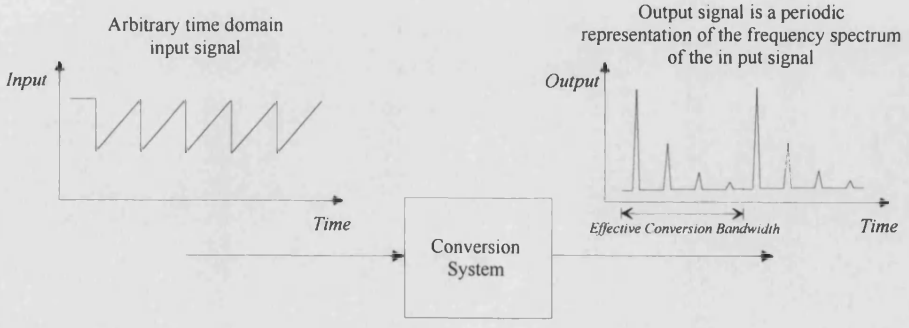

Figure 5.1. Schematic representation of functional operation of a time domain to frequency domain conversion system. It can be seen that the arbitrary input signal (shown in the simple example above as a sawtooth signal) has been converted so that the output signal is a genuine, periodic, time domain representation of the frequency spectrum of the input signal. Therefore, the time axis of the output signal can be directly calibrated as '*frequency*'.

If the amplified output from the external cavity optical position sensor were fed into the 'black-box' module depicted in figure 5.1, the output produced would be similar in form to that shown in figure 5.2 - i.e. it would consist of a periodic representation of the resonance peaks present in the frequency spectrum of the input signal. Considering the nature of this output waveform, it can be easily converted into a periodic digital pulse train using threshold detection. A simple measurement of the time delay between these digital pulses can then be used to determine the frequency separation of the resonance peaks (if the sweep rate is known or calibrated). For example, if the limits of the input bandwidth are given by f_{max} and f_{min} respectively, and the time delay of the first two resonance peaks within the bandwidth is given by T_{FS}, then the frequency separation of these peaks is given by,

$$\Delta f_{FS} = \frac{T_{FS}}{T_{SWEEP}} \cdot (f_{\max} - f_{\min}), \qquad (5.1)$$

where T_{sweep} is the periodic sweep time of the system. Consequently the absolute position of the optical target can be determined. Figure 5.3 indicates in block diagram form how the RF downconversion module would be implemented into a complete sensor system.

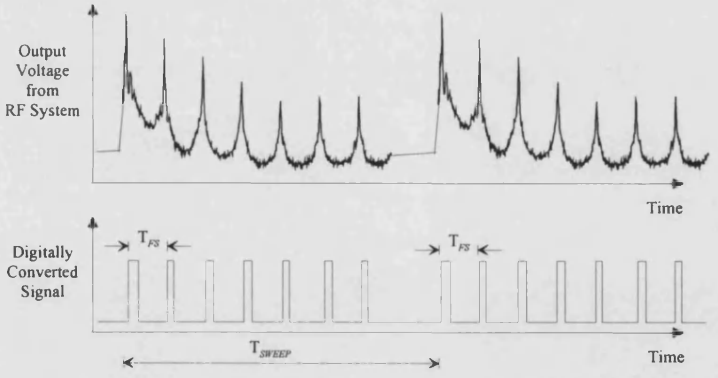

Figure 5.2. Representation of the downconverter module output signal and its subsequent conversion to a digital pulse train. Measurement of the pulse separation allows determination of the absolute position of the optical target.

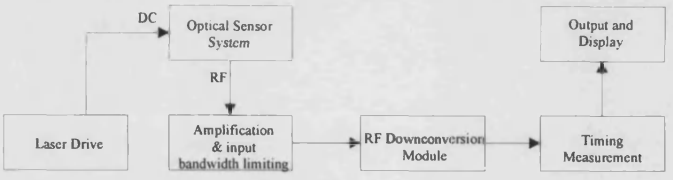

Figure 5.3. Block diagram indicating the implementation of a RF downconversion module within a complete sensor arrangement.

5.2.1. Dual Heterodyne downconversion

A suitable arrangement for performing this frequency domain to time domain conversion of the output of the optical sensor is presented in figure 5.5. This arrangement consists of a double heterodyne downconversion system of the type commonly used to construct RF swept source spectrum analyser systems [11,12]. The progress of the input signal through the system may be described in the following way.

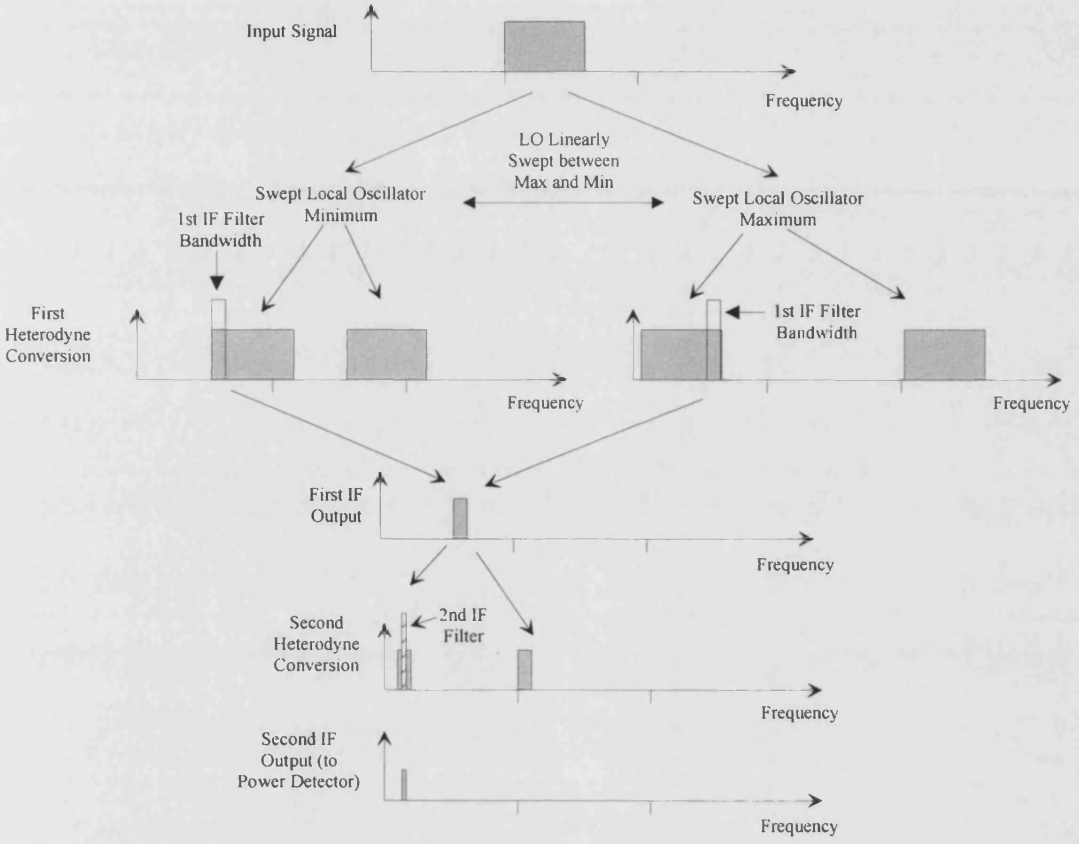

Figure 5.4. Schematic illustration of the frequency conversions which occur during dual heterodyne downconversion process.

The RF input signal consisting of the amplified output from the optical sensor passes through an image reject filter which limits the input signal bandwidth. This bandwidth limited signal is then mixed with the first local oscillator whose frequency is periodically swept according to the tuning signal from the sweep drive controller as shown in figure 5.4. The sweep range is chosen so that all the frequencies within the input bandwidth are successively downconverted to a first

intermediate frequency (IF) at some point during the local oscillator frequency sweep cycle. The signal at this intermediate frequency is then bandpass filtered to remove all other frequency components and image signals prior to undergoing a second downconversion. This second downconversion allows the first IF to be shifted to a lower frequency (second IF). This second IF is also bandpass filtered by a filter possessing a much narrower passband. It is the bandwidth of this filter which dictates the resolution bandwidth of the complete system. A simple RF power measurement of the output signal of this bandpass filter provides the temporal output which is representative of the frequency spectrum of the input signal.

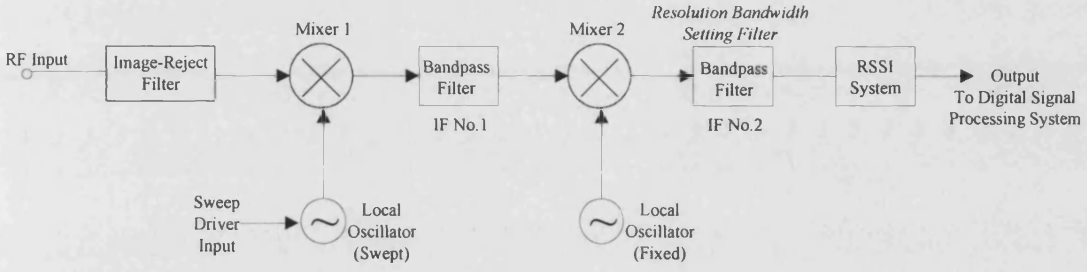

Figure 5.5. Schematic representation of a RF downconverter system utilising a double heterodyne conversion.

Such a system can be constructed as shown in figure 5.5 in a very cost effective manner, by taking advantage of advances in mobile communications and mass market technologies. Use of common low cost chip-sets primarily designed for mobile communication systems allows the construction of a high-performance, yet low-cost unit.

5.2.2. Specification of transducer stand-off distance

In order to test the suitability of this interfacing technique, a prototype system was constructed which was designed to measure variations in the external cavity length of 1m. Ideally, it is advantageous to minimise the physical size of the optical transducer required. However, as the frequencies of the resonance peaks are governed by an inverse relationship, a reduction in the minimum allowed external cavity length leads to an increasingly large frequency separation which is required to be monitored. As all electronics systems are inevitably subject to a finite bandwidth, a minimum cavity length requirement, (or stand-off distance) has to be specified in

the design which in turn places a limitation on the minimum physical size of the transducer used. If this stand-off is limited to 25cm which is a practical value for a transducer with a 1m stroke length, a separation of ~600MHz would be obtained. Consequently, the required bandwidth of the downconversion system is well in excess of 600MHz, since at least two resonance peaks are required to be present at any one time within the input bandwidth to provide a valid timing measurement.

5.2.3. Choice of Input Bandwidth

In order to minimise the required stand-off distance and to provide an image free downconversion to a suitable first IF, it was decided to limit the RF input frequency range to 900-1900MHz. This was achieved by filtering the input signal from the optical system prior to it entering the conversion system as illustrated in figure 5.3. Use of this particular operating bandwidth allows a continuous range of operation for external cavity lengths greater than 25 cm, up to a maximum which is dictated only by optical and digital signal processing requirements. Effectively, the maximum operational external cavity length is limited by divergence of the optical beam in the transducer and the resolution bandwidth of the downconversion system.

The suitability of this 900-1900MHz input bandwidth range for this application can be assessed by examining figure 5.6. This figure depicts schematically the frequencies of the resonance peaks as a function of external cavity length.

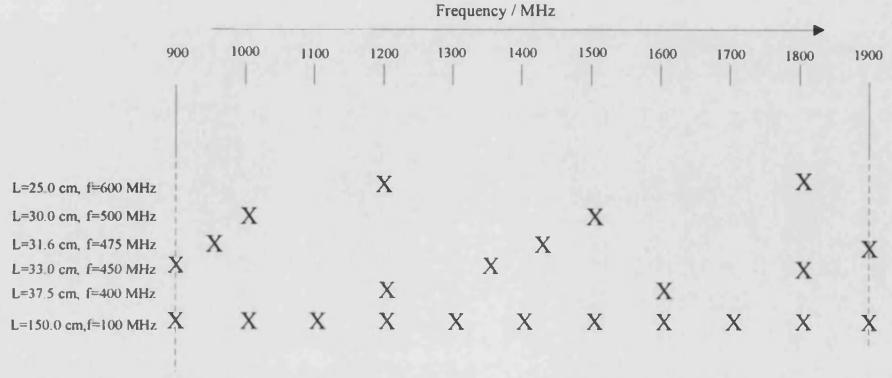

Figure 5.6. Schematic representation of resonance peak frequencies within the downconverter input bandwidth. Positions of the resonance peaks within the bandwidth are denoted by 'X' with the approximate resonance peak frequency separation given by '*f*'.

It can be seen that for cavity lengths greater than 25cm, there are always at least two resonance peaks present within the input bandwidth. It can also be seen from figure 5.6 that as the external cavity is gradually increased, the lowest order resonance peak will eventually leave the bandwidth. However, before it does so, a higher order replacement peak will enter at the other extreme of the passband.

In order to carry out the timing measurement of peak separation, care must be taken in the case where the lowest order resonance peak is about to exit the bandwidth. If this first peak exists at the very beginning of the bandwidth, then it is possible that as the external cavity length increases, the position of the first digital pulse identified by threshold detection may remain static at the edge of the bandwidth, instead of completely exiting the bandwidth. However, error free decoding may be achieved by measuring the frequency separation of the first pulse with respect to the front of the bandwidth. If this was less than a specified value, then the first peak would be ignored for measurement purposes, and the second and third order peaks used to measure peak separation and hence the optical target position.

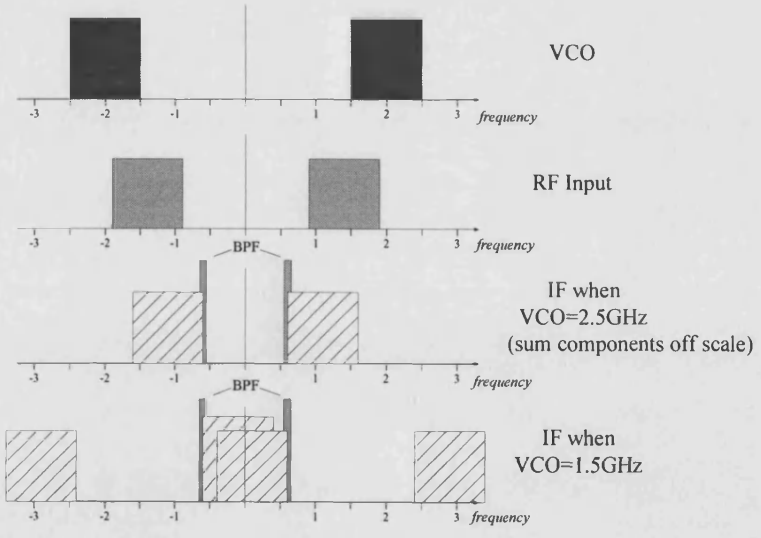

Figure 5.7. Schematic demonstration of the image-free first downconversion stage with input bandwidth range of 0.9-1.9GHz and local oscillator range of 1.5-2.5GHz. (BPF denotes the bandpass filter frequency response).

As the choice of input bandwidth described above covers a 1GHz tuning range then accordingly a local oscillator with a tuning range of 1GHz is required. A convenient voltage controlled oscillator (VCO) which can provide this tuning range

is the Hewlett-Packard (Avantek) VTO-8150, the output frequency of which may be swept from 1.5-2.5GHz. When used in conjunction with the chosen input bandwidth, the VCO provides an image-free first downconversion to a first IF of 600MHz. This is shown in figure 5.7, which illustrates that as the frequency of the local oscillator is swept between the two extremes of operation, no overlap of the downshifted input bandwidth into the negative component of the first IF passband occurs. In addition the 'sum' components of the downconversion process are not coupled into the output of the first downconversion stage (the 'difference' components of each mixing stage being used for the downconversion). The choice of 600MHz as the first IF allows the use of commercial high-quality, low-cost bandpass filters which are readily available (e.g. Toko 252HA-1559F).

5.2.4. RF System Design

A variety of suitable, low-cost active mixers are available for use over the frequency of operation specified above. For example the Hewlett-Packard IAM-81008 active mixer has a RF and local oscillator (LO) input frequency range of 50MHz to 5GHz and an IF gain bandwidth from DC to 1GHz (8dB typ.), whilst having excellent LO and RF feedthrough attenuation. This low-cost device provides good performance while not requiring a high power local oscillator, which is desirable for reasons of EMC compatibility.

One important point to note, however, is that since the tuning characteristics of the first local oscillator VCO (HP VTO-8150) are non-linear, if it is swept by applying a linear ramp signal to the tuning port, it will correspondingly produce a non-linear frequency sweep. To obtain stable measurement results, particularly when the resonance peaks leave the front of the passband, this non-linearity should ideally be removed from the system. This may be carried out by means of prior linearisation of the sweep by digital or analogue techniques or by post-calibration of the system output. However, if post-calibration is to be used, the inherent non-linearity of the sweep must be small enough so that no discontinuous jumps occur in the timing measurement when peaks move out of (or into) the front of the sweep passband [13].

The second downconversion may be carried out using a stabilised VCO, crystal oscillator, or frequency synthesiser as a fixed local oscillator. This would convert the 600MHz first IF signal down to a convenient second IF such as 83MHz, for which commercial bandpass filters are again available. (Proper first IF filtering, should preclude the presence of any images in this second downconversion).

The final stage of the system requires measurement of the RF power output of the second IF bandpass filter. Typically such a power measurement may be carried out using a received signal strength indicator system (RSSI), or by a simple Schottky power detector diode. Commercial integrated circuits are now commonly available which include a *RSSI* function on-chip such as the Philips NE/SA626 or similar systems. These devices are generally developed for use in radio applications although they may be readily applied to this type of use. They are often of multi-functional design, with most providing a temperature compensated logarithmic output signal. However, these systems are generally limited in input bandwidth and may typically be used for input signal frequencies of up to 50MHz. Accordingly, they are not ideally suited for use if a second IF of 83MHz is used. In this case the simplest solution is to use a Schottky detector diode which provides a stable output signal which is a function of the input RF power. Extra RF amplification may be required prior to the detector diode in order to raise the input power well above the tangential sensitivity level [14] of the detector diode.

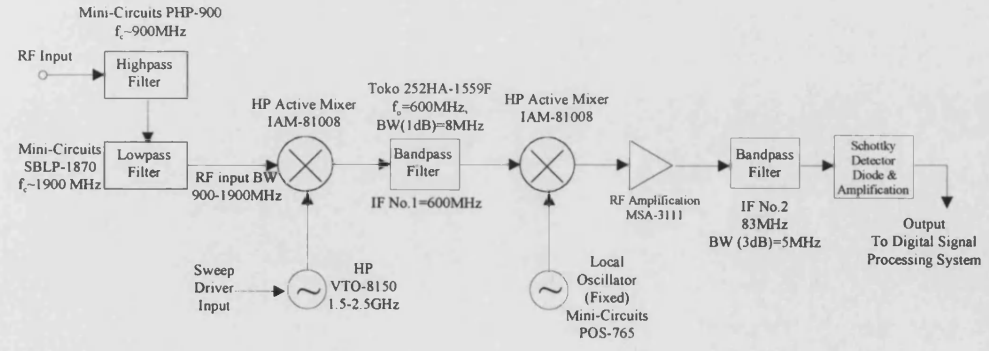

Figure 5.8. Proposed downconverter system with suggested components.

Following the arguments discussed above, a RF downconversion system was designed which is illustrated in figure 5.8. Pre-amplification of the input signal was carried out using two INA-51063 monolithic microwave integrated circuit (MMIC)

amplifiers, each providing 20dB of gain over a bandwidth reaching to 2.4GHz. Any signal attenuation which was required (for example to reduce the signal level of the VCOs to the optimum level for use with the active mixers selected) was carried out using low-cost surface mount attenuator chips (Mini-Circuits). Throughout the design and construction of the system, proper RF fabrication and circuit layout techniques were used in order to achieve optimum system performance.

5.2.5. Linearisation of VCO sweep using digital synthesis

As previously mentioned, the particular VCO used as a swept local oscillator in the first downconversion stage of the RF module possesses a frequency/voltage tuning curve which is non-linear. This non-linearity in the tuning characteristic (as illustrated in figure 5.9), correspondingly leads to a non-linear frequency sweep. One method of linearising the frequency sweep is to apply a periodic, non-linear ramp signal which is the inverse of the tuning characteristic shown in figure 5.9, to the VCO tuning port. The consequence of any deviation from this non-linear ramp function is a reduction in sweep linearity and in extreme cases of deviation, the occurrence of discontinuous jumps in the sensor output when the resonance peaks exit and enter the front of the system passband.

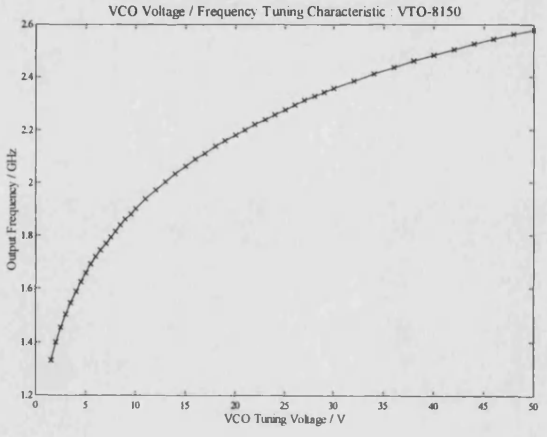

Figure 5.9. An example of the measured voltage/frequency tuning characteristic exhibited by a VTO-8150 voltage controlled oscillator.

In practice, the required non-linear tuning signal was digitally synthesised using the configuration outlined in figure 5.10. Prior analysis of the tuning waveform

allowed a series of polynomial coefficients to be obtained which were used to generate a calibrated data set characterising the required tuning curve. A clock signal was applied to a CMOS counter to generate a digital address signal. The address signal was used to access the calibrated data stored within two 32k x 8 bit EPROMs which provided an output signal of 16 bit resolution. A D/A converter was then used to convert to an analogue signal, with final amplification and filtering used to produce the exact waveform required. The design of this system allowed a variety of waveform ranges and forms to be selected using a DIP switch array, which allowed different frequency scan ranges to be selected, as required.

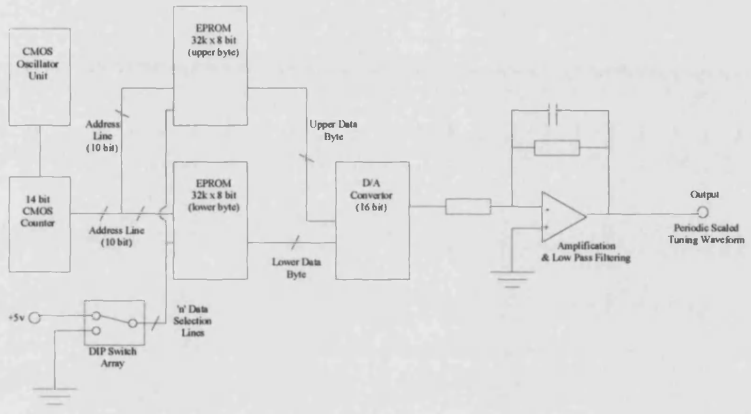

Figure 5.10. Schematic representation of digital waveform synthesis module.

This frequency sweep control system has been found to work extremely well, allowing a typical sweep linearity much better than 0.5% to be attained. This should prove to be of sufficient quality for satisfactory system operation. At present, the sweep rate of the system is limited by the slew rate of the high voltage amplifier used to raise the tuning waveform voltage up to the level required by the VCO. To avoid distortion of the carefully synthesised waveform, the sweep rate of the VCO drive waveform must be restricted to 1kHz.

Consequently, it can be seen that the measurement rate of this technique is, in practice limited by the performance of available components. Should a particular application require a much faster measurement response or operating bandwidth, then an alternative means of signal processing would be required, such as the slope-detection method, which is discussed in section 5.3. However, it is hoped that further

development work will allow an increase in the maximum permissible sweep rate attainable.

5.2.6. Performance of Swept Oscillator Downconversion System

The performance of the prototype RF downconversion system which has been constructed may be assessed by viewing figure 5.11. This shows the frequency spectra obtained from the optical sensor system at two different external cavity lengths, measured using both a commercial spectrum analyser (HP8593A) and the prototype RF downconversion system. In this figure the two upper graphs show the frequency spectrum measured using the commercial spectrum analyser, while the lower graphs have been measured using the RF system described above.

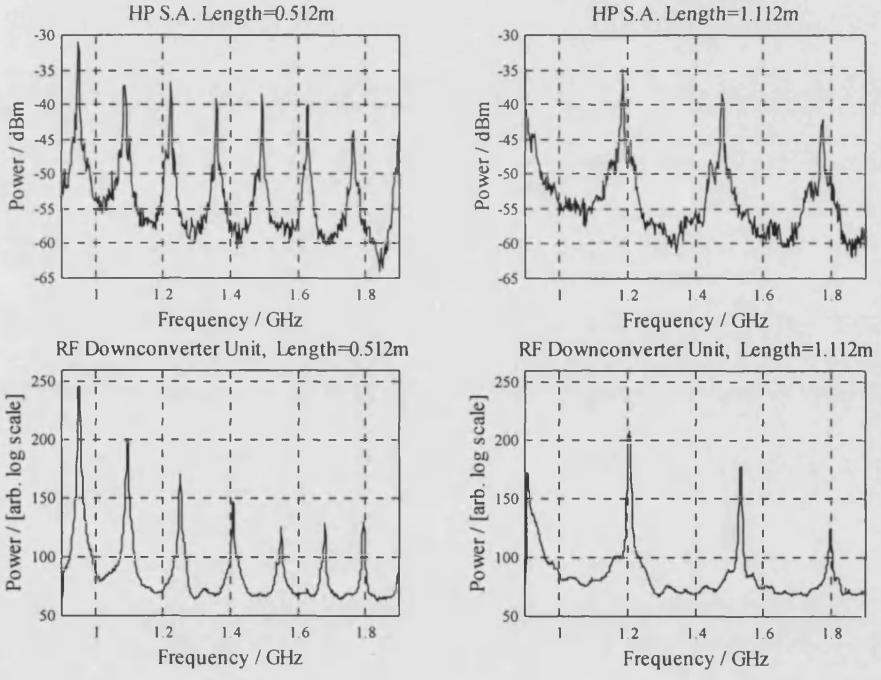

Figure 5.11. Comparison of frequency spectra measured using a commercial spectrum analyser and prototype RF downconversion unit.

It can be seen that the purpose built system performs very well in comparison with the extremely expensive commercial RF spectrum analyser. The majority of features which can be seen in the spectra measured with the spectrum analyser, are present in the spectra produced by the prototype module. For example, the spectra

obtained at both cavity length examples, contain the same number of resonance peaks, occurring at approximately the same frequencies. The slight non-linearities produced by the prototype system which can be seen are due to an uncorrected non-linear frequency sweep. In the example of figure 5.11 an early analogue equalisation system for sweep compensation was used, which provided only moderate improvements in linearity. Subsequent implementation of the digital synthesis technique described in section 5.2.5. provided a very large comparative improvement in sweep linearity.

The x-axis scaling applied to the data generated by the downconverter module is obtained by simply scaling the output data according to the extremes of operation, namely 900 and 1900MHz. The resonance peaks appear to be of the same form in both measurement techniques with the characteristic central peak superimposed upon a wider base with an approximate 1/f dependency present. It is evident that the spectra obtained using the prototype downconverter module do not possess as large a dynamic range as that produced by the commercial unit, with a higher measurement system noise floor obscuring the complete depth of the signal. However, recent improvements have allowed a dynamic signal range of greater than 35dB to be obtained. This is ample for successful digital threshold conversion to a pulse train.

From the example of figure 5.11, it can be seen that the RF module performs well enough to be used to decode the signal produced by the external cavity optical position sensor. In fact, initial system results have produced a measurement accuracy of approaching 0.1% using this prototype RF module. However, this means of processing the output data is, at the time of writing, being continually improved in order to enhance the performance level. This method of decoding is particularly suited to medium to long range measurements, where cavity lengths are greater than 25cm, because of bandwidth limitations and the required stand-off distance. However, the resolution bandwidth can be tailored in order to produce a high resolution system, at only moderate cost. The timing measurement also produces an attractive digital output signal.

5.3. Slope Detection Decoding using Electrical Filters

Slope detection or edge detection has been recently applied to the measurement of optical component performance for high speed transmission systems [15]. However, it is most commonly found in electrical communications as a method for the demodulation of frequency modulated (FM) signals. It is one of the most simple methods available for performing this task. Detailed descriptions of this technique when applied to FM demodulation can be found in a variety of texts (for example see [16]). However, a brief description is provided in the following section.

5.3.1. Background to slope detection

If a constant amplitude signal is passed through a low pass filter, and is swept in frequency over a range above its low frequency cut-off point, the roll-off of the filter frequency response causes the amplitude of the signal to decrease. Therefore a simple low-pass filter has the capability of causing a translation of a frequency variation into an amplitude variation. Consequently, in order to demodulate FM signals, a *discriminator* is required, which can perform frequency to amplitude conversion linearly, so that an amplitude modulated (AM) signal results. This AM signal itself can subsequently be easily demodulated using envelope detection. The use of a discriminator to perform this transformation is illustrated in figure 5.12.

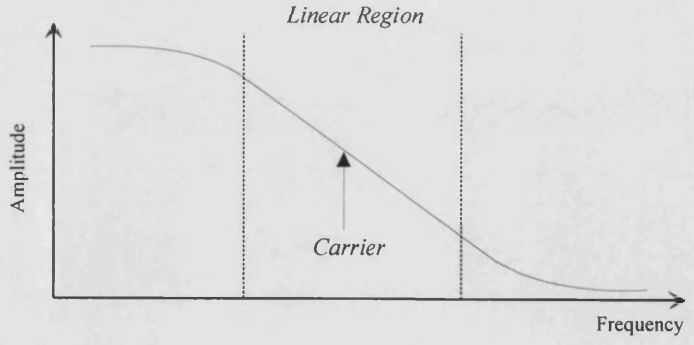

Figure 5.12. FM to AM conversion using a linear discriminator.

Considering this simple approach to FM to AM conversion, it can be seen that this technique may be suitable for identifying the frequencies of the resonance peaks generated by the external cavity position sensor.

5.3.2. Application of slope detection to interfacing with the optical sensor

The method of slope detection may be applied to the optical sensor in the manner shown in figure 5.13. The RF output component of the junction voltage variation is amplified and fed into a power splitter. This allows a multiple channel detection system to be used, if required, to cover a wider frequency range and hence position range or even multiple peaks. Each channel monitors a particular region of frequency space, and isolates a single resonance peak within it by using a bandpass filter. The cut-off frequencies of the bandpass filters used are chosen so that only a single mode may be present within the bandwidth of the filter at any time. Due to the nature of the input signal this criterion limits the frequency range of the lowest channel to an octave, with all other channels having equal frequency range. The particular frequency range chosen is determined by the physical characteristics of the sensor such as maximum external cavity length and working range, which in turn dictates the range of frequency separations experienced by the sensor.

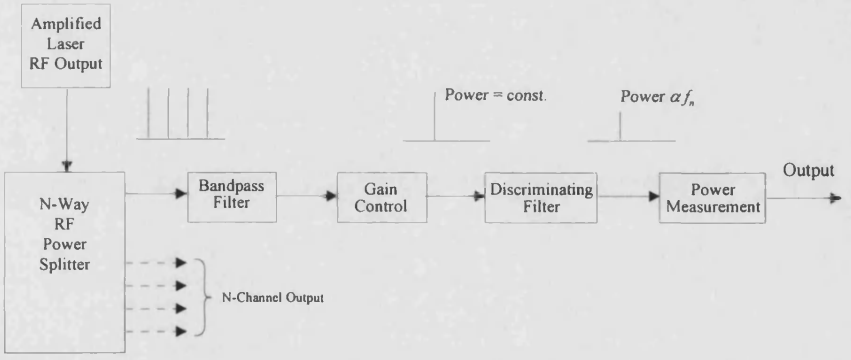

Figure 5.13. A multi-channel approach for applying the edge-detection filter decoding technique to the optical sensor.

This bandpass filter is followed by a suitable discriminator in order to convert any frequency variation of the resonance peak into an amplitude variation. The discriminator may take the form of a simple high or low pass filter whose transition region coincides with the passband of the bandpass filter, as shown in figure 5.14. Finally, measurement of the RF power output from the discriminator filter provides a voltage output which is dependent upon the frequency of the

resonance peak within that channel, and hence the absolute position of the optical target.

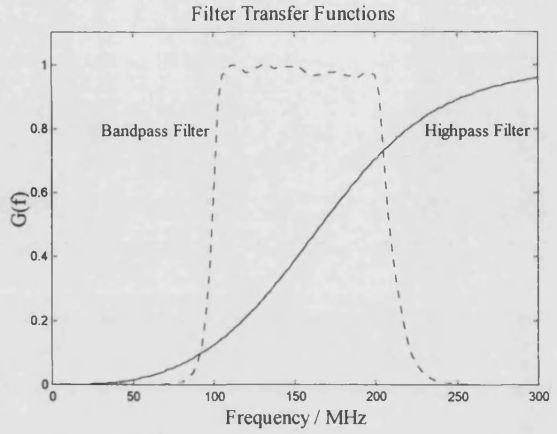

Figure 5.14. An example of the use of a high pass filter as a discriminator, and its frequency response when compared with the bandpass filter used for peak separation.

It is important that the input signal to the discriminator filter remains at a constant level. Otherwise, any variation in the input power level would lead to a error in the perceived frequency measurement. An automatic gain control system is therefore included in the signal chain in order to maintain a constant power level prior to the input of the discriminator filter.

It should be noted that use of an edge detection filter system similar to that described by figure 5.13 will provide an output which will be in the form of a simple analogue voltage. In order to maintain absolute position sensing over a particular range, this output voltage will have to be single valued over the operating range of the sensor. However, if the output is single valued, calibration of the system allows the absolute position of the optical target to be determined in real time.

5.4. Stability testing of optical sensor system using filter interfacing technique

The edge-detection signal processing system described above was used to test the stability of the optical sensor over a long time scale. The sensor to be tested was constructed on the optical bench from discrete components. Since each optical component is individually mounted with respect to one another, it would be expected that any prototype system tested in a similar way would possess a more

stable output signal over long time scales as it would be less likely to suffer from drift in the relative position of the optical components. However, such a test, even on a system based on individually mounted components can provide a good prediction of the future performance of a fully assembled system.

5.4.1. Experimental Arrangement

The experimental arrangement used to construct the optical system is shown in figure 5.15 and consisted of a folded cavity configuration. This allowed a convenient cavity to be constructed in the laboratory, so that the range of cavity lengths required that the fundamental resonance peak was always present within the bandwidth of an available filter. This bandpass filter had a passband ranging from 100 to 200 MHz, allowing the use of external cavity lengths ranging from 0.75m to 1.5m. The retroreflector used as the optical target was mounted upon a computer controlled mechanical translation stage. The maximum range of movement of this stage was 30cm, allowing for a change in cavity length of 60cm. The laser used was the HP VCSEL, the performance of which was described in chapter 2. This was driven with a constant bias current of 9.50mA by a precision, low-noise current source (ILX Lightwave LDX-3620) and maintained at a constant temperature of 22.6°C through the use of a temperature controller (ILX Lightwave LDT-5910).

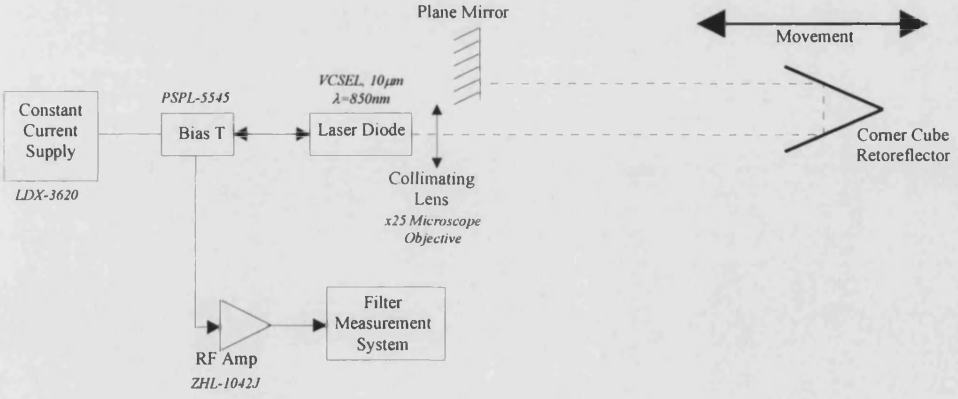

Figure 5.15. Configuration of optical sensor arrangement used for stability measurements.

Figure 5.16 shows a schematic representation of the signal processing used to assess the operational stability of the optical sensor configuration shown in figure 5.15. The output signal was pre-amplified by 35dB to raise the extremely low level

output signal so that a degree of noise immunity was obtained. Following this pre-amplification stage, the fundamental resonance peak was selected by the bandpass filter. Further amplification (45dB) was then employed to raise the signal power so that a Schottky detector diode could be used to measure the power level of the input signal. In order to keep the total input power constant, the signal was passed through automatic gain control (AGC) circuitry. This took the form of a variable attenuator with a RF detector diode and an error signal integrator in a feedback control loop. The constant power signal from the AGC system then passed on to the discriminator filter. The discriminator filter used was a 3rd order Chebyschev high pass filter with a cut-off frequency at 220MHz. The actual frequency response of both the bandpass and discriminator filters used is shown in figure 5.14. The power level of the output signal was detected by a second Schottky detector diode which provided a dc voltage output. This voltage was subsequently amplified and offset so that it covered a suitable range for sampling by a computer controlled data acquisition card (PCL812).

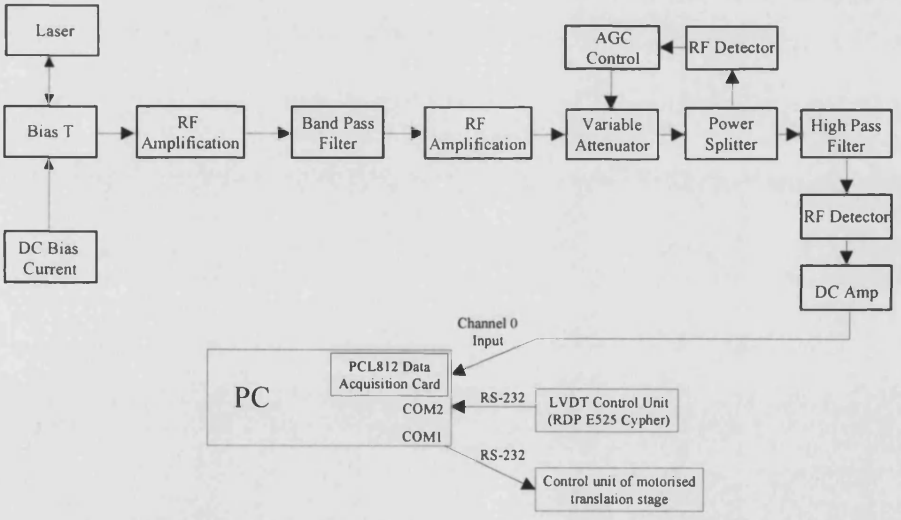

Figure 5.16. Filter based signal processing system and computerised control system used to assess sensor stability in conjunction with optical system shown in figure 5.15.

The process of acquiring the stability measurements was completely automated and controlled using a personal computer. A program was developed which controlled the movement of the stage bearing the optical target (retroreflector) while also sampling data from the output of the optical position sensor signal

processing system. The position of the target at any one time was determined by measuring the output of a LVDT (RDP ACT6000) which was mechanically coupled to the retroreflector sub-mount. A LVDT microprocessor based signal conditioning unit (RDP E525 Cypher) was simultaneously sampled along with the output of the optical sensor, to provide the position calibration data.

5.4.2. Results of Stability Testing

An example of a typical set of results is shown in figure 5.17. This figure describes the output of the sensor as a function of target position with each sequential data point connected by a line, no marker points being used. This stability scan was taken over the course of 3 hours with the output from the sensor sampled every second. It can be seen that the optical sensor output is stable over time, with only a small widening of its characteristic response curve, due to temporal variations in output. An increase in the relative position as defined in figure 5.17 denotes a movement away from the collimating mirror of the external cavity.

The output signal itself has been inverted by an amplifier. However, the performance of the discriminator filter can be seen quite clearly in the form of the characteristic output. It is also clear that the output voltage sensitivity as a function of position is reduced as the optical target is moved past the relative position datum shown on the figure of +50mm. This reduction in sensitivity is due to the high attenuation of the resonance peak at the lower peak frequencies generated by these longer external cavity lengths. In fact, the resonance peak itself is attenuated to a level below the general noise floor present at the lightly attenuated higher frequency end of the channel bandwidth (200MHz). The reversal of the signal which is observed at even higher positive position values is due to the emergence of the second resonance peak into the high end of the channel passband as described by figure 5.14.

It should be noted that the kink in the lower left hand side of the scan was due to an impedance mismatch caused by a faulty cable connecting the discriminator

filter and the final detection diode. This caused an effective change in the frequency response of the high-pass filter, leading to the apparent kink.

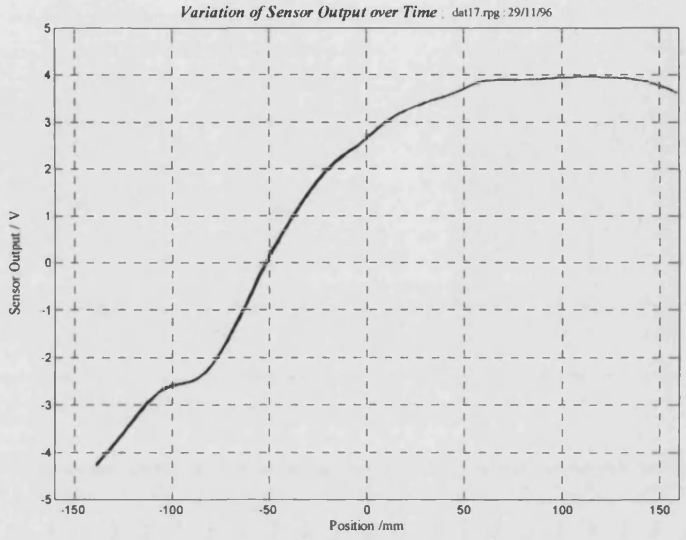

Figure 5.17. Variation of sensor output over a 3 hour timescale.

While initial inspection of the broadening of the characteristic curve over the 3 hour scan time may lead to the conclusion that the signal is slightly noisy, this is not the case. If one inspects the data closely, it can be seen that there is very little noise on the trace itself and that the widening of the response curve is almost entirely due to signal drift. This is further illustrated by figure 5.18, which shows an expanded view of a section of figure 5.17. It can be seen that rather than appearing as noisy signal lines, the various 'passes' of the optical target through the particular position range shown appear as predominately straight lines, subject to a varying offset from one another, this offset being caused by drift. It was found that the error due to drift was <0.5% of the realistic operating range over 3 hours.

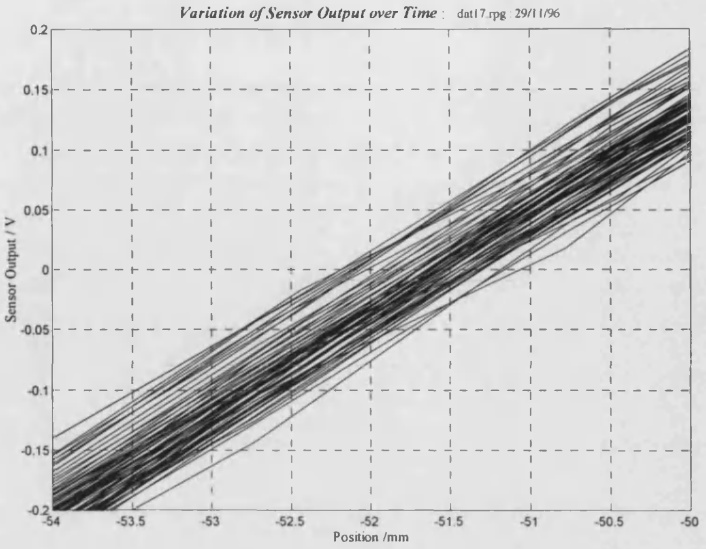

Figure 5.18. Example of signal drift from closer examination of figure 5.17

Various experiments were carried out to determine the cause of this drift. This included the removal of the entire optical system from the experiment and replacing it with an RF signal synthesiser. This produced results which were characterised by extremely low noise and drift. Although some noise could be introduced into the system by subjecting the Schottky detector diodes and their power supply to some severe mechanical disturbances, this was less than would be produced by the complete sensor system. Therefore, it was concluded that the drift in the output signal was predominately due to mechanical drift in the optical components.

5.4.3. Discussion of Stability Results

The result shown in figure 5.17 shows that the optical displacement sensor operates satisfactorily over a long period of time, with very little noise and only a small amount of signal drift. It is important in the long run to reduce the amount of this optical drift, as the optics are mounted as discrete, isolated components. However, it would have been meaningless to attempt to reduce the output signal drift of this experimentally arranged system, since to attain a significant improvement, the fabrication of an integrated sensor head prototype would effectively be required. Once such a prototype has been constructed, however, it is important that this is

tested in the same way as this experimental bench arrangement has been, in order to assess its performance and to highlight the presence of any optical design errors which may be present.

The technique of using the slope detection system can provide high resolution results, at a potentially higher operating bandwidth than the swept oscillator downconversion system described in section 5.2 which has to periodically scan the frequency spectrum. Indeed initial application of the technique to vibration analysis has proved promising [17]. In addition, this arrangement may be used for shorter range, higher resolution applications, as the discriminator filter can be designed with as sharp or shallow a transition slope as required. In fact, a system similar to that shown in figure 5.16 has been used to provide a resolution of 2μm over a 30 cm range to date [18]. However, prior calibration will be required before use of the system, as the output of the system is in the form of an analogue voltage.

5.5 Resonance peak measurement using RF frequency meter based system

Another method of determining the frequencies of the external cavity resonance peaks is to carry out a direct measurement using a RF frequency meter or another suitable counter/timer system. This approach has the advantage of providing a directly digital output signal which is in some way proportional to the length of the external cavity.

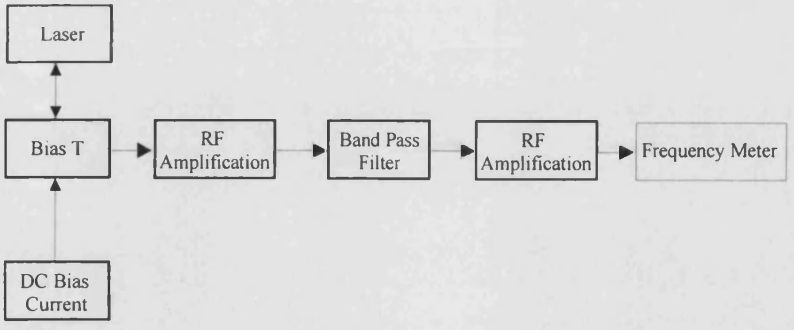

Figure 5.19. Sensor electronics and signals processing for frequency measurement experiment.

Experiments were carried out in order to assess the suitability of using a such a method to directly assess the output of the optical sensor. Figure 5.19 depicts the typical experimental arrangement required to carry out these experiments. A

bandpass filter was used to isolate a single resonance peak in a similar manner to that used in the slope detection technique. Once again, multiple channels may be used, with the frequency range of each channel equal to that of the lowest channel, which is limited to an octave. This is due to the nature of the input signal.

Bandpass filtering the input signal reduces the spectrum to the form shown in figure 5.20. This spectrum was obtained from the amplified output signal of the optical position sensor after it had been passed through a bandpass filter with a passband ranging from 100 to 200MHz. The resonance peak can be clearly seen to be superimposed upon the amplified noise floor, with high attenuation of all frequency components outside the filter bandwidth. Further amplification was applied to the signal prior being applied to the frequency meter. This was to ensure that the signal was of sufficient magnitude to exceed the input detection threshold of the frequency meter. In these investigations a RACAL frequency meter (type 9917) was used.

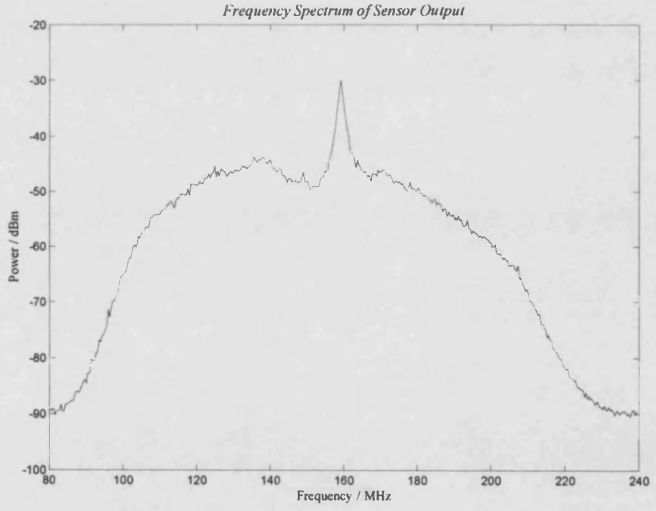

Figure 5.20. Frequency spectrum of sensor output for a cavity length of 0.957 m.

When a signal of the form of figure 5.20 is passed into the frequency meter, a value is displayed which is in some way proportional to the position of the resonance peak. However, it should be noted that the reading given by the meter is not the actual frequency of the resonance peak itself, since the spectrum shown in figure 5.20 does not consist of a 'delta' function, (i.e. a pure tone sine wave). Each point in

the frequency spectrum therefore has to be considered as a noise source, with the output reading corresponding to the expectation value of the spectral distribution of the input voltage squared. This may be written as

$$f_{meas} = \frac{\sum_{i=1}^{n} f_i V_i^2(f_i)}{\sum_{i=1}^{n} V_i^2(f_i)}, \qquad (5.2)$$

where $V_i(f)$ is the spectral voltage component at a frequency f_i. The summations of equation 5.2 being carried out over the full input bandwidth of the frequency meter. Figure 5.21 describes typical experimental results obtained by such a frequency measurement. It can be seen that the frequency values displayed by the meter differ quite sharply from the actual frequencies of the resonance peaks, which were measured simultaneously using a RF spectrum analyser (HP8593A). However, agreement is shown with the theoretically predicted values obtained by using equation 5.2. Any slight deviations between the frequency meter measured values and the theoretical predictions are most likely due to the possible non-uniform frequency response of the frequency meter used. The slight 'up-turn' of the measured readings at the long external cavity extreme of measurement shown in figure 5.21, is due to the resonance peak being measured moving out of the passband of the bandpass filter with its first harmonic entering higher up in the passband.

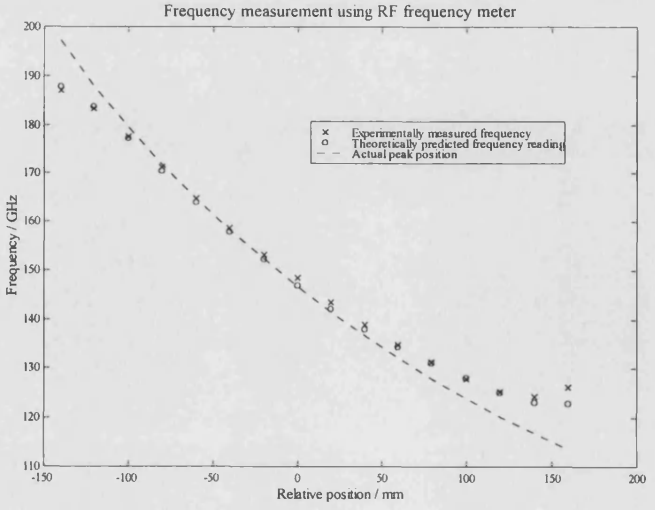

Figure 5.21. Output of frequency meter for a range of external cavity lengths.

It was found that the variation in the digital output reading was better than 1 part in 10000 for 1 second gating time. This is a most promising result considering that no specialised pre-processing of the signal was carried out prior to its input to the frequency meter.

Although the frequency meter does not provide a direct measurement of the peak frequency, it does provide an excellent characteristic monatonic measure of the sensor output within the bandwidth of the channel selection filter used. Therefore such a system can be calibrated to provide an absolute position measurement. It is envisaged that a suitable counting mechanism could be constructed cost-effectively using standard logic IC's. As with the filter edge-detection scheme, multiple channel systems can be produced to cater for potentially larger displacement measurement ranges.

This simplistic interfacing scheme has the advantage of providing an inherently digital reading. Accuracy of output is directly proportional to the measurement time. However, due to the nature of the noise source response of the system a calibration would be required to provide absolute sensing.

5.6. Conclusions

In this chapter three separate techniques have been proposed for use in decoding the signals produced by the resonant cavity optical position sensor. Each technique has been tested in use with the optical sensor and has been shown to provide convenient means of interfacing with the optical system. In addition, each of these systems can be developed at potentially low-cost, by taking advantage of new advances in chip-sets designed for the mobile communications mass markets.

The output format of the three systems are quite different. The edge-detection system provides an analogue voltage output while both the RF downconversion system and the frequency meter technique produce an output which is inherently digital. However, the origins of these digital signals differ as the downconversion system carries a discrete timing measurement on a highly processed and converted

signal while the frequency measurement is carried out on essentially the raw input signal.

Due to the nature of these systems it was found that certain interfacing techniques were particularly suited to certain measurement applications. For example, due to the immediate response of the edge-detection filter system, this arrangement is particularly suited to high bandwidth and high resolution applications. However, to cover long displacement ranges many channels of operation would be required. The RF downconversion system is far better suited to long range applications as it is essentially only limited in its range by the resolution bandwidth of the system. Therefore, it can be seen that the novel external cavity sensor which is described in this thesis, does not constitute a single specific system but may be operated in a variety of configurations, each designed for a specific measurement application.

The improvement and implementation of the signal processing systems described in this chapter is the focus of ongoing development work. It is envisaged that in the near future these signal processing techniques along with the optical sensor system will be incorporated into commercial products designed for real industrial position sensing applications.

5.7. References

[1] B.Culshaw and J.P.Dakin *eds.* "Optical fibre sensors : systems and applications (volume 2)", Artech House, London, 1989, pp.435-436.

[2] C.D.Kissinger and B.Howland, "Fibre optic displacement measuring apparatus", U.S. Patent No. 3,940,608, 1976

[3] W.E.Frank, "Detection and measurement device having a small flexible transmission line", U.S. Patent No. 3,273,447.

[4] C.Menadier, C.D.Kissinger and H.Adkins, "The fotonic sensor", *Instr. Contr. Sys.*, **40**, pp.114-120, 1967.

[5] M.Durana, R.Gallay, Ph.Robert and F.-C.Pruvot, "Novel type submicrometre resolution pseudorandom position optical encoder", *Electron. Lett.*, **29**, No.20, pp.1792-1794, 1993.

[6] A.Dandridge, A.B.Tveten and T.G.Giallorenzi, "Homodyne demodulation scheme for fibre optic sensors using phase generated carrier", *IEEE J. Quantum. Electron.*, **QE-18**, pp.1647, 1982.

[7] T.Bosselman and R.Ulrich, "High accuracy position sensing with fibre coupled white light interferometers", *Proc. 2nd int. Conf. on optical Fibre Sensors*, Stuttgart, Berlin:VDE, pp.361-364, 1984.

[8] S.Kakuma, R.Ohba, M.Kondoh and N.Takahashi, "Time based length measurement method by optical heterodyne beat counting", *Proc. Sensors and their applications VIII*, Glasgow, IOP Publishing, Bristol, pp.285-290, 1997.

[9] I.P.Giles, D.Uttamchandani, B.Culshaw and D.E.N.Davies, "Coherent optical fibre sensors with modulated laser sources, *Electron. Lett.*, **19**, No.1, pp.14-15, 1983.

[10] P.Horowitz and W.Hill, "The art of electronics", 2nd edition, Cambridge University Press, Cambridge, UK, pp.1035-1038, 1989.

[11] F.Labbrozzi, "Designing for spectrum analysis", *Electronics World*, pp.488-494, June 1996

[12] G.Roberts, "200MHz Spectrum analyser displays to -75dB", *Electronics World*, pp.500-501, June 1996.

[13] R.P.Griffiths, "Remaining work involved in the DTI/EPSRC LINK Photonics project 'Salome'", *Internal report*, RDP Electronics Ltd, November 1997.

[14] Hewlett-Packard Application Note 923, "Schottky Barrier Diode Video Detectors", (5954-2079), May 1996.

[15] M.S.Bergano, "Wavelength discriminator method for measuring dynamic chirp in DFB lasers", *Electron. Lett.*, **24**, No.20, pp.1296-1297, 1988.

[16] The ARRL Handbook for Radio Amateurs (1997), Seventy Fourth Edition, Edt. P.Danzer, Publ. The American Radio Relay League, Newington, CT, USA, pp15.12

[17] N.Lieven, I.H.White, C.Mignosi, R.P.Griffiths and R.V.Penty, "External cavity laser diode sensing for vibration measurement in aerospace applications", *Proc SPIE Conf. on Laser vibrometry*, Italy, 1998 - to be published.

[18] R.P.Griffiths and I.H.White, " A high resolution optical position sensor using optical feedback to a semiconductor laser", *Proc Sensors and their applications VIII,* Glasgow, pp 291-296, 1997.

CHAPTER 6

DYNAMIC ANALYSIS OF A SEMICONDUCTOR LASER SUBJECT TO DELAYED OPTICAL FEEDBACK

In this chapter a dynamic analytical approach is used to analyse the response of the external cavity configuration which further develops the theoretical understanding of the optical sensor system first analysed theoretically in chapter 3. This allows the analysis of dynamic effects and stability phenomena which was not possible using the concept of effective reflectivities developed in chapter 3. A delayed feedback rate equation model is developed which is capable of analysing systems with an arbitrary feedback level, requiring considerations of multiple reflections within the external cavity. The model is used to confirm a wide variety of experimental observations and suggest system improvements.

6.1. Introduction

The theoretical study of semiconductor laser diodes operating within an external optical cavity is one which has developed a great deal of interest over the last two decades. Much of the reason for this is the potential application of these configurations to coherent communications systems, where the external cavities can, in practice, improve the performance of the optical source.

The appeal of the external cavity arrangement can be seen since it has been found to produce linewidth narrowing [1-3], linewidth broadening [4-5], (whether linewidth narrowing and broadening is produced is dependent upon the phase and strength of the optical feedback) and a reduction in induced frequency chirp [6,7]. Indeed, theoretical studies have been mainly concentrated in this area where the theoretical conditions required for achieving the above phenomena and also the spectral characteristics of the laser [8-12] have been studied.

The existence of RF fluctuations in the optical spectrum of a semiconductor laser operated within an external cavity were first noted by Broome et al [13], with

other workers also producing similar effects with fibre coupled laser diodes [14,15]. However, some early attempts at studying the system theoretically fell short as the important phase variable was neglected [16,17]. Subsequently the Lang and Kobayashi [18] set of coupled rate equations have provided the common form for calculating the dynamic properties of a semiconductor laser system subject to delayed optical feedback. Originally, this system of rate equations catered only for the cases where either weak [3], or strong (using AR coated laser facets) [19], levels of feedback were in operation. However, subsequent improvements have been carried out which allow arbitrary feedback levels, requiring consideration of multiple feedback contributions [20-22]. Further modifications have allowed asymmetry and angular alignment effects to be considered [23-26].

Studies of the external cavity arrangement have examined such diverse topics as instability [27,28] and the examination of low frequency fluctuations in optical output and self pulsations [29-32], in addition to general modal noise behaviour [33-37].

It has also been found that the levels of feedback applied to the laser can be classified into a number of regimes [3,38]. Figure 6.1 depicts schematically the commonly supported regimes of operation as assigned by Tkach and Chraplyvy [38]. They assigned five separate regimes of operation. For the lowest levels of feedback (regime I) narrowing or broadening of the linewidth is observed dependent upon the feedback phase. At a feedback level which is cavity length dependent, splitting of the emission line can be observed (regime II), which is due to multiple external cavity modes. A third regime (III) operates where the laser ceases to mode hop between the external cavity modes and operates on a single narrow line. With the highest levels of feedback (regime V), the system operates as an extended cavity with a small active region. It is typically necessary to anti-reflection (AR) coat the laser to achieve operation within this regime. However, for external cavity feedback levels between $\sim 10^{-4}$ and ~0.3 (between regimes III and V) one regime of particular interest (IV) can be defined. This is commonly known as the coherence collapse regime [39]. Within this region of operation strong instabilities exist with multiple external cavity modes,

spectral linewidths of several tens of GHz and a large degree of intensity noise. Whilst operations within this region can be devastating for coherent communications systems (due to the extreme broadening of the optical linewidth), this is typically the regime of operation of the optical feedback sensor if AR coated devices are not being used.

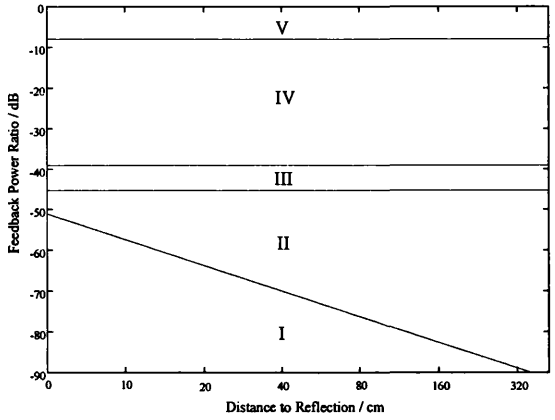

Figure 6.1. Regimes of operation of a semiconductor laser subjected to delayed optical feedback (after [38]).

As an aside, the dynamic study of delayed optical feedback to a semiconductor laser operated within the coherence collapse regime has also been investigated by several authors as a means of observing deterministic chaos [40-50]. When operated within this region, the optical output is found to be subject to a characteristic low frequency intensity fluctuation. Investigation of this fluctuation has been claimed to be a method of studying chaotic itinerency [40,51]. The effect of this LFF on the sensor system will be discussed in detail throughout this chapter, with qualitative comparisons made to the experimental results discussed within chapter 4.

In order to confirm the results obtained experimentally when using the optical sensor configurations described in the preceding chapters, a rate equation model will be developed in this chapter. This model further develops the approach of Hui and Tao [20], so that it can be applied to the calculation of the junction voltage variations of the laser diode. Analysis of the frequency spectra of this parameter can be used to determine the performance of the sensor system as a function of a number of physical parameters.

It is the aim of this model to provide a fundamental understanding of the physical mechanisms involved and to provide confirmations and predictions that were unobtainable when using the simple, but descriptive approach taken in chapter 3. The development of this model should also act as a tool for providing further qualitative predictions of performance to be made, allowing optimisation of the system for future applications.

6.2. Evolution Of Rate Equation Model For An Arbitrary Level Of Feedback

In order to develop the rate equations required to describe the properties of a semiconductor laser operating within an external cavity (for an arbitrary level of feedback), one must consider the variation of the electromagnetic field within the laser cavity.

The complex field equation of Lang and Kobayashi [18] used to describe the external cavity system, was originally written for an edge-emitting laser as

$$\frac{dE(t)}{dt} = \left(i\omega + \frac{1}{2}(G(n) - \xi) \right) E(t) + \kappa_{ext} E(t - \tau_{ext}), \qquad (6.1)$$

where $G(n)$ is the total cavity gain and ξ represents the total losses within the cavity (which are defined explicitly in equations 6.14 and 6.15 respectively), while $E(t)$ represents the time varying electric field. The lasing frequency of the laser is given by $\omega/2\pi$, while τ_{ext} and τ_l denote the round-trip delays of the external cavity and the laser cavity respectively. This equation is very similar to a standard complex field rate equation for a semiconductor laser, except that there is an extra term present. This additional term accounts for the presence of an optical flux entering the laser from the external cavity as a result of the delayed optical feedback. In this expression κ_{ext} has the same physical meaning as in the theoretical approach taken in chapter 3. However, as it stands, this equation has a number of flaws. Firstly, the expression was formulated before the postulation of the linewidth enhancement factor α_H [52,53]. This structure dependent parameter is required to account for the process of carrier density dependent refractive index variations. Equation 6.1 must therefore be updated to include it. The linewidth enhancement factor may by defined as

$$\alpha_H = -\frac{4\pi}{\lambda_o}\frac{\partial \mu_e / \partial n}{\partial g / \partial n}, \tag{6.2}$$

where $\partial \mu_e / \partial n$ denotes the variation in the refractive index as a function of carrier density, while $\partial g / \partial n$ is the differential gain term. The lasing wavelength of the solitary device is given by λ_o.

The second flaw present in equation 6.1 is that the delayed feedback term is only valid for the cases where the level of feedback from the external cavity is either very high, or very low. This is because the feedback coefficient κ_{ext} is an approximation which only accounts for a single reflection within the external cavity. With the inclusion of multiple feedback reflections [1,21], the following improved rate equation may be obtained [20],

$$\frac{dE(t)}{dt} = \left(i\omega + \frac{1}{2}(G(n) - \xi)(1 + i\alpha_H) + \frac{1}{\tau_l}\ln f \right) E(t). \tag{6.3}$$

Here, the complex arbitrary feedback parameter, f, replaces the single reflection feedback coefficient κ_{ext} and τ_l is the round trip delay of the semiconductor laser. It should be noted that the effective reflectivity, r_{eff} of the compound cavity may be given by [54]

$$r_{eff} = r_2 f, \tag{6.4}$$

where r_2 is as usual, the field reflectivity of the laser output facet facing the external cavity. Taking into account multiple reflections, the effective reflectivity may be expanded as [25],

$$r_{eff} = r_2 + r_3(1 - r_2^2)\sum_{p=1}^{\infty}\sqrt{\frac{P(t - p\tau_{ext})}{P(t)}}(-r_2 r_3)^{p-1}.\exp\left\{i\left[p\omega\tau_{ext} + \phi(t) - \phi(t - p\tau_{ext})\right]\right\}. \tag{6.5}$$

In equation 6.5, $P(t)$ denotes the photon density while $\phi(t)$ denotes the accompanying phase variable. The summation accounts for multiple reflections within the cavity with the total delay time of the p^{th} reflections being given by $p\tau_{ext}$. Note that r_3 (the field reflectivity of the external reflector) includes any coupling or diffraction losses which may occur within the external cavity.

Following the arguments of Hui and Tao [20], the electric field and hence both the photon density and phase of the field can be said to be random variables in stationary stochastic processes. Such variables (denoted by Ψ) are found to obey the following relation,

$$\Psi[t-(n+1)\tau]-\Psi(t-n\tau)=\Psi(t-\tau)-\Psi(t). \qquad (6.6)$$

Using this mathematical tool, a simple, non-recursive relation for f may be obtained, for use in the rate equations for analysis of external cavity arrangements subject to multiple reflections.

$$f=\frac{1+\frac{r_3}{r_2}\sqrt{\frac{P(t-\tau_{ext})}{P(t)}}\exp\{i[\omega\tau_{ext}+\phi(t)-\phi(t-\tau_{ext})]\}}{1+r_2r_3\sqrt{\frac{P(t-\tau_{ext})}{P(t)}}\exp\{i[\omega\tau_{ext}+\phi(t)-\phi(t-\tau_{ext})]\}} \qquad (6.7)$$

It can be seen from equation 6.7 that if there is no external cavity in operation (i.e. r_3=0) then the value of f simply reduces to unity. Likewise, equation 6.3 correspondingly reduces to the form associated with standard solitary semiconductor laser operation.

In some cases, particularly when an analysis of dynamic physical parameters is to be carried out, it is convenient to split the complex electric field rate equation into separate photon density and phase rate equations. Since the electric field may be considered to be of the form,

$$E(t)=\sqrt{P(t)}\exp[i(\omega t+\phi(t))], \qquad (6.8)$$

the two rate separate equations may be constructed using the following relations [55].

$$\frac{dP(t)}{dt}=2\Re\left\{E^*(t).\frac{dE(t)}{dt}\right\} \qquad (6.9)$$

and

$$\frac{d\phi(t)}{dt}=\Im\left\{E^*(t).\frac{dE(t)}{dt}\right\}\Big/P(t) \qquad (6.10)$$

where $\Re(x)$ and $\Im(x)$ denote the real and imaginary components of a function respectively.

If equations 6.3 and 6.8 are substituted into the above expressions, an interrelated set of rate equations result which when used in conjunction with the unaltered carrier density rate equation, provide the basis for examining the performance of the external cavity system.

$$\frac{dn(t)}{dt} = -\frac{c}{\mu_e}\cdot\frac{\partial g}{\partial n}\left(n(t)-n_0\right)\cdot\frac{P(t)}{1+\varepsilon P(t)} - \frac{n(t)}{\tau_s} + \frac{j}{ed} \tag{6.11}$$

$$\frac{dP(t)}{dt} = \frac{\Gamma c}{\mu_e}\cdot\frac{\partial g}{\partial n}(n(t)-n_o).\frac{P(t)}{1+\varepsilon P(t)} - \frac{P(t)}{\tau_p} + \Gamma B\beta n^2(t) + \frac{2}{\tau_l}\Re\{\ln f\}.P(t) \tag{6.12}$$

$$\frac{d\phi(t)}{dt} = \frac{\alpha_H c}{2\mu_e}\cdot\frac{\partial g}{\partial n}\left(n(t)-n_{th}\right) - \frac{1}{\tau_l}\Im\{\ln f\} \tag{6.13}$$

The cavity gain term *G(n)* in equation 6.1 has been expanded in equations 6.11 - 6.13 in the following manner,

$$G(n) = \frac{c}{\mu_e}\frac{\partial g}{\partial n}(n-n_0)\frac{P(t)}{1+\varepsilon P(t)}, \tag{6.14}$$

while the total photon losses ξ, may, as usual be expressed in terms of the photon lifetime τ_p, unlike in the theoretical approach taken in chapter 3. In this case, the photon lifetime is not dependent upon the effective reflectivity of the external cavity, but purely on the laser facet reflectivities and scattering losses.

$$\xi = \frac{1}{\tau_p}, \quad where \quad \frac{1}{\tau_p} = \frac{cg_{th}}{\mu_e} = \frac{c}{\mu_e}\left(\alpha_S + \frac{1}{l}\ln\left(\frac{1}{r_1 r_2}\right)\right) \tag{6.15}$$

In the phase rate equation, 6.13, the losses are taken into account and expressed using the threshold current density term, n_{th}.,

$$n_{th} = n_0 + \left[\frac{\partial g}{\partial n}\right]^{-1}\cdot\left(\alpha_s - \frac{1}{l}\ln(r_1 r_2)\right). \tag{6.16}$$

Non-linear gain [55] has been included in this set of rate equations by introducing the factor $1+\varepsilon P(t)$ into the gain terms of both the phase and photon density equations [56,57]. This has been introduced to account for the experimentally observed, reduced laser modulation bandwidth. The equations also include the differential gain term $\partial g/\partial n$, which is material dependent along with the

refractive index μ_e. The dynamic variation of the refractive index is also taken into account through the following expression,

$$\mu_e = \mu_0 - \frac{\alpha_H \lambda_0}{4\pi} \cdot \frac{\partial g}{\partial n}(n - n_0). \qquad (6.17)$$

The theoretical approach used in chapter three, tackled the physical system by considering the multiple external cavity modes present in the system. Consequently, a set of multimode rate equations were required to assess the steady state optical power output. However, in this case only a single longitudinal mode of the laser cavity is considered, with the presence of the external cavity being introduced into the equations through the use of the multiple feedback term, *f*. The presence of the external cavity modes are therefore apparent as sidebands in the frequency modulation of this single optical mode. It is assumed in this case that if any other longitudinal modes are present within the optical spectrum of the solitary laser, the presence of the external cavity will provide identical modulation of these other modes. Therefore, it is likely that any other solitary longitudinal lasing modes present in the optical spectrum will possess a similar collection of sidemodes as the single mode considered at present. As the RF spectrum is produced by the beating together of all these sidemodes, it is likely that even if multiple longitudinal modes are in existence for the solitary laser, the appearance of the RF spectrum will be subject to only very minor changes.

6.3. Dynamic Variation In Laser Junction Voltage Due To External Cavity

While the approach taken in chapter 3 was able to demonstrate that the presence of the external cavity led to the existence of resonance peaks in the frequency spectrum of the output voltage, it could not address any temporal change of the laser diode junction voltage because it was, in essence, a steady state theoretical approach. However, as the most practical physical configuration of the sensor would monitor the junction voltage and not the optical signal itself, it would be advantageous to be able to theoretically predict this variation. This would allow a more complete understanding of the system performance, to be obtained.

The current density applied to the laser may be determined by the following expression [58]

$$j = \left[V - V_{DH}(n)\right] / wlR_s, \tag{6.18}$$

where V is the applied voltage and V_{DH} is the voltage drop across the double heterojunction of the laser which has a width, w and length, l. The series resistance of the cladding lasers in the laser is given by R_s. The voltage drop across the double heterojunction may be given by [59]:

$$V_{DH} = \frac{E_g}{q} + \frac{kT}{q}\left[2\ln\left(\frac{n}{\sqrt{n_c n_v}}\right) + \chi_1 n\right], \tag{6.19}$$

where n_c and n_v are the effective densities of state of the conduction and valence bands respectively, whilst E_g is the bandgap voltage of the junction. The coefficient χ_1 is given by:

$$\chi_1 = \frac{1}{2\sqrt{2}}\left[\frac{1}{n_v} + \frac{1}{n_c}\right]. \tag{6.20}$$

When used in conjunction with the rate equations detailed in equations 6.11 to 6.13, this expression can be used to provide a dynamic measure of the variation in junction voltage due to the presence of the external cavity. It can therefore be seen that unlike the previously developed theoretical analysis, this treatment provides a link between the presence of the external cavity and any dynamic variation in both the optical output and junction voltage of the semiconductor laser in the time domain.

6.4. Numerical Analysis of Rate Equations

As the rate equations developed in section 6.2 comprise a set of coupled differential equations, obtaining time domain information from them requires a numerical solution using an iterative process. It is generally the case that use of a fourth-order Runge-Kutta algorithm [60] provides a satisfactory method for numerical solution of the rate equations. When most conventional laser models which are unconcerned with optical feedback are considered, a step size of the order of 5ps is found to be sufficiently small enough when used with such a numerical

method to avoid instability in the solution. However, in this application, a much smaller time step is required since the rate of change of phase is very high when compared to the other variables. Typically, it has been found necessary in this application to use a step size as small as 100 femto-seconds in order to preserve the stability of the model.

When applied to a practical sensing application, the external cavity may be quite long (at least tens of centimetres), therefore such a numerical model should be run for several microseconds (simulation time) to obtain the desired frequency resolution.

Although the non-recursive relation for the multiple reflection feedback parameter, f, given in equation 6.7 may be further approximated (as done by Hui and Tao [20]) to allow frugal memory use during calculation, the model was instead written so as to incorporate the delayed factor in a delay-line memory array. The time separation of this array was made equal to the time step of the iterative solution to the rate equation. It should be noted that the use of such a delay line to simulate the progress of the optical signal within the external cavity precludes the use of a variable time-step solution algorithm. A fixed time step was therefore required by necessity. While many authors omit noise sources in the analysis of feedback systems (for example [19,30,40]), a noise source has been included into this model. This has been included by applying a Gaussian distribution to the spontaneous emission of the laser in line with Zhu et al [61]. In practice this means that the third term of equation 6.12 is weighted by a Gaussian distribution of unity mean and a variance equal to 2.

Considering these requirements, the model was written in *GNU C* and compiled into machine code (32 bit compiler). A timestep of 0.1ps was chosen to achieve accurate numerical integration without excessive calculation time penalty. Typically the model was run over a simulation time span of 4000nsec to achieve the desired frequency resolution. This required a 200MHz Pentium based computer to run for approximately 45 minutes to complete the calculations, for each set of parameter values.

6.5. Results obtained from the Delayed Feedback Rate Equation Model

In order to assess the performance of a typical Fabry-Perot laser, operating at a wavelength of 1300nm, the device parameters listed in table 6.1 were used. Theoretical analysis of the performance of such a relatively simple device can be conveniently compared to previously measured experimental results. It is important to note that the device parameters associated with the lasers used for the experimental work described in chapters 2 and 4 are largely unknown. Therefore, the results of this model will not provide exact quantitative agreement with experiment. However, the parameters given in table 6.1 describe a typical Fabry-Perot laser and as such, should provide qualitative agreement with experiment, with all the optical trends observed in practice being confirmed by the theory.

Parameter	*Description*	*Value*
α_H	*Linewidth enhancement factor*	*6.0*
Γ	*Optical confinement factor*	*0.35*
λ_0	*Lasing wavelength*	*1300nm*
n_o	*Carrier density for zero gain*	$1x10^{17} cm^{-3}$
μ_o	*Average refractive index*	*3.7*
l	*Laser length*	*250 μm*
w	*Laser width*	*5 μm*
d	*Laser depth*	*0.2 μm*
α_s	*Scattering losses*	$30cm^{-1}$
ε	*Non-linear gain coefficient*	$2x10^{-17} cm^3$
$\partial g/\partial n$	*Differential gain constant*	$3x10^{-16} cm^2$
A	*Non-radiative recombination coefficient*	$1x10^8 s^{-1}$
B	*Radiative recombination coefficient*	$1x10^{-10} cm^3 s^{-1}$
C	*Auger recombination coefficient*	$1x10^{-30} cm^6 s^{-1}$
β	*Spontaneous emission coefficient*	*1e-4*
R_1	*Facet 1 power reflectivity*	*0.32*
R_2	*Facet 2 power reflectivity*	*0.32*
χ_1	*Junction voltage calculation coefficient*	$8.09x10^{-19} cm^3$

Table 6.1. Laser device parameters

It should be noted that a theoretical analysis of a VCSEL which is subject to optical feedback is possible using the method outlined in the preceding sections. However, care should be taken in assessing the laser cavity parameters and in

treating the complex phase changes which occur as the light enters the Bragg stacks of the output reflector. Such an analysis is left for future research work.

The laser described by the device parameters listed in table 6.1 possesses a theoretical light/current (L/I) dependency under solitary operation of the form shown in figure 6.2.*a*. This is obtained by solving the rate equations for the case where r_3=0, and assessing the output power at equilibrium as a function of bias current. It can be seen from this figure that the threshold current of this 'theoretical' device is approximately 19mA. Using this final device parameter, a complete model can be constructed from analysis of the delayed optical feedback rate equations, to describe the behaviour of the laser characterised by the parameter list of table 6.1.

6.5.1 Time Domain Dynamics

Figure 6.2.*b* describes the temporal evolution of the output power of the laser operated with reasonably strong optical feedback ($R_3=r_3^2=0.1$). In this example, a constant current step of 20.0mA has been applied to the laser at time t=0.

It can immediately be seen that the optical output of the system is quite unlike that obtained when using a laser without optical feedback. A typical semiconductor laser operated without feedback, would exhibit damped relaxation oscillations in its optical output following the application of a current pulse. These oscillations would eventually die down to an equilibrium value after a time which is dependent upon the biasing level. By contrast, when the feedback arrangement is analysed, this behaviour is replaced by what appears, (at least at first glance) to be an almost random, noisy, output behaviour which is composed by a series of irregular pulses. This is illustrated in figure 6.2.*c*. Here, it can be seen that these pulses are of a picosecond timescale width, which are limited in this example by the time resolution of the data set (100ps). This is the rate at which the output variables are sampled and saved into the data set.

If the optical output variation is examined more closely with the application of smoothing (to take into account the limited bandwidth of any detector used to observe the signal) it can be seen that the output power is subject to quasi-periodic

intensity drops which are followed by gradual step like increases as shown in figure 6.3. The time between each discrete step is roughly equivalent to the round trip time of the external cavity. These features of the temporal response are due to the low frequency fluctuations present in the system which has been described in chapters 2 and 4. The behaviour of the output power is also mirrored in the carrier density and the emission frequency variation as shown in figure 6.3.

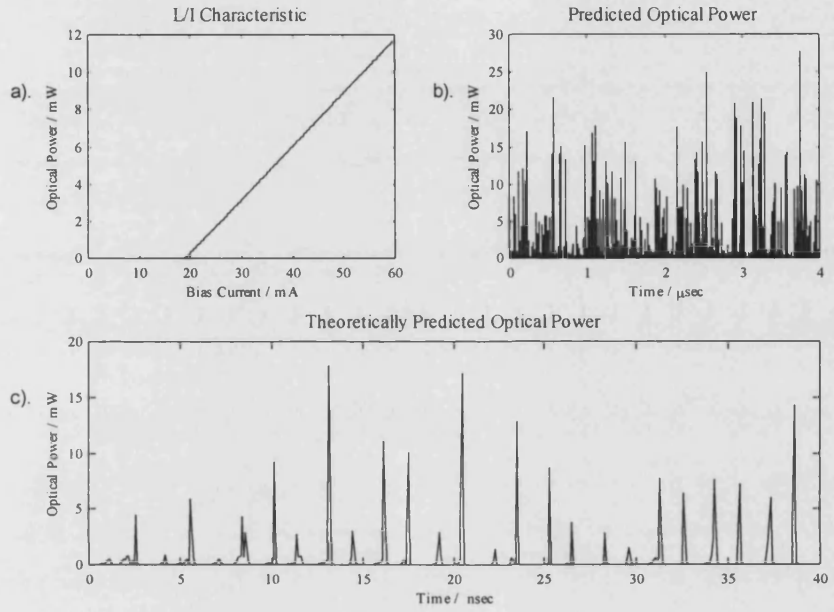

Figure 6.2. Typical output from the multiple reflection feedback model a). Theoretical L/I dependency of the solitary laser characterised by the parameter list given in table 6.1, b). Optical power output predicted by theoretical model for the above laser operating in an external cavity with L_{ext}=0.45m, R_3=0.1 and I=20mA, c). Expanded scale of figure 6.2.*b*. showing nature of optical pulses (Note: time origin shifted by 200ns).

A simple moving average filter has been used to smooth the optical output in order to reduce the effective bandwidth of the signal to that obtained when using a typical *pin* photodiode. This has been done to enhance the presence of the quasi-periodic intensity drops as carried out by Sano [40]. The presence of these intensity drops shows agreement with several previous authors [40,41] and hence shows the validity of the model.

The quasi-periodic intensity drops can be observed most clearly in the carrier density output, where they take the form of sharp increases in carrier density. However, the characteristic discrete downward steps corresponding to effects of the round-trip time of the cavity can be clearly seen preceding these jumps.

The characteristic behaviour of these time domain parameters as illustrated by figures 6.2 and 6.3 has been confirmed experimentally by several authors [19,41] who acknowledge the pulse-like, noisy output response of the optical system.

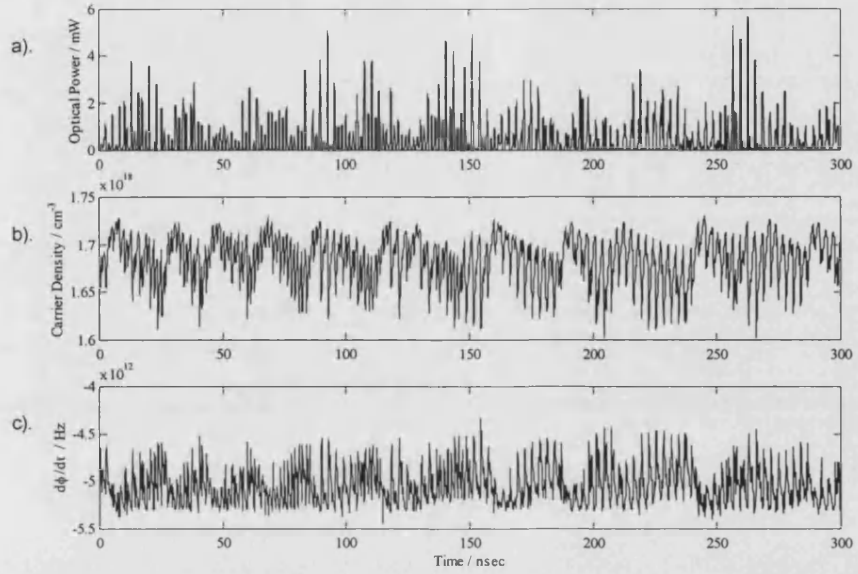

Figure 6.3. Theoretically predicted variation sin some dynamic parameters of the laser as a function of time. L_{ext}=0.45m, R_3=0.1 and I=20mA . a). Optical output power (smoothed), b). Carrier density, c). Variation in lasing frequency from solitary operation value, i.e. $d\phi/dt=2\pi(\nu-\nu_0)$.

6.5.2. Frequency domain results

While figures 6.2 and 6.3 clearly illustrate the temporal effects produced by the external cavity arrangement, a Fast Fourier Transform (FFT), must be performed on the data in order to provide a representation of the frequency spectra of the quantities concerned. It is found however that due to the numerical techniques used in this analysis a frequency spectrum produced in this manner would possess a significant noise content. In order to directly compare the output from the theoretical model with the frequency spectrum observed experimentally, a finite resolution bandwidth was applied to the data. This mimics the operation of the final bandpass filter of a swept source spectrum analyser and allows enhancement of the major features of the frequency spectrum. A simple low-pass digital filtering algorithm can be used to perform this operation.

Figure 6.4 shows the frequency spectrum of the laser diode junction voltage variations obtained from the data set illustrated in figures 6.2 and 6.3. This compares very favourably with the examples of spectra obtained experimentally from devices of a similar type to that described by the parameter list given in table 6.1. The model predicts a series of peaks separated by approximately the round trip frequency (which in this case is 333MHz), the structure of the peaks consisting of a narrow main resonance peak superimposed upon a much broader base peak which decays with an approximate *1/f*-like form either side of the main peak centre. From the analysis carried out in chapter 3 this *1/f*-like dependency can be seen to be due to beating between external cavity modes. The distribution of these modes gives this characteristic form. Also evident in the spectra is the existence of a low frequency peak at a frequency < 25% of the round-trip frequency and of comparable peak power to that possessed by the conventional resonance peaks. Therefore the presence of the LFF is confirmed. All features which are present in the theoretical prediction are observed in the experimental data.

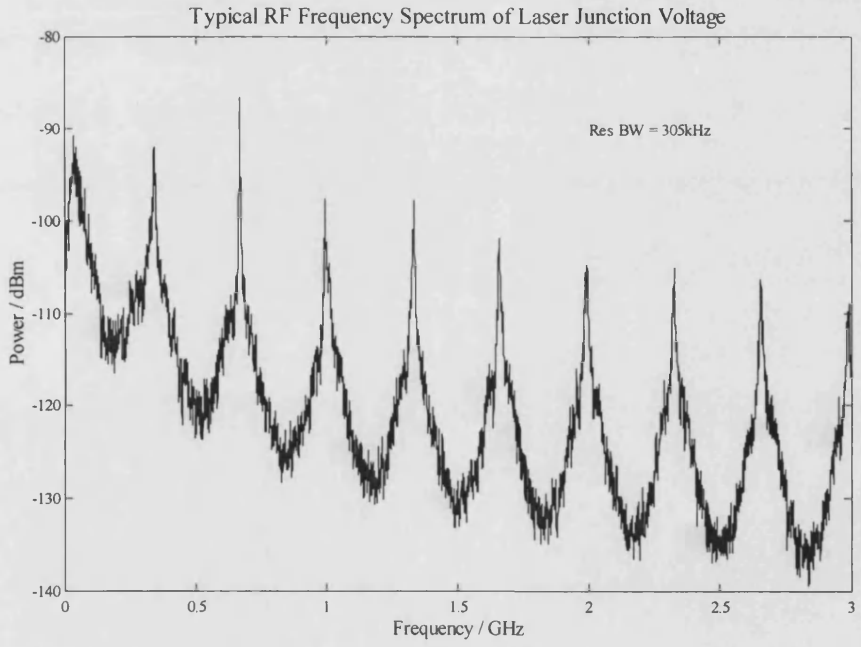

Figure 6.4. A typical theoretically predicted RF spectrum of the laser junction voltage obtained by dynamic analysis using the delayed optical feedback rate equations. In this example L_{ext}=0.45m, R_3=0.1 and I=20mA.

In the example shown in figure 6.4 an effective resolution bandwidth (305kHz) has been imposed upon the system. This is taken into account when calculating the spectral power in dBm of the junction voltage, since in doing so, the voltage is referenced to 1mW of electrical power into the same measurement resolution bandwidth, by dividing V_{DH}, by the number of points used in the FFT, N. Assuming a 50Ω electrical system, the power in dBm may be given by

$$P_{dBm} = 20\log_{10}\left(\frac{V_{DH}(f)}{\sqrt{0.05}\,N}\right). \qquad (6.21)$$

When one compares the power levels theoretically produced with those measured experimentally a good agreement is again observed.

Figure 6.5 shows the direct comparison of an experimentally measured spectrum with a theoretical prediction that has been generated by attempting to match the external cavity parameters such as L_{ext} and R_3 as closely as possible. The experimental data has been obtained using the BNR Fabry-Perot device whose operation has been described previously in chapter 2. The lasing wavelength of this device is approximately 1300nm, and because of its structure and design is characterised by device parameters which are somewhat similar to those given in table 6.1. Whilst these are not exactly known, it is known that they will be similar in magnitude to those listed table 6.1. Therefore the experimental spectrum may be used as a direct qualitative comparison to the theoretical prediction.

The upper trace in figure 6.5 depicts the experimentally measured frequency spectrum generated by the Fabry-Perot device to which 35dB of amplification has been applied to bring it clear of the noise floor of the RF spectrum analyser (HP8593A). Video averaging was applied (100 scan) to the raw data from the analyser, in order to smooth the trace. For comparison the lower trace shows the theoretically predicted frequency spectrum which has been amplified by only 20dB in order to allow a convenient offset for graphical display purposes. A non-recursive smoothing filter algorithm has been applied to this spectrum in order to remove noise and emphasise the resonance frequency structure.

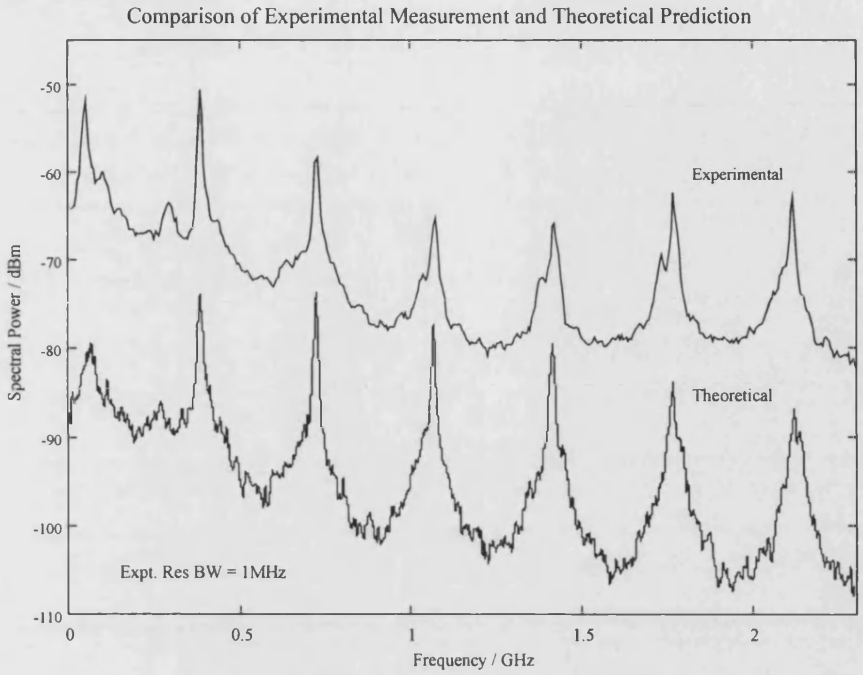

Figure 6.5. Comparison of experimental data and theoretical predictions. Key: *Upper trace*: Experimental data from BNR Fabry-Perot laser, I=23.0mA. Gain=35dB *Lower Trace*: Theoretical prediction L_{ext}=0.421 m, R_3=0.05, I=22.0mA, Gain=20dB.

It can be seen immediately that the two spectra bear direct comparison, sharing several common characteristics. The resonance peaks appear at the same frequencies while the positions of the low frequency fluctuation peaks in both spectra match quite well. Other features appear in both traces - for example, the apparent splitting of the first resonance peak providing a large resonance peak as well as a smaller peak at a slightly lower frequency. In addition, the general form of the resonance peaks agree well between theory and experiment.

Other dynamic quantities can also be examined in the frequency domain. For example, in some sensing applications, it may be advantageous to make use of a separate photodetector in order to monitor the frequency spectrum of the actual optical signal. This point is illustrated in figure 6.6. Figure 6.6.*a* shows a frequency spectrum obtained by performing a FFT on the optical power data shown in figure 6.2, whilst figure 6.6.*b* shows the same operation performed upon the frequency variation of the optical power output of the device.

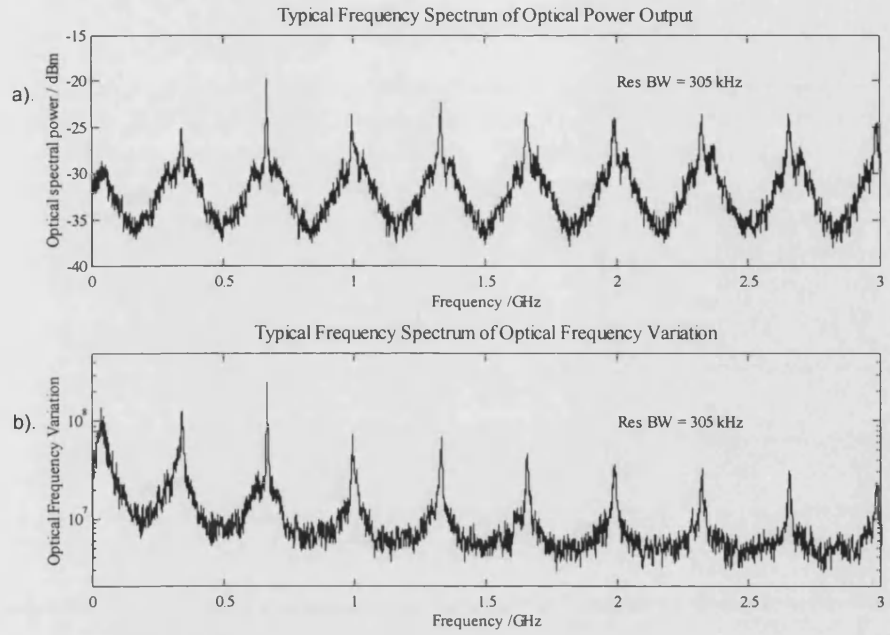

Figure 6.6. Theoretically predicted frequency spectra of dynamic laser parameters for direct comparison with that obtained from the junction voltage. a). Optical output power, b). Frequency variation of the optical output of the device.

In comparison with figure 6.4 it can be seen that the spectra obtained from these parameters are mainly similar in form (although possessing certain minor characteristic differences) to that obtained from analysis of the laser junction voltage. This fact emphasises the point that dynamic parameters other than the junction voltage may be analysed in order to perform position measurements.

The results shown in this section illustrate that by applying a delayed feedback term to the standard semiconductor laser rate equations, a good qualitative prediction can be obtained of the operating characteristics of the external cavity sensor system described in chapter 2. The theoretical predictions of the laser diode junction voltage frequency spectra exhibit all the main characteristics of the experimentally measured spectra.

As this method of analysis has been proven to be genuinely reliable, it can now be used to assess how the frequency spectra will change as a function of various external variables.

6.5.3. The Effect of External Cavity Length Upon Predicted Frequency Spectra

The resonant cavity optical position sensor described in this thesis is based on the fact that the frequencies of the resonance peaks produced by the system are dependent upon the external cavity length. It has been repeatedly stated that the frequencies of the peaks approximately obey the simple inverse law given by,

$$f_m = \frac{mc}{2L_{ext}}. \tag{6.22}$$

However, it has been shown experimentally that when the frequency spectrum of the laser junction voltage is analysed, this simple inverse dependency is indeed approximate and not exact, with slight departures evident. These departures apparently caused by the presence of the LFF which provides a frequency offset to the resonance peaks. Therefore, in order to try and obtain a clarification of the experimental results, the theoretical model was used to simulate typical spectra from the system as a function of external cavity length.

Figure 6.7 shows the theoretically predicted frequency spectra obtained from the model as a function of external cavity length. In this example the applied bias current to the laser was 22.0mA, while the power reflectivity of the external cavity reflector, R_3 was 0.05. It can be seen that when the external cavity length is quite small the resonance peaks in the frequency spectrum are spaced far apart, and possess a relatively wide linewidth. However, as the length of the cavity is increased, the frequency separation, as expected is reduced, roughly according to the inverse law. A corresponding reduction in the linewidth of the resonance peak also occurs, with the peaks sharpening in appearance.

The presence of a low frequency fluctuation in the spectra can also be clearly observed. The frequency of this also appears to reduce as a function of external cavity length, with a corresponding reduction in linewidth and slight reduction in power level relative to the other resonance peaks in the spectrum.

If the exact frequencies of the resonance peaks produced by the delayed feedback rate equation model are noted, the theoretically produced spectra such as

those shown in figure 6.7 may be compared to the actual system behaviour measured and discussed in chapters 2, 4 and 5.

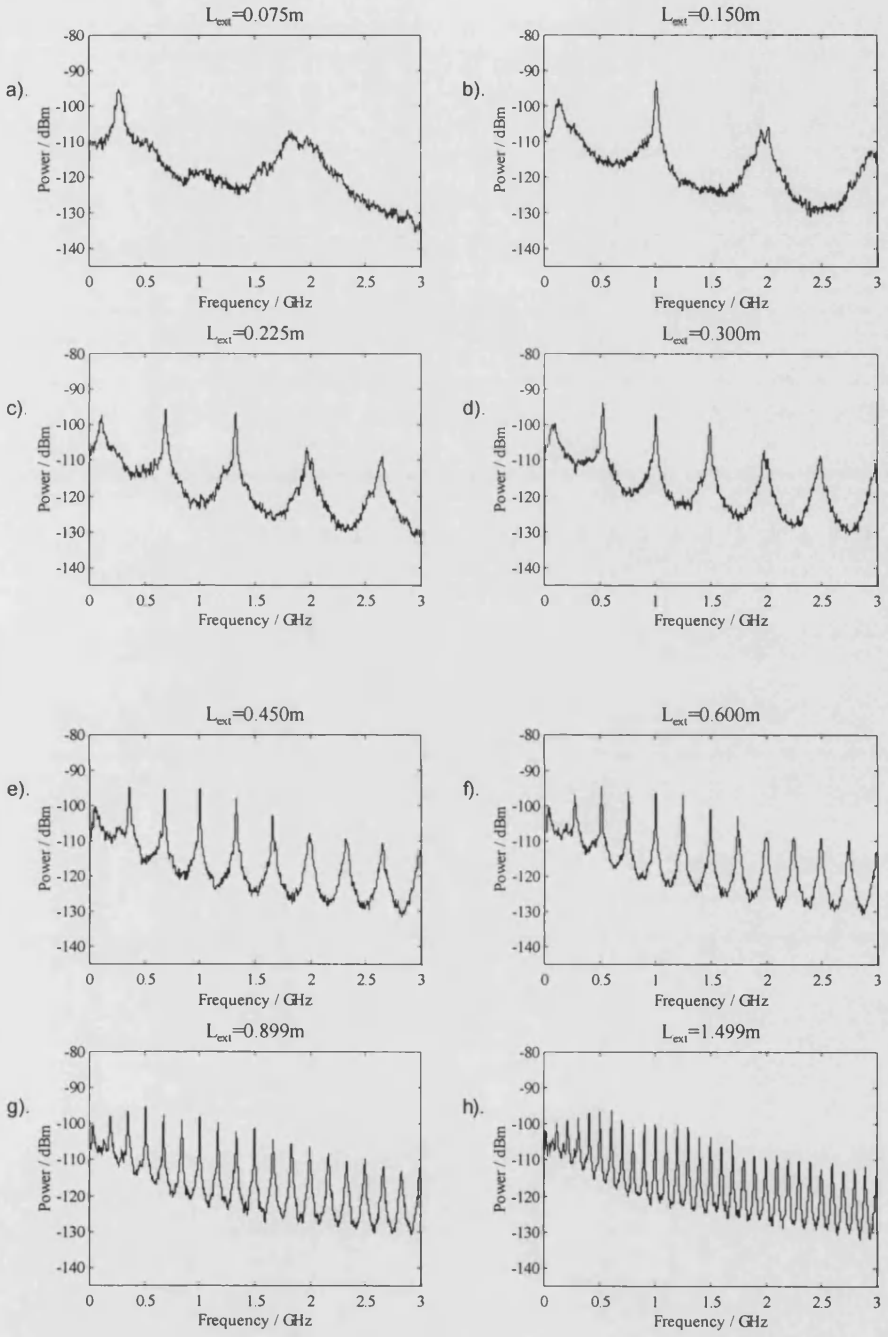

Figure 6.7. The theoretically predicted variation in frequency spectra as a function of external cavity length. In this example, R_3=0.05, and I = 22.0mA. a). L_{ext}=0.075m, b). L_{ext}=0.15m, c). L_{ext}=0.225m, d). L_{ext}=0.300m, e). L_{ext}=0.450m, f). L_{ext}=0.600m, g). L_{ext}=0.899m, h). L_{ext}=1.499m

If the peak positions are plotted as a function of order, it can be seen that a straight line is obtained, the slope of which is dependent upon the external cavity

length. This is illustrated in figure 6.8.*a*. It should be noted however, that the intercepts of the straight lines described by these data series are in fact non-zero, suggesting that there is a slight positive frequency shift present on each peak position. It is found that this offset is approximately equal to the low frequency fluctuation peak present in the spectra.

It has been found experimentally [62], that if the frequency separation of the resonance peaks is measured, a value much closer to the simple inverse law defining the cavity resonance frequency, f_c, is obtained. This is illustrated in figure 6.8.*b*. Here it can be seen that the simple inverse law (solid line) is closely obeyed by the output from the model.

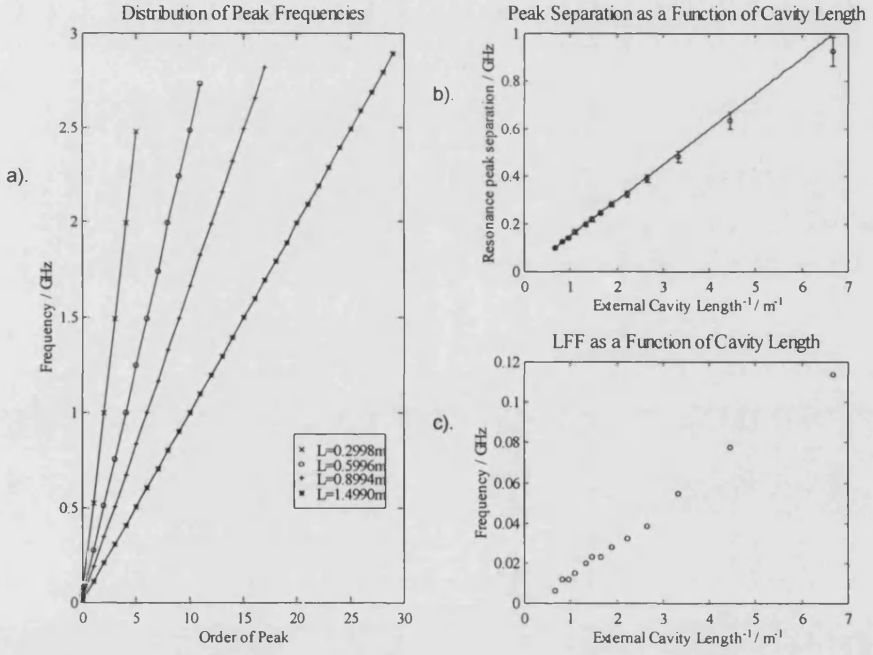

Figure 6.8. a). The theoretically predicted variation of peak position as a function of order and external cavity length. b). Mean peak separation as a function of external cavity length, 'x' - From theoretical model, '-' - inverse law, c). Evidence of the variation of the LFF as a function of cavity length. In these examples I=22.0mA.

If the frequency of the LFF is plotted, it is also found to vary as a function of external cavity length - a fact that was predicted by the theoretical approach taken in chapter 2. Again, a clear inverse dependency upon cavity length can be observed, with the LFF peak having a fractional value of that of the first resonance peak.

In summary, the results presented in this section are in agreement with the experimental observations made in chapter 4 where the frequency offset was found to be equal to the LFF. Therefore the theoretical results appear to confirm the link between the frequency of the LFF and the offset present upon each resonance peak.

6.5.4. Variation in radio frequency spectra as a function of bias current

As discussed in chapters 2 and 4, the appearance of the radio frequency spectrum obtained experimentally from the external cavity sensor system is dependent upon the bias current applied to the laser diode. In order to produce some theoretical predictions with which to compare the experimentally measured behaviour of the device, the delayed feedback rate equation model was used to analyse how the spectra would in fact change as a function of bias current.

Analysis was again carried out using the device parameters contained in table 6.1, which characterise a typical Fabry-Perot device emitting at a wavelength of 1300nm. In this case, the external cavity length was kept at a constant value of 0.433m, with the external cavity power reflectivity, R_3 (including losses) being equal to 0.05.

The results obtained from the model in this study are shown in figure 6.9. As the bias current is increased from below the threshold current of the device (~19mA) to well above this value, significant changes occur in the nature of the spectral response of the laser. At just below threshold, 6.9.*a*, small peaks can just be seen starting to appear in the frequency spectrum. The vertical scale used in this figure allows only a portion of the signal to be viewed. This has been done in order to 'mimic' the inherent noise floor of the RF amplifier required to amplify the signal to a reasonable level for subsequent analysis. While the theoretically predicted signal may have some structure below the axis shown in figure 6.9.*a*, in reality this would fall below the noise floor of the amplifier, which for a good quality device would typically be of the order of -120dBm.

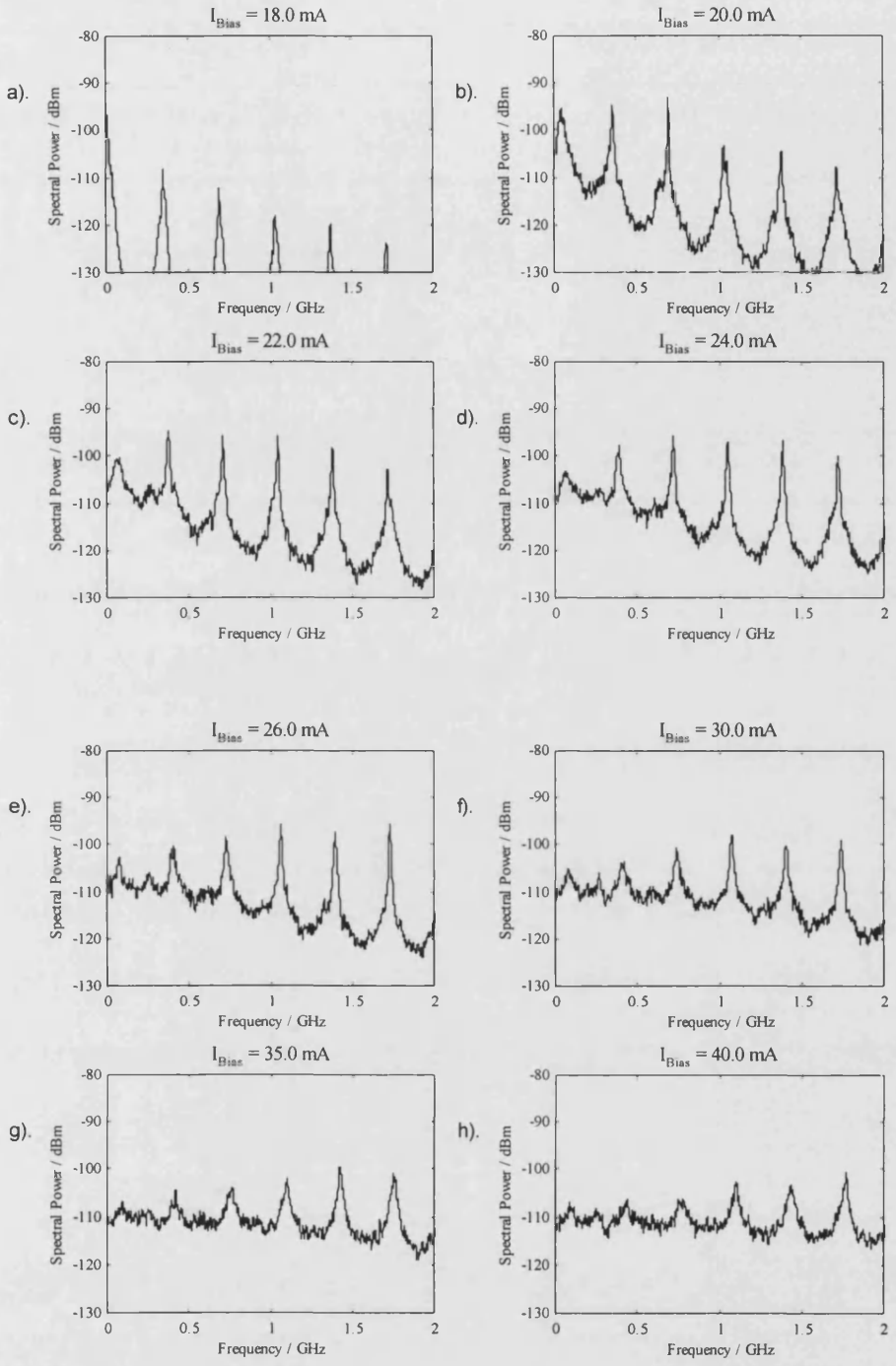

Figure 6.9. The theoretically predicted variation in appearance of laser junction voltage frequency spectra as a function of bias current. L_{ext}= 0.433m, R_3=0.05. a). I = 18.0mA, b). I = 20.0mA, c). I = 22.0mA, d). I = 24.0mA, e). I= 26.0mA, f). I = 30.0 mA, g). I = 35.0mA, h). I = 40.0mA.

As the bias current to the laser is increased, the amplitude of the resonance peaks increases until an optimum value is reached where the signal to noise levels of the peaks is maximal (~20.0-22.0mA as shown in figure 6.9.*b*. After this point, as

the bias current is further increased, the quality of the resonance peaks begin to degrade (figure 6.9c). This degradation continues as the bias current is increased still higher until the appearance of the resonance peaks has become quite distorted, with the initial peaks having almost disappeared.

These results agree extremely well with the experimental measurements described in detail in chapter 2. The form of the spectra agree almost exactly with the experimental data - from the initial growth of the resonance peaks through to an optimum bias point where maximal peaks occur - to increased current levels where extreme distortion of the original spectrum is observed.

Analysis of the positions of the resonance peaks show that they vary as a function of bias current. This is again in agreement with experimental observation as discussed in chapter 4. Figures 6.10.*a* to 6.10.*c* illustrate the variation in frequency of the first three resonance peaks in the frequency spectrum as a function of bias current. Inspection of this figure shows that over the current range investigated by the model, a positive frequency shift is observed in each of the cases which has a degree of linearity. It should be noted that the error generated by the theoretical system is likely to be ±5MHz. It is important to note that these current induced variations are all of a similar value. Therefore, it is likely that the bias current change causes a variation in the frequency offset of each mode and not the harmonic frequency of the mode itself. This is confirmed by the variation of the LFF as shown in figure 6.10.*d*. If this were not the case, the variation would be harmonic, with the third peak experiencing a variation three times the size of that experienced by the first peak. It should also be noted that these results agree with the experimental measurements of Temkin et al. [37], who measured the change in the position of the frequency peaks in the *optical* RF spectrum as a function of bias current. They also found an approximately equal shift in the position of the LFF and the first resonance peak on the variation of the bias current.

In addition to illustrating the current induced variation of the LFF, figure 6.10.*d*, plots the *variation* of the frequency separation as a function of bias current. It can be seen that this provides a measurement which is subject to a much smaller

current induced variation than measurement of the absolute peak frequencies. In fact, the standard deviation of the predicted variation is only 4MHz which is a significant reduction from the large shift obtained from monitoring the absolute positions of the peaks.

While these theoretical results do not necessarily match quantitatively with those obtained experimentally in chapter 4, it must be remembered that they were obtained using a VCSEL as the active device. Consequently, the operating dynamics and device parameters of the VCSEL are much different to those of the simple Fabry-Perot which has been theoretically modelled. What is important, however, is that qualitatively, the mechanisms involved appear to show good agreement with experiment. Finally, it should be remembered that while the frequency shift of the individual peaks is quite large, the bias current variation which is being applied is between the extremes of operation and at least two orders of magnitude greater than any shift likely to be experienced in a practical system. Therefore, it can be seen that under normal operating circumstances, good stability would be achieved.

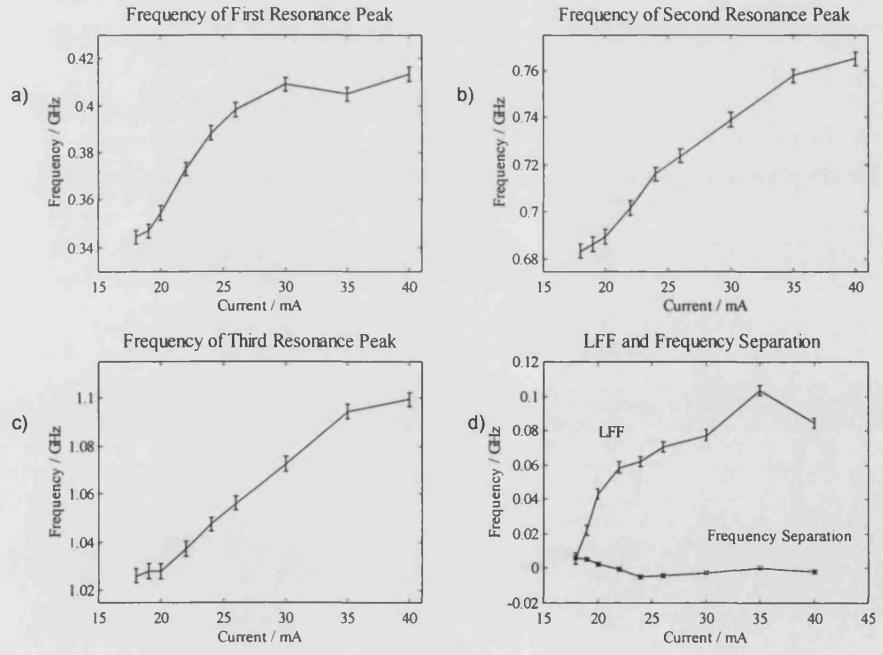

Figure 6.10. The theoretically predicted variation in resonance peak position as a function of laser bias current a). First resonance peak, b). Second resonance peak, c). Third resonance peak, d). LFF peak and variation of frequency separation as function of bias current (f_3-f_2). In all cases I=22.0mA and L_{ext}=0.433m.

In summary, from examination of the results shown in figure 6.10, it can be seen that measurement of the frequency separation of the resonance peaks provides a result which is far more insensitive to any variations in bias current than measurement of the absolute frequency of a single peak.

6.5.5. Variation in theoretically predicted frequency spectra as a function of feedback strength

It is expected that if the feedback level from the external cavity is altered, an effect would be observed in the response of the sensor. Therefore, in order to assess the degree to which the sensor was vulnerable to a change in external reflectivity over time, the theoretical rate equation model was applied to this problem. The model was run several times with the effective reflectivity of the external cavity R_3, being varied. Any variation of this quantity is equivalent to a variation in the optical loss experienced within the cavity.

The results generated by the model are shown in figure 6.11. It should be noted that the reflectivity level at which the quality of the spectrum is optimised is in fact the maximum reflectivity level considered (as shown in figure 6.11.*a*). It is shown that maximum resonance peak signal to noise ratios of 40dB are achieved with an external power reflectivity of 0.3. Considering the practical limitations of optical coupling and alignment losses, this would be around the maximum level for this parameter that would be achievable for a cavity of this length, even with careful selection of coated optics and an informed choice of lens. As discussed in chapter 2, a more typical level for the power reflectivity would be 0.05.

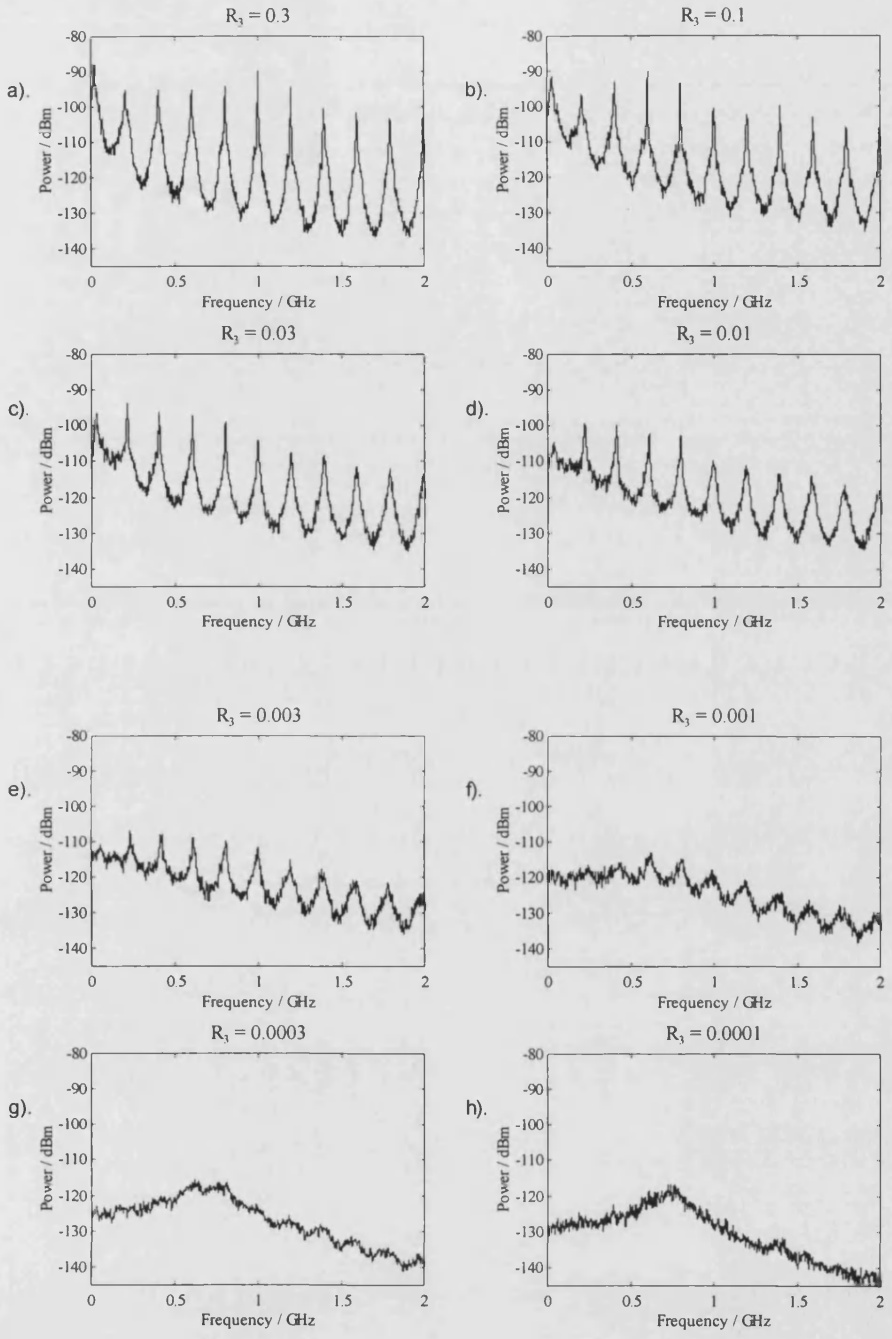

Figure 6.11. The theoretically predicted RF frequency spectra of the laser junction voltage for various values of the external reflectivity, R_3. The cavity length L_{ext} = 0.750m and the applied bias current I = 20.0mA. a). R_3=0.3, b). R_3=0.1, c). R_3=0.03, d). R_3=0.01, e). R_3=0.003, f). R_3=0.001, g). R_3=0.0003, h). R_3=0.0001.

As the level of reflectivity is decreased, the signal to noise level decreases steadily until the resonance peaks begin to disappear as shown in figure 6.11.*h* at a power reflectivity value of 10^{-4}. It can be seen that whilst ongoing resonance peak degradation is occurring for decreasing reflectivity, the system is still capable of

producing resonance peaks with up to 20dB of optical loss inserted into the external cavity. From analysis of figures 6.11.*d* and 6.11.*e*, it is likely that for the particular Fabry-Perot laser described by table 6.1 10dB of loss in the optical system could be tolerated in practice during operation. A loss of this level does not appear to greatly disrupt the resonance pattern to so great an extent that that it is not possible to accurately measure the peak frequencies. However, further optimisation of the laser diode used should allow an increase in this figure of merit. The characteristic loss dependency shown in figure 6.11 agrees with experimental results previously produced [63], which analysed the behaviour of the external cavity system as a function of feedback strength.

If the resonance peak positions predicted by the theoretical model are examined, it can be seen that they vary as a function of external reflectivity. This is shown in figure 6.12. In this figure the frequencies of the first three resonance peaks, along with the LFF are plotted as a function of external reflectivity, R_3, where this has been plotted using a logarithmic scale. It can be seen that for the first resonance peak (figure 6.12.a) there is an almost linear relationship evident, with a decrease in frequency occurring for an increase in external reflectivity. This is also evident in figures 6.12.*b* and 6.12.*c* although the response depicted does not appear as linear as for the first mode. This behaviour is also mirrored in the low frequency fluctuation with a similar variation apparent. The fact that the frequency varies as a function of external reflectivity, and in essence loss within the optical cavity was established experimentally in chapter 4.

Examination of figure 6.12 illustrates that once again, the theory predicts a variation in the resonance peak positions as a function of a physical parameter, which in this case is the external power reflectivity of the cavity, R_3. However, it can again be noticed that any variation can be minimised by actively measuring the frequency separation of the resonance peaks and not the absolute peak positions. This is demonstrated in figure 6.12.*d*, where the frequency separation between the second and third peaks is plotted. It can be seen that this provides a five-fold reduction in variation. Once again, while the results obtained theoretically do not

agree quantitatively with the experimental results that were obtained using the VCSEL (chapter 4), it has been shown that measurement of the frequency separation does provide a result which is of increased stability.

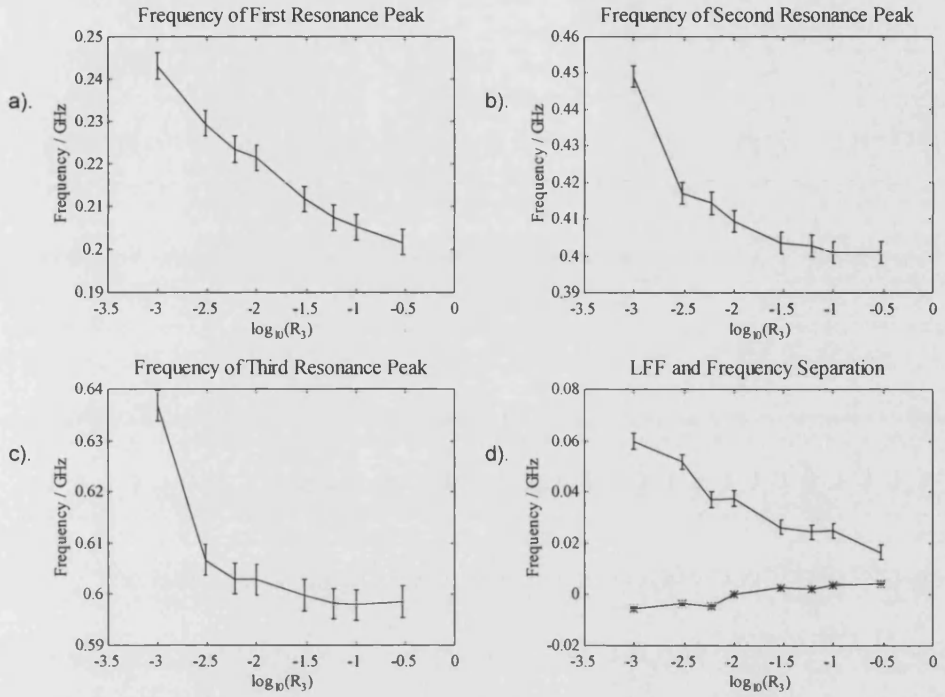

Figure 6.12. The theoretically predicted frequencies of the resonance peaks as a function of external reflectivity, R_3. a). First peak, b). Second peak, c). Third peak, d). Low frequency fluctuation and variation in peak separation (*).

Finally, it should be stated that while the frequency shift may seem quite large, it must be remembered that in this theoretical study the power reflectivity has been varied over more than 3 orders of magnitude.

6.5.6. Anti-Reflection Coating of Laser Facet

In chapter 3 it was shown that the act of anti-reflection (AR) coating the laser facet closest to the external cavity had the effect of increasing the number of allowed external cavity mode solutions, and therefore increasing the effect the delayed optical feedback has upon the solitary laser. Consequently, if the performance of a laser with an AR coated facet is compared to one without, a change in the output characteristics would be expected.

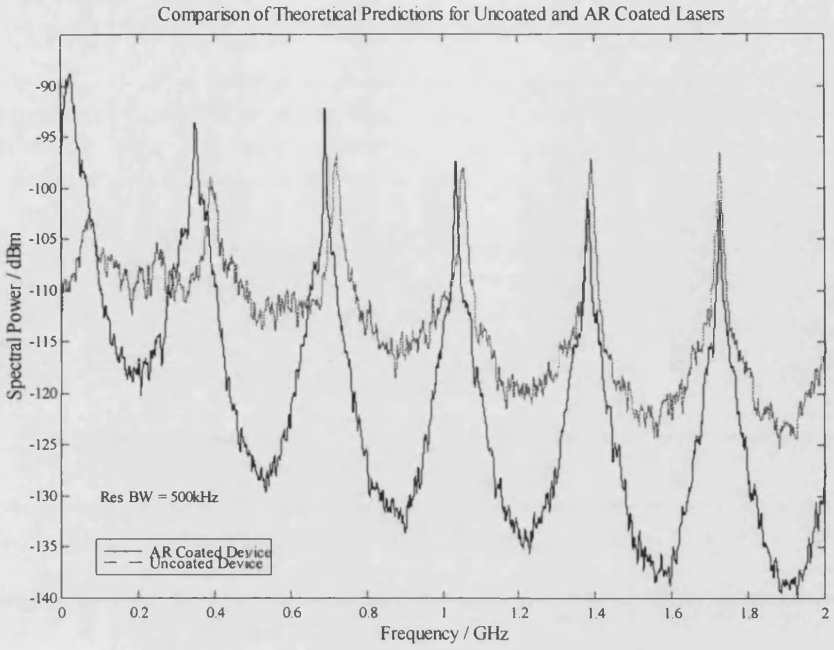

Figure 6.13. Comparison of theoretical predictions for uncoated and AR coated lasers. In this example L_{ext}=0.433m, I=25.0mA and R_3=0.05. The uncoated laser has a facet reflectivity of 0.32 while in the AR coated case the reflectivity has been reduced to 0.05.

Figure 6.13 depicts the response predicted by the theory for a laser which has had the facet closest to the external cavity moderately anti-reflection coated, so that R_2=0.05. In this figure the frequency spectrum shown has once again been obtained by performing a FFT on the laser junction voltage output of the model. This output being characteristic of when a bias current of 25.0mA is applied to the device. For comparison, the response of the system without any coating applied to the laser facet with the same bias current applied, is also shown. The uncoated facet possessing a power reflectivity, R_2 equal to 0.32.

As might be intuitively expected, the theoretical model predicts that the act of AR coating the device would cause a significant change in the system response. It can be clearly observed from figure 6.13 that coating the laser facet will cause a significant increase in the signal to noise ratio of the resonance peaks. An increase to approximately 40dB can be seen, with a corresponding increase in quality factor (Q) of the peaks evident.

As discussed in section 6.5.4, with no coating applied to the laser facet the model predicts that there exists an optimum bias current for observing the resonance

peak structure. This optimum biasing point occurs at approximately 21mA as observed from figure 6.9. By contrast, the model predicts that with the facet AR coated so that R_2 is equal to 0.05, the optimum bias current for observing the resonance peak structure will rise to approximately 25mA. It is this optimum condition which is illustrated in figure 6.13. This increase is entirely understandable since when the device is AR coated, the effective optical loss of the laser cavity is significantly increased. Therefore to maintain the same effective gain level per round trip within the device, the bias current has to be increased. It should be noted however, that the act of AR coating the device has raised its solitary bias current from 19mA to 25.5mA.

Furthermore, as discussed in chapter 4, it may be seen that the AR coated system is predicted to have a response subject to a far lower offset frequency than that evident for the non-AR coated device. This can be noted by observing the reduction in the frequency of the LFF in figure 6.13.

Therefore it can be concluded from these theoretical predictions that an AR coated device would provide an enhanced response, which, when compared to a non-coated device would be of great advantage in several sensor configurations.

6.5.7. Alignment Effects and Cavity Asymmetries

There has been much interest in the study of the effect of asymmetries in external cavity semiconductor laser systems [23-26]. These asymmetric geometry systems have been found to have an effect in the response of the laser system. Analysis of asymmetric systems requires a theoretical approach of far more depth than that outlined within this chapter, which is beyond the scope of this thesis. However, in most cases, the rate equations are modified in order to take into account the cavity asymmetry. For example, Besnard et al [25] modified the complex, multiple reflection feedback fraction f in the following manner,

$$f = 1 + \sqrt{\left(1-r_2^2\right)}\frac{r_3}{r_2}\sum_{p=1}^{\infty}(-r_2 r_3)^{p-1}. \\ R_{ef}(p)\frac{\sqrt{I(t-p\tau_{ext})}}{\sqrt{I(t)}}\exp(i[\phi(t-p\tau_{ext})-\phi(t)-p\omega\tau_{ext}]) \tag{6.23}$$

where $R_{ef}(p)$ denotes the effective reflectance for the p^{th} round-trip component. $R_{ef}(p)$ being a geometry dependent parameter, taking into account any perceived cavity asymmetries. This method is based upon the expansion of the Gaussian output beam onto the basis of Hermite-Gauss modes which allows the definition of the coefficients $R_{ef}(p)$ [64].

These asymmetries have been found to provide a plethora of sub-harmonic resonances at frequencies such as $mc/4L_{ext}$ and $mc/6L_{ext}$ [26] where m possesses an integer value. This suggests that when subject to a degree of misalignment the optical system may produce these subharmonic resonances. Care must therefore be taken when interfacing with the optical system to provide real time 'on-line' measurements and that the method used to do so does not misinterpret any of these subharmonic peaks which may exist for main resonance peaks.

6.6. Conclusions

This chapter develops a method which is capable of carrying out an in depth analysis of the behaviour of the external cavity system used to construct the sensor. The theoretical approach which is used requires the addition of a delayed optical feedback term to the standard semiconductor rate equations. It is also noted that while in many applications of the rate equations the phase variable may be ignored without detrimental effect, in this case its inclusion within the theoretical analysis is paramount.

The improved rate equations are applied to the type of cavity configurations which are in operation in the optical sensor, with the aim of confirming the experimental observations discussed in the preceding chapters. Analysis of the performance of a typical Fabry-Perot laser operating within the external cavity system shows that in the time domain, the system provides a noisy output consisting of a series of high frequency pulses. This, corresponds to the coherence collapse regime of operation, commonly described in the literature.

This theoretical approach has demonstrated that the laser junction voltage can be used to monitor the state of the external cavity. The frequency spectra derived

by taking the FFT of the theoretically produced junction voltage signal has been shown to produce excellent agreement with experimentally observed spectra.

The main features of the experimentally measured spectra have been mirrored by the theoretical analysis. The frequency spectrum being dominated by the presence of a series of resonance peaks whose separation is inversely proportional to the external cavity length.

The theoretical model has shown that the positions of the resonance peaks also vary as a function of physical parameters other than length. Variations in parameters such as bias current, and feedback strength have been found to alter the peak frequencies. Importantly however, the model has also predicted that measurement of the frequency separation of these peaks rather than the absolute peak frequency value drastically reduces any variation which may occur during normal operation. Therefore the dynamic variations induced by changes in external reflectivity and bias current are much weaker for the frequency separation measurement than would be the case if individual peak frequencies were measured. This produces a measurement which is closer to that predicted by the simple, inverse relationship describing the cavity. This important prediction of stability is supported by experimental evidence in the preceding chapters, which may allow the system to be operated without specialised dynamic control of these parameters, in many situations.

In fact, the model predicts that the system is tolerant to a large amount of optical loss within the cavity. Even when 20dB of optical loss has been applied to the cavity, there are still resonance peaks present in the frequency spectrum which may be analysed to allow determination of position to be carried out.

It is important to note that for simplicity, the type of laser simulated throughout this chapter was a simple Fabry-Perot device of standard performance. However, using slight alterations to the theoretical approach used, this analysis could be extended to VCSELs, although care should be taken when analysing the complex phase changes involved in transmission through the output Bragg stack.

While it has been shown that correct operation of the Fabry-Perot laser can provide high stability, it does not mean that this device has been identified as providing the optimum performance. Indeed, it is predicted from the theory that the optical configuration used within the sensor could be further optimised by using an AR coated laser diode. It is predicted that the Q of the resonance peaks would be improved by use of such a device whilst the frequency of the resonance peaks so produced is much closer to the inverse law prediction than that of a non-coated laser.

The act of AR coating the device provides operation within the high feedback regime (regime V as given by [38]), commonly quoted in the literature. It also provides the important effect of reducing the frequency of the LFF and the influence which it has on system stability.

It is hoped that this initial theoretical work will lead to further studies of the sensor system. In addition it is envisaged that further development and application of the theoretical model outlined within this chapter will lead to the production of quantitative predictions of the behaviour of the external cavity sensor system. This in turn will allow the optimisation of the construction of the sensor for future applications.

6.7. References

[1] F.Favre, D.Le Guen and J.C.Simon, "Optical feedback effects upon laser diode oscillation field spectrum", *IEEE J. Quantum Electron.*, vol QE-18, pp.1401-1409, 1987.

[2] G.P.Agrawal, "Line narrowing in a single mode injection laser due to external optical feedback", *IEEE J.Quantum Electron.*, vol., QE-20, No.5, pp.468-471, 1984.

[3] N.Schunk and K.Petermann, "Minimum Bit Rate of DPSK Transmission for semiconductor laser with a long external cavity and strong linewidth reduction", *J.Lightwave Technol.*, vol. LT-5, No.9, pp.1309-1314, 1987.

[4] R.O.Miles, A.Dandridge, A.B.Tveten, H.F.Taylor, T.G.Giallorenzi, "Feedback induced line broadening in CW channel-substrate planar laser", *Appl. Phys. Lett.*, vol 37, pp.990-992, 1980.

[5] A.Olsson and C.Tang, "Coherent optical interference effects in external-cavity semiconductor lasers", *IEEE J. Quantum Electron.*, vol QE-17, pp.1320-1323, 1981.

[6] R.F.Kazarinov and C.H.Henry, "The relation of line narrowing and chirp reduction resulting from the coupling of a semiconductor laser to a passive resonator", *IEEE J.Quantum Electron.*, vol. QE-23, pp.1401-1409, 1987.

[7] G.P.Agrawal and C.H.Henry, "Modulation performance of a semiconductor laser coupled to an external high-Q resonator", *IEEE J.Quantum Electron.*, vol. 24, pp 134-142, 1988.

[8] L.Goldberg, H.F.Taylor, A.Dandridge, J.F.Weller, R.O.Miles, "Spectral characteristics of semiconductor lasers with optical feedback", *IEEE J.Quantum Electron.*, vol. QE-14, No.4, pp.555-564, 1982.

[9] N.A.Olsson and N.K.Dutta, "Effect of external optical feedback on the spectral properties of cleaved-coupled-cavity semiconductor lasers", *Appl. Phys. Lett.*, **44**, No.9, pp.840-842, 1984.

[10] N.K.Dutta, N.A.Olsson and K.-Y.Liou, "Effect of external optical feedback on spectral properties of external cavity semiconductor lasers", *Electron. Lett.*, **20**, No.14, pp.588-589, 1984.

[11] S.Jiang, Z.Pan, M.Dagenais, R.A.Morgan, K.Kojima, "Influence of external optical feedback on threshold and spectral characteristics of vertical-cavity surface-emitting lasers", *IEEE Photon. Technol.Lett*, **6**, No.1, pp.34-36, 1994.

[12] Y.C.Chung and Y.H.Lee, "Spectral characteristics of vertical cavity surface-emitting lasers with external feedback", *IEEE Photon, Technol.*, **3**, No.7, pp.597-599, 1991.

[13] R.F.Broome, E.Mohn, C.Risch, and R.Salathé, "Microwave self-modulation of a diode laser coupled to an external cavity", *IEEE J.Quantum Electron.*, vol. QE-6, pp.328-334, 1970.

[14] I.Ikushima and M.Maeda, "Self-coupled phenomena of semiconductor lasers caused by an optical fibre", *IEEE J.Quantum Electron.*, vol QE-14, No.5 pp. 331-332, 1978.

[15] I.Ikushima and M.Maeda, "Lasing spectra of semiconductor lasers coupled to an optical fibre", *IEEE J.Quantum Electron*, vol QE-15, No.9 pp. 844-845, 1979.

[16] R.P.Salathé, "Diode lasers coupled to external resonators", *App. Phys.*, **20**, pp.1-18, 1979.

[17] K.Kobayashi, *Trans IECE Japan E*, **59**, pp.8, 1976.

[18] R.Lang and K.Kobayashi, "External optical feedback effects on semiconductor injection laser properties", *IEEE J.Quantum Electron.*, **QE-16**, No.3, 1980, pp.347-355.

[19] M.-W.Pan, B.-P.Shi, and G.R.Gray, "Semiconductor laser dynamics subject to strong optical feedback", *Optics Lett.*, **22**, No.3, pp.166-168, 1997.

[20] Hui Rong-Qing and Tao Shang-Ping, "Improved rate equations for external cavity semiconductor lasers", *IEEE J.Quantum Electron.*, **25**, No.6, pp.1580-1584, 1989.

[21] D.R.Hjelme and A.R.Mickelson, "On the theory of external cavity operated single-mode semiconductor lasers", *IEEE J Quantum Electron.*, **QE-23**, No.6, pp.1000-1004, 1987.

[22] F.Favre and D. Le Guen, "Spectral properties of a semiconductor laser coupled to a single-mode fiber resonator", *IEEE J. Quantum Electron.*, **QE-21**, pp.19-37, 1985.

[23] D.-S.Seo, J.-D.Park, J.G.McInerney and M.Osinski, "Effects of feedback asymmetry in external cavity semiconductor laser systems", *Electron. Lett.*, **24**, No.12, pp.726-727, 1988.

[24] D.-S.Seo, J.-D.Park, J.G.McInerney and M.Osinski, "Multiple feedback effects in asymmetric external cavity semiconductor lasers", *IEEE J. Quantum Electron.*, **QE-25**, No.11, pp.2229-2238, 1989.

[25] P.Besnard, B.Meziane and G.-M. Stéphan, "Feedback phenomena in a semiconductor laser induced by a distant reflector", *IEEE J. Quantum Electron.*, **QE-29**, No.5, pp.1271-1284, 1993.

[26] P.Besnard, B.Meziane, K.Ait-Ameur, G.-M. Stéphan, "Microwave spectra in external-cavity semiconductor lasers: theoretical modelling of multipass resonances", *IEEE J. Quantum Electron.*, **QE-30**, No.8, pp.1713-1722, 1994.

[27] C.H.Henry and R.F.Kazarinov, "Instability of semiconductor lasers due to optical feedback from distant reflectors", *IEEE J. Quantum Electron.*, **QE-22**, No.2, pp.294-301.

[28] B.Tromborg, J.H.Osmundsen and H.Olesen, "Stability analysis for a semiconductor laser in an external cavity", *IEEE J. Quantum Electron.*, **QE-20**, No.9, pp.1023-1032, 1984.

[29] J.-D.Park, D.-S.Seo and J.G.McInerney, "Self-pulsations in strongly couples asymmetric external cavity semiconductor lasers", *IEEE J. Quantum Electron.*, **QE-26**, No.8, pp.1353-1362, 1990.

[30] J.Mørk, B.Tromborg and P.L.Christiansen, "Bistability and low-frequency fluctuations in semiconductor lasers with optical feedback: A theoretical analysis", *IEEE J. Quantum Electron.*, **QE-24**, No.2, pp.123-133, 1988.

[31] M.Fujiwara, K.Kubota and R.Lang., "Low frequency intensity fluctuation in laser diodes with external optical feedback", *Appl. Phys. Lett.*, **38**, No.4, pp.217-220, 1981.

[32] B.Meziane, P.Besnard, G.-M. Stéphan, "Low-frequency resonances in asymmetric external cavity semiconductor lasers: theory and experiment", *IEEE J.Quantum Electron.*, **QE-31**, No.4, pp.617-622, 1995.

[33] P.Spano, S.Piazzolla and M.Tamburrini, "Theory of noise in semiconductor lasers in the presence of optical feedback", *IEEE J. Quantum Electron.*, **QE-20**, No.4, pp.350-357, 1984.

[34] J.Wang and K.Petermann, "Noise analysis of semiconductor lasers within the coherence collapse regime", *IEEE J. Quantum Electron.*, **27**, No.1, pp.3-9, 1991.

[35] J.W.M.Biesterbos, A.J.Den Boef, W.Linders and G.A.Acket, "Low frequency mode-hopping optical noise in AlGaAs channelled substrate lasers induced by optical feedback.

[36] G.A.Acket, D.Lenstra, A.J.Den Boef and B.H.Verbeek, "The influence of feedback intensity on longitudinal mode properties and optical noise in index-guided semiconductor lasers", *IEEE J. Quantum Electron.* , **QE-20**, No.10, pp.1163-1169, 1984.

[37] H.Temkin, N.A.Olsson, J.H.Abeles, R.A.Logan and M.B.Panish, "Reflection Noise in Index-Guided InGaAsP Lasers", *IEEE J. Quantum Electron*, **QE-22**, No.2, pp.286-293, 1986.

[38] R.W.Tkach, and A.R.Chaplyvy, "Regimes of feedback effects in 1.5μm distributed feedback lasers", *J.Lightwave Technol.*, **LT-4**, No.11, pp.1655-1661, 1986.

[39] D.Lenstra, B.V.Verbeek and A.J.Den Boef, "Coherence collapse in single-mode semiconductor lasers due to optical feedback", *IEEE J. Quantum Electron.*, **QE-21**, pp.674, 1985.

[40] T.Sano, "Antimode dynamics and chaotic itinerancy in the coherence collapse of semiconductor lasers with optical feedback", *Phys. Rev. A*, **50**, No.3, pp.2719-2726, 1993.

[41] I.Fischer, G.H.M.van Tartwijk, A.M.Levine, W.Elsässer, E.Goebl, D.Lenstra, "Fast pulsing and chaotic itinerancy with a drift in the coherence collapse of semiconductor lasers", *Phys. Rev. Lett.*, **76**, No.2, pp.220-223, 1996.

[42] T.Mukai and K.Otsuka, "New route to optical chaos : successive subharmonic-oscillation cascade in a semiconductor laser coupled to an external cavity", *Phys. Rev. Lett.* , **55**, pp.1711-1714, 1985.

[43] Y.Cho and T.Umeda, "Observation of chaos in a semiconductor laser with delayed feedback", *Opt. Commun.*, **59**, pp.131-136, 1986.

[44] R.Müller and P.Glas, "Bistability regular self-pulsing and chaos in lasers with external feedback", *J.Opt. Soc. Amer.*, **2**, pp.184-192, 1985.

[45] G.C.Dente, P.S.Durkin, K.A.Wilson and C.E.Moeller, "Chaos in the coherence collapse of semiconductor lasers", *IEEE J. Quantum Electron.*, **QE-24**, pp.441-447, 1988.

[46] J.Mørk, J.Mark and B.Tromborg, "Route to chaos and competition between relaxation oscillations for a semiconductor laser with optical feedback", *Phys. Rev. Lett.*, **65**, pp.1999-2002, 1990.

[47] B.Tromborg and J.Mørk, "Stability analysis and the route to chaos for laser diodes with optical feedback", *IEEE Photon. Technol. Lett.*, **2**, pp.549-552, 1990.

[48] J.Mørk, B.Tromborg and J.Mark, "Chaos in semiconductor lasers with optical feedback : Theory and experiment", *IEEE J. Quantum Electron.* ,**28**, No.1, pp.93-108, 1992.[

[49] A.T.Ryan, G.P.Agrawal, G.R.Gray, E.C.Gage, "Optical-feedback induced chaos and its control in multimode semiconductor lasers", *IEEE J. Quantum Electron.*, **30**, No.3, pp.668-679, 1994.

[50] Y.Lin and J.Ohtsubo, "Dynamics and chaos stabilisation of semiconductor lasers with optical feedback from an interferometer", *IEEE J. Quantum Electron*, **33**, No.7, pp.1163-1169, 1997.

[51] K.Otsuka, *Phys. Rev. Lett.*, **65**, pp.329, 1990.

[52] C.H.Henry, "Theory of the linewidth of semiconductor lasers", *IEEE J.Quantum Electron.*, **QE-18**, pp.259-264, 1982.

[53] M.Osinski and J.Buus, "Linewidth broadening factor in semiconductor lasers - an overview", *IEEE J. Quantum Electron.*, **23**, pp.9-29, 1987.

[54] J.H.Osmundsen and N.Gade, "Influence of optical feedback on laser frequency spectrum and threshold conditions", *IEEE J. Quantum Electron*, **QE-19**, pp.465-469, 1983.

[55] K.Petermann, "Laser diode modulation and noise", 1991, Kluwer Academic Publishers, Chapter 9., pp.268.

[56] J.E.Bowers, T.L.Koch, B.R.Hemenway, D.P.Wilt, T.J.Bridges and E.G.Burkhardt, "High frequency modulation of 1.52μm vapour-phase transported InGaAsP laser", *Electron. Lett.*, **21**, pp.297-299, 1985.

[57] G.P.Agrawal, "Modulation bandwidth of high power single-mode semiconductor lasers : Effect of intraband gain saturation", *Appl. Phys. Lett.*, **48**, pp.613-615, 1986.

[58] G.Morthier and P.Vankwikelberge, "Handbook of Distributed Feedback Laser Diodes", Artech House Publishers, Boston and London, 1997.

[59] W.B.Joyce, "Current-crowded carrier confinement in double-heterodyne lasers", *J. Appl. Phys.*, **51**, No.5, pp.2394-2401, 1980.

[60] "Numerical Recipes in C - The art of scientific computing", W.H.Press, B.P.Flannery, F.A.Teukolsky and W.T.Vetterling, Cambridge University Press, Cambridge, 1988.

[61] B.Zhu, I.H.White, R.V.Penty, A.Wonfor, E.Lach and H.D.Summers, "Theoretical analysis of timing jitter in monolithic multisection mode-locked DBR laser diodes", *IEEE J. Quantum Electron*, **33**, No.7, pp.1216-1220, 1997.

[62] R.P.Griffiths, I.H.White, P.J.Smith, "A novel high resolution optical absolute position sensor", *Proc. Sensors and Transducers Conference at MTEC'98*, N.E.C. Birmingham, Session 3, pp.1, 1998

[63] C.Mignosi, "Report of the research carried out on free-space optical sensors", *Internal report*, University of Bristol, July 1997.

[64] G.Stephan and M.Trumper, "Inhomegeneity effect in a gas laser", *Phys. Rev.* , **28** pp.2344-2362, 1983.

CHAPTER 7

AN INTRINSICALLY SAFE OPTICAL POSITION SENSOR WITH ABSOLUTE POSITION READOUT

This chapter outlines the design, construction and operation of a novel optical position sensor for intrinsically safe applications. Intrinsically safe sensing is achieved using optical addressing, with no electrical signals being present within the sensing head. Position measurement is absolute and the sensor requires no datum point or reference position whatsoever. The design and construction of a prototype sensor is described, and experimental verification is given of its satisfactory operation. This prototype provides a resolution of 5μm over a range of 4 centimetres. Improved designs allow potential resolutions of 0.002% of full scale to be obtained.

7.1. Introduction

Translational displacement may be practically measured using for example, incremental counting techniques [1-4] or absolute encoding methods [5-8]. Incremental counting methods are generally simpler to implement than absolute encoding techniques. Most optical encoders operate using incremental techniques and are analogue in nature. Interpolation of the fringe patterns obtained from the relatively coarse pitch gratings used provides an enhanced resolution [2]. Corruption of these analogue signals produces a reduction in accuracy. Furthermore, these analogue systems also suffer from the drawback that they are dependent upon a reference point. Power loss or signal corruption can lead to this reference or datum point being lost. In many applications the need for regular or occasional re-establishment of the datum point may not be possible, or may be undesirable. In these cases some type of absolute sensor is required. Absolute sensors also offer the ability to multiplex many sensors together to save power, since they only need be switched on when a measurement is required. Consequently, there has been much interest in the development of absolute translational displacement sensors using

optical techniques with digital outputs to replace traditional electronic sensors to provide enhanced performance.

However, there is also a demand for intrinsically safe sensors, which can have no adverse affect upon the process in which they are being used or on any neighbouring process. For example, the presence of electrical signals in the sensing head could induce unwanted noise in sensitive equipment, or present a possible fire hazard. In order to address these problems a sensor has been developed using optical addressing, without any electrical power in the sensor head which is capable of providing absolute positioning sensing. The sensor head may be positioned remotely using optical fibres to connect it to its control unit which may be positioned far away in a designated safe area, which can, theoretically be positioned over 100m away from the sensor.

7.2. Sensor Design

The new sensor was designed with the aim of keeping the number of optical components within the sensor head to a minimum. There are several reasons for taking this approach. Optical component costs are generally quite high and in addition, exact positioning and the use of precision engineered mounts may be required. Also, since increased computational and digital signal processing power is now more readily available at lower cost, elaborate signal processing techniques may be employed in order to keep the optical system as simple as possible.

The concept of the sensor is illustrated schematically in figure 7.1. The sensor consists of a remote sensor head which is addressed using optical fibre by a control unit. Encased within the sensor head is a reflective grating which is mechanically coupled to the device under test. A pattern is encoded onto the grating so that depending upon its position relative to the optical input, it either reflects the optical signal, or does not. Therefore as the device under test moves, the amount of light reflected by the grating is varied. Consequently, knowledge of the pattern encoded onto the grating allows the position of the device under test to be decoded by the control unit. It can be seen that as the sensor head itself contains no electrical

signals, it can be deemed an inherently safe sensor. Therefore, in hazardous areas commonly found in the mining and petrochemicals industries, the sensor head can operate without any possibility of causing an explosion. (A definition of an intrinsically safe device is given in chapter 1). The sensor control unit being deployed in a designated safe area.

In several fibre optic displacement sensors, separate source and return fibres are used (for example, [9,10]). However in this sensor only a single fibre is used for each channel of the grating to be monitored, thus reducing the complexity of the sensor head construction, although it should be noted that many other grating based systems have used only a single input/output fibre in the past. For example in wavelength encoded position sensing, where such an approach has been used for both rotary [11] and linear [12] position sensing systems. Consequently, this fibre would act as both the optical input to the channel, as well as the optical output, returning any light reflected by the reflection grating.

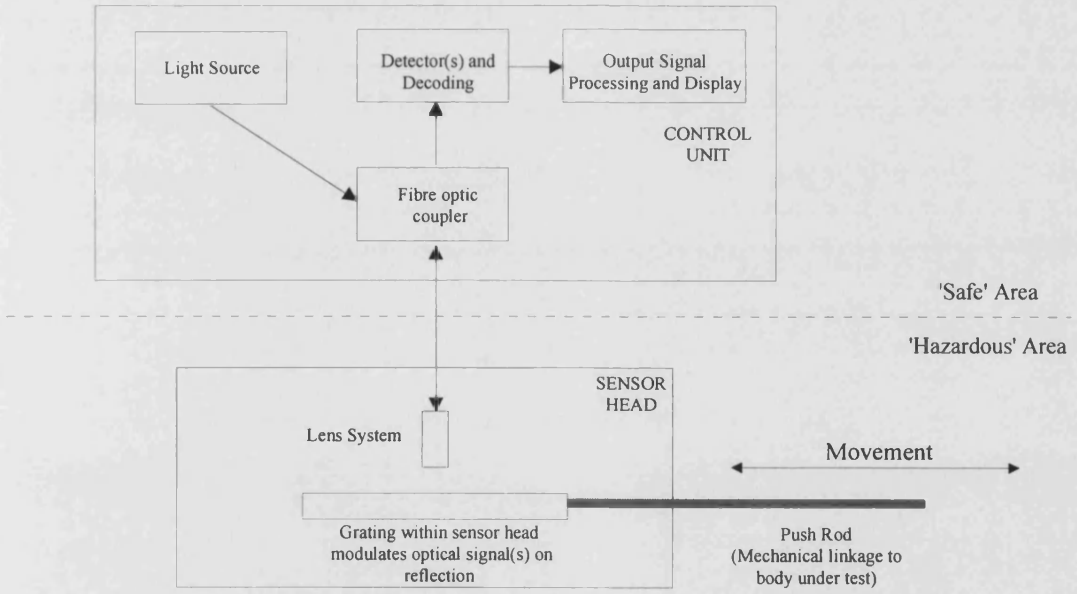

Figure 7.1. Schematic representation of initial sensor concepts.

7.2.1. Pseudo-Random Binary Sequences

In order to achieve absolute position sensing, means were required of encoding onto the grating an unique identifier of each position along the working range of the sensor. It was decided that the best means of accomplishing this would be to use a pseudo-random binary sequence (PRBS). Pseudo-random binary

sequences have been used previously in mechanical systems for absolute displacement control [13]. They have also been used in optical systems using multi-detector sensing heads for displacement measurement [6], rotation control [7], and in conjunction with Moiré fringe measuring heads for machine-tool control systems [14]. All these examples require multiple optical detector units to be positioned within the sensor head. They require a power supply and often a large working area. Consequently these techniques are not suited to intrinsically safe sensing processes or the construction of a compact sensor head. However, it is possible to make use of the unique properties of PRBS in the design of electrically powerless position sensor heads using solely optical addressing. The properties of a PRBS which allow absolute sensing to be achieved are described in the following section.

7.2.2. Properties of a PRBS

The properties of pseudo-random binary codes are well documented [15,16]. A PRBS is a digital binary sequence which may be categorised by its order *n*. A PRBS of order *n* is a periodic string of binary digits ordered in such a way that any combination of *n* consecutive digits within a period is unique, i.e. if a window of bit length *n* is moved along a PRBS one bit at a time then each of the 2^n*-1* non-zero binary combinations of the PRBS is seen only once. From this definition it can be seen that pseudo-random binary sequences have a direct application in the field of position sensing. This is illustrated schematically in figure 7.2. This figure illustrates the simple example of a PRBS of order 3. If a *'window'* of width 3 bits is moved along the sequence a single bit at a time, it can be demonstrated that each non-zero binary combination occurs during 2^n-1 movements along the sequence. It can be seen that after seven (2^3-1) movements the sequence repeats itself, thus illustrating the periodicity of the sequence.

PRBS

0	0	1	0	1	1	1	0	0	1

Sequence	Value
001	1
010	2
101	5
011	3
111	7
110	6
100	4
001	1

Figure 7.2 Example of a PRBS of order 3.

A PRBS of order n may be produced by a linear feedback shift register of n stages, whose input is a feedback digit produced by the modulo-2 sum (or exclusive OR) of the contents of a particular subset of its memory stages. The particular stages (or *taps*) that are used in the feedback term are governed by a well documented set of equations which are known as the *primitive polynomials*. These may be found tabulated in the literature [15-16]. The primitive polynomials specify a recurrence relation from which an algorithm may be formulated to calculate a maximal length PRBS of the particular order required. An example of such an arrangement is shown in figure 7.3. This depicts a shift register system which is governed by the following recursion relation;

$$y_n = C_1 y_{n-1} \oplus C_2 y_{n-2} \oplus C_3 y_{n-3} \oplus \ldots C_k y_{n-k} \ldots \oplus y_0 \qquad (7.1)$$

where the p^{th} term in the relation is given by y_p. The recursion coefficients C_{n-p} which are obtained from the required primitive polynomial are binary digits which may take the value of zero or unity.

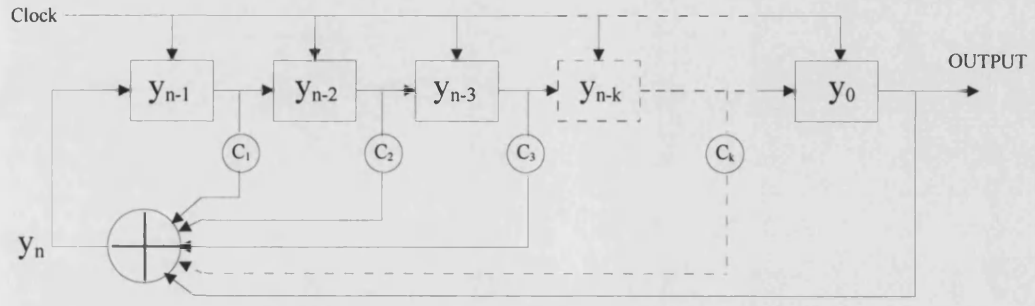

Figure 7.3. Example of the generation of a particular PRBS.

As the PRBS is periodic with a period of 2^n-1 bits, it can be shown [15] that the (*n bit*) binary representation of zero cannot occur from this arrangement unless it is loaded into the register as the initial condition. If this occurred the output of the register architecture shown in figure 7.3 would never change and so no other binary pattern would be created. Therefore, an initial non-zero condition must be loaded into the register in order to initiate the PRBS generation. The actual non-zero pattern entered into the shift register as the initial condition is not important, since the PRBS is periodic. A change in the initial condition would only result in the occurrence of a phase shift in the periodic sequence.

7.2.3. Utilisation of PRBS in the Sensor Head

In order to develop a working sensor, means must be found of discriminating between successive bits of the PRBS and determining the direction of motion of the grating. This may be achieved by using a second grating scale placed alongside the PRBS which consists of a periodic grating, the pitch of which corresponds to the bit width of the PRBS. This periodic grating track provides a clock signal which allows the boundary between successive bits of the PRBS to be determined.

It is common practice in many optical scale based linear encoders to use at least two interrogating heads (although usually four are used to achieve merely incremental sensing). These are placed in quadrature in order to detect movement of the periodic grating scale and hence infer the direction of motion of the body under test. If used in conjunction with a PRBS, such a system would produce the response shown in figure 7.4, the direction of motion being determined by analysing the relative phases of the two read heads. In the example shown in figure 7.4, if read head 'A' leads read head 'B', then the direction of motion is right to left. Whereas, if head 'B' leads head 'A' then the direction of motion is left to right.

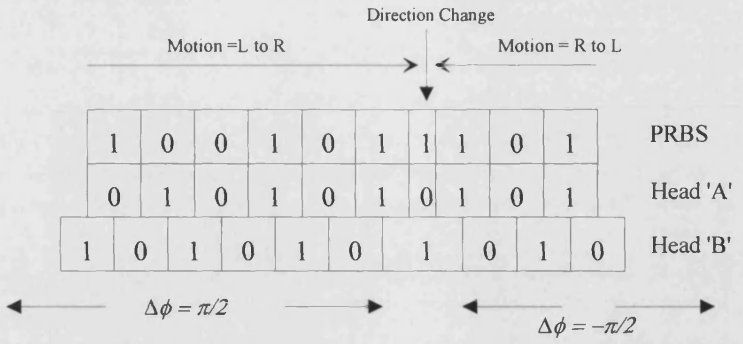

Figure 7.4. A schematic representation of signals at a direction change for three head digital sensor.

If this arrangement was to be implemented along with a PRBS grating code, three read heads would be required. Therefore, in order to reduce the component costs required to assemble the sensor, it would be advantageous to replace this with a somewhat simpler arrangement. This may be achieved by using a novel asymmetric tri-level grating in conjunction with the PRBS track - which reduces the number of read heads required to two.

The asymmetric track (AS track) as shown in figure 7.5 can be used to provide both a clock signal and direction of motion information using only a single reading head. (The dark regions in figure 7.5 denote high reflectivity metal.) When the grating is moved with respect to the lens, the reflected signal has the form of high, intermediate and low levels which correspond to various regions of the asymmetric grating track. In figure 7.5 the intermediate reflectivity regions of the asymmetric grating are denoted schematically by a 'chequered flag' pattern.

Figure 7.5. A schematic representation of the PRBS and asymmetric (AS) grating

To distinguish between successive bits in the PRBS, the period of the asymmetric grating would be made equal to the bit width of the PRBS. Further position resolution can be obtained from the asymmetric grating, which can be resolved to 1/3 of a bit of the PRBS. For example a sensor with a required resolution of 5μm would require the bit width of the PRBS to be set to 15μm. The use of such a asymmetric grating in conjunction with a PRBS is covered by a UK patent [17].

As the PRBS is read using only a single reading head, (i.e. being read in a serial manner) an initial movement of n bits in one direction is required to achieve absolute decoding, where n is the order of the PRBS being used. Until this initial movement occurs, the system can only be operated as an incremental sensor. However, as the order of the PRBS increases, the initial movement required to allow absolute decoding to take place becomes a diminishing fraction of the maximum possible range. This is illustrated in figure 7.6. For example, a sensor with a range 10cm and PRBS bit width of 15μm requires a PRBS of order 13 for unambiguous absolute position determination. The initial movement required in one direction for absolute position determination is therefore 195μm, which is 0.16% of the maximum possible full scale range.

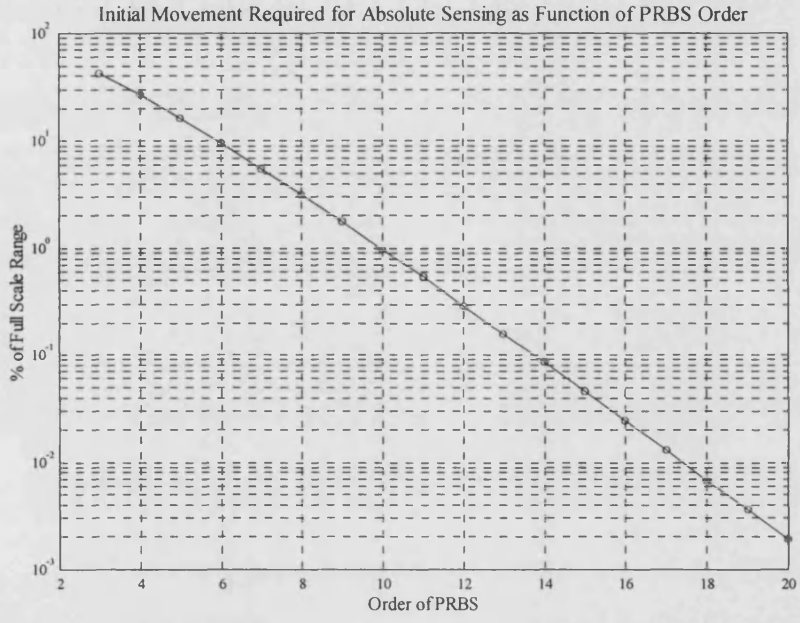

Figure 7.6. A graph showing how the initial unidirectional movement required before absolute position sensing can take place decreases as a percentage of full scale range, as the order of PRBS used is increased.

7.3. Grating Design Considerations

A pseudo-random binary sequence of suitable order may be easily produced using a computer simulation of a binary shift register, with the sequence being represented on a grating by a sequence of (reflecting/transmitting) bars and spaces. However, the design of the asymmetric grating poses a more difficult problem. As low cost photolithographic techniques available limit the dimension of the smallest

structure on such a grating to around 1μm [18], it is important that the design used to produce the asymmetric grating be optimised. Although greater resolution can be achieved from expensive electron beam mask production processes, low-cost copying processes of a master grating, such as contact photolithography copying can at present only be relied upon for feature sizes of 1μm and above. This requires that the high, low and intermediate regions needed for successful decoding of the PRBS track can be easily identified.

It is also desirable to keep the grating design as simple as possible, thus facilitating easier, and more accurate fabrication. Therefore, it would be better to use a grating design that only consisted of a one dimensional structure, if at all possible, i.e. a system of lines would be used instead of two dimensional structures such as squares and triangles to produce the region of medium reflectivity.

Many different grating designs may be used to provide the asymmetric response suitable for successful position determination. However, figure 7.7.*a* illustrates the grating design which was found to perform optimally. It is of a simple form allowing straightforward, cost-effective grating fabrication, whilst providing a well defined three-state reflection response. The theoretical response of this grating is shown in figure 7.7.*b*. This has been calculated by considering the overlap integral defining the reflection response. This is of the form,

$$R(x,y) = \iint f(x)\,dx\,dy\,, \qquad (7.2)$$

where the function *f(x)* defines the reflection of the grating as a function of position. The integral is performed over the limits of a circular area corresponding to the spot size of the illuminating beam. It should be noted that this circular illumination is an approximation as in reality the grating would be illuminated by a beam of Gaussian cross-section. This approximation has been used for simplicity in order to calculate an estimation of the characteristic reflection response of the grating.

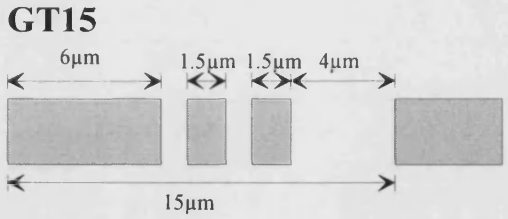

a).

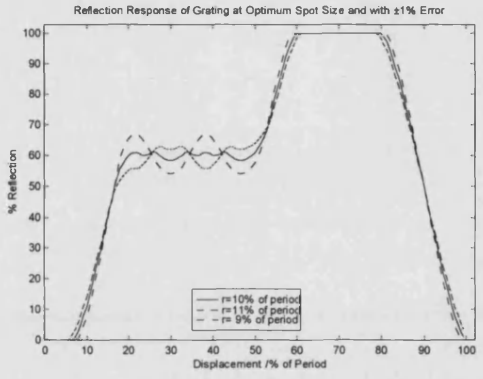

b).

Figure 7.7. Reflection response of asymmetric grating a). Design structure of asymmetric grating GT15, b). Reflection response of grating GT15 as a function of radius of illumination, '*r*'.

The reflection response was calculated for a number of illumination spot sizes. Figure 7.7.*b* shows the response of the grating for the optimum spot size (radius which is 10% of grating period) and for a slightly larger and smaller (±1%) radius of illumination. For a grating period of 15µm (as shown in figure 7.7.*a*), the optimum illumination spot diameter is 3µm. At this optimum spot size, the reflection response obtained as a function of grating position exhibits three distinct, well separated logic levels which are suitable for straightforward position decoding. The code assigned to this grating was GT§§ where §§ denotes the grating period in microns.

7.4. Prototype Sensor Construction

7.4.1. Overview

In order to demonstrate the operation of the sensor a prototype system was developed using a dual track grating. This was designed to provide a resolution of 5µm over a range of 4cm. An asymmetric regular grating was used along with the

PRBS channel, which as previously explained required the use of only two read heads. Two duplicate electronic systems were used to gather and process the information from the two channels of operation

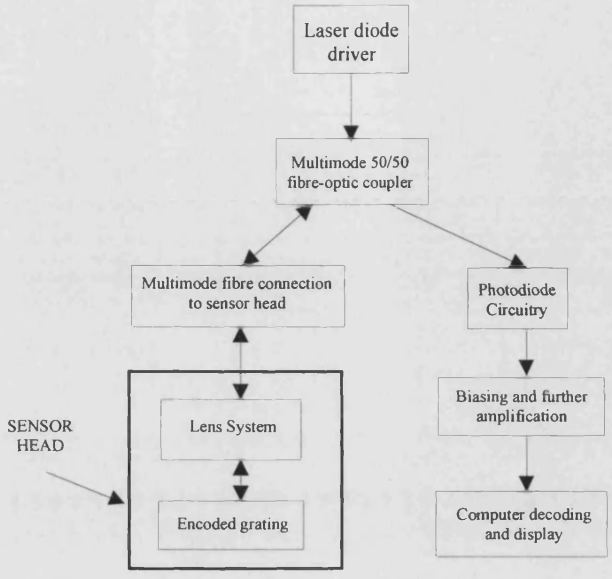

Figure 7.8. Block diagram of one sensor channel.

Figure 7.8 shows a block diagram of the processes carried out for both channels of the prototype sensor. Light from a laser diode propagates along an optical fibre to a 3dB coupler and is evenly split into the two output ports. One port of the coupler is not used whilst the other propagates the optical signal down to the sensor head. Within the sensor head light emerging from the fibre is focused using a single lens system onto the grating track in question. According to the section of grating illuminated, the reflected light passes back through the lens and returns down the fibre to the fibre optic coupler.

As before, the returned light is split to the two input ports of the couplers with one portion travelling back towards the laser while the other travels towards a photodiode where the optical signal intensity is determined. The signal produced by this photodiode is conditioned so that it is in a suitable form for input to a computer for software decoding.

Laser feedback problems which may arise from the portion of the reflected beam which is returned to the laser, are minimised by using a low coherence multimode laser diode (SHARP LT023MD). These devices are low-cost laser diodes

commonly found in compact disc players. Figure 7.9 shows a schematic diagram of the whole sensor, with the two channel system of operation evident.

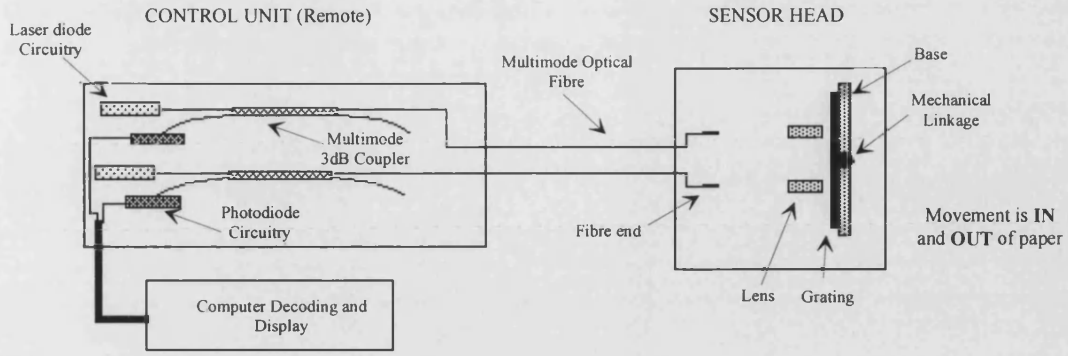

Figure 7.9. Schematic diagram of whole sensor.

7.4.2. Optical Considerations

To achieve a resolution of 5μm, the asymmetric grating design shown in figure 7.7 (GT15) of period 15μm was used in conjunction with a PRBS of bit width 15μm. To provide a measurement range of 4cm, the PRBS used was of the order 12.

In order to reduce system costs, a single Selfoc lens was used per channel to achieve the desired spot size on the grating. Multimode (50/125μm) fibre was chosen for use in the prototype for ease of coupling. Therefore, in order to image the correct spot size onto the grating, a magnification of 3/50 is required. The magnification of such a lens is given by [19];

$$M = \frac{-1}{n_0\sqrt{A}\,d_0 \sin\left(L\sqrt{A}\right) - \cos\left(L\sqrt{A}\right)}, \tag{7.3}$$

where n_0 is the refractive index at the optical axis, L is the lens length in mm and A is a constant of the lens material. d_0 is the object distance of the lens (again in mm). For (Melles-Griot) Selfoc type lenses of pitch 0.23 and N.A. 0.46 and length 4.4mm an object (fibre-end/lens) distance of 31.6mm is required to achieve the desired magnification. As the image distance of the lens is given by;

$$d_1 = \frac{1}{n_0\sqrt{A}}\left[\frac{n_0\sqrt{A}\,d_0 \cos\left(L\sqrt{A}\right) + \sin\left(L\sqrt{A}\right)}{n_0\sqrt{A}\,d_0 \sin\left(L\sqrt{A}\right) - \cos\left(L\sqrt{A}\right)}\right], \tag{7.4}$$

it can be shown that a corresponding image distance of 0.322mm is required between the lens and the grating. This optical arrangement used for each channel of the sensor, is shown in figure 7.10.

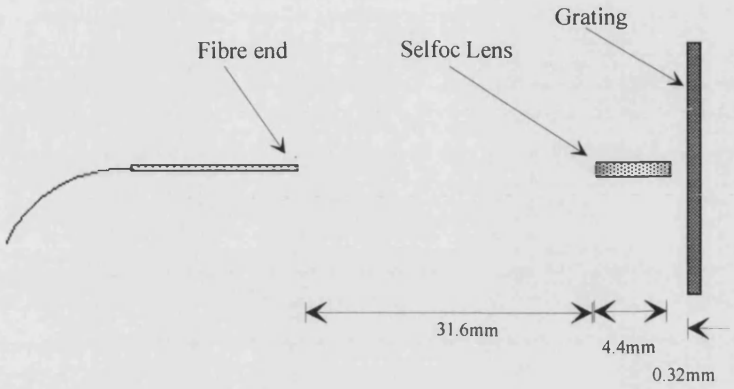

Figure 7.10. Single lens arrangement to provide required spot diameter of 3μm at grating.

Such a simple system does not necessitate the 'scanning plate' required in Moiré fringe applications [3]. This brings with it the requirement that the grating definition is of higher quality since, unlike the Moiré systems, only a single point in the grating pattern is addressed at any one time. Any damage or poor pattern reproduction on the grating will lead to significant drop-outs in signal strength. These will inevitably lead to errors in position determination, which can (to a certain extent) be masked in Moiré systems. However, considering the digital nature of the present approach (at most three level compared to one hundred level systems common in some optical encoder systems) and assuming that the grating is carefully handled, this should not be a problem. Accordingly. a system can be developed which is far simpler in construction than a typical Moiré system, without the exacting tolerances in the alignment of the scanning plate with the grating scale.

Unfortunately, it can be seen from this configuration that to achieve the desired spot size using a single lens, a large amount of the light available will be lost by divergence from the optical fibre. This situation could be rectified by the addition of an extra lens. However, this would increase the system costs. It was found experimentally that the tolerance in the positioning of the optical fibre was ±0.8mm. In comparison, the required tolerance in the positioning of the grating with respect to the lens was ±10μm. This is dependent upon the required degree of magnification.

7.4.3. Mechanical Construction

The prototype sensor head is shown schematically in figure 7.11. This prototype consists of an adapted optical mount made from aluminium which allows a translational movement of 40mm. The grating was attached to the moveable 'bed' of this mount using index-matching gel. This allowed very stable adhesion to the 'bed' of the mount while allowing the grating to be removed, and replaced by one of a slightly different design when desired.

The Selfoc lenses were placed within an aluminium block which rested upon a thin rubber layer placed upon the top of the mount. They were secured into the block using nylon screws The layer of rubber allowed the lens/grating distance to be altered by adjusting the four corner screws, thus compressing or uncompressing the rubber by the required amount. Around this mount, a holder for the optical fibre was constructed in aluminium which allows the fibres to be placed at the correct distance from the lenses.

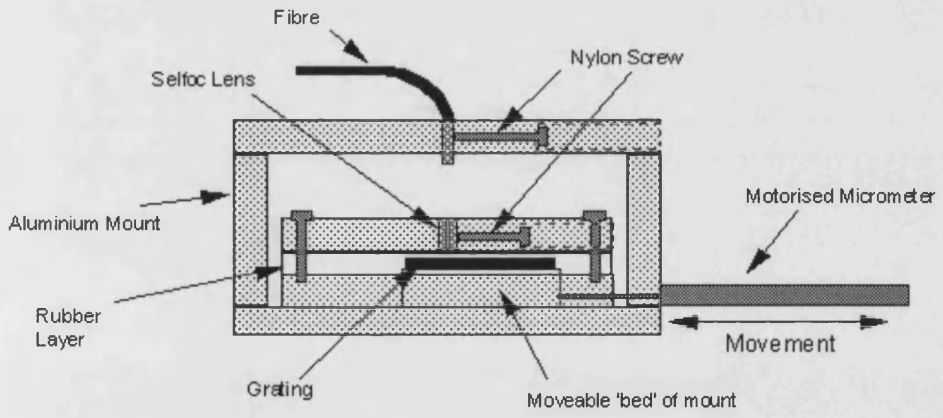

Figure 7.11. A representation of the sensor head (end view)

7.4.4. Electronics Design

As the sensor works on the principle of reflection variation, it is crucial that the optical output power remains constant. A specialised laser driver integrated circuit (SHARP 3C01) was used to control the power output of the laser diode. A

feedback loop was employed, using the built-in monitor photodiode situated within the laser package to sense the output power of the device.

The device can be driven continuous wave (cw) or pulsed using this driver by means of a single connection. When operated in pulsed mode, a reduction in system noise and removal of background ambient light signals can be achieved, by using synchronous detection. In this case power output is kept constant during the *'on'* section of the pulse. As the pulse frequency will not exceed much more than 10kHz, the output level settles quickly, although care should be taken to ensure that data is not sampled until this has occurred. Use of synchronous detection provides a system immune to ambient light effects and minimises undesirable effects such as amplifier offset and drift.

The reflected optical signal from the sensor head was detected using a general purpose silicon photodetector (BPX65). A schematic of the photodetection circuitry is shown in figure 7.12. A transimpedance amplifier was used to amplify the photodiode output signal. If the laser diode was being used in pulsed mode operation, then the pulsed behaviour would be removed using synchronous detection by means of an analogue switch (Siliconix DG211CJ), after which the signal may be filtered and buffered for output to the next signal conditioning stage. If the laser is being driven c.w., the last two stages are not required as the output signal may be taken directly after amplification.

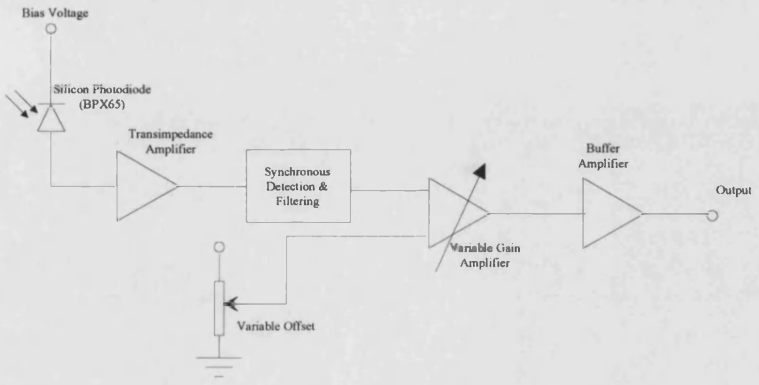

Figure 7.12. Schematic of photodetection circuitry.

The fibre-air interface present within the sensor head causes a back reflection, which returns some light to the photodetector which has not even reached

the grating. This leads to a time invariant signal to be present in the photodiode signal which cannot be removed by synchronous detection. Simply AC coupling the signal would not be appropriate since the sensor is required to track changes in position over long timescales, where the body under test may move only occasionally. A variable gain differential amplifier was therefore used in order to reduce this unwanted component and to amplify the remaining signal to a voltage level suitable for input to a computer data acquisition board for digital signal processing. The use of angle cleaved fibre connectors will also further reduce this effect.

All the electronics required for sensor operation was housed within a single electronics module (the sensor control unit) along with the fibre-optic couplers. This allowed the sensor head to be completely remote and connected to the sensor control unit using only optical fibre.

7.4.5. Computer Decoding of Signals

To achieve greater flexibility in developing a working system for the initial prototype, it was decided that decoding the electronic signals by computer would be more convenient than using electronic hardware. This leads to the constraint that the system decoding will not be as fast when using available facilities - thus limiting the maximum allowable speed of the grating for satisfactory sensor operation. However for the development of a prototype, speed is not of immediate concern since once successful sensor operation has been established, the algorithms used for decoding can be implemented within a fast, low-cost digital signal processing (DSP) system to provide successful sensor decoding at a suitable sample rate.

During the development of this prototype a PCL812 personal computer data acquisition board was used to acquire the signals, which were then subsequently decoded by compiled BASIC code running on a 286 PC.

The basic structure of the program used for decoding and display of results is described schematically in figure 7.13. After initialisation of the graphics display and the data acquisition card, the decision levels for assigning states for both input

channels are allocated. In order to carry this out, the system monitors a few periods of motion of the sensor. From this initial movement the discrimination levels can be set, allowing for normal incremental sensing to be achieved. From this point onward the sensor successively samples the input from both channels and displays the calculated incremental data. This state of operation continues until the required initial movement has been carried out to allow the absolute position of the sensor to be determined.

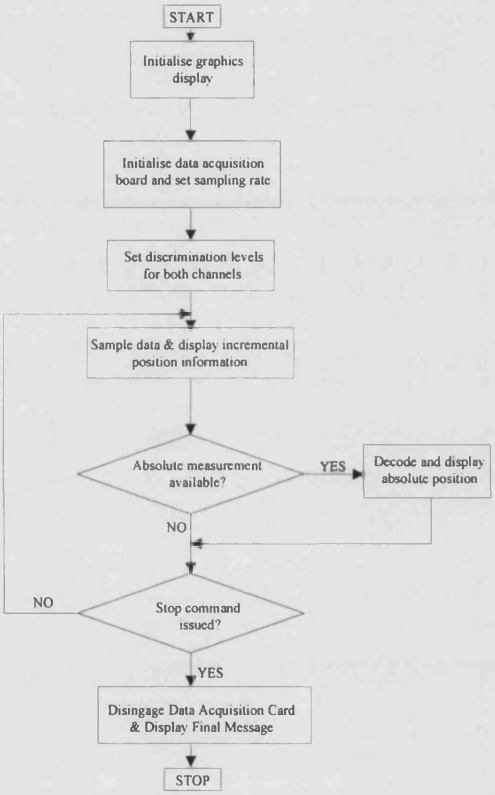

Figure 7.13. Flow diagram of control program basic structure

Decoding the PRBS track signal is quite straightforward as only one binary threshold decision level is required to resolve the reflected waveform from the PRBS into one of two states. However, the decoding of the AS track is more complicated due to the fact that there are not just two, but three possible levels which could be assigned to a particular data sample. The main difficulty in decoding the AS grating arises when the grating passes from a low to a high state directly, briefly passing through a region with values which lie between the discriminator levels defining the high and low regions. This is due to the finite slope in the transition between the low

and high regions of the reflection response profile. This is limited by the relative spot size of the incident optical signal. If a data sample was to be taken within this region the signal level may well be incorrectly decoded as being intermediate, thus giving an erroneous result suggesting that the body under test has changed its direction of motion.

To avoid an incorrect level assignment a 'state algorithm' approach to this problem was undertaken. The state diagram used to decode the 15μm asymmetric grating is shown in figure 7.14. This takes into account the present and past states of the asymmetric grating with respect to the two discriminator levels. In addition the occurrence of maxima and minima in reflected optical power caused by the grating structure within the intermediate region are also monitored, to provide correct decoding of this channel.

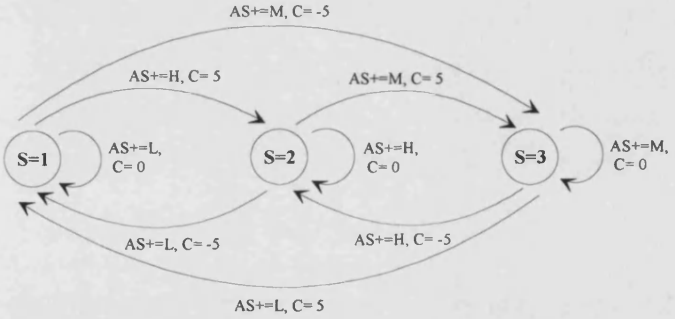

Key To State Diagram
AS+ = Next data point from AS grating. Can take one of 3 values;
H - data point above the highest discriminator level
L - data point below the lowest discriminator level
M - neither of the above plus a local maximum or minimum has been detected
C = Change in the displacement in microns
S = State variable

On switch-on the following states are assigned
AS=H - S=2, AS=L - S=1, AS=M - S=3

Figure 7.14. State Diagram Used for Decoding the AS Grating.

An auto-scaling algorithm is included within the software, which continually checks and alters the discrimination levels for both grating tracks. This is done to allow correct decoding of signals when the focus of the lens system changes from the optimum (i.e. walk-off due to slight changes in the position of the lens with respect to the grating over the full range of travel of the grating) or the detected offset voltage changes due to temperature effects etc. These disturbances have the

effect of changing the strength of the received signal. The algorithms used to achieve this are of a simple nature and should pose no problem for future implementation into a DSP system or discrete hardwired electronics.

7.5. Performance of the Prototype Sensor

To demonstrate correct operation of the prototype sensor some sample results are given in figures 7.15 and 7.16. These figures illustrate the decoding of displacement as a function of time, and can be compared with the reflectivity data points for the asymmetric grating. In each case the sensor has been moved using a motorised micrometer.

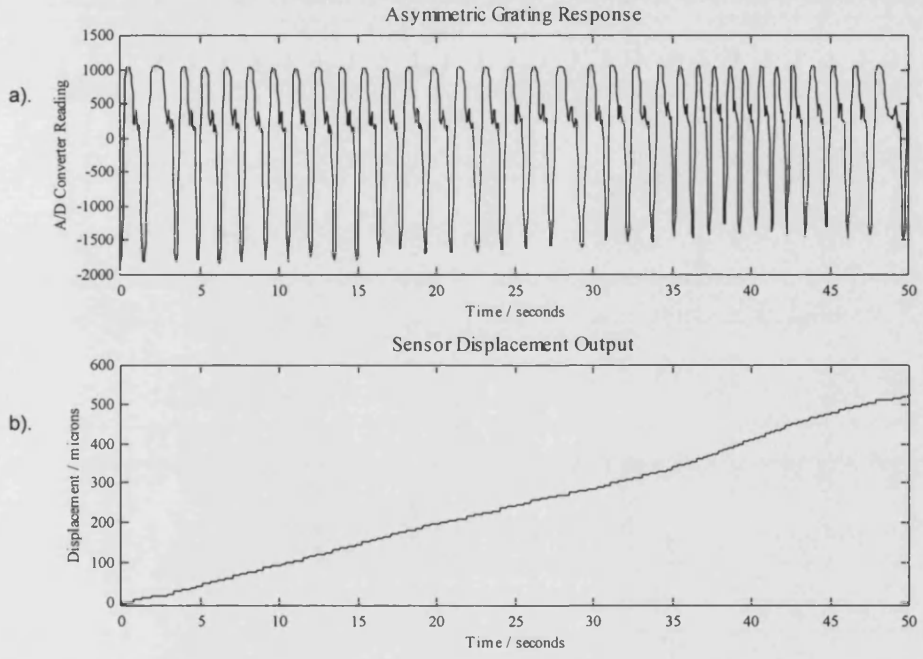

Figure 7.15. Plot showing calculated displacement against time for sensor operation.

Figure 7.15 shows a unidirectional scan of the grating. It can be seen that the discrete 5μm step increases in the inferred displacement measurement correspond to every third of a period of the asymmetric grating scanned. In contrast, figure 7.16 demonstrates successful bi-directional movement determination. During this scan, two changes in the direction of motion have occurred. It can be seen that both changes in direction present in figure 7.16.*a* are evident in the inferred displacement reading of 7.16*b*.

In addition to the correct operation of the AS grating in an incremental mode demonstrated by figures 7.15 and 7.16, the PRBS scale allowed absolute position measurements to 'kick-in' after the required minimum unidirectional movement had taken place. After this had occurred, the display of the sensor was updated in terms of the absolute position of the grating rather than in an incremental form.

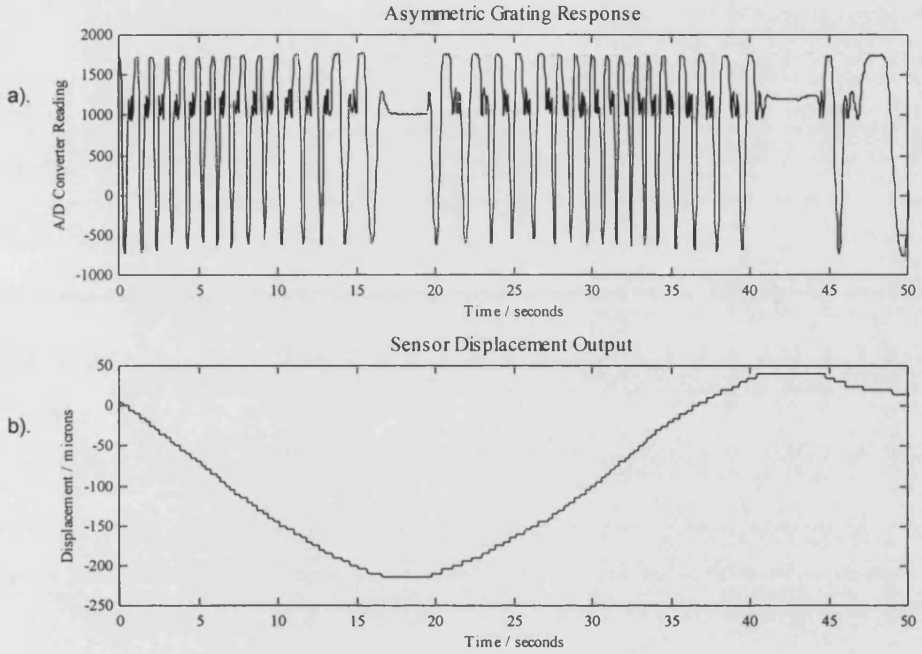

Figure 7.16. Plot showing calculated displacement against time for sensor operation.

It was found under operation that correct decoding of the AS signal was achieved even when the magnitude of the periodic variations was less than an eighth of its optimum, due to a walk-off from focus. However the decoding does eventually break down when the shape of the profile changes sufficiently so that certain key points such as maxima and minima within the mid region cannot be distinguished.

It is calculated that the maximum speed of the grating that can be tolerated in order to provide correct sensing action is approximately $0.3mms^{-1}$ for this software driven prototype. However this figure could be improved by using either a *hardwired* digital electronics architecture or a programmed DSP solution, to carry out decoding of the signals. This would increase the maximum allowable grating velocity to around 10 ms^{-1} which is greater than most commercial optical encoders [20]. This figure is obtained by assessing the number of samples required per period

of the asymmetric grating and considering the sample rate of fast ADCs currently available (>10Ms per sec).

Finally, while the grating sensor used in the prototype sensor demonstrated the successful operation of the measurement principle to a resolution of 5μm, subsequent grating design enhancements have allowed an improved grating to be fabricated. This has been designed to produce a resolution of 2μm over a range of 10.2cm. This equates to 0.002% of the full scale range. This required the design of a PRBS of order 15 and bit width 6μm. It is hoped that this grating will be used in a pre-production prototype system in the near future.

7.6. Measurement Errors and Performance Limitations

7.6.1. Measurement Resolution and Errors

Every measurement device is subject to measurement errors of varying degrees. This sensor is no exception. Due to its design and concept the sensor has a resolution which is one third of the period of the asymmetric grating. This can be verified by examination of figures 7.15 and 7.16. Therefore the resolution of the sensor is governed purely by the period of the AS grating and the bit width of the PRBS which are used, as long as the correct illumination spot size is used.

The precision of the sensor, however, depends upon the mechanical linkage between the sensor and the body under test. If there is any hysteresis involved in this coupling then this will result in a poor precision. In reality the precision of the sensor is a function of the mechanically engineered sensor mounting and not the sensor itself. Nonetheless, only reasonable mechanical coupling is required to provide sufficient performance such that the limiting factor on system accuracy is the inherent resolution of the sensor. It should also be noted that thermal expansion of the linkage may lead to an error. This would be linked together with other thermal effects, such as the thermal dependency of the grating and mechanical bearings used. However, this effect is inherent in any sensor such as this which relies upon a mechanical coupling to the body under test.

The accuracy of the sensor is limited by a number of factors. Firstly, any variation in the reproduction of the asymmetric grating from period to period may affect the accuracy of the sensor, if the variation is large enough. As previously explained, the master mask was copied commercially using contact photolithography copying processes. Whilst these processes do allow copies to be made at low cost, a limit on the smallest feature reproducible with these processes is imposed. The origins of this resolution limit being due to diffraction effects in the contact copying process, which will appear to smear out features of less than 1μm dimension. Typically, only structures of 2μm and above are guaranteed commercially [21]. However, on inspection, it was found that the quality of the copies actually produced was accurate to approximately ±0.2μm for 1μm features. It was also noted that the quality of small features near to the edge of the mask, were reproduced better than those at the centre of the mask. This was due to improved contact between the master and the copy mask at their edges during the copying process, so limiting unwanted diffraction effects.

The second factor that must be considered is that the original mask manufacturing process is only accurate to 0.1μm. Therefore the mask with a smallest feature of 1μm may have a 10% error associated with it on the master. This error may be further accentuated by the copying process.

However, the small feature variations on the mask have only limited effect on the final sensing process, since linewidth variations will only result in slight variations in the reflection response of the gratings. In most cases, this will only serve to introduce an error which is a fraction of the resolution produced by the grating design.

Finally one further source of error that may be present is due to the misalignment of the grating with respect to the direction of motion. This is depicted in figure 7.17. If there is a misalignment of angle θ between the direction of movement and the normal to the grating structure then a measurement displacement d_{meas} is related to the actual displacement d_{act} by;

$$d_{meas} = d_{act} \cos\theta \qquad (7.5)$$

which means that a misalignment of the grating of 2 degrees leads to a percentage error of 0.06%. While over short movements this error is very small, it does become noticeable over larger displacements. For example, a 2 degree misalignment will lead to an under measurement of ~30 microns over a displacement range of 5cm.

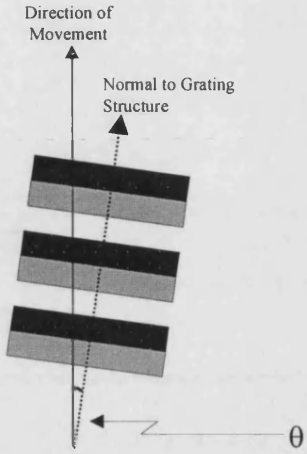

Figure 7.17. Effect of mis-alignment of grating (θ is the angle of misalignment).

This requires that during sensor head assembly, care must be taken to align the grating to a tolerance which provides a maximum error over the full measurement range which is less than the sensor resolution.

Therefore taking all the above sources of measurement error into account, as long as the grating is well aligned with respect to the direction of motion, the maximum measurement error in normal operation would be likely to be ±5μm. However, further long-term testing of the system is recommended in order to test the 'error rate' produced in the decoding of the asymmetric grating scale. A study of this kind will determine whether this eventuality is also an important factor to be taken into consideration.

7.6.2. Limitations of Operation

Other limitations to the operation of this sensor must be considered. Firstly, as a multimode optical fibre system has been employed, this may be susceptible to mode selective loss. In the 2x2 fibre coupler the sections of fibre are fused together, and some of the spatial modes of the fibre will couple into one port of the coupler, whilst other spatial modes will be coupled into the second port. Consequently, if the

fibre is subject to a disturbance some of the light which was previously being guided in one mode, may then be excited into another. The portion of the returned light may then as a consequence exit the coupler through a different port to that in the case when no disturbance was present. It may even be coupled into a radiative mode and be lost.

This mode selective loss manifests itself as amplitude noise superimposed upon the desired reflection variations in the detected signal. When a severely violent disturbance was applied to the system described above, noise levels typically as high as 20% of the normal periodic reflection induced signal variation were found to be resultant. However for milder measures of disturbance, more in keeping with what might be generally expected within the normal operation of the sensor, the sensor operated successfully with no adverse effects or errors induced by the applied disturbances.

The ideal sensor produces an output which is a function of one variable only. Unfortunately, in the real world this is rarely the case. When considering the limitations of operation of the sensor one would have to consider the mechanics of the sensor head design and how much it would be affected by external factors. Since the prototype sensor was designed only to provide a proof of the general measurement principle, to analyse its performance with respect to any factors outside the general sensor response in too much detail would be inappropriate. However, when an improved prototype or commercial device is fabricated the sensor should be subjected to a detailed testing programme to prove its reliability in a industrial environment.

7.7. A Single Mode Fibre Based Version of the Sensor

As explained in the previous section, the multimode fibre system was affected by mode selective noise. To combat this, a single mode fibre version of the sensor was examined in order to test its feasibility. Whilst single mode fibre has the disadvantage of being potentially more awkward for use in an intensity modulation system of this kind due to more exacting alignment procedures, it is far more

immune to mode selective noise. In addition, due to the design of the imaging system used in the multimode fibre arrangement, a high degree of optical loss was prevalent which provided a return signal of extremely small modulation index. The single mode fibre system however, when used with a fibre lens, should provide a much lower loss figure and hence an inherently more stable return signal from the grating. To test these assumptions, some experiments were therefore carried out to assess the suitability of single mode fibre for this sensor.

7.7.1. Experimental Arrangement

A simplified sensor system was used to test the suitability of single mode fibre as shown in figure 7.18. As only initial tests were being carried out the sensor was reduced to its individual components for testing purposes.

A section of grating GT15 was used for this test. The light incident upon the grating was generated by a suitable laser diode of emission wavelength 1550nm which was in this case a Toshiba DFB laser (TOLD335S). A similar fibre architecture was used as before in the multimode case but now single mode fibre components were used. Also, rather than using a single Selfoc lens as before, a fibre lens (Nortel) was used in order to form a spot upon the grating.

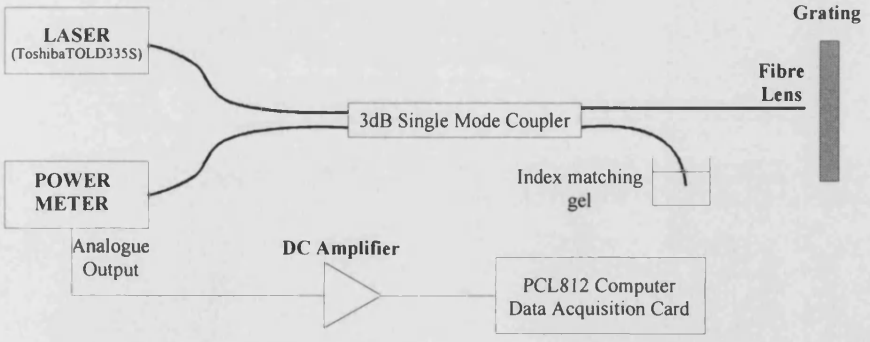

Figure 7.18. Experimental arrangement for testing single mode fibre sensor system.

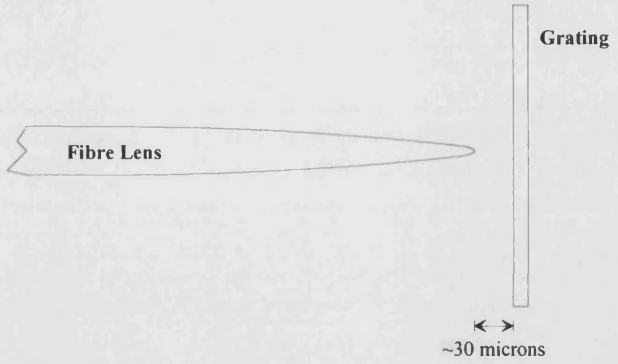

Figure 7.19. Schematic representation of alignment of fibre-lens to grating.

In order to carry out a measurement the grating was moved with respect to the lens, and a characteristic reflection response was obtained, which was dependent upon the pattern of the grating.

7.7.2. Response of Single Mode Fibre System

The characteristic response achieved with optimum lens to grating separation is given in figure 7.20. It can be clearly seen that the fine structure present in the intermediate region of the asymmetric grating structure can be distinguished by the single mode fibre system, thus demonstrating that the system can be operated successfully with a single mode fibre arrangement.

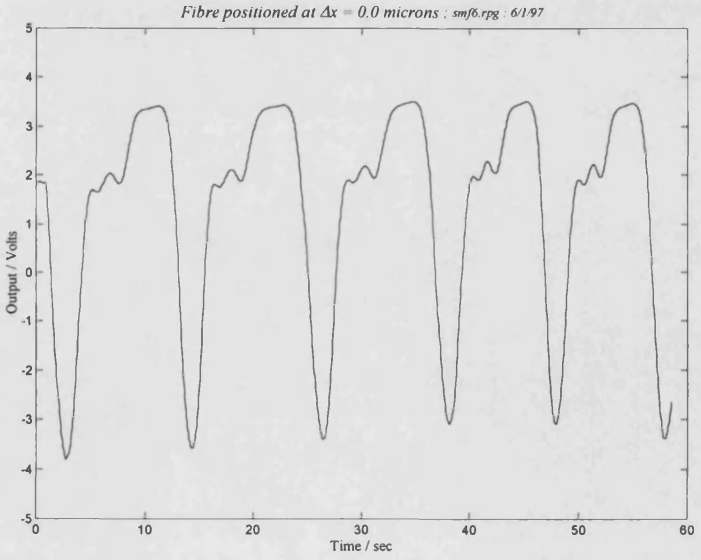

Figure 7.20. Reflection response from grating GT15 using single mode fibre addressing system.

The optimum fibre lens/grating separation was defined as the separation at which the intensity of the reflected signal was a maximum. It was found that with the particular fibre lens used in this case, the optimum separation was found to be 30 microns. It was found that the tolerance of the separation was greater than ±5 microns. Over this range of misalignment a reflection profile suitable for decoding could be achieved.

7.7.3. Comparison of Singlemode and Multimode Sensor Arrangements

The results presented in the previous section, show that the single mode fibre variant of the sensor can be used to satisfactorily address the reflection grating. In order to directly compare the single-mode and multimode configurations, the optical loss in the addressing system was measured for an optimum reflection from the grating. The optical loss in the sensor was defined as the loss of optical power from the fiberised input to the sensor head, to the received power by the photodetector for an optimally high reflection for the grating, (neglecting the 3dB loss incurred in the return signal due to the fibre coupler). It was found that the single mode fibre system was subject to a loss of 1.5±0.3 dB, whilst the multimode fibre arrangement was found to have a loss of 10.3±0.3dB. This shows that while the multimode fibre system demonstrates ease of coupling of the optical source into the fibre, it suffers from the serious drawback of losing the majority of the optical signal within the sensor head. This is entirely due to the fact that a single lens system was used in the configuration shown in figure 7.10, which whilst providing high magnification, suffers from being highly lossy.

Furthermore, if the modulation depth of the sensor in both configurations is measured for grating track GT15 it was found that for the single mode fibre system a modulation depth of 12.5dB is obtained, whilst the multimode configuration attains a modulation depth of only 0.3dB. Due to the large amount of loss suffered by the multimode system, the returned signal consists of a large dc component upon which the reflection variations are superimposed. As the singlemode system is not subject to these initial losses, a much higher modulation depth results.

This increase in modulation depth also means that the decision levels required for digitisation of the input signals are less likely to waver. These improvements in the returned signal strength and modulation depth allow a more stable system to be constructed which is far less likely to incorrectly identify the states of the particular gratings.

Considering these experimental results, it can be seen that the single mode fibre arrangement overwhelmingly outperforms the multimode system in terms of loss and modulation depth. Also, considering figures 7.10 and 7.19, the single mode system could provide a much smaller sensor head package due to the close proximity of the optical components required. However, to become a practical solution the fibre lens used in the single mode system must be positioned with a tolerance of ±5μm relative to the grating over its complete range of travel. Obviously this requires a high quality mechanically engineered stage to be produced. However, when one considers that the tolerance required for the positioning between the grating and the Selfoc lens used in the multimode system is of the order of ±10μm then the required improvement isn't too significant. However, it should be remembered that in order to produce a successful commercial device, the optical system will be designed after considering all the relevant parameters including component cost, positioning tolerance and optical throughput efficiency. This may dictate the use of a two element lens system which may relax the positioning requirements (i.e. increase the working distance and tolerance of the lens with respect to the grating). However, considering the small spot size required on the grating, conventional lenses are not ideally suited due to their inferior diffraction limited performance when compared to Selfoc, ball and fibre lenses.

7.8. Conclusions

A novel sensor has been constructed utilising a pseudo-random binary sequence to allow absolute position determination in conjunction with an asymmetric periodic grating. This grating is addressed using solely optical means

leaving the sensing head free of any electrical signals. Therefore, the sensor system may be applied to intrinsically safe sensing applications.

It can be seen from figures 7.15 and 7.16 that the sensor can correctly measure displacements with a resolution of 5μm. This is limited by the design of the asymmetric grating. The initial prototype of the sensor achieved a working range of 4 cm which was limited solely by maximum mechanical stage movement, with a maximum working grating velocity of $0.3mms^{-1}$. The maximum velocity was limited by the signal processing required to decode the received signal from the sensor head. In the case of the initial prototype this decoding was carried out by software running on a relatively slow computer. However, considering the simplicity of the control algorithms used, if the decoding system is implemented as a hardwired electronics system, or in a DSP architecture it is envisaged that the maximum grating velocity would be increased to approximately $10ms^{-1}$.

Multimode optical fibre was utilised in order to address the sensor head of the initial prototype. However, the performance of a single mode fibre sensor addressing system was subsequently investigated and found to be superior to that of the initial multimode fibre system. It has been shown that the single mode fibre was far less lossy, with an optical power loss of 1.5dB compared with 10.3dB for the multimode fibre system. Furthermore, the modulation depth obtained with single mode addressing is 12.6dB compared with 0.3dB for multimode addressing. A discussion of the possible measurement errors has been included with the conclusion that a typical sensor operating in the same manner as the prototype would have a measurement error of ±5μm. Minor improvements to the grating design should allow resolutions down to 2μm over measurement ranges of up to 10cm.

7.9. References

[1] CSO de Measures, Grenoble, France, "HC250 micro-laser interferometer", Product catalogue, January 1995.

[2] Dr. Johannes Heidenhain Gmbh, Traunreut, Germany, "NC linear encoders", Product catalogue, September 1993.

[3] A.T.Shepherd, "25 years of Moiré fringe measurement", *Precision Engineering*, **1**, pp.61-69, 1979.

[4] J.-D.Lin and H.-B.Kuo, "Development of a new optical scale system by the diffractive phase interference method", *Meas. Sci. Technol.*, **6**, pp.293-296, 1995.

[5] M.Durana, R.Gallay, Ph.Robert and F.-C.Pruvot, "Novel type submicrometre resolution pseudorandom position optical encoder", *Electron. Lett.*, **29**, No.20, pp.1792-1794, 1993.

[6] E.M.Petriu, "Scanning method for absolute pseudorandom position encoder", *Electron. Lett.*, **24**, No.19, pp.1236-1237, 1988.

[7] E.M. Petriu, "Absolute-type position transducers using a pseudorandom encoding", *IEEE Trans. Inst. & Measmnt.*, **IM-36**, No.4, pp.950-955, 1987.

[8] B.Arazi, "Position Recovery Using Binary Sequences", *Electron. Lett.*, **20**, No2, pp.61-62, 1984.

[9] A.M.Scheggi, M.Brenci, G.Conforti, R.Falciai and A.G.Mignani, "Optical Fiber Displacement Sensor", Proc. *SPIE Vol. 798 Fiber Optic Sensors II*, pp.72-75, 1987.

[10] P.T.Gardiner and R.A.Edwards, "Fibre optic position sensing for aircraft flight control systems, *Fibre Optic Sensors,* IoP Short Meetings Series, Bristol, 1987.

[11] M.Maghoo, "A wavelength encoded rotary displacement fibre sensor", *Meas Sci. Technol.*, **5**, pp.260-266, 1994.

[12] K.Fritsch and G.Beheim, "Wavelength-division multiplexed digital optical position transducer", *Optics Lett.*, **11**, No.1, pp.1-3, 1986.

[13] B.E.Jones and K.Zia, "Digital displacement transducer using pseudo-random binary sequences and a microprocessor", *Trans Inst. Meas. Control*, **3**, No.1, pp13, 1981.

[14] J.T.M.Stevenson and J.R.Jordan, "Absolute position measurement using optical detection of coded patterns" *J. Phys. E: Sci. Instrum.*, **21**, pp.1140-1145, 1988.

[15] F.J.MacWilliams and N.J.A.Sloane, "Pseudo-random sequences and arrays", *Proc. IEEE*, **64** , pp.1715-1729, 1976.

[16] W.Stahnke, "Primitive binary polynomials", *Math. Comput.*, **27**, pp.977-980, 1973.

[17] R.P.Griffiths and I.H.White, GB Patent Application No. GB9602772.7, 1994

[18] P.J.Hallowell, Notes for Users of Central Microstructure Facility, Rutherford Appleton Laboratory, 1991.

[19] Selfoc lens catalogue, Nippon Glass Company.

[20] R.P.Griffiths, "A market assessment of position sensing technology", *Internal Report*, RDP Electronics Ltd., March 1998.

[21] Private communication with A.Strathe, Managing Director, Compugraphics Ltd., Glenrothes, Scotland, UK

CHAPTER 8

CONCLUSIONS

A novel optical technique for absolute position measurement has been demonstrated in chapter 2, which uses a semiconductor laser diode that is subjected to delayed optical feedback from a target reflector. The sensor has been designed for medium range measurement applications which typically cover distances varying from several centimetres to a few metres, for which the production of cost effective, robust, optical techniques has proved difficult. This 'resonant cavity optical position sensor' operates by using an extremely simple optical configuration, which requires only a single optoelectronic component. Therefore, it may be engineered so that it is not only rugged and stable, but also potentially low cost. The sensor operates with low optical powers and may be implemented either as a free-space sensor or a fibre-coupled sensor for use in intrinsically safe sensing applications. Furthermore, it has been shown that the sensor is not device specific, with operation using a wide variety of devices demonstrated. These include VCSELs, conventional Fabry-Perot lasers and also AR coated devices.

Unlike other proposed applications which measure distances by subjecting a semiconductor laser diode to delayed optical feedback, this novel arrangement monitors the frequencies of RF beat modes generated within the laser diode to produce an accurate position measurement. By biasing the laser appropriately with a constant current, optical feedback from a target reflector causes the laser to oscillate in a number of modes which are determined by the external cavity. These lasing modes beat together and generate an RF signal within the laser diode, which manifests itself as a variation in the junction voltage of the laser. If the frequency spectrum of this voltage is monitored, a series of peaks can be observed. The frequencies of these RF peaks correspond approximately to the round trip frequency of the external cavity and its harmonics. Measurement of the frequencies of these

resonance peaks allows the external cavity length to be measured. Therefore the absolute position of the target reflector can be determined.

To date, this sensor has been operated with optical path lengths of up to 4 metres. This maximum operating range is imposed by practical, physical space constraints. However, operation of a fibre-coupled version of the sensor has been demonstrated with a cavity consisting of over 100m of optical fibre which was used to address a bulk optical sensing cavity of approximately 1m length. Successful operation of the sensor using a variety of different cavity configurations and lengths has been demonstrated. This illustrates the fact that the sensor may potentially be applied to a wide variety of different applications. Studies carried out to date have not demonstrated an obvious limit on the external cavity length. In the case of the free space sensor, it is likely that beam divergence will be the major limiting factor. However, for the fibre coupled sensor configuration, it is presently not clear what limitations may exist.

The sensor outlined above has been shown to provide a resolution of 2μm over a measurement range of 30cm when operated in combination with an on-line electronic interfacing system. In this case the slope detection method described in chapter 5 was used to interface with the optical system and provided a real-time analogue output voltage. In general, this method of interfacing has been found to be best suited to applications where high resolution, and/or high dynamic response is required. For applications where larger displacement ranges are to be measured, it was generally found that the swept source heterodyne downconversion interfacing method was better suited to covering the larger ranges of frequency separation which are encountered.

The downconversion system works in an analogous way to a spectrum analyser in that it provides an output signal which is an accurate time-domain representation of the frequency spectrum of the input signal. In order to demonstrate the suitability of this approach, a prototype version of this system was constructed. This was designed for the measurement of external cavity lengths greater than 25cm. When operated with cavity lengths of up to 1.25cm, it was found that an initial

measurement accuracy of 0.1% was obtained. The lower limitation on external cavity length is imposed due to the finite frequency bandwidth and maximum frequency sweep range of the heterodyne downconversion system. Currently, the electronic techniques which have been used to interface with the optical system are undergoing further development in order to improve the stability and general performance of the sensor. It is hoped that an order of magnitude improvement can be achieved with careful system design.

In order to assess the stability of the experimental systems developed to date, investigations were carried out to ascertain what effect changes in physical parameters such as bias current and feedback strength have upon the output of the sensor. It was found that when subjected to extreme variations in these parameters, a shift in the frequencies of the resonance peaks was observed. However, it was also found that each of the resonance peaks were affected equally by these variations. Considering this, it is recommended that for enhanced stability, the separation between the resonance peaks be measured rather than the absolute frequency of a single peak. For example, when the bias current to a VCSEL was varied over the full operating range, a measurement carried out in this manner was found to be subject to a variation of 0.5% of the resonance peak separation. It should be noted though that at the extremes of operation, this value was limited by the inherent measurement error. However, when the applied bias current remained within 2% (±0.05mA), of the ideal operating current, a variation of less than 0.05% was obtained.

It has therefore been demonstrated that the experimental sensor configuration is capable of relatively stable operation under general conditions, with the measurement of the frequency separation between the peaks providing the most stable means of operation. If operation in demanding environments or if extremely high accuracies are required then feedback control systems can be used to maintain constant operating levels, to compensate for variations in parameters such as bias current and temperature. If properly designed, these should also be able to cope with effects such as the ageing of the laser and difficult operating environments.

Analysis of the experimental results shows that, the dynamic behaviour of resonance peaks is inexorably linked to the behaviour of the low frequency fluctuation (LFF) present in the frequency spectrum. There has been much conjecture as to the direct cause of the LFF, however, the results in this thesis suggest that it is generated by the beating of external cavity modes which are closely spaced in frequency. It is likely that the resultant beat signals that are produced by the modes are then further enhanced by spontaneous effects.

Experimental results have shown that the offset present on the frequencies of the resonance peaks is equal to the value of the LFF. It has also been found that any dynamic change in the LFF leads to an equal shift in the frequencies of the resonance peaks. These do not vary in a harmonic way and so the frequency separation between the modes remains unchanged. This leads to the observations regarding stability of measurement discussed above. Therefore, it would be an advantage if the effects of the LFF could be minimised. Accordingly, it has been shown that this may be achieved by using an anti-reflection (AR) coated laser. Consequently, the potential stability of the sensor in many applications may be improved through the use of a suitable AR coated device.

In order to fully understand the operation of the optical system used in the sensor, a substantial theoretical analysis has been carried out. While the optical system is itself quite simple in construction, the dynamic physical effects which it produces are quite complex. Two separate methods have been used to analyse the sensor arrangement in this thesis. The first method used a steady-state approach which is simple in concept, allowing an excellent insight to be gained into the physical processes connected with the operation of the system. This technique considered the complex effective reflectivity which exists at the front facet of the laser cavity due to the optical feedback from the external reflector. Analysis of this function allows the distributions of allowed external cavity modes to be developed, which in turn can be used to produce reasonable theoretical predictions for the beat frequency output spectrum. However, due to the steady-state nature of the technique,

the evidence of many dynamic effects observed experimentally cannot be reproduced by this model.

Therefore, in order to assess the dynamic behaviour of the system, an elaborate rate equation model was developed, which applied delayed optical feedback to the laser. This has been found to be very successful in confirming the existence of a variety of dynamic effects which have been observed in practice. It is envisaged that future work will be carried out in order to provide predictions of the system which are more quantitative in nature and may be used to further optimise the configuration of the optical system for particular applications.

The resonant cavity optical position sensor system holds a distinct advantage over many other, otherwise excellent systems, due to the inherent simplicity of the optical arrangement used to construct the sensor. While a variety of optical configurations may be used, (these being selected according to the application area), it has been shown that the sensor may be constructed using only three optical components which are mounted along the same optical axis. This reduces the complexity of the engineering required to enable successful operation of the sensor. This in turn allows the production of systems capable of high stability operation and rugged performance in demanding industrial applications. At the time of writing further work is being undertaken into the development of prototype optical measurement heads. It is hoped that along with the further development of electronic signal processing modules, these prototype heads will form the springboard for a series of successful products based upon this system.

Finally, in chapter 7 the operation of a separate, absolute optical position sensor was described which operates by using a novel coded grating to modulate an optical signal as a function of position. This used a pseudo-random binary sequence (PRBS) to provide an unambiguous measure of the absolute position of the body under test (to which the sensor is mechanically linked). This is in contrast to most optical encoders which provide only incremental operation. The PRBS was encoded onto the grating in parallel with a periodic asymmetric grating. When operated alongside the PRBS track, this novel grating design allowed the position to be

determined using a minimum of only two reading heads. Considering the low number of read heads required for operation, a cost effective sensor may be constructed which exhibits good stability. Furthermore, the unique design of the grating allows an intrinsically safe system to be developed by using solely optical addressing of the sensor head.

A prototype system was developed in order to demonstrate the successful operation of this sensor. This was found to provide a resolution of 5μm over a 4cm range. Subsequent design improvements have lead to the production of gratings capable of providing 2μm resolution over a 10cm range. As the accuracy of the device should, at worst, be only twice the resolution, this equates to a fractional accuracy of 0.004% of full measurement range. Other optical encoders which produce this degree of accuracy typically have to rely upon the accurate analogue interpolation of Moiré fringe output signals. However, this novel grating system produces an output which is inherently digital. This provides excellent stability and increased immunity from effects such as amplitude noise, temporal changes in fibre losses and grating contamination.

Final designs are currently being considered before the development of a pre-production prototype of this sensor. This will be designed primarily for intrinsically safe and aerospace applications, where it should exhibit an enhanced performance when compared with current technology within these areas.